# Abstract

Title of Dissertation: ANALYSIS OF ROTOR WAKE AERODYNAMICS DURING MANEUVERING FLIGHT USING A FREE-VORTEX WAKE METHODOLOGY

Shreyas Ananthan, Doctor of Philosophy, 2006

Dissertation directed by: Minta Martin Professor J. Gordon Leishman
Department of Aerospace Engineering

The problem of helicopter rotor wake aerodynamics during maneuvering flight conditions was analyzed using a time-accurate, free-vortex wake methodology. The free-vortex method consists of a Lagrangian representation of the rotor flow field using vortex elements, where the evolution of the flow field is simulated by tracking the free motion of these vortex elements and calculating their induced velocity field. Traditionally, free-vortex methods are inviscid, incompressible models, but in the present approach the viscous effects are incorporated using a viscous splitting method where the viscous and inviscid terms are modeled as successive sub-processes. The rotor aerodynamics and rigid blade flapping dynamics are closely coupled with the wake model and solved for in a consistent manner using the same numerical scheme.

Validations of the methodology with experimental data were performed to study the wake response to perturbations in collective and cyclic pitch inputs. The numerical

simulations captured all the essential wake dynamics observed in flow visualization. The predictions of the transient inflow and airloads response were found to be in excellent agreement with the available experimental measurements. It was observed that the rotor wake was extremely sensitive to perturbations in collective and cyclic blade pitch inputs. The characteristic wake response was found to be the bundling of the wake vorticity into a vortex ring structure. The evolution, convection and subsequent breakdown of this bundled ring of tip-vortices was found to be highly nonlinear, and occurs with a temporal lag. The nonlinear induced velocity field associated with unsteady wake evolution can cause considerable fluctuations in the rotor airloads time-history if the bundled tip-vortex structure comes into close proximity to the rotor blades. Furthermore, the interaction of these tip-vortices with the blades results in steep gradients in the rotor airloads across the rotor disk, thereby contributing to impulsive rotor noise.

Several free-flight maneuver simulations were analyzed to gain better insight into the unsteady, nonlinear wake development under high-rate, large-amplitude maneuvers such as roll to starboard or port, roll reversals, and the quickstop maneuver. It is shown that the rotor wake response in almost all maneuvering flight conditions is highly nonlinear and emphasizes the need to accurately predict the transient wake aerodynamics to obtain accurate estimates of the unsteady rotor airloads and the resulting rotor acoustics.

# ANALYSIS OF ROTOR WAKE AERODYNAMICS DURING MANEUVERING FLIGHT USING A FREE-VORTEX WAKE METHODOLOGY

by

Shreyas Ananthan

Dissertation submitted to the Faculty of the Graduate School of the
University of Maryland, College Park in partial fulfillment
of the requirements for the degree of
Doctor of Philosophy
2006

Advisory Committee:

Minta Martin Professor J. Gordon Leishman, Chairman/Advisor
Professor Roberto Celi
Professor Inderjit Chopra
Associate Professor James D. Baeder
Associate Professor Jian-Guo Liu, Dean's representative

# Acknowledgements

I take this opportunity to thank everyone who has, directly or indirectly, helped me in my research endeavour at the University of Maryland. I have great pleasure in expressing my deep sense of gratitude to my advisor, Prof. John Gordon Leishman, for his keen interest and critical evaluation of my work. Over the last five years, he has constantly set me against challenging problems, which have motivated me to work harder, helped me better understand the underlying physical principles, and stay focused on the ultimate goal. Without his encouragement and constant guidance, this thesis would not have seen the light of the day.

I would like to sincerely thank my advisory committee, Professors Inderjit Chopra, James Baeder, and Juan Guo Liu, for their support and encouragement. Special thanks are due to Prof. Roberto Celi for his guidance in the simulation of maneuvers; his suggestions contributed greatly in the improvement of the present work.

The joint research effort with Prof. Ken Brentner and his acoustics research group at Pennstate University has been a very enjoyable and rewarding experience for me. I would like to thank Prof. Brentner for providing me with the opportunity to work with his research group. Sam Chen, the graduate student with whom I worked on the maneuvering rotor aerodynamic and acoustic problem, deserves special mention for all the assistance he has provided me. Without the flight dynamics data provided by Sam, the analysis of free flight maneuvers would have been impossible. I thank him for his patience and perseverance, which proved crucial in successful completion of the research during our misunderstandings with the data transfers. Thanks are due to Chris Hennes for his help in the joint research effort.

Many thanks to my colleagues at the Rotorcraft Center, particularly Jaina Sitaraman,

Karthikeyan Duraisamy, Arun Isaac Jose, Carlos and Abhishek, for providing a friendly atmosphere. It was my pleasure to interact with them. I thank Manikandan Ramasamy and Sandeep Gupta for all the enlightening discussions, which helped me gain much insight into the subject matter. I was fortunate to be thrown in the company of Maria Ribera during my stay at University of Maryland. We have shared many pleasant memories and some anxious moments over the last five years. I am indebted to her for her help, support and encouragement which contributed greatly to the successful completion of this dissertation.

Last, but not least, I am eternally grateful to my parents who have sacrificed much so that I could pursue my dreams. To them, I dedicate this dissertation.

# Table of Contents

# List of Tables

# List of Figures

# Nomenclature

| | |
|---|---|
| $A$ | Influence coefficient matrix in Weissinger-L model |
| $A_1,\ A_2,\ b_1,\ b_2$ | Indicial response function coefficients |
| $A_{\mathrm{B}}$ | Influence coefficient matrix for bound circulation |
| $A_{\mathrm{NW}}$ | Influence coefficient matrix for near-wake circulation |
| $a$ | Sonic speed, $\mathrm{ms}^{-1}$ |
| $\mathbf{a}$ | Acceleration at the collocation point, $\mathrm{ms}^{-2}$ |
| $a_1$ | Turbulent viscosity constant |
| $C_d$ | Drag coefficient |
| $C_{d_0}$ | Zero-lift drag coefficient |
| $C_l$ | Lift coefficient |
| $C_{M_x}$ | Coefficient of rolling moment, $M_x/(\pi\rho\Omega^2R^5)$ |
| $C_{M_y}$ | Coefficient of pitching moment, $M_y/(\pi\rho\Omega^2R^5)$ |
| $C_P$ | Coefficient of rotor power, $P/(\pi\rho\Omega^3R^5)$ |
| $C_Q$ | Coefficient of rotor torque, $Q/(\pi\rho\Omega^2R^5)$ |
| $C_n$ | Normal force coefficient at the blade section |
| $C_T$ | Rotor thrust coefficient, $T/(\pi\rho\Omega^2R^4)$ |
| $e$ | Non-dimensional flapping hinge location |
| $f$ | Flow separation point as fraction of chord |

| | |
|---|---|
| $I_b$ | Mass moment of inertia of the rotor blade in flapping, kgm$^2$ |
| $\mathbf{i}, \mathbf{j}, \mathbf{k}$ | Unit vectors along the coordinate axes, m |
| $J$ | Jacobian matrix |
| $K_D$ | Empirical factor for nonlinear airfoil drag model |
| $l$ | Length of a vortex filament, m |
| $\mathbf{l}$ | Vector representing the vortex filament, m |
| $M$ | Local Mach number ($= \lvert\mathbf{V}\rvert/a$) |
| $M_A$ | Aerodynamic blade flapping moment, Nm |
| $M_I$ | Inertial blade flapping moment, Nm |
| $M_{\text{tr}}$ | Trace Mach number of a BVI sound source |
| $m$ | Mass per unit length of the rotor blade, kgm$^{-1}$ |
| $N_b$ | Number of blades |
| $N_s$ | Number of spanwise segments along the rotor blade |
| $\mathbf{n}$ | Unit normal vector at a blade collocation point, m |
| $p,\ q,\ r$ | Roll, pitch and yaw rates, rads$^{-1}$ |
| $R$ | Rotor radius, m |
| $R_H$ | Distance of the rotor hub from the center of gravity, m |
| $R_c$ | Root cut out, m |
| $r$ | Radial distance of a point on the blade from the rotation axis, m |
| $\bar{r}$ | Non-dimensional radial distance ($= r/R$) |
| $r_c$ | Viscous core radius of a vortex filament, m |
| $r_{c_0}$ | Initial core radius of a vortex filament, m |
| $\mathbf{r}$ | Position vector of collocation point, m |
| $S$ | Cross sectional area of a vortex filament, m$^2$ |
| $S_1,\ S_2$ | Empirical coefficients for nonlinear airfoil lift model |

| | |
|---|---|
| $\mathbf{s}$ | Material line segment, m |
| $t$ | Time, s |
| $U$ | Effective incident velocity at a blade section, $\mathrm{ms}^{-1}$ |
| $U_P$ | Normal velocity at a given blade section, $\mathrm{ms}^{-1}$ |
| $U_T$ | Tangential velocity at the blade section, $\mathrm{ms}^{-1}$ |
| $u,\ v,\ w$ | Components of velocity along principal axes, $\mathrm{ms}^{-1}$ |
| $\mathbf{V}$ | Velocity vector at collocation point, m |
| $\mathbf{V}_\infty$ | Forward flight speed of the helicopter, $\mathrm{ms}^{-1}$ |
| $\mathbf{V}_\mathrm{B}$ | Induced velocity component from bound circulation, $\mathrm{ms}^{-1}$ |
| $\mathbf{V}_\mathrm{FW}$ | Induced velocity component from free-vortex trailers , $\mathrm{ms}^{-1}$ |
| $V_i$ | Induced inflow velocity at a given blade section, $\mathrm{ms}^{-1}$ |
| $\mathbf{V}_i$ | Induced velocity vector at collocation point, $\mathrm{ms}^{-1}$ |
| $\mathbf{V}_\mathrm{man}$ | Velocity component introduced by helicopter maneuver, $\mathrm{ms}^{-1}$ |
| $\mathbf{V}_\mathrm{NW}$ | Induced velocity component from near wake trailers, $\mathrm{ms}^{-1}$ |
| $\mathbf{V}_\mathrm{v}$ | Convection velocity of a vortex filament, $\mathrm{ms}^{-1}$ |
| $V_\theta$ | Tangential swirl velocity associated with a vortex, $\mathrm{ms}^{-1}$ |
| $x,\ y,\ z$ | Cartesian coordinate system, m |
| $\mathbf{x}$ | Vector of control input parameters |
| $\mathbf{y}$ | Vector of response variables |
| | |
| $\alpha$ | Blade sectional angle of attack, rad |
| $\alpha_0$ | Zero-lift angle of attack, rad |
| $\alpha_1$ | Transition point corresponding to $f = 0.7$, rad |
| $\alpha_D$ | Drag divergence angle of attack, rad |
| $\beta$ | Semi-vertical angle of the radiation cone, rad |

| | |
|---|---|
| $\beta$ | Blade flapping angle, rad |
| $\beta_0$ | Blade coning angle, rad |
| $\beta_{1c}$ | Lateral cyclic flap angle, rad |
| $\beta_{1s}$ | Longitudinal cyclic flap angle, rad |
| $\Gamma$ | Circulation associated with a vortex filament, $m^2s^{-1}$ |
| $\Gamma_b$ | Bound circulation along the blade, $m^2s^{-1}$ |
| $\Gamma_t$ | Trailed circulation in the near wake, $m^2s^{-1}$ |
| $\Gamma_v$ | Circulation associated with a finite length filament, $m^2s^{-1}$ |
| $\gamma$ | Interaction angle of a vortex filament with the rotor blade, rad |
| $\Delta C_n$ | Change in normal force coefficient |
| $\Delta l$ | Change in the length of a vortex filament, m |
| $\Delta q$ | Step change in pitch rate, $rads^{-1}$ |
| $\Delta r_c$ | Change in the core radius of a vortex filament, m |
| $\Delta S$ | Change in the cross sectional area, $m^2$ |
| $\Delta\alpha$ | Step change in angle of attack, rad |
| $\Delta\zeta$ | Discretization along spatial direction, rad |
| $\Delta\psi$ | Azimuthal (or temporal) discretization, rad |
| $\delta$ | Turbulent or eddy viscosity parameter |
| $\varepsilon$ | Strain rate, $(= \Delta l/l)$ |
| $\zeta$ | Wake age, rad |
| $\theta$ | Blade pitch at any given section, rad |
| $\theta_0$ | Collective pitch, rad |
| $\theta_{1c}$ | Longitudinal cyclic pitch, rad |
| $\theta_{1s}$ | Lateral cyclic pitch, rad |
| $\theta_{tw}$ | Linear blade twist, rad $m^{-1}$ |

| | |
|---|---|
| $\lambda$ | Non-dimensional inflow velocity ($= V_i/\Omega R$) |
| $\lambda_0$, $\lambda_{1c}$, $\lambda_{1s}$ | Non-dimensional Fourier coefficients of induced inflow |
| $\mu$ | Advance ratio ($= (\mathbf{V}_\infty \cdot \mathbf{i})/\Omega R$) |
| $\mu$ | Mach angle of a supersonic sound source, rad |
| $\nu$ | Kinematic viscosity of air, $\mathrm{m^2 s^{-1}}$ |
| $\nu_\beta$ | Non-dimensional rotating blade flap frequency ($= \omega_\beta/\Omega$) |
| $\rho$ | Density of air, $\mathrm{kgm^{-3}}$ |
| $\tau$ | Time constant of dynamic inflow response, s |
| $\phi$ | Induced angle of attack, rad |
| $\phi$ | Indicial response function |
| $\psi$ | Azimuthal angle, rad |
| $\psi_b$ | Blade azimuth ($= \Omega t$), rad |
| $\Omega$ | Rotational speed of the rotor, $\mathrm{rads^{-1}}$ |
| $\vec{\omega}$ | Vorticity, $\mathrm{rads^{-1}}$ |
| $\vec{\omega}$ | Net angular velocity of the helicopter, $\mathrm{rads^{-1}}$ |
| $\omega_\beta$ | Rotating blade flapping frequency, $\mathrm{rads^{-1}}$ |

**Superscripts**

| | |
|---|---|
| $\dot{(\,)}$ | Time derivative ($= \partial(\,)/\partial t$) |
| $(\,)^\star$ | Azimuthal derivative ($= \partial(\,)/\partial\psi = \Omega\partial(\,)/\partial t$) |
| $c$ | Circulatory component |
| $nc$ | Non-circulatory component |

**Subscripts**

| | |
|---|---|
| $b$ | Blade-fixed coordinate system |

| | |
|---|---|
| $B$ | Body-fixed coordinate system |
| $G$ | Ground-fixed coordinate system |
| $i,\ j$ | General summation indices |
| $l,\ u$ | Lower and upper rotors (coaxial configurations) |
| $NR$ | Non-rotating coordinate system |
| $x,\ y,\ z$ | Components of vectors along the principal coordinate axes |

**Abbreviations**

| | |
|---|---|
| BEMT | Blade Element Momentum Theory |
| BVI | Blade Vortex Interaction |
| CFD | Computational Fluid Dynamics |
| IGE | In Ground Effect |
| OGE | Out of Ground Effect |
| PC2B | Predictor Corrector $2^{nd}$ Backward difference |
| PSP | Port-starboard-port roll reversal maneuver |
| SPS | Starboard-port-starboard roll reversal maneuver |
| TPP | Tip Path Plane |

# Chapter 1

# Introduction

Chinese flying tops and Leonardo da Vinci's *aerial screw* drawings are testimony to mankind's fascination with rotary winged vehicles over the centuries. Rotorcraft posses the unique ability to hover motionless and take-off or land vertically, which have made them indispensable in many military and civilian applications. While attempts to build a manned helicopter started around the same time as the development of fixed-wing aircraft (at the end of nineteenth century), the first successful flight did not occur until the late 1930s, almost three decades after the successful flight of an airplane. Even to this day, advancements in rotorcraft have always lagged behind their fixed-wing counterparts.

Over the last few decades, there has been considerable research into mitigating obtrusive noise and vibration issues and in designing aerodynamically efficient helicopters. However, the efforts have met with only a limited success. This is because the fundamental principles governing the flight of rotary-winged vehicles are very complex, and essential technical aspects have not yet been fully understood. The complex physics governing the rotor wake aerodynamics has been identified as one of the primary aspects critical for predicting all aspects of helicopter flight. This is

especially true in maneuvering flight, where the wake dynamics and its interactions with the rotor blades can become exceedingly complex.

While several experiments and flight tests have been conducted in steady state flight conditions to characterize the nature of the wake geometry and its effect on the rotor performance, few studies of the rotor wake under unsteady, maneuvering flight conditions have been performed. Performing measurements under maneuvering flight conditions is also a daunting task, and as of yet very little has been done to measure loads and performance etc. Furthermore, existing numerical tools lack the fundamental capability to capture all the essential features of the rotor wake aerodynamics necessary to gain better insight into free flight maneuvers. The development of numerical tools capable of predicting the unsteady flow features of maneuvers is essential for the development of quiet and efficient helicopters.

In this introductory chapter, an overview of the aerodynamic environment associated with a rotor in steady flight and in maneuvering flight will be presented. The physical features governing the generation of the aerodynamic forces will be explained, and the challenges encountered in predicting these effects will be outlined. The rotor wake aerodynamic behavior in response to perturbations in the control pitch inputs will then be discussed. This will be followed by a brief survey of the methodologies adopted by researchers to solve the rotor wake problem in unsteady flight conditions and their limitations within the context of maneuvering rotor problem. The chapter will conclude with a summary of the objectives of the work and an outline of the dissertation.

## 1.1 Challenges in Predicting Helicopter Aerodynamics

For controlled flight, an aircraft has to generate three different forces: 1. Lift to balance the weight of the aircraft, 2. A propulsive force to overcome the aerodynamic drag, and 3. Control forces to maintain the aircraft in a desired orientation and fly along the desired trajectory. In a fixed-wing aircraft, these three forces are generated in different ways: the lift to counteract the aircraft's weight is generated by the wings, the propulsive forces are generated by propellers or jet engines, and the control forces are generated by fixed surfaces such as ailerons, elevators, rudder and flaps. Because of the specific functionality of different control surfaces there is little or no coupling between the dynamic response of the fixed-wing aircraft to control inputs, i.e., a longitudinal control stick input produces only a nose up or nose down response without generating much of a yaw or a roll response.

In a conventional helicopter, the main rotor generates most of the lifting, propulsive and control forces. The lifting and propulsive forces are generated by tilting the rotor tip-path-plane (TPP) relative to the rotor shaft – see Leishman (Ref. 1). The net integrated thrust generated by the rotor is controlled by adjusting the pitch (the collective pitch) of the rotor blades simultaneously. Tilting the TPP requires differential aerodynamic forcing on the individual blades by introducing differential or cyclic pitch inputs. The net pitch at any rotor blade section is a combination of the collective, and the lateral and longitudinal cyclic pitch inputs, which varies as a function of the azimuth. Furthermore, the blades have freedom of motion about blade flap and lag hinges. The flap, lag, and pitch modes are closely coupled through centrifugal, Coriolis, inertial and aerodynamic forces acting on the rotating blades. The close coupling of the rotor modes complicates the dynamic response of a helicopter. For example, unlike a fixed-wing aircraft, a longitudinal stick input in a conventional helicopter

not only produces a nose up/down moment, but also results in a significant off-axis response, a rolling moment for example.

Accurate prediction of the dynamic response of the helicopter in free flight requires the capability to model all the forces and moments accurately, and this is a significant challenge task for the helicopter analyst. Deficiencies in modeling of rotor wake dynamics and the resulting induced inflow is known to be a key culprit in limiting predictive capability for flight mechanics simulations (Refs. 2–5) and also for aeroacoustic predictions (Refs. 6–10).

### 1.1.1 Aerodynamics of the Rotor Blade

As mentioned previously, rotor aerodynamics plays a very important role in determining the rotor response. The lift and drag forces generated at any blade section depend primarily on the effective incident velocity, $U_T$, and the blade pitch, $\theta$. The pitch at any given instant is a function of the collective ($\theta_0$), cyclic ($\theta_{1s}, \theta_{1c}$) pitch and the blade twist, ($\theta_{\text{tw}}$). For an elastic blade, the blade pitch at any location will also be a function of the elastic blade torsion. Besides the effective velocity and the blade pitch angle, the rotor airloads are heavily influenced by the vorticity present in the wake. The vorticity present in the the wake is generated at the rotor blades and is a function of the lift generated by the blade sections. The wake vorticity induces a downwash, $V_i$, at the rotor blade sections which decreases the effective angle of attack at these sections under most flight conditions.

Furthermore, in forward flight, the effective tangential velocity at any blade section is a function of the rotor azimuth and the radial location. Notice that for increasing forward flight speeds, certain regions on the retreating side of the rotor disk experience a reverse flow which decreases the lift generated at these sections. The

net induced angle of attack is also a function of the incident velocity and varies as the blades rotates. The flow field around the rotor blades is effectively unsteady, even for steady flight conditions. Furthermore, for an elastic blade, the angle of attack is also a function of blade bending and torsion arising from the flap, lag, and pitch motion.

### 1.1.2 Structure of Rotor Wakes

For a fixed-wing, the wing constantly moves away from the vorticity deposited into the flow field from the trailing edges and wing tips. Therefore, the induced effects of the wake vorticity on the wing is not significant beyond a few chord lengths behind the trailing edge. In contrast, the rotor blades, by virtue of their rotational motion, constantly interact with the wake vorticity that is shed and/or trailed from individual blades over several rotor revolutions. Furthermore, the wake structure is a function of the flight condition. The wake vorticity quickly rolls up into root and tip vortices. The tip vortices are the most dominant structures in the rotor wakes. The effect of the inboard sheet is pronounced only for a few chord lengths beyond the trailing edge. The tip vortex is nominally helical in hovering flight condition, but becomes progressively more distorted and intertwined as the forward flight speed of the rotor is increased. Figure 1.1 shows representative geometries of the rotor tip vortices as they are convected in the flow field for hovering and forward flight conditions. Notice especially the intertwined and skewed structure on the advancing and retreating side of the rotor in forward flight. The induced velocities from the wake are a function of the wake geometry and, therefore, the wake structure varies depending on the flight condition.

Interactions of these tip vortices with the rotor blades are responsible for many adverse effects such as unsteady impulsive airloads, blade–vortex interaction (BVI) noise (Refs. 11–14), vibration issues, and performance degradation from wake–airframe

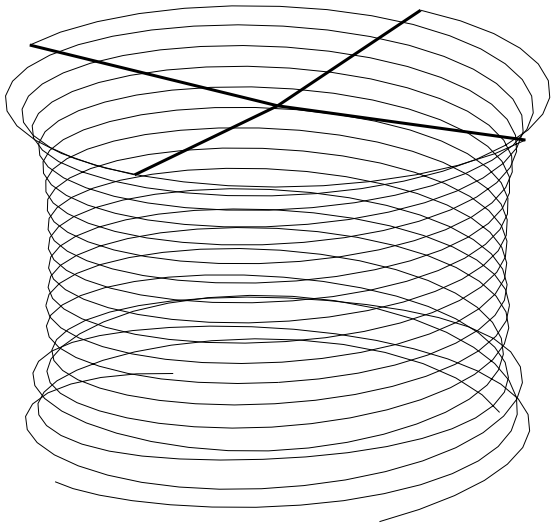

(a) Hover

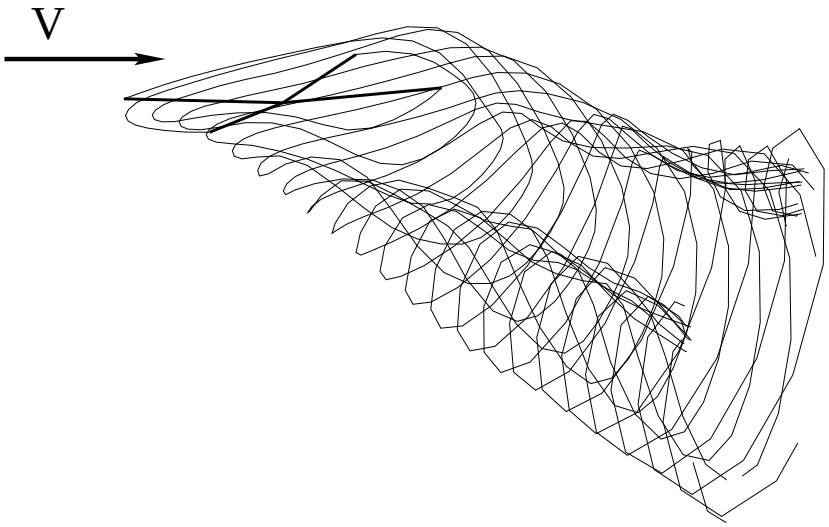


(b) Forward flight

Figure 1.1: Wake geometries showing the topologies of the tip vortices for a helicopter rotor in hovering and forward flight conditions.

interactions (Refs. 15, 16). As the tip vortices come into close proximity to the rotor blades, the induced velocities locally alter the angle of attack at these blade sections, which result in a temporal fluctuation of airloads. The steep gradients in the lift time-history give rise to impulsive noise commonly known as BVI noise (Ref. 11). The intensity of this noise depends on the strength of the vortices, the viscous core radius of the vortex, the miss distance between the blade and the vortices, the location of the interaction on the rotor disk, and the relative velocity of the tip vortex relative to the rotor blade (Refs. 17, 18).

It is clear from the preceding discussion that the dynamic response of the rotor blades is inherently coupled with the aerodynamics of the rotor blade and the wake aerodynamic response. The blade flap, lag, and pitch degrees of freedom are a function of the aerodynamic forces generated at the blade sections. The aerodynamic forces are a function of the blade sectional angle of attack. This, in turn, depends on the incident and the wake induced velocities, as well as the effective velocities from flap, lag, and torsion modes. The wake vorticity, and, therefore, its induced velocity at the rotor blade sections, is a function of the blade aerodynamic lift. Any numerical model capable of predicting the trimmed flight of a helicopter at any desired flight condition must be capable of modeling accurately the physics associated with: (a) the flap, lag, and torsion moments experienced by the rotating blade, (b) unsteady aerodynamics at the rotor blade sections, (c) the highly nonlinear wake induced velocity field across the rotor disk, and (d) the generation of vorticity at the rotor blades.

The numerical simulation of helicopter flight, even for steady flight conditions, quickly becomes a computationally intensive process of solving for the blade elastic deformations, and tracking the vorticity in the flow field and its integrated induced velocity effects at each rotor blade section in a consistent and time-accurate manner.

The process of tracking the convection of the wake vorticity has posed the biggest challenge to the rotorcraft analyst, and has been solved only subject to several major simplifying assumptions.

Various induced inflow models have been proposed over the years, based on both experimental and theoretical considerations, which provide reasonable approximations to the wake induced inflow at the rotor disk, at least for steady, level flight conditions. The validity of these approximations are questionable for maneuvering flight conditions, and also for flight conditions where there is a preponderance of enhanced blade–vortex interactions, such as descending flight. Vortex ring state can be considered as an extreme example of such a flight condition where the flow field around the rotor breaks down completely, and traditional linearized methods of analysis are unsuitable for analysis of these flight regimes. Existing methodologies are incapable of capturing the finer details of wake interactions even under nominally steady flight conditions such as hover in ground effect, or hovering flight of coaxial rotors where the wake vorticity from the upper rotor interacts with the blades of the lower rotor (Refs. 19, 20).

### 1.1.3 The Maneuver Problem

The flight capabilities of a helicopter are often limited by the types of maneuvers it can perform and, therefore, the behavior of helicopter under transient, maneuvering flight is of particular interest to the rotor analyst. To perform a maneuver, the pilot perturbs the helicopter from its steady operating condition or transitions from one steady operating condition to another by applying appropriate control inputs. The accelerations experienced by the helicopter during the course of a maneuver cause a time variation of the freestream velocities, as well as to introduce additional velocity

components depending on changes in the roll, pitch, and yaw attitudes of a helicopter.

The changes in the operating conditions alter the lift generated at individual blade sections and, therefore, the vorticity shed and/or trailed into the wake. The wake itself evolves in a highly nonlinear fashion during the course of the maneuver. Various researchers have studied the wake dynamics during unsteady flight conditions such as wake evolution for an impulsively started rotor (Ref. 21), inflow and airloads response to ramp changes in the collective pitch (Ref. 22), inflow response to harmonic oscillations of collective and cyclic pitch inputs in hovering flight (Ref. 23) and in forward flight conditions (Ref. 24).

Experimental evidence indicates that the wake is highly sensitive even to small perturbations in the collective pitch inputs and the resulting response is highly nonlinear in nature. Under these conditions, the wake has a tendency to bundle into a toroidal "ring" structure of accumulated vorticity, which persists as long as the conditions promote it. The formation, convection and the intensity of this toroidal structure depends on the operating conditions and the nature of control pitch inputs applied.

The bundled "ring" structure is clearly evident in Fig. 1.2, which is a photograph of the balsa dust flow visualization of an impulsively started rotor from the experiments of Taylor (Ref. 21). The toroidal structure can be considered analogous to the starting vortex shed from an airfoil in response to a change in angle of attack (Ref. 25). Depending on the intensity of the bundling, these structures can cause steep gradients in the local induced velocity field and also a net increase in the average induced inflow at the rotor plane. Figure 1.3 shows a good example of the bundling of wake tip vortices during a starboard roll maneuver. Under certain operating conditions, the vortex bundles can come into close proximity to the rotor blades resulting in more intense forms of BVIs (so called "super-BVI.")

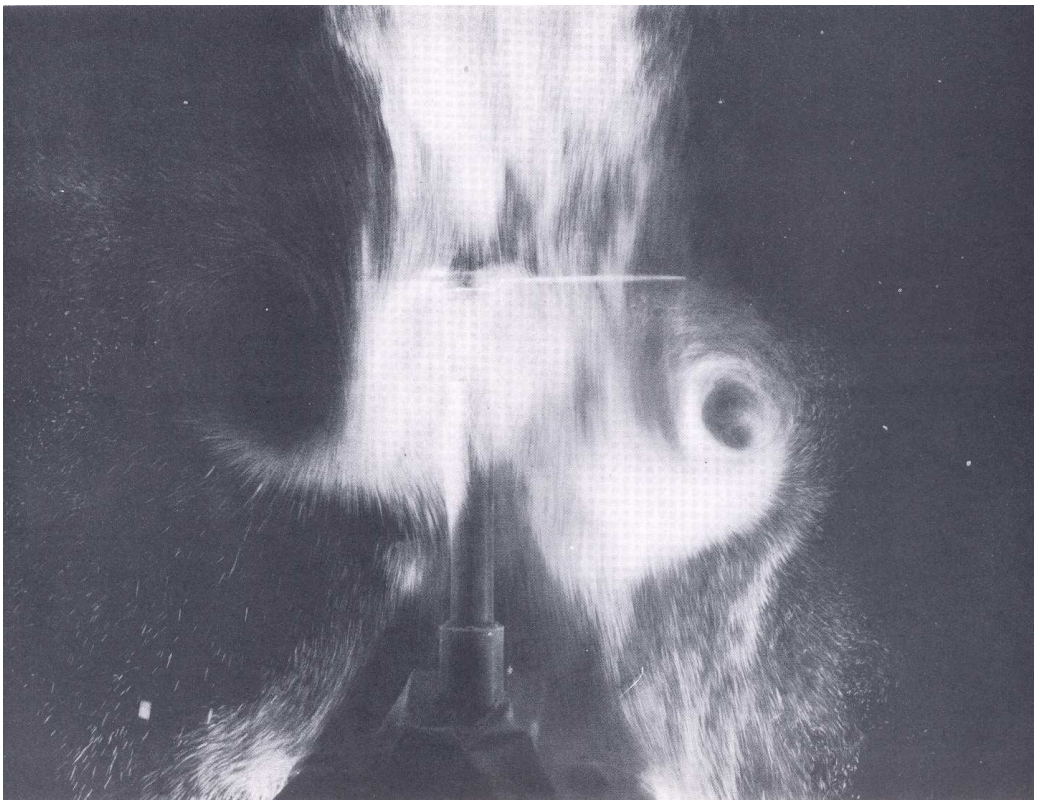

Figure 1.2: Photograph showing evidence of vortex bundling during the wake evolution of an impulsively started rotor. Photograph from Taylor (1950).

The measurements of transient inflow and the thrust time-histories in the experiments of Carpenter & Friedovich (Ref. 22) show considerable nonlinearities that can be attributed to the induced effects of the wake at the rotor tip-path-plane (TPP). For increasing ramp rates, significant overshoots of the instantaneous thrust values, in some cases twice the final steady state value, were observed. A further complication is that the aerodynamic response at the rotor to the changes in the flight condition is not instantaneous, and occurs with an aerodynamic lag in terms of rotor revolutions. Unsteady effects introduced by time-varying control inputs affect the strength of the vorticity shed or trailed into the wake, as well as their detailed interactions, and so

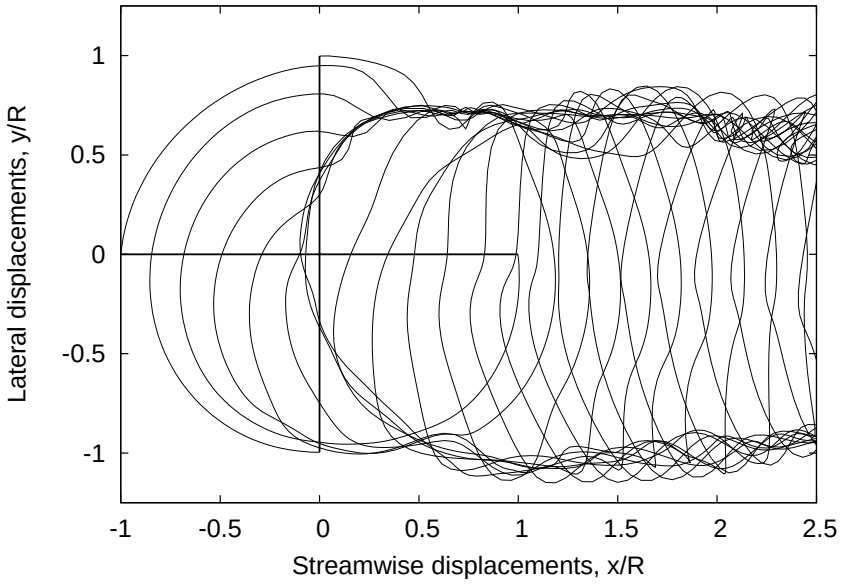


Figure 1.3: Top view of the instantaneous wake geometry of a rotor executing a starboard roll maneuver showing the bundling of the wake tip vortices.

affect the resulting wake evolution. This produces a hereditary effect on the net rotor response.

It has also been observed that the wake response depends very much on the type and sequence of control input perturbations. Experiments by Ellenrider & Brinson (Ref. 23) show significant differences in the amplitude and phase response of inflow for harmonic excitations of collective or cyclic pitch inputs. In reality, an actual maneuver is usually performed by introducing various control inputs simultaneously. To obtain reliable predictions of the transient dynamic response of the helicopter, the cumulative effects of all these perturbations on the rotor wake evolution must be solved for consistently. While in many practical cases control inputs are smaller in amplitude and are applied at low frequencies, the effects on the wake can be quite subtle and can have pronounced nonlinear effects on the resulting aerodynamic response of the rotor.

The persistence of unsteady conditions over long time scales and the inherent nonlinearities in the wake evolution mean that the simulations of wake evolution under maneuvering conditions cannot be carried out using simplified quasi-steady forms of analyses.

## 1.2 Survey of Existing Rotor Wake Models

The crux of the rotor wake aerodynamic problem is the estimation of the induced velocity field at the rotor disk. The simplest analysis for the estimation of the induced inflow is the so-called momentum theory analysis, first developed by Rankine (1865) for axial turbine flow. The theory was extended later by Froude (1878) and generalized by Glauert (1928). The momentum theory is useful for estimating the average inflow across the rotor disk, and the induced power requirements for a given operating rotor thrust.

A combination of the momentum theory with blade element theory (BET) provides a radial variation of the induced inflow distribution depending on the operating thrust and properties of the blade, such as the sectional chord, the blade twist, and the airfoil characteristics. More complicated approaches for the estimation of the induced angle of attack at the blade sections using vortical wake was pursued by several researchers in the early 1920s. This appears to be the basis for the vortex methods for helicopters existing today (Refs. 1, 26). The combined blade element–momentum theory approach has proved a very successful and reliable engineering tool and is used extensively in preliminary design analysis even to this day.

### 1.2.1 Inflow Models

Several linear inflow models have been developed for forward flight conditions that can be used with the blade element theory to predict the rotor performance in forward flight conditions. For example, inflow models of Drees (1949) and Mangler & Squire (1950) provide good approximations to the longitudinal and lateral inflow variations across the rotor disk at moderate to high advance ratios – see Refs. 1, 27 for further details. However, these inflow models are valid only for steady flight conditions. The unsteady inflow at the rotor blade sections can be very different during a transient maneuver for successive rotor revolutions.

A popular approach to approximating the unsteady inflow is to account for the unsteady effects on the net thrust and moments. This approach was first explored by Carpenter & Friedovich (Ref. 22) in their analysis of the rotor thrust response during jump takeoff conditions in an autogiro. In this study, the rotor thrust was written using a modified form momentum theory equation where the unsteady forces were attributed to an *apparent mass* effect, i.e., inertia of the fluid surrounding the rotor. The change in the inflow can then be rewritten as a simple first-order differential equation that relates the perturbations in inflow to the changes in the rotor thrust.

A more generalized formulation for forward flight condition is to use a linear perturbation to the inflow as a function of the radial and azimuthal position of the blade. The dynamic inflow components are then related to the perturbation forces on the rotor disk, the rotor thrust $C_T$, the pitching moment $C_{M_y}$ and the rolling moment $C_{M_x}$ respectively using actuator disk theory – see Johnson (Ref. 27) for more details.

Other approaches have used vortex theories to determine the time constants and coupling matrices. A popular formulation of the dynamic inflow model is given by Pitt & Peters (Ref. 28). The Pitt–Peters model has been generalized into a finite state

model by Peters and his colleagues (Refs. 29–31). The dynamic inflow models have found extensive use in comprehensive aerodynamic analyses for rotor aeroelasticity and helicopter flight dynamics problems (Refs. 32–34).

### 1.2.2 Classical Vortex Models for the Rotor Wake

Vorticity based models represent the flow field, mainly the wake structure, using discrete elements of vorticity. These methods were first developed for the analysis of axial flow in turbines and propellers (Ref. 35). The classical vortex theories were based on a prescribed wake model first developed by Goldstein (Ref. 36). The development of rigid wake models involved the simplification of the nonlinear source terms in the governing equations using average constant velocity terms obtained from momentum theory considerations. The simplified linear equations were then solved analytically to obtain a wake geometry composed of undistorted, uniformly-spaced, helical filaments. The effect of the wake on the induced velocity of the rotor disk can then be obtained by the application of the Biot–Savart law (see Ref. 37, pp. 87). The self induced effects of the wake and the wake contraction effects were neglected in this approach.

Landgrebe (Ref. 38), based on extensive flow visualization measurements, developed a semi-empirical wake model applicable to hovering flight, for both the tip vortex and the inboard sheet, as a function of the rotor geometry and the operating thrust in hovering flight. This was motivated by the earlier lack of success in predicting the hovering wake using time-marching, free-vortex wake algorithms (Ref. 39). The need for improved wake models for performance analysis in hovering flight, especially the capability to model the wake contraction, was identified by Jenny et al. (Ref. 40). Predictions of the inflow and the rotor performance based on Landgrebe's model were

found to be better than those based on the classical rigid wake models.

Kocurek & Tangler (Ref. 41) proposed a semi-empirical model similar to that of Landgrebe based on measurements made on a sub-scale rotor. Similar prescribed wake models for forward flight have been proposed by Egolf & Landgrebe (Ref. 42) and Beddoes (Ref. 43) using semi-empirical functions to obtain the distorted wake structure during forward flight. Despite their simplicity and computational efficiency, prescribed wake models suffer from a major drawback in that their application is limited to flight regimes and rotor geometries for which experimental data is already available. Furthermore, these models cannot predict the distortions of the wake and the bundling of tip vortices, discussed previously in Section 1.1.3, and, therefore, they are inadequate for maneuvering rotor applications.

### 1.2.3 Free-Vortex Wake Models

Free-vortex wake methods present the next level of modeling complexity over prescribed wake models. In this approach, the velocities induced by the vorticity in the wake are computed by repeated application and numerical integration of Biot–Savart law over all vortex elements. Several researchers have used different vorticity elements to describe the flow field, for example, finite straight line-vortex segments (Refs. 44, 45), finite curved line-vortex filaments (Ref. 46), and three-dimensional vortex blobs (Ref. 47).

The most common implementation found in literature is the finite straight line segment formulation. Under inviscid, incompressible assumptions, Helmholtz's law states that the vortex lines move as material lines (Ref. 48). The motion of the discrete elements to force free locations under the influence of the induced velocity field is then computed using the Navier–Stokes equations (Ref. 49). The strengths and the origin

of these vortex elements are obtained from the rotor blade aerodynamic and flapping solutions to satisfy the Kutta–Jukowski condition (Ref. 37). Free-vortex wake methods are broadly categorized into relaxation methods and time-marching methods depending on the numerical algorithm used to solve the wake governing equations.

**Relaxation Based Free-Vortex Wake Methods**

Relaxation (or iteration) based free-vortex wake methods assume periodicity of the rotor wake solution. The wake is allowed to distort freely under the influence of the induced velocity field from an initial solution, which is usually a prescribed wake solution. The vortex elements are tracked using wake markers, and the governing equations are solved at these discrete markers. The numerical scheme uses a relaxation parameter for updating the position vectors of the wake markers, i.e., position updates at each iteration is a weighted average of the old and new solution. The wake solution is "relaxed" successively until the position vectors remain essentially unchanged over successive iterations.

The earliest implementation of the relaxation methodology found in literature is that of Clark & Leiper (Refs. 50, 51) for hovering rotor performance analysis. Only the first two revolutions of the tip vortex were modeled as free-vortex filaments. The far wake was modeled as a set of thirty ring vortices to minimize the effect of wake truncation. The spacing between the vortex rings in the far wake was a function of the number of rotor blades, and the vortex ring radius was obtained based on the final turn of the free tip vortex. The method was shown to predict hover performance of isolated rotors relatively successfully.

After unsuccessful attempts with time-marching algorithms, Scully (Ref. 52) developed a weighted-averaging scheme for calculating the induced velocity field at the

wake markers. It was found that the weighted averaging procedure increased the overall stability of the numerical scheme. Both hover and forward flight conditions were studied using this algorithm. For analysis of hovering flight, the wake was modeled using six to twelve turns of the tip vortex. A semi-infinite vortex cylinder was used to approximate the far wake condition. The wake was represented using finite straight line segments, with an azimuthal resolution of 15°. The scheme used a viscous core growth model, which became very popular and is used in rotor wake analyses even today, but with several additional improvements. In forward flight, the number of wake turns was adjusted depending on the advance ratio and varied from two to four turns over the flight conditions studied. The wake model was used in the computation of higher-harmonic loads. However, a large vortex core size was used to avoid impulsive airloads from blade-vortex interactions (BVIs). This scheme was later adapted by Johnson in the development of CAMRAD (Ref. 53).

Miller (Ref. 54) modeled the rotor blades as Weissinger-L lifting surfaces along with a semi-infinite trailed wake. The wake was assumed to roll up into a tip vortex, an inboard trailer and a root vortex. Only four turns of the trailer vortices were modeled and the far wake condition was approximated using a semi-infinite vortex cylinder, as used by Scully (Ref. 52). The starting solution for the wake was arrived at based on momentum considerations. It was shown that the inclusion of the root vortex had negligible effect on rotor hover performance analysis.

Bliss et al. (Ref. 55) used curved vortex filaments to account for the self-induced velocities. The numerical algorithm used a predictor-corrector approach. Replacing straight line filaments with curved filaments allowed for coarser discretizations, and claimed to improve computational efficiency without significant loss of accuracy, specifically for hover and axial climb flight conditions. The core model used a very

large core radius (5% of the rotor radius or greater than 50% of the blade chord) and had provision for an inboard vortex sheet. The far-field wake was composed of stacked ring vortices composed of four curved filaments. A sink singularity was included in the far wake to conserve mass flow and to improve stability of the numerical scheme. However, numerical convergence was only achieved for axial climb conditions. Later, Bliss et al. (Ref. 56) used a "self-preserving wake" concept to replace the time derivative in terms of an azimuthal and space derivative, along with the iterative scheme used in their previous work. A far-field boundary condition was imposed using constant radius, constant pitch helical filaments extending to infinity. Converged solutions for hover were achieved using the "self-preserving wake" concepts.

Quackenbush et al. (Ref. 57) extended this methodology to analyze the rotor airloads and performance estimates in hovering flight. An eigenvalue analysis based on the induced influence coefficients showed several unstable modes corresponding to positive eigenvalues that were linearly dependent on the rotational frequency of the rotor. The tip vortex structure in hovering flight was shown to be unstable, an observation corroborated by flow visualization experiments.

Crouse & Leishman (Refs. 16, 58) utilized a predictor-corrector sequence with a central differencing scheme for the space discretization of the governing equations. The method was used to study rotor/airframe interactions, and it was shown that using a predictor-corrector algorithm greatly improved the stability of the numerical scheme in comparison to explicit schemes.

Bagai (Ref. 59) developed the concepts of predictor-corrector algorithm used by Crouse & Leishman into a comprehensive relaxation methodology. A five-point central differencing scheme was adopted for both the space and time discretizations. A pseudo-implicit predictor-corrector scheme with a suitable relaxation parameter was

used to converge the wake solution in an iterative manner. A Weissinger-L blade model was used to obtain the strengths of the bound circulation on the rotor blade. A centroid of vorticity approach was used to determine the release points of the trailed tip vortices. Methods to determine the strengths of the trailed vortices were developed based on the bound circulation on the blade. For hovering flight, boundary condition turns were introduced to overcome the non-physical wake expansion because of wake truncation. Velocity field interpolation techniques were developed to allow for unequal discretizations steps in the time and space. The methodology was successfully used in the analysis of the rotor wake geometry, the induced velocity predictions of isolated rotors in both hover and forward flight (Refs. 60, 61) and also for coaxial and tandem rotor configurations (Ref. 15). The code was released as the Maryland Free Wake (Refs. 62, 63), and is used extensively in several comprehensive rotor and flight dynamic simulations (Refs. 33, 64).

**Time-Marching Free-Vortex Wake Methods**

A time-marching algorithm allows the free-vortex wake models to capture the transient wake aerodynamics, and is an attractive option for the simulation of unsteady or maneuvering flight conditions. It has been shown that the wake of a helicopter rotor is aperiodic, even for nominally steady flight conditions such as hover (Refs. 57, 65, 66). Therefore, the numerical algorithm must be robust enough to capture the aperiodicity in rotor wakes, while keeping the errors from numerical approximations to an acceptable minimum.

Pioneering work with time-marching algorithms was done by Crimi (Ref. 67) in 1965. Two years later, Scully (Ref. 68) developed an explicit Euler time-marching algorithm for rotor wake simulations. However, a converged solution of the wake in

hover was not obtained because of numerical instabilities. Setbacks with the time-marching algorithm motivated Scully to develop the "relaxation-based" algorithms that have been discussed in the previous section.

Landgrebe (Ref. 39) used an explicit time-marching approach to solve the rotor wake problem in forward flight. The wake was discretized into straight line vortex filaments, with a relatively coarse discretization of 15° to 30° because of computational limitations. The wake was truncated after five turns to keep the number of vortex elements required for computation to a minimum. This was achieved by adding a new filament near the blades at every iteration and deleting the last segment. The method distinguished between the "near" and "far" wake. Induced velocities from the "far" wake were computed only once to facilitate faster computations. A viscous core size of 1% of the rotor radius was assumed, and it was argued that the results were insensitive to the viscous core radius. The computations showed good correlation with experimental results for forward flight. However, hovering flight conditions could not be modeled because of numerical instabilities found in the wake solution. This motivated the development of the famous Landgrebe's prescribed wake model, as discussed in Section 1.2.2 of this dissertation.

Sadler (Ref. 69) applied an explicit Euler time-marching scheme to study the wakes of multiple rotor configurations. Both the trailed and shed wake were modeled in the near wake, while the far wake consisted of only one tip vortex trailed from each blade. Straight line segments were used to model the shed and trailed wake. A vortex core model, similar to a Rankine vortex (Ref. 70), was used to represent the vortex filaments, and the core radius was adjusted based on experimental observations. The rotor was started impusively from rest and a minimum cutoff distance was prescribed to avoid high induced velocities. The scheme worked well for the forward

flight conditions analyzed, where the instabilities were less severe than in hovering flight.

Bliss et al. (Ref. 71) analyzed the use of curved vortex segments in a time-marching scheme, and showed that the curved segments were more accurate than straight line segments for large discretizations. The scheme used a predictor-corrector method to solve the governing equations of the wake. A far-wake boundary condition, based on momentum considerations, was applied. The scheme was applied mainly to study forward flight conditions (Ref. 72).

A vortex lattice was used to represent the rotor wake in the time-marching scheme developed by Egolf (Ref. 73). The study focused on high-speed forward flight conditions. The effect of vortex core size was examined and was found to be an important parameter affecting the modeling of rotor wakes. A larger core radius resulted in "smoother" airload predictions. The convergence condition was based on time-averaged thrust rather than actual wake convergence.

A constant vorticity contour methodology has been developed for the analysis of the rotor wake in the comprehensive rotor analysis code, CHARM (Refs. 46, 74). The vortex elements track the regions in the flow field, which have the same circulation strengths. The approach uses curved line segment filaments, which allows for coarser resolutions ($> 30^{\circ}$) without significant loss in the accuracy of induced velocity computations. The method has been applied to the study of wake/airframe interactional aerodynamics (Ref. 75) and BVI noise predictions (Ref. 76).

Brown (Ref. 77) developed a grid based, Eulerian formulation of the Navier–Stokes equation written in velocity–vorticity form, called the vorticity transport method (VTM). This methodology addresses the deficiencies inherent in the Eulerian approaches, namely the numerical diffusion of the vorticity in the computational do-

main. The model is capable of representing the blade-wake interactions, as well as giving a very realistic simulation of the evolution of the vortical wake (Ref. 78). Toro's Weighted Average Flux (WAF) algorithm is used to march the solution in time. A weighted average flux scheme allows for tight control on the rate of dissipation of vorticity, allowing the method to retain the vortical structures in the flow field over many rotor revolutions. The method has been applied successfully in the analysis of various helicopter flight conditions (Refs. 79, 80), especially operations in vortex-ring state (Ref. 81). The methodology can be readily coupled with a Navier–Stokes solver for the flow field near the rotor blades and has the potential to overcome the shortcomings of CFD-based wake capturing schemes that are discussed in Section 1.2.4.

Bhagwat (Ref. 82) extended the ideas developed in Bagai's Maryland Free Wake analysis to incorporate a time-accurate scheme capable of simulating the rotor wake dynamics during arbitrary flight conditions. Several outstanding issues were addressed in this work. A second-order, two-step backward, predictor-corrector time-marching algorithm was developed. The error terms arising from the numerical truncation were independent of the local velocity field, and provided implicit damping that helped stabilize the scheme for a wide range of flight conditions. The stability and the accuracy of the scheme were rigorously tested and compared with other existing numerical schemes (Ref. 83).

The accuracy of the straight line vortex segment in the modeling of rotor wakes was also analyzed (Ref. 84). It was shown that the straight line segmentation was second-order accurate for discretizations less than $5^{\circ}$. A detailed eigenvalue analysis of the stability of the rotor wake was conducted, and it was shown that the hovering wake was susceptible to the development of instabilities (Ref. 85).

The desingularization of the vortex core in the line-vortex elements was addressed.

An empirical vortex core growth model based on experimental data was developed, and successfully implemented to account for the laminar as well as the turbulent viscous diffusion effects on the tip vortices (Ref. 86).

A good review of the relaxation and the time-accurate numerical algorithms and other aspects of the Maryland Free Wake method can be found in Ref. 45. The method was validated extensively for various steady and unsteady flight conditions, and particularly with the experiments of Carpenter & Friedovich (Ref. 22). This methodology has been adopted and extended in the present work.

**A Note on Vortex Core Growth Models for Free-Vortex Wake Analyses**

Besides being convected under the influence of the local velocity field, the vortex filaments in the rotor wake are also subjected to strain and diffusion effects, which can become important in certain flight conditions such as the vortex ring state (Ref. 87) and operations in ground effect (Refs. 20, 88). However, most free-vortex wake methodologies in the existing literature use an arbitrary core size to facilitate convergence of the numerical scheme, without any physical consideration. Furthermore, almost all existing analyses ignore the effects of filament strain without proper justification (Ref. 89). Proper modeling for the tip vortices is essential to account for the physical effects of viscous diffusion, especially in applications involving blade–vortex interactions (Ref. 90), wake/airframe interactions, etc.

The impact of the viscous core growth model becomes important in the analysis of maneuvering flight conditions, where there is a preponderance of enhanced interactions between the blade and airframe surfaces with the bundled "ring" structure. Under these conditions, the blades might interact with vortices from much later wake ages than are usually encountered during steady flight conditions. Furthermore,

bundling of tip vortices introduces steep gradients in the local induced velocity field, which can further strain the tip vortices. The integral effects of strain on the vortices since their inception at the blade tips must be accounted for over several rotor revolutions. The implications of the vortex core growth over several rotor revolutions must be carefully considered for maneuvering flight applications.

Closed-form solutions of the Navier–Stokes equations for the evolution of the tip-vortices cannot be achieved without many simplifying assumptions. Algebraic approximations are often employed in engineering analysis for their computational efficiency. Algebraic models proposed by Scully & Sullivan (Ref. 91) and Vatistas (Ref. 92) are quite popular.

Fluid viscosity causes the smearing of the vorticity in the vortex filaments over time. The simplest model for this phenomena is the classic Lamb–Oseen core growth model, obtained by solving the one-dimensional Navier–Stokes equation (Ref. 93). However, this model is fully laminar and the core growth predictions from the Lamb–Oseen model are found to be unrealistically slow in comparison to experimental measurements. Squire (Ref. 94) suggested the inclusion of an apparent or eddy viscosity parameter $\delta$ to account for effects of turbulence on vortex diffusion. Squire also proposed an effective origin offset to allow for a finite vortex core at the origin of the trailing vortex.

Bhagwat & Leishman (Ref. 86) have further refined the model based on tip vortex measurements from rotating-wing experiments. None of the earlier measurements attempted to quantify the effect of filament strain on the evolution of the tip vortices. Ramasamy (Ref. 95) was the first to study the effect of filament strain on vortex core growth based on measurements of a hovering rotor in ground effect. A generalized, multi-region, transitional model based on the Reynolds number was proposed

by Ramasamy & Leishman (Ref. 96), which incorporates the viscous diffusion, turbulence, scaling and stretching effects on the vortex core growth. The model developed in Refs. 86 and 96 forms the basis for the viscous splitting methodology that is adopted in the present work.

### 1.2.4 CFD-Based Methods

With the advent of faster and cheaper computers in recent years, full-fledged solutions of the Navier–Stokes equation for the flow field surrounding the rotor have become possible using comprehensive computational fluid dynamic (CFD) analyses. The CFD-based models are solved in a grid-fixed, Eulerian formulation, in contrast to the Lagrangian formulation adopted in the free-vortex models. While the emphasis of the present work is on the development of free-vortex based methods for aerodynamic simulations, CFD-based methods have gained much attention in recent years and, therefore, a brief overview of the concepts pursued by researchers is presented.

Datta et al. (Ref. 97) present a detailed review of the development of CFD approaches adopted by researchers in the simulation of rotary wing aerodynamics over the last decade. The primary advantage of CFD-based methods is the accurate description of the flow field around the rotor blades, i.e., with sufficient resolution of the computational grid, these methods can capture the formation of vorticity on the surface of the rotor blades, its convection into the trailing vortex sheet, and the eventual rollup of this sheet into one or more concentrated vortex structures. However, these methods require very fine grid resolution to avoid numerical dissipation of the vortex structures present in the flow field.

Two different types of formulations, the potential Euler formulation and the Navier–Stokes formulation, have been applied in rotor aerodynamic simulations. The Euler

formulations are inviscid, but allow coarser grids sized to resolve the surface geometry rather than the viscous flow scales. Earlier formulations failed to retain the vorticity beyond one rotor revolution. Several approaches have been pursued to minimize the numerical dissipation of vorticity.

One such approach is to use a Lagrangian free-vortex wake model to represent the far field wake and solve flow equations in an Eulerian grid in a small region around the rotor blades. These *hybrid formulations*, or vortex embedding methods, were first adopted by Steinhoff & Ramachandran and was later implemented in the HELIX code, which was successful in predicting the helicopter performance in hover and forward flight conditions. Sitaraman (Ref. 98) developed a field-velocity approach which uses the relaxation based free-vortex model of Bagai & Leishman (Ref. 99) to simulate the far-wake along with a Navier–Stokes formulation near the blade. This approach is slowly being abandoned in favor of the direct wake capturing schemes (Ref. 100).

*Direct wake capturing* by solving the Euler or Navier–Stokes formulations over the entire computational domain has been tried by several researchers using different strategies to minimize the numerical dissipation of vorticity, such as unstructured meshes for local grid refinements (Ref. 101), overset meshes (Refs. 100, 102), and vorticity confinement techniques (Ref. 103). CFD-based concepts are under active development and might prove to be an attractive proposition for the simulation of rotor wake aerodynamic problems. However, these methodologies are still in their infancy, and further research in low-cost computational models is necessary before they can replace free-vortex based methodologies for routine use in comprehensive rotorcraft aeroelastic or flight dynamics applications.

## 1.3 Limitations of Existing Methodologies

It is evident based on the discussions in Section 1.1.3 that the aerodynamic environment at the rotor in a maneuver is extremely complicated, and the capability to accurately model nonlinear phenomena over several rotor revolutions is essential to gain better insight into such flight conditions. Such an endeavor requires a sophisticated computational model capable of simulating faithfully all the essential physics involved in a maneuvering rotor problem. While modeling every physical aspect of the flow is desirable, the computational expenses involved with such sophisticated methodologies can quickly render them impractical for routine use. To conserve computational costs, the aerodynamic models in comprehensive rotor analysis codes often employ several simplifying assumptions that render them inadequate for analysis of maneuvering flight. Modeling all the essential flow features without incurring a severe computational penalty is a delicate task. The deficiencies and the drawbacks of the existing methodologies must be properly understood before a suitable model capable of reliably predicting maneuvering flight can be developed.

Comprehensive rotor analysis codes use linearized inflow models such as the dynamic inflow model, discussed previously in Section 1.2.1, to predict the unsteady wake induced inflow at the rotor disk. Such inflow models were originally developed to predict the integrated effects on the inflow to sudden changes in the collective pitch inputs (Ref. 22). Therefore, such models perform satisfactorily for analysis of total rotor performance, namely the net thrust and power. However, these models provide no insight into the rotor wake geometry nor do they have the capability to capture the BVI locations and intensities that are essential for estimating rotor noise. Furthermore, experimental evidence indicates that the wake is aperiodic and its induced effects at the rotor disk are nonlinear, especially when the bundled "ring" structure

comes into close proximity to the rotor blades and causes steep gradients in the lift distribution.

Hennes et al. (Ref. 9) compare the noise predictions based on airloads obtained from two different analyses, the linearized dynamic inflow model (Ref. 32) and the time-accurate free-vortex wake model. It was observed that the dynamic inflow model does not capture the BVIs and, therefore, the noise calculations using airloads obtained from a dynamic inflow analysis fails in predicting the impulsive rotor noise.

Free-wake methodologies can capture the rotor wake geometry in free flight and are, therefore, capable of providing more comprehensive information about the rotor wake geometry, nonlinear induced inflow, and BVI. However, most free-wake methodologies are based on relaxation schemes which assume periodicity of the flow conditions. Experimental evidence (Refs. 22, 23) clearly shows that the wake dynamics is highly aperiodic and the unsteady, aperiodic conditions persist for considerable periods of time depending on the kind of maneuver performed.

The thrust time-histories measured by Carpenter & Friedovich (Ref. 22) show large overshoots in the instantaneous values after the introduction of collective pitch inputs. Modeling the rotor wake evolution as a series of quasi-steady intermediate steps will not properly predict the unsteady wake evolution, particularly the vortex wake bundling phenomena, and will fail to capture these thrust overshoots. It must be emphasized that the intermediate steps during the relaxation iterations are not indicative of the true transient wake aerodynamics but merely a numerical artifact arising from convergence of the solution from any arbitrary starting guess.

The limitations of periodicity assumptions can be eliminated by using a time-marching algorithm, which can then capture the transient wake aerodynamics. Historically, time-marching methodologies were explored before relaxation methods, but

had very limited success. Earlier attempts (Refs. 67, 68) at solving the rotor wake problem with time-marching schemes used an explicit first-order difference in time, which can be shown to be numerically unstable. In fact, this was the primary reason for the success of the relaxation based free-wake methodologies for analysis of rotorcraft aerodynamics in steady flight conditions.

The rotor wake is inherently unstable and aperiodic even for hovering flight conditions (Refs. 65, 85). The numerical scheme used must be capable of capturing the inherent aperiodicity without introducing numerical errors (which can be misinterpreted as a physical phenomena) or being susceptible to divergence because of the physical aperiodicity. However, most numerical time-marching algorithms commonly are sensitive to the operating conditions, i.e., the error terms from the numerical approximations depend on the local velocity gradient and can diverge for certain flight conditions (Ref. 83).

Numerical schemes based on free-vortex methodologies are inviscid and can solve only for the motion of discrete vortex particles in the flow field. Such methods are incapable of predicting the creation of vorticity on the surface of rotor blades, the formation of the vortex sheet at the trailing edge, its evolution and the roll-up mechanism. The positions and strengths of vorticity deposited into the wake must be obtained from theoretical and empirical considerations. Also solving for the entire sheet structure trailed behind the blades can be computationally cost prohibitive, especially for maneuvering flight, where the calculations need to be carried out for a large number of rotor revolutions depending on the duration of the maneuver under consideration. CFD schemes (Refs. 64, 100) are capable of capturing the generation of vorticity over the rotor blades. However, these methods require very high grid resolutions to prevent numerical dissipation of the vortical wake structure. Several approaches such as wake

coupling (Ref. 64) and wake capturing (Refs. 100, 104) are being explored to capture the wake dynamics with desired accuracy. These methods hold much promise for improved prediction of the rotor airloads for arbitrary flight conditions. However, the computational costs incurred with such approaches render them unsuitable for routine use in prediction of maneuvering flight, at least at present.

## 1.4 Objectives of this Dissertation

While several methodologies are available for simulating the rotor wake aerodynamics, these methods have been primarily developed for the analysis of steady flight conditions. The issues surrounding maneuvering flight aerodynamics have gained attention only in the recent years. None of the existing methodologies satisfactorily models all the issues that are critical for the study of maneuvering flight conditions through numerical simulations.

Conducting experiments and/or flight tests to study the entire gamut of maneuvering flight conditions and different rotor configurations is impractical because of the costs involved in such a venture. With the recent interest in the development of quieter rotors, heavy-lift helicopters, and in studies on optimized, noise-abatement trajectories for operations in civilian areas, it is clear that a new methodology specifically tailored to handle arbitrary maneuvering flight conditions is necessary.

The objective of the present dissertation is to develop a reliable computational tool capable of capturing the nonlinear wake aerodynamics in response to arbitrary large amplitude, high rate maneuvering flight conditions for generic rotor configurations. The primary objective is to develop and validate a fully time-accurate, free-vortex wake model capable of capturing the unsteady, nonlinear, transient wake aerodynam-

ics under arbitrary maneuvering flight conditions. The numerical scheme must be stable, i.e., is must not be susceptible to numerical instabilities while capable of predicting the physical instabilities of the rotor wake under various flight conditions. The numerical algorithm must be capable of computing the wake dynamics at high spatial and temporal resolutions necessary for computations of impulsive noise arising from BVIs.

It has been shown that the induced effects of tip vortices can be prominent, even at older wake ages, under positive filament straining conditions. Predictions of transient wake aerodynamics must, therefore, take into account the viscous diffusion and filament straining effects experienced by the wake vorticity as it is convected in the flow field. This necessitates a tip-vortex core growth model capable of simulating the vortex core growth over a wide range of Reynolds numbers and under arbitrary strain fields. The objective of this dissertation is to incorporate a suitable viscous core growth model, within the framework of the free-vortex wake algorithm, that can properly predict the growth of the tip-vortex core as a function of time and the velocity field.

To satisfy the boundary conditions for the wake equations, the initial position of the tip vortices trailing from the blades and their circulation strengths must be specified. A blade aerodynamic model with the capability to predict the spanwise variation of the nonlinear aerodynamic lift and drag characteristics, the bound circulation and the additional influence of unsteady and dynamic stall effects is necessary. The circulation strengths of the wake vortices can then be obtained from the bound circulation strengths. Furthermore, a blade flapping model capable of capturing the independent blade flapping dynamics is necessary to obtain the positions of the blade tips, which is where the tip vortices originate.

The individual components must be chosen after careful consideration so that high resolution solutions of the induced velocity field and airloads, over several rotor revolutions, are possible without incurring large computational penalties. Each component must be solved consistently during each time step, the coupled effects must then be calculated and the solution marched to the next time step.

The ultimate objective of this work is to couple the rotor wake methodology into a comprehensive aeroelastic or flight dynamic analysis tool (Ref. 34) to perform a true closed-loop analysis. In this approach, the aerodynamics module would benefit from the higher-order modeling of the blade dynamics and helicopter motion in free flight and the nonlinear wake induced velocity field across the rotor disk is feedback to the flight dynamic simulation.

Another objective of this dissertation is use the model developed to gain a deeper insight into the wake aerodynamics in maneuvering flight conditions. As mentioned previously, conducting experiments in various maneuvering flight conditions is impossible. Furthermore, the basic understanding of maneuvering flight is very limited. It is, therefore, difficult to design suitable experiments and decide on the data that need to be measured during these experiments a priori. However, before proceeding with the analysis of various maneuvers, the code must be validated against a broad spectrum of experimental data for maneuvering flight and different rotor configurations to prove its versatility and reliability.

Once the capability to simulate maneuvers for which experimental measurements are available is established, the code can be used to study other flight conditions. Different flight maneuvers such as pop-up and pop-down maneuver from hovering flight conditions, arrested descent or pull-up maneuver from steady, descending flight conditions, starboard and port roll maneuvers, roll reversals and quickstop manuevers

will be analyzed to understand the characteristic wake response common to all maneuvering flight conditions, and the subtle differences in the wake aerodynamics and the resulting airloads for different maneuvers. The airloads time histories obtained will be used to analyze the rotor noise during the transient maneuvers and identify the source of impulsive noise, by studying the wake geometry, rotor airloads and the intensity and positions of BVIs.

## 1.5 Outline of the Dissertation

The maneuvering rotor problem and the challenges involved in predicting such flight conditions were introduced in this introductory chapter. A brief survey of the existing computational methodologies to solve the rotor wake aerodynamics was presented in Section 1.2. The shortcomings of the existing methodologies in the simulation of the maneuvers were explored in Section 1.3, which laid the groundwork for the objectives of the present dissertation.

The remainder of this dissertation is divided into four chapters. The methodology adopted for simulation of unsteady, maneuvering flight is described in detail in Chapter 2. In addition to the free-vortex wake model, the chapter also discusses the tip-vortex core growth model, the blade aerodynamic model (both the Weissinger-L lifting surface model and the nonlinear airfoil model), the time-accurate blade flapping model, the rotor trim algorithm, and the concepts of wave tracing for acoustic directivity analyses.

Chapters 3 and 4 discuss the numerical results obtained using the free-vortex wake analysis. Chapter 3 presents a comprehensive validation of the free-vortex wake model with existing experiments under unsteady flight conditions, particularly experi-

ments by Carpenter & Friedovich, and Ellenreider & Brinson. The chapter concludes with validation of the performance predictions obtained from free-vortex analyses for rotors operating in ground effect, and for coaxial rotor configurations. Chapter 4 presents a detailed analysis of the transient wake aerodynamics associated with various maneuvers. Both idealized and free flight maneuvers results are presented. Finally, Chapter 5 summarizes the main conclusions drawn from the present work.

# Chapter 2

# Methodology

This chapter explains in detail the methodology developed in the present study. The computational model developed for the analysis of maneuvering flight conditions is made up of various sub-components, as outlined previously in Section 1.4, each dealing with a different aspect of the problem, namely the rotor blade, wake. In the following sections, the governing equations and the computational scheme used in solving these equations are described.

The rotor blade aerodynamic model is described first. The equations for rigid blade flapping are then derived with a special emphasis on the inertial terms introduced during maneuvering flight. The rotor wake governing equations and their solution methodology is described next. The viscous splitting strategy to account for viscous diffusion and filament strain are presented. The basics of wave-tracing concepts to determine the acoustically significant BVI interactions over the rotor disk and the primary directivity patterns of these sound sources will be outlined. The BVI locations at any given time instant are readily obtained from the rotor wake geometry solution using analytical geometry concepts. Finally, the rotor trim methodology for both single and dual rotor configurations is explained. While rotor trim depends

on many parameters, some form of trim is essential to establish a steady state flight condition, which serves as an initial solution for the maneuvering rotor problem.

## 2.1 Coordinate Systems

Four different right-handed, Cartesian coordinate systems are used in the present work, namely: 1. Gravity-axes or inertial frame of reference, 2. Body-fixed frame of reference with the origin at the helicopter center of mass, 3. Hub-fixed, non-rotating coordinate system with the $z$-axis along the axis of rotation, and 4. Blade-fixed rotating coordinate system. The emphasis in the present work is the simulation of the aerodynamics of the rotor and its wake. For the rotor aerodynamics problem, especially the analysis of steady flight conditions, the formulation requires only the last two coordinate systems. However, to simulate maneuvering flight the freestream velocities, helicopter attitude, rates, and accelerations must be prescribed to the free-vortex wake analysis from a comprehensive flight dynamics analysis. For this the exchange of information between the flight dynamics analysis and the aerodynamics analysis requires the use of the ground-fixed and the hub-fixed coordinate systems. Therefore, these coordinate systems are now discussed.

Figure 2.1 shows the four coordinate systems used in the present study. The gravity axis system $(x,y,z)_G$ is such that the $z_G$-axis always points in the direction of the vertical towards the earth regardless of the orientation of the helicopter. The choice of $x_G$- and $y_G$-axes can be somewhat arbitrary. The body axis system $(x,y,z)_B$ has its origin at the center of mass of the helicopter. Its axes are fixed to, and rotate with, the helicopter. The $x_B$-axis points towards the nose of the aircraft, the $y_B$-axis points towards the starboard, and the $z_B$-axis points downward. The hub-fixed coordinate

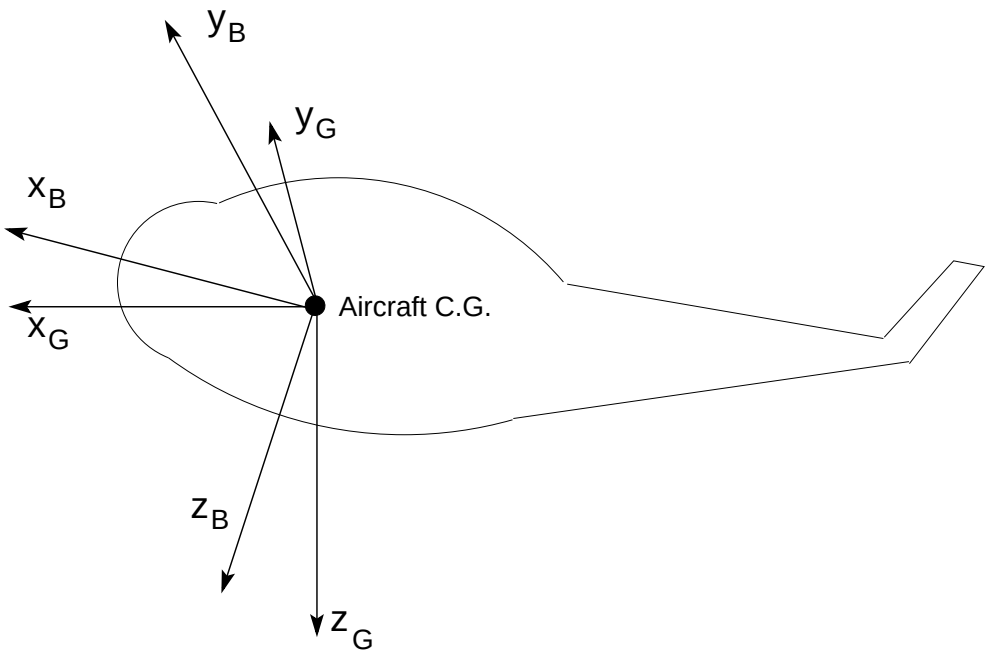


(a) Helicopter coordinate systems

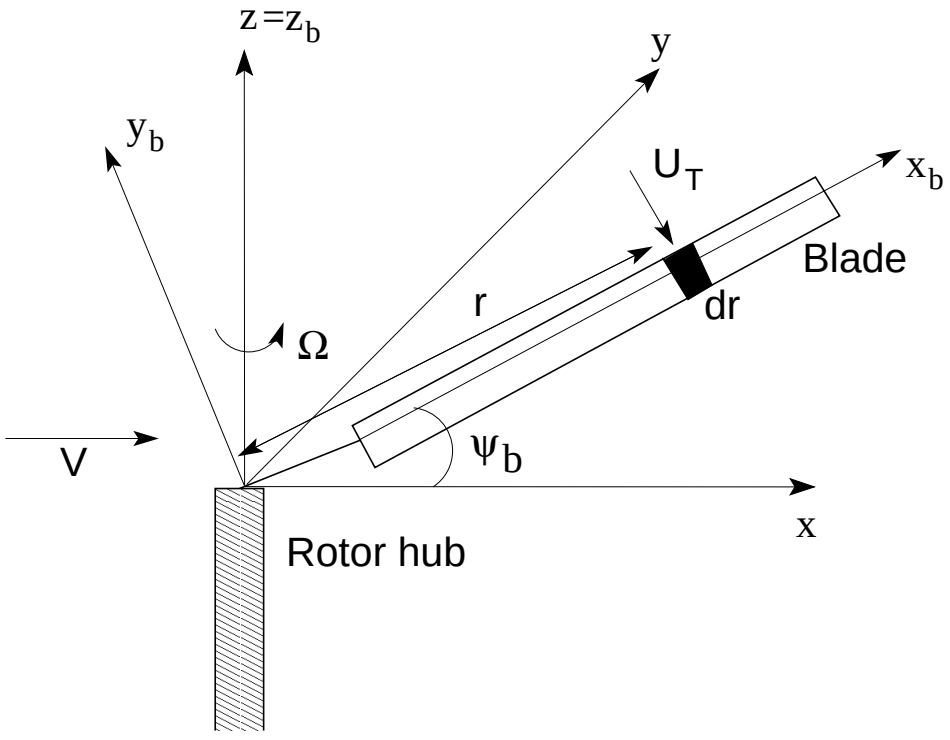


(b) Rotor coordinate systems

Figure 2.1: Coordinate systems used in the development of the free-vortex wake methodology.

system has its origin where the blades are attached to the hub. The $z$-axis points along the axis of rotation of the rotor. The $x$-axis points towards the tail of the helicopter and the $y$-axis points towards starboard. Notice that the orientation of $x_B$- and $x$-axes are opposite to each other. The rotating, blade-fixed coordinate system has the $x_b$-axis along the span of the rotor blade. The $y$-axis is along the chord pointing towards the leading edge of the blade, and the $z$-axis is normal to the blade. The $x-y$ plane of the rotating coordinate system coincides with that of the hub-fixed coordinate system such that $\mathbf{k}_b = \mathbf{k}$. Also $\mathbf{i}_b = \mathbf{i}$ when the blade is over the tail of the helicopter, i.e., $\psi_b = 0^\circ$.

## 2.2 Free-Vortex Models

The free-vortex model adopts a Lagrangian description of the flowfield where the computational domain including the blade and the rotor wake is represented using discrete elements of vorticity. It is assumed that the entire wake vorticity is confined within these particles and the flowfield is essentially irrotational outside these particles. The initial vorticity of these filaments are governed, in part, by the blade aerodynamic loading. Finding a solution for the subsequent motion of these wake vortex markers under the influence of the local induced velocity field, along with the changes in the vorticity of these elements, defines the free-vortex wake problem.

Several mathematical representations have been adopted by researches to describe these vortex elements — see the discussion in Section 1.2.3. For the rotor wake problem, which is dominated by the tip-vortices trailing from the blade tips, the most natural and useful representation is the straight-line filament. The straight-line decomposition of the filaments and the subsequent numerical reconstruction of the velocity

field has been shown to be second-order accurate (Refs. 84, 105).

### 2.2.1 Integration of the Induced Velocity: Biot–Savart Law

The essence of the rotor wake problem is the computation of the induced velocity field for points in the regions of interest in the flow field. In a free-vortex model, the wake induced velocity at any point is computed by the repeated application of the Biot–Savart law, and by numerically integrating the induced velocity contribution from each vortex element over the entire flowfield. The velocity induced by a distribution of vorticity in the domain, $\tau$, at any point, $\mathbf{r}_i$, is given by (Ref. 70, pp. 526–530)

$$\mathbf{V}_i = \nabla \times \frac{1}{4} \int_{\tau} \frac{\vec{\omega}_\tau(\mathbf{r}_\tau, t)}{|\mathbf{r}_i - \mathbf{r}_\tau|} d\tau \tag{2.1}$$

For a line vortex with circulation strength, $\Gamma$, in the flowfield, this equation can be rewritten in terms of the circulation associated with the filament as

$$\mathbf{V}_i = \int \frac{\Gamma_j}{4\pi} \frac{d\mathbf{l}_j \times \mathbf{r}_i}{|\mathbf{r}_i - \mathbf{r}_j|^3} \tag{2.2}$$

An exact solution is available for the velocity induced by a finite straight line vortex segment, $\overrightarrow{AB}$, with constant circulation, $\Gamma$, at any point C in space (see Fig. 2.2), namely

$$\mathbf{V} = \frac{\Gamma}{4\pi} \left\{ \mathbf{a} \cdot \left( \frac{\mathbf{r}_1}{|\mathbf{r}_1|} - \frac{\mathbf{r}_2}{|\mathbf{r}_2|} \right) \right\} \frac{\mathbf{a} \times \mathbf{r}_1}{|\mathbf{a} \times \mathbf{r}_1|^2} \tag{2.3}$$

Equation (2.3) is a better numerical representation of the velocity field than the usual formulation using sines and cosines of the angles subtended by the vectors connecting the end points of the filament to the point of interest. This is because repeated calculation of sines and cosines using a computer requires considerable processor cycles, while vector calculations are much faster because it involves arithmetic manipulation of floating numbers.

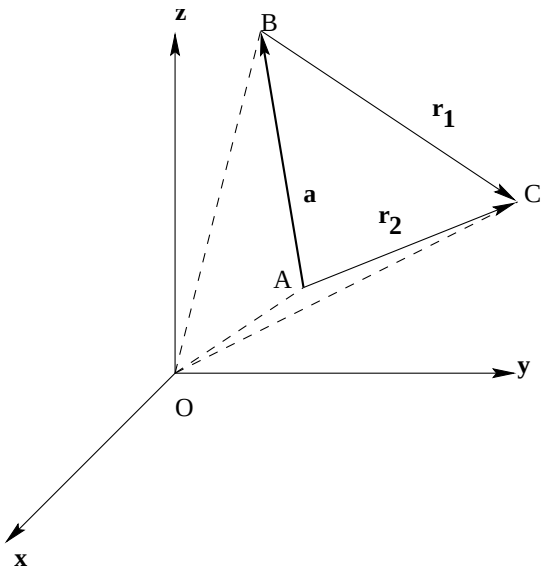


Figure 2.2: Induced velocity of a straight line segment using Biot–Savart law.

The velocity induced by a curved vortex filament is approximated using straight line segmentation and numerically integrating for the velocity field using the trapezoidal rule. The errors incurred in the numerical approximation can be estimated using a Taylor series analysis. It can be shown that (Ref. 82) the dominant truncation error term is of the form

$$\mathbf{V}_{\text{discrete}} = \mathbf{V}_{\text{exact}} + \frac{1}{12}\frac{\partial^2 \mathbf{V}}{\partial \zeta^2}\Delta\zeta^2 + \ldots \tag{2.4}$$

The leading error term is second-order and, therefore, the numerical approximation is second-order accurate in $\Delta\zeta$. The accuracy issues of the summation of mutually induced velocities of the free-vortex elements is discussed in detail in Ref. 105. It was shown that to maintain an overall second-order accuracy, the wake filament discretizations must be less than $5^\circ$. This can become an important issue for capturing BVIs in aeroacoustic computations, which will be discussed later in Section 2.7.

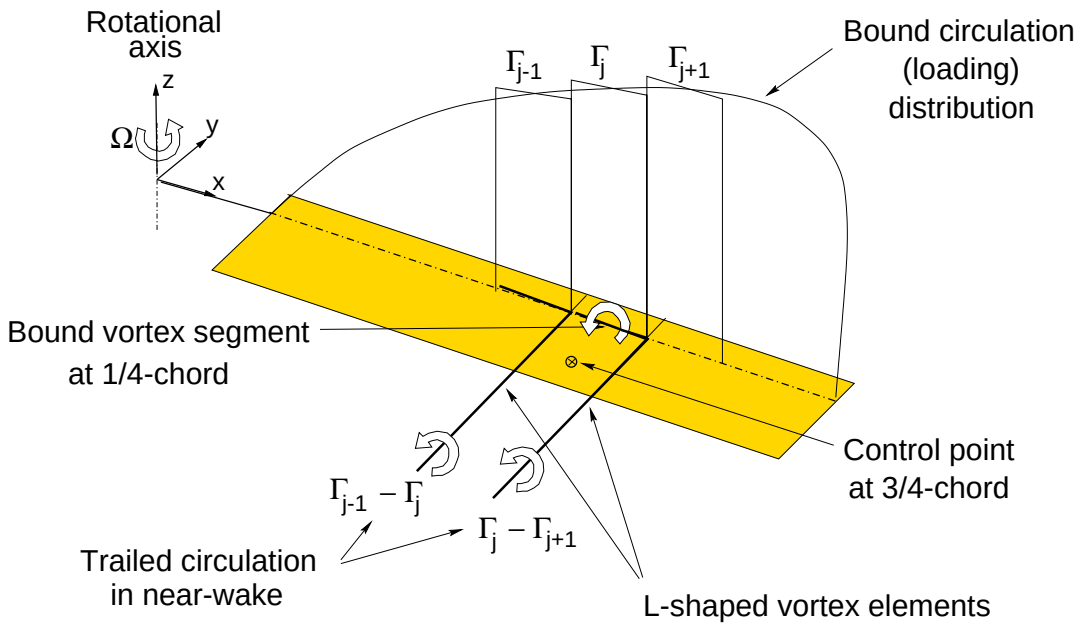


Figure 2.3: Weissinger-L lifting surface model for the rotor blade.

## 2.3 Blade Aerodynamic Model

In the present work, the rotor is modeled as $N_b$ rigid, articulated blades, which execute fully independent, time-accurate, flapping motion. The blade aerodynamic model (developed in Refs. 59, 82) has been adopted and extended for the analysis of maneuvering flight. Aerodynamically, each blade is modeled as a distribution of vortex singularities in the flowfield. The simplest vortex model for a rotor blade is the lifting line model (Ref. 25), which models the rotor blade as a single line vortex of length equal to the blade span. However, this model is unsatisfactory for rotor applications because it does not capture the spanwise variation of circulation and lift, especially the three-dimensional effects at the rotor blade tips.

A more sophisticated approach is to use a lifting surface model where the blade is divided into spanwise and chordwise segments, enabling the resolution of the three-dimensional effects on the rotor blade. A popular lifting surface model suitable for

the rotor blade problem is the Weissinger-L lifting surface model (Ref. 106). This model represents the blade using multiple horse-shoe vortices (see Fig. 2.3) and is used in the present approach. Each blade is divided into $N_s$ equal spanwise segments, with a bound vortex located at $1/4$ chord and only one chordwise segment. There is provision to use unequal spanwise segments with a cosine distribution to bias the number of segments towards the blade root and tip. In this case, the end points of the individual spanwise segments are given by

$$\bar{r}_i = \frac{1}{2}\left[\left(1+\frac{R_c}{R}\right)+\left(1-\frac{R_c}{R}\right)\cos\left(\pi\,\frac{N_s+1-i}{N_s}\right)\right], \qquad i=1,\ldots,N_s+1 \quad (2.5)$$

Alternately, the cosine distribution can be used to provide a concentration of spanwise segments only near the blade tip, given by

$$\bar{r}_i = \frac{R_c}{R}+\left(1-\frac{R_c}{R}\right)\cos\left(\frac{\pi}{2}\frac{(N_s+1-i)}{N_s}\right), \qquad i=1,\ldots,N_s+1 \quad (2.6)$$

Such distributions allow a fine resolution of the steep gradients in the distribution of spanwise circulation near the rotor blade tips. The strengths of the trailers are determined using Helmholtz's laws of vorticity conservation (Ref. 49) and are given by

$$\Gamma_t\big|_j = \Gamma_b\big|_j - \Gamma_b\big|_{j+1} \quad (2.7)$$

The trailing line vortices from the Weissinger-L model comprise the near wake of the rotor blade. In the present work, the near wake is assumed to be rigid and trails off smoothly from the trailing edge of the rotor blades. These near wake trailers are truncated after a short distance, typically $\Delta\psi = 30^\circ$. It is assumed that, beyond this point, the vortex sheet has completely rolled up and all the circulation in the flowfield is concentrated in the free trailers, which comprise the far-wake.

### 2.3.1 Solution for Blade Circulation Distribution

The strengths of the bound circulation for individual segments are determined by the application of the boundary condition at 3/4-chord location of the mid-point of each segment. The no-penetration or tangential flow boundary condition implies that the component of incident velocity on the blade section that is normal to the spanwise segment at 3/4-chord location must be identically zero to prevent flow through the rotor blades (Ref. 35), i.e.,

$$\mathbf{V}_i \cdot \mathbf{n}_i = 0, \qquad i = 1, \ldots, N_s \tag{2.8}$$

The velocity, $\mathbf{V}_i$, at any spanwise location is composed of the local free stream velocity, additional velocities introduced by maneuver (Section 1.1.3), the induced velocities from the bound circulation, the near wake, and the far wake composed of the free vortex filaments. This gives

$$\mathbf{V}_i = \mathbf{V}_\infty + \mathbf{V}_{\text{man}} + \mathbf{V}_{\text{B}} + \mathbf{V}_{\text{NW}} + \mathbf{V}_{\text{FW}} \tag{2.9}$$

where $\mathbf{V}_{\text{B}}$ and $\mathbf{V}_{\text{NW}}$ depend on the bound circulation strengths and can be evaluated using Eq. (2.3). Therefore, at any blade control point, the velocity induced by the bound segments and the near wake can be written as

$$\begin{aligned} \mathbf{V}_{\text{B}_i} &= \sum_{j=1}^{N_s} A_{b_{ij}} \Gamma_j \\ \mathbf{V}_{\text{NW}_i} &= \sum_{j=1}^{N_s} A_{\text{NW}_{ij}} \Gamma_j \end{aligned} \tag{2.10}$$

Substituting Eq. (2.10) into Eq. (2.9), an expression for the bound circulation can be obtained by solving Eq. (2.8), which can now be rewritten as a linear system of equations

$$\left[A_{ij}\, \mathbf{n}_i\right] \left\{\Gamma_j\right\} = \left\{(\mathbf{V}_\infty + \mathbf{V}_{\text{man}} + \mathbf{V}_{\text{FW}}) \cdot \mathbf{n}\right\}_i \qquad i, j = 1, \ldots, N_s \tag{2.11}$$

The bound circulation is then obtained by inversion of the influence coefficient matrix, i.e.,

$$\{\Gamma_j\} = \left[A_{ij}\ \mathbf{n}_i\right]^{-1} \{(\mathbf{V}_\infty + \mathbf{V}_{\text{man}} + \mathbf{V}_{\text{FW}}) \cdot \mathbf{n}\}_i \tag{2.12}$$

The blade and the near wake are assumed rigid, therefore the influence coefficient matrix, $A_{ij}$, and the normal vectors, $\mathbf{n}_i$, in the blade-fixed frame of reference remain constant. The matrix inversion for the solution of bound circulation needs to be performed only once during the computation.

**Effect of Blade Twist on Near Wake**

The near wake trailers in the Weissinger-L model are assumed to trail off smoothly from the trailing edges of the blade sections. Therefore, for a twisted blade the successive near wake trailers are not in the same plane but at an angle to each other, and so to the chord passing through the blade control point in the section of interest. This means that for a twisted blade the velocity induced by the near wake trailers is not exactly normal to the blade sections at the control point. Previous formulation (Ref. 82) neglected the effects of blade twist and modeled the trailers in the same plane stating that the velocities induced by the successive trailers will cancel the tangential component. However, this assumption is exact only for the trailers immediately adjacent to the blade control point. Furthermore, this assumption is not valid for nonlinear blade twist. The effects of twist are fully accounted for, in the present formulation, by evaluating the component of near wake induced velocities normal to the blade sections, as shown on the left-hand side of Eq. (2.11).

### 2.3.2 Two-Dimensional, Nonlinear Airfoil Model

Often during flight, certain sections of the rotor blade operate at high angles of attack and can stall. The nonlinear lift and drag characteristics (close to the airfoil stall angles and beyond) need to be modeled properly to obtain accurate estimates of the rotor airloads. Furthermore, because of rotational motion, different sections of the rotor blade operate at different Mach numbers. Beddoes' (Ref. 107) two-dimensional, nonlinear airfoil model is used to predict the normal and tangential force coefficients for the airfoil sections. In this model, the normal force component is related to the effective flow separation point, $f$, using the following expression

$$C_n = 2\pi \left( \frac{1+\sqrt{f}}{2} \right)^2 \alpha \tag{2.13}$$

The expression is modified using the Prandtl–Glauert correction factor to account for the compressibility effects and rewritten as

$$C_n = \frac{2\pi}{\sqrt{1-M^2}} \left( \frac{1+\sqrt{f}}{2} \right)^2 \alpha \tag{2.14}$$

The spanwise variation of Mach number changes the effective angle of attack at each section and introduces an effective aerodynamic twist. Beddoes suggests a generalized empirical model for $f$ given by

$$f = \begin{cases} 1 - 0.3 \, \exp\left( \frac{(\alpha - \alpha_0) - \alpha_1}{S_1} \right), & \alpha \leq \alpha_1 \\ 0.04 + 0.66 \, \exp\left( \frac{\alpha_1 - (\alpha - \alpha_0)}{S_2} \right), & \alpha > \alpha_1 \end{cases} \tag{2.15}$$

where $\alpha_0$ is the zero-lift angle of attack of the airfoil. The variables $S_1$ and $S_2$ define the static stall characteristics, which are dependent on the incident flow Mach number.

For a NACA 0012 airfoil, the empirical model for these parameters is given by

$$\begin{aligned} S_1(M) &= 1.8\ \exp\left\{-\left(\frac{(M-0.45)}{0.3}\right)^2\right\} \\ S_2(M) &= 3.6\ \exp\left\{-\left(\frac{(M-0.525)}{0.24}\right)^2\right\} \\ \alpha_1(M) &= 21.5-25M+2\ \exp\left\{-\left(\frac{(M-0.65)}{0.125}\right)^2\right\} \end{aligned} \tag{2.16}$$

Similarly, the drag coefficient is obtained using

$$C_d = C_{d_0} + 0.035\, C_n\ \sin\alpha + K_D C_n \sin(\alpha-\alpha_D) \tag{2.17}$$

The zero lift drag coefficient, $C_{d_0}$, the drag divergence angle of attack, $\alpha_D$, and the factor, $K_D$ is given by

$$C_{d_0}(M) = 0.01 + 0.02\,\mathrm{erf}(50(M-0.8)) \tag{2.18}$$

$$\alpha_D(M) = 16-20M+0.5\ \exp\left\{-\left(\frac{M-0.6}{0.225}\right)^2\right\} \tag{2.19}$$

$$K_D = \begin{cases} 0, & \alpha \le \alpha_D \\ 2.7\ \exp\left(-d_f f\right), & \alpha > \alpha_D \end{cases} \tag{2.20}$$

$$d_f = 6.1-7M+0.5\ \exp\left\{-\left(\frac{M-0.6}{0.125}\right)^2\right\} \tag{2.21}$$

### 2.3.3 Two-Dimensional, Unsteady Aerodynamics Model

The angle of attack and the incident velocities at any blade section vary with time even under non-maneuvering flight conditions. In addition, there can be pronounced unsteady aerodynamic effects when the blade section encounters the tip vortices, causing impulsive changes in the angle of attack. The lift response occurs with a temporal lag. The fluctuations in the rotor airloads and the aerodynamic lags need to be mod-

eled properly during maneuvering flight simulations to capture the transient behavior accurately.

In the present approach, the indicial response method, proposed by Leishman & Beddoes (Refs. 14, 108, 109), is used to calculate the unsteady aerodynamic forces on the blades during unsteady flight. The time-variation in angle of attack is caused by several factors such as the change in blade pitch from cyclic inputs, blade flapping velocities, blade torsion effects and changes in the wake induced inflow. The blade geometric pitch, $\theta$, and the blade pitch rate, $\dot{\theta}$ at any azimuth is given by

$$\theta(\psi_b) = \theta_0 + \theta_{1c}\cos\psi_b + \theta_{1s}\sin\psi_b + \theta_{\text{tw}}\left(\bar{r} - \frac{R_c}{R}\right) \tag{2.22}$$

$$\dot{\theta}(\psi_b) = -\theta_{1c}\sin\psi_b + \theta_{1s}\cos\psi_b \tag{2.23}$$

The present analysis does not include the blade elastic torsion deformations, contributions from lag, and higher order flap bending effects. However, when coupled with an aeroelastic blade model, the torsion effects, $\theta_{\text{tor}}$ and $\dot{\theta}_{\text{tor}}$ must be prescribed to the blade aerodynamic model and included in Eq. (2.22) for consistency. The flapping rate, $\dot{\beta}$ is obtained from solving the rigid blade flapping equations, as discussed later in Section 2.4.

The expression for the normal velocity at the blade control point can be written as

$$U_P(r,\psi_b) = V_z + V_{i_z} + \frac{\dot{\theta}c}{2} + \dot{\beta}\,(r - eR) \tag{2.24}$$

and the effective angle of attack at any instant of time for a given blade section can then be written as

$$\alpha(r,\psi_b) = \theta - \arctan\left(\frac{U_P}{U_T}\right) \tag{2.25}$$

The terms introduced by blade flap, lag and torsional effects must be included in Eq. (2.24) when coupled with an aeroelastic blade model.

The unsteady aerodynamic effects are then computed as a series of step changes in the angle of attack and pitch rate over successive time steps. The indicial response function is composed of circulatory and non-circulatory components. The indicial response function for a step change in angle of attack, $\Delta\alpha$, is given by

$$\Delta C_n(s) = \left( \frac{C_{n_\alpha}}{2} \phi_\alpha^c(s,M) + \frac{4}{M} \phi_\alpha^{nc}(s,M) \right) \Delta\alpha \tag{2.26}$$

Similarly, the indicial response function for a step change in the pitch rate about quarter-chord is given by

$$\Delta C_n(s) = \left( \frac{C_{n_\alpha}}{16} \phi_q^c(s,M) + \frac{1}{M} \phi_q^{nc}(s,M) \right) \Delta q \tag{2.27}$$

where $s$ is the distance traveled by the airfoil in semi-chords after the step input, $C_{n_\alpha}$ is the local lift-curve slope of the airfoil, and $\phi_\alpha^c$, $\phi_\alpha^{nc}$, $\phi_q^c$, $\phi_q^{nc}$ are the indicial response functions for the conservative and non-conservative components associated with step changes in angle of attack and step change in the pitch rate. The indicial response functions are approximated by using exponential functions and the above step responses are then superimposed using finite-difference approximation to the Duhamel integral (Ref. 108) to take into account the time-histories of the change in angle of attack and the pitch rate.

Although a linearized model, the indicial method is formulated in the time-domain and has sufficient fidelity to capture the airloads associated with the wake induced velocity field and the blade motion under arbitrary conditions. The indicial method is, therefore, ideal for analysis of maneuvering flight problems where time-history information about the aerodynamics must be accounted for over very long periods of time.

**Duhamel Recurrence Solution for the Circulatory Component**

The circulatory lift function, $\phi^c$, takes the general two-term exponentially growing function of the following form

$$\phi^c(s,M) = 1 - A_1 e^{-b_1 \beta^2 s} - A_2 e^{-b_2 \beta^2 s} \tag{2.28}$$

where $A_1$, $A_2$, $b_1$, $b_2$ are positive constants determined from relating the results of frequency domain with measurements for oscillating airfoils in subsonic flow. It can be then shown that effective, unsteady, instantaneous angle of attack at any given time instant can then be written as (Ref. 1, Ch. 8)

$$\alpha_{\text{eff}}(s) = \alpha(s) - X(s) - Y(s) \tag{2.29}$$

where $X$ and $Y$ are determined using the recurrence algorithm (Ref. 110)

$$X(s) = X(s-\Delta s)\, e^{-b_1 \beta^2 \Delta s} + A_1 \Delta\alpha\, e^{-b_1 \beta^2 \Delta s/2} \tag{2.30}$$

$$Y(s) = Y(s-\Delta s)\, e^{-b_2 \beta^2 \Delta s} + A_2 \Delta\alpha\, e^{-b_2 \beta^2 \Delta s/2} \tag{2.31}$$

Similar expression can be derived for the indicial lift function for calculating the response of changes in the pitch rate. The $\alpha_{\text{eff}}$, in Eq. (2.29), is used in calculating the normal and tangential force coefficients in Eqs. (2.13)–(2.18).

**Recurrence Solution for the Non-Circulatory Lift Terms**

The non-circulatory normal force coefficients are given by (Ref. 1)

$$C_{n_\alpha}^{nc} = \frac{4}{M}\phi_\alpha^{nc} = \frac{4}{M}\exp\left(\frac{-s}{T'_\alpha}\right) \tag{2.32}$$

$$C_{n_q}^{nc} = \frac{1}{M}\phi_q^{nc} = \frac{1}{M}\exp\left(\frac{-s}{T'_q}\right) \tag{2.33}$$

where

$$T'_{\alpha} = \frac{2M}{(1-M)+\pi\beta M^2(A_1 b_1 + A_2 b_2)} \tag{2.34}$$

$$T'_{q} = \frac{2M}{(1-M)+2\pi\beta M^2(A_1 b_1 + A_2 b_2)} \tag{2.35}$$

The advantage of representing $T'_{\alpha}$ and $T'_{q}$ in this manner is that regardless of the values chosen for $A_1$, $A_2$, $b_1$, and $b_2$, the non-circulatory constants will be automatically adjusted to give the correct initial value and slope of the total indicial response as given by the exact linear theory (Ref. 1). The recurrence solution can then be written as

$$C^{nc}_{\Delta\alpha}\big|_s = C^{nc}_{\Delta\alpha}\big|_{s-\Delta s}\, e^{-\Delta s/T'_{\alpha}} + \left(\Delta\alpha\big|_s - \Delta\alpha\big|_{s-\Delta s}\right)\frac{2V}{c\Delta s}e^{-\Delta s/2T'_{\alpha}} \tag{2.36}$$

$$C^{nc}_{n_\alpha} = \frac{4T_{\alpha}}{M}\left\{\left(\frac{2V}{c\Delta s}\right)\Delta\alpha - C^{nc}_{\Delta\alpha}\right\}_s \tag{2.37}$$

Similarly,

$$C^{nc}_{\Delta q}\big|_s = C^{nc}_{\Delta q}\big|_{s-\Delta s}\, e^{-\Delta s/T'_{q}} + \left(\Delta q\big|_s - \Delta q\big|_{s-\Delta s}\right)\frac{2V}{c\Delta s}e^{-\Delta s/2T'_{q}} \tag{2.38}$$

$$C^{nc}_{n_q} = \frac{T_q}{M}\left\{\left(\frac{2V}{c\Delta s}\right)\Delta q - C^{nc}_{\Delta q}\right\}_s \tag{2.39}$$

The contribution from non-circulatory terms are added to the normal force coefficients obtained from the nonlinear airfoil model. The spanwise normal and tangential loads are then numerically integrated for all the blades to obtain the net forces and moments acting on the rotor at any given instance of time.

## 2.4 Rigid Blade Flapping Dynamics

Blade flapping dynamics plays a very influential role in the maneuvering flight aerodynamic response. The rotor airloads are closely coupled with the blade-flapping

response. Because the elemental lift depends on the local induced inflow velocity, the blade flapping response is dictated by the vortical wake solution. Also, the blade attachment boundary condition required for the wake vortex filaments depends on the blade flapping solution. This necessitates the solution of the rotor wake and the blade flapping solution in a fully coupled manner. Most rotor aerodynamic analyses use simplified blade flapping equations, which assume steady, straight-and-level flight conditions. For purposes of maneuvering flight simulation, the contributions of the helicopter dynamics to the inertial and aerodynamic terms in the flapping equation must be modeled accurately. Furthermore, the blade flapping equations must be solved independently for each rotor blade because the aerodynamic environment can be considerably different for each rotor blade at different times. In this section, the development of the equations of flapping motion will be presented. The final equations will be recast into a set of first-order differential equations, and the solution strategy for these equations will then be discussed.

Consider a helicopter executing arbitrary pitch and roll motions about the body-fixed axes with the rates $p$ and $q$, respectively. The rotor is rotating about the $z$-axis with a rotational speed $\Omega$. Figure 2.4 shows the coordinate systems used for deriving the flap equations of motion. $(x,y,z)_B$ is the helicopter-fixed coordinate system. The helicopter rolls and pitches about this axis. The $(x,y,z)_{NR}$ frame of reference is the hub-fixed, non-rotating frame of reference. The rotor is at a distance $\mathbf{R}_H$ from the helicopter center of gravity. The frame $(x,y,z)$ is the rotating coordinate system, with $z$-axis along the axis of rotation of the rotor blades. The frame $(x,y,z)'$ is the blade-fixed coordinate system whose $x-y$ plane is at an angle, $\beta$, to the rotating frame of reference. For simplicity, it will be assumed that the rotor axis of rotation coincides with the $z_B$- axis, i.e., $\mathbf{k}_B \cdot \mathbf{k} = -1$. Therefore, for the purposes of this derivation,

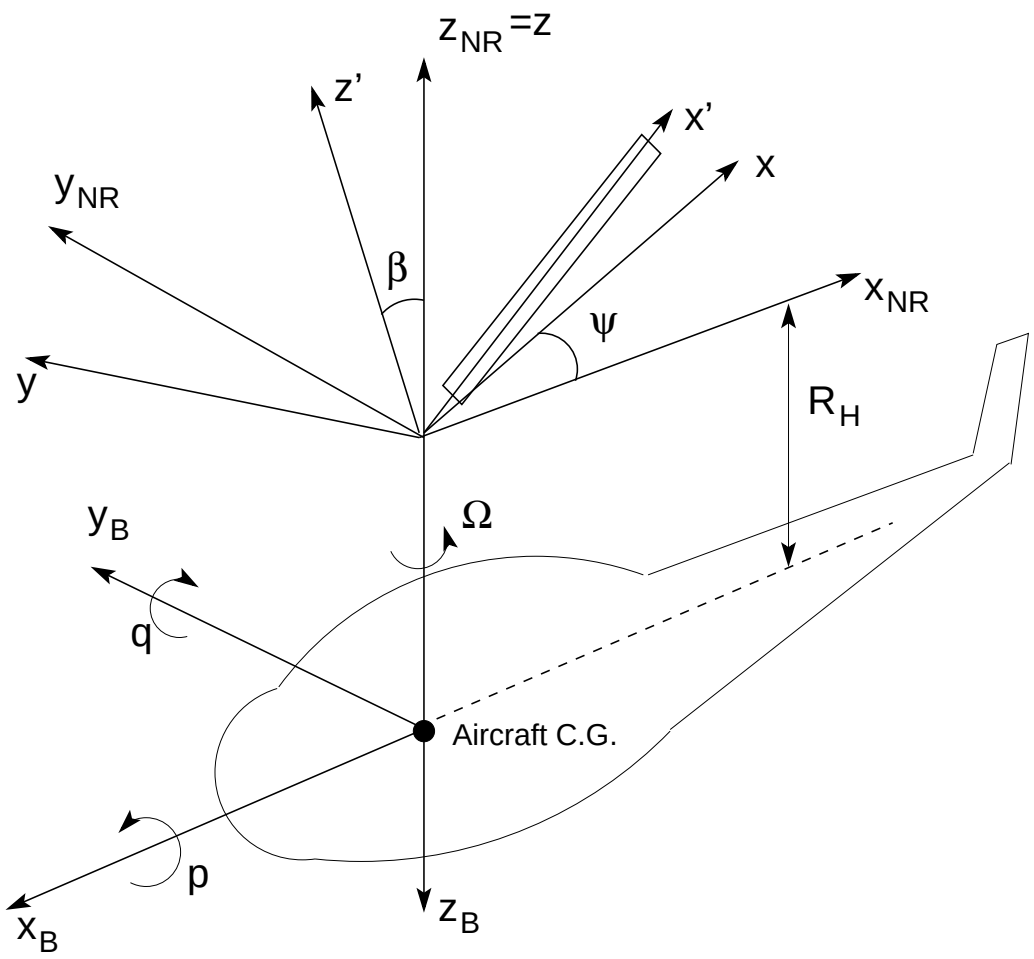


Figure 2.4: Helicopter and blade coordinate systems for a flapping blade.

$\mathbf{R}_H = -R_H\mathbf{k}_B$. The position vector $\mathbf{r}_P$ of any point $P$ on the flapping blade can then be written as

$$\mathbf{r}_P = r_p\cos\beta\mathbf{i} + (R_H + r_p\sin\beta)\mathbf{k} \tag{2.40}$$

The angular velocity vector $\mathbf{A}$ for a helicopter executing pitch and roll motion can then be written as

$$\begin{aligned} \mathbf{A} &= -p\mathbf{i}_{NR} + q\mathbf{j}_{NR} + \Omega\mathbf{k} && (2.41)\\ &= (q\sin\psi - p\cos\psi)\mathbf{i} + (p\sin\psi + q\cos\psi)\mathbf{j} + \Omega\mathbf{k} && (2.42) \end{aligned}$$

### 2.4.1 Derivation of Inertial Flap Moment

The moment about the flapping hinge introduced by inertial forces is given by

$$\begin{aligned} M_I &= R^2 \int_0^1 m a'_{P_z} \bar{r} d\bar{r} \\ &= R^2 \int_0^1 m \left( a_{P_z} - \beta a_{P_x} \right) \bar{r} d\bar{r} \end{aligned} \tag{2.43}$$

where $a'_{P_z}$ is the acceleration normal to the blade in the blade-fixed frame of reference. The expressions for $a_{P_x}$ and $a_{P_z}$ can be derived in the following manner. The velocity $\mathbf{V}_P$ at point $P$ is given by

$$\mathbf{V}_P = \frac{d}{dt}\mathbf{r}_P = \frac{\partial}{\partial t}\mathbf{r}_P + \mathbf{A} \times \mathbf{r}_P \tag{2.44}$$

$$\begin{aligned} \frac{\partial}{\partial t}\mathbf{r}_P &= -r_P \dot{\beta} \sin\beta \mathbf{i} + r_P \dot{\beta} \cos\beta \mathbf{k} \\ &\approx -r_p \dot{\beta} \beta + r_p \dot{\beta} \end{aligned} \tag{2.45}$$

$$\mathbf{A} \times \mathbf{r}_P = \begin{vmatrix} \mathbf{i} & \mathbf{j} & \mathbf{k} \\ (q\sin\psi - p\cos\psi) & (p\sin\psi + q\cos\psi) & \Omega \\ r_P \cos\beta & 0 & (R_H + r_p \sin\beta) \end{vmatrix} \tag{2.46}$$

The components of velocity are

$$V_{P_x} = (R_H + r_p \sin\beta)(p\sin\psi + q\cos\psi) - r_p \dot{\beta} \sin\beta \tag{2.47}$$

$$V_{P_y} = r_P \Omega \cos\beta - (R_H + r_p \sin\beta)(q\sin\psi - p\cos\psi) \tag{2.48}$$

$$V_{P_z} = r_p \dot{\beta} \cos\beta - r_p \cos\beta (p\sin\psi + q\cos\psi) \tag{2.49}$$

The expression for acceleration $\mathbf{a}_P$ for the point $P$ is given by

$$\mathbf{a}_P = \frac{d}{dt}\mathbf{V}_P = \frac{\partial}{\partial t}\mathbf{V}_P + \mathbf{A} \times \mathbf{V}_P \tag{2.50}$$

The components of acceleration are given by

$$\begin{aligned}
\mathbf{a}_x &= (R_H + r_p \sin\beta)(\dot{p}\sin\psi + p\Omega\cos\psi + \dot{q}\cos\psi - q\Omega\sin\psi) \\
&\quad -r_p\ddot{\beta}\sin\beta - r_p\dot{\beta}^2\cos\beta + V_{P_z}(q\cos\psi + p\sin\psi) - \Omega V_{P_y} \qquad (2.51)\\
\mathbf{a}_y &= -\Big[r_p\Omega\dot{\beta}\sin\beta + r_p\dot{\beta}\cos\beta(q\sin\psi - p\cos\psi) + +\Omega V_{P_x} - V_{P_z}(q\sin\psi - p\cos\psi) \\
&\quad (R_H + r_P\sin\beta)(\dot{q}\sin\psi + q\Omega\cos\psi - \dot{p}\cos\psi + p\Omega\sin\psi)\Big] \qquad (2.52)\\
\mathbf{a}_z &= -r_P\dot{\beta}\sin\beta - r_P\cos\beta(\dot{p}\sin\psi + p\Omega\cos\psi + \dot{q}\cos\psi - q\Omega\sin\psi) \\
&+ V_{P_y}(q\sin\psi - p\cos\psi) - V_{P_x}(q\cos\psi + p\sin\psi) + r_P\ddot{\beta}\cos\beta - r_P\dot{\beta}^2\sin\beta \qquad (2.53)
\end{aligned}$$

The time derivative $\partial/\partial t$ is replaced with $\partial/\partial\psi$ with respect to the blade azimuth, such that $\partial/\partial t = \Omega\partial/\partial\psi$. Furthermore, the derivative with respect to the azimuth $\partial/\partial\psi$ is represented with a '$\star$' for compactness. Further, introducing small angle assumption for $\beta$, and also assuming that $q/\Omega = p/\Omega = O(\varepsilon)$, and neglecting the higher order terms, the expressions of $\mathbf{a}_x$ and $\mathbf{a}_z$ simplify to

$$\begin{aligned}
\mathbf{a}_x &= \Omega^2 R\bar{r}_P\beta \qquad (2.54)\\
\mathbf{a}_z &= \Omega^2 R\bar{r}_p\left(\overset{\star\star}{\beta} + 2\left(\frac{q}{\Omega}\right)\sin\psi - 2\left(\frac{p}{\Omega}\right)\cos\psi - \left(\frac{\overset{\star}{q}}{\Omega}\right)\cos\psi - \left(\frac{\overset{\star}{p}}{\Omega}\right)\sin\psi\right) \qquad (2.55)
\end{aligned}$$

Substituting the above expressions into Eq. (2.43) we have

$$\begin{aligned}
M_I &= \Omega^2 R^3\int_0^1 m\left[\overset{\star\star}{\beta} + \beta + 2\left(\frac{q}{\Omega}\right)\sin\psi - 2\left(\frac{p}{\Omega}\right)\cos\psi \right.\\
&\quad \left. -\left(\frac{\overset{\star}{q}}{\Omega}\right)\cos\psi - \left(\frac{\overset{\star}{p}}{\Omega}\right)\sin\psi\right]\bar{r}^2 d\bar{r} \\
&= I_b\Omega^2\left[\overset{\star\star}{\beta} + \beta + 2\left(\frac{q}{\Omega}\right)\sin\psi - 2\left(\frac{p}{\Omega}\right)\cos\psi - \left(\frac{\overset{\star}{q}}{\Omega}\right)\cos\psi - \left(\frac{\overset{\star}{p}}{\Omega}\right)\sin\psi\right] \qquad (2.56)
\end{aligned}$$

where $I_b = R^3 \int_0^1 m\bar{r}^2 d\bar{r}$ is the mass moment of inertia of the rotor blade about the flapping hinge.

### 2.4.2 Flapping Equation of Motion

The inertial moment about the flap hinge must be balanced by $M_A$, the aerodynamic moment about the flapping hinge. Therefore, the flapping equation of motion can be written as

$$\overset{\star\star}{\beta} + \beta = \underbrace{\frac{M_A}{I_b \Omega^2}}_{\overline{M}_A} \underbrace{- 2\left(\frac{q}{\Omega}\right)\sin\psi + 2\left(\frac{p}{\Omega}\right)\cos\psi + \left(\frac{\overset{\star}{q}}{\Omega}\right)\cos\psi + \left(\frac{\overset{\star}{p}}{\Omega}\right)\sin\psi}_{M_I'} \tag{2.57}$$

$M_I'$ represents the additional inertial terms introduced by the rolling and pitching motion of the hub about the helicopter center of mass. The flapping equations can be rewritten as a linear system of first-order differential equations with two variables $\beta$ and $\overset{\star}{\beta}$ in the following form

$$\frac{\partial}{\partial\psi}\begin{Bmatrix} \overset{\star}{\beta} \\ \beta \end{Bmatrix} + \begin{bmatrix} 0 & \nu_\beta^2 \\ -1 & 0 \end{bmatrix}\begin{Bmatrix} \overset{\star}{\beta} \\ \beta \end{Bmatrix} = \begin{Bmatrix} \overline{M}_A + M_I' \\ 0 \end{Bmatrix} \tag{2.58}$$

Equation (2.58) is of the same mathematical form as the governing equations of the wake (discussed later in Section 2.5.1), and can be solved simultaneously using the same numerical scheme and also to the same level of numerical approximation.

## 2.5 Free-Vortex Wake Modeling

In the free-wake analysis, Lagrangian markers are placed along a series of contiguous vortex filaments trailing from ends of the blades. Successive markers on the vortex filament are linked together, for which the simplest and most natural is a piecewise linear reconstruction (as shown in Fig. 2.5).

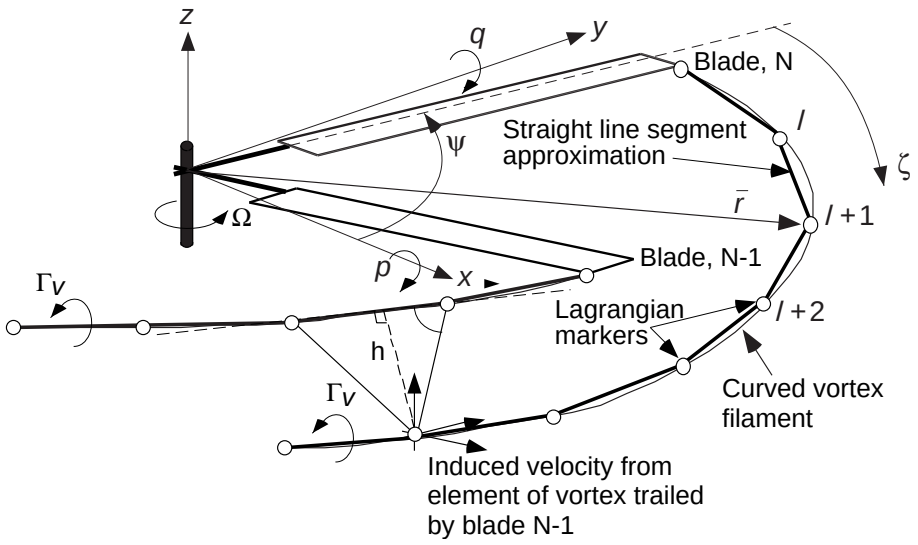


Figure 2.5: Schematic showing the coordinate system and the Lagrangian description of the vortex filaments trailing from the blade tips.

Unlike the bound vortices, whose position is determined by the blade position, the wake vortices are free and convect to force-free locations under the influence of the local velocity field. This process is governed by the three-dimensional, incompressible, Navier–Stokes equation written in velocity-vorticity form as

$$\frac{D}{Dt}\vec{\omega} = \underbrace{\left(\vec{\omega}\cdot\vec{\nabla}\right)\mathbf{V}}_{1} + \underbrace{\nu\Delta\cdot\vec{\omega}}_{2} \tag{2.59}$$

This equation defines the change in vorticity associated with a fluid element moving in the flow in terms of the instantaneous value of vorticity $\vec{\omega}$ and the local velocity $\mathbf{V}$. The left-hand side is the material derivative of vorticity, which represents both the time rate of change of vorticity and the convection term. The right-hand side has two terms. The first term represents the strain and rotation effects on the vortex filament. It represents two phenomena as the vorticity is convected along the flow, i.e., the change in the length of the vortex filaments (strain effect) and the change in the orientation of the vorticity vector (rotation effect). The second term represents the diffusion of

vorticity as a result of the viscosity of the fluid. In most practical problems, the viscous effects will be confined to much smaller length scales compared to the potential flow phenomena, and the remainder of the flow field can be considered essentially inviscid. Under these assumptions Eq. (2.59) reduces to

$$\frac{D}{Dt}\vec{\omega} = \left(\vec{\omega}\cdot\vec{\nabla}\right)\mathbf{V} \tag{2.60}$$

Consider now an arbitrary material line segment $\delta\mathbf{s}$ in the fluid. Its motion is given by the equation (Ref. 49)

$$\frac{D}{Dt}\delta\mathbf{s} = \left(\delta\mathbf{s}\cdot\vec{\nabla}\right)\mathbf{V} \tag{2.61}$$

Combining Eqs. (2.60) and (2.61) gives

$$\frac{D}{Dt}\left(\vec{\omega} - \varepsilon\delta\mathbf{s}\right) = \left\{\left(\vec{\omega} - \varepsilon\delta\mathbf{s}\right)\cdot\nabla\right\}\mathbf{V} \tag{2.62}$$

for some positive $\varepsilon > 0$. If, for some time $t = t_0$, the material line happens to coincide with the vortex line, then it follows that

$$\left(\vec{\omega}_0 - \varepsilon\delta\mathbf{s}_0\right) = 0 \tag{2.63}$$

Equation (2.62) has only one unique solution, namely

$$\left(\vec{\omega} - \varepsilon\delta\mathbf{s}\right) = 0 \tag{2.64}$$

for any time $t > t_0$ provided the flow is solenoidal, i.e., $(\nabla\cdot\mathbf{V})$ is continuous. Equation (2.64) implies that the vorticity vector and the material line coincide at all times, i.e., a material line continues to be a vortex line and the vorticity moves along with the fluid.

In the present formulation, the vortex model uses a Lagrangian description of discrete line vortices. This means that all the vorticity is concentrated along the axis of

each vortex filament, forming a vortex line singularity. Under inviscid, incompressible, irrotational flow conditions these vortex lines move along with material lines (Eq. (2.64)) whose motion is described by the motion of the Lagrangian fluid markers. Thus, the problem of tracking vortex particles reduces to a simple convection (advection) equation of the form

$$\frac{d}{dt}\mathbf{r} = \mathbf{V}, \qquad \mathbf{r}(t=0) = \mathbf{r}_0 \tag{2.65}$$

where $\mathbf{r}_0$ is the initial position vector of the vortex marker. In case of a helicopter rotor blade, rotating with a constant angular velocity $\Omega$, the position vector $\mathbf{r}$ of a wake element can be expressed as a function of the azimuthal position $\psi$ of the blade and the age of the filament $\zeta$ relative to the blade when it was deposited into the wake. Equation (2.65) can, therefore, be written in the non-rotating, hub-fixed coordinate system (see Fig. 2.5) as

$$\frac{\partial \mathbf{r}}{\partial \psi} + \frac{\partial \mathbf{r}}{\partial \zeta} = \frac{\mathbf{V}}{\Omega} \tag{2.66}$$

where the velocity $\mathbf{V}$ has contributions from the free stream, the highly nonlinear, self and mutually induced velocities from the vortex wake structure, and the additional velocities imposed during the maneuver.

The additional velocities introduced by a maneuver are a function of the angular roll $p$, pitch $q$ and yaw $r$ rates along the $x$-, $y$- and $z$-axes respectively

$$\vec{\omega} = p\mathbf{i} + q\mathbf{j} + r\mathbf{k} \tag{2.67}$$

and is given by

$$\mathbf{V}_{\text{man}} = \vec{\omega} \times \mathbf{r} = (ry - qz)\mathbf{i} + (pz - rx)\mathbf{j} + (qx - py)\mathbf{k} \tag{2.68}$$

where $\mathbf{r}$ is the position vector of the point of interest from the center of mass of the helicopter in a body-fixed frame of reference.

The induced velocities are computed by repeated application of the Biot–Savart law (straight line segment formulation given by Eq. (2.3)) to the discretized vorticity field. This is the main computational expense that is associated with vortex methods. The wake solution is coupled with the blade flapping response through the blade attachment boundary condition at the origin of the trailing vortex filaments and with the blade lift solution through the trailed vortex strengths.

### 2.5.1 PC2B Finite Difference Approximation

The terms on the left-hand side of Eq. (2.66) represent the derivatives in the temporal direction, $\psi$, and spatial direction, $\zeta$. These derivatives are approximated using finite difference approximations. The time-accurate, two-step backward, predictor-corrector scheme (PC2B) proposed by Bhagwat & Leishman (Ref. 111) is used in the present work. The computational domain is divided into a grid with steps of $\Delta\psi$ and $\Delta\zeta$. The governing equations are solved at the midpoints $(\psi+\Delta\psi/2, \zeta+\Delta\zeta/2)$ of the grid cell.

It was previously shown in Eq. (2.4), that the velocity computations using the numerical integration of Biot–Savart law for line segments is second-order accurate. The velocity at the center of the grid cell is further approximated by averaging the velocities at the four surrounding grid points. The leading error terms from the velocity averaging can be written as (Ref. 82)

$$\mathbf{V}_{\text{discrete}} = \mathbf{V}_{\text{exact}} + \frac{5}{24}\frac{\partial^2 \mathbf{V}}{\partial \zeta^2}\Delta\zeta^2 + \frac{1}{8}\frac{\partial^2 \mathbf{V}}{\partial \psi^2}\Delta\psi^2 + O(\Delta\zeta^4) \tag{2.69}$$

Once again, the leading error terms are of second-order and the numerical approximation retains an overall second-order accuracy. The spatial derivative is approximated

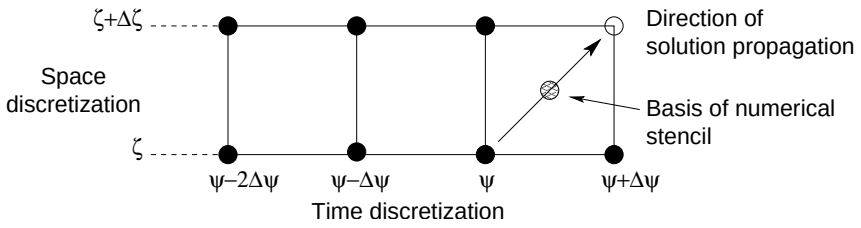


Figure 2.6: Schematic showing the numerical stencil for PC2B algorithm.

using a five-point central differencing scheme, i.e.,

$$\begin{aligned}\frac{\partial \mathbf{r}}{\partial \zeta} &\approx D_\zeta \mathbf{r}\Big|_{\psi+\Delta\psi/2,\zeta+\Delta\zeta/2} \\ &= \frac{\mathbf{r}(\psi+\Delta\psi,\zeta+\Delta\zeta)+\mathbf{r}(\psi,\zeta+\Delta\zeta)-\mathbf{r}(\psi+\Delta\psi,\zeta)-\mathbf{r}(\psi,\zeta)}{2\Delta\zeta} \end{aligned} \tag{2.70}$$

The temporal derivative is written using a second-order, backward differencing algorithm – see Fig. 2.6. This requires three previous time steps as given by

$$\begin{aligned}\frac{\partial \mathbf{r}}{\partial \psi} &\approx D_\psi \mathbf{r}\Big|_{\psi+\Delta\psi/2,\zeta} \\ &= \frac{3\mathbf{r}(\psi+\Delta\psi,\zeta)-\mathbf{r}(\psi,\zeta)-3\mathbf{r}(\psi-\Delta\psi,\zeta)+\mathbf{r}(\psi-2\Delta\psi,\zeta)}{4\Delta\psi} \end{aligned} \tag{2.71}$$

The left-hand side of the governing equation can now be rewritten as

$$\begin{aligned}D_\psi + D_\zeta &= \frac{\partial \mathbf{r}}{\partial \psi}+\frac{\partial \mathbf{r}}{\partial \zeta}+\left(-\frac{5}{24}\frac{\partial^3 \mathbf{r}}{\partial \psi^3}+\frac{1}{8}\frac{\partial^3 \mathbf{r}}{\partial \psi^2 \partial \zeta}\right)\Delta\psi^2+\left(\frac{1}{24}\frac{\partial^3 \mathbf{r}}{\partial \zeta^3}+\frac{1}{8}\frac{\partial^3 \mathbf{r}}{\partial \psi \partial \zeta^2}\right)\Delta\zeta^2 \\ &\quad +\frac{1}{4}\frac{\partial^4 \mathbf{r}}{\partial \psi^4}\Delta\psi^3+\ldots \end{aligned} \tag{2.72}$$

The leading error terms in Eq. (2.72) are of second-order with respect to the grid discretization parameters $\Delta\psi$ and $\Delta\zeta$, indicating an overall second-order accuracy of the numerical scheme used for the finite difference approximations of the derivatives. The modified equation solved for by the finite difference equations can be obtained

by combining Eqs. (2.69) and (2.72) to get

$$\frac{\partial \mathbf{r}}{\partial \psi}+\frac{\partial \mathbf{r}}{\partial \zeta} = \mathbf{V}+\Delta\zeta^2\left[\left(\frac{5}{24}\frac{\partial^2 \mathbf{V}}{\partial \zeta^2}+\frac{1}{8}\frac{\partial^2 \mathbf{V}}{\partial \psi^2}\right)-\left(-\frac{5}{24}\frac{\partial^3 \mathbf{r}}{\partial \psi^3}+\frac{1}{8}\frac{\partial^3 \mathbf{r}}{\partial \psi^2 \partial \zeta}\right)\right.$$
$$\left.-\left(\frac{1}{24}\frac{\partial^3 \mathbf{r}}{\partial \zeta^3}+\frac{1}{8}\frac{\partial^3 \mathbf{r}}{\partial \psi \partial \zeta^2}\right)\underline{-\frac{1}{4}\frac{\partial^4 \mathbf{r}}{\partial \psi^4}\Delta\zeta}\right]+O(\Delta\zeta^4) \qquad (2.73)$$

The above equation assumes equal spacing of $\Delta\psi$ and $\Delta\zeta$.

Notice that the leading truncation error terms are not dependent on the gradient of the local velocity field, therefore, the numerical scheme is essentially problem independent. The underlined term in Eq. (2.73) is a fourth-order dissipative term. This implicit artificial dissipation makes the numerical scheme stable. Furthermore, this term is $O(\Delta\zeta^3)$ and so the overall solution is still second-order accurate.

### 2.5.2 Treatment of Viscous and Strain Effects

Equation (2.66) neglects the effects of viscosity and filament strain on the vorticity associated with the elements as defined in Eq. (2.59). This can be justified in many flight conditions because these effects are usually confined to much smaller length scales compared to the scales associated with the overall developments of the wake. However, during maneuvering flight the wake undergoes considerable reorganization and may, in this process, come into close proximity to the rotor blades. Also the effect of filament strain on the induced velocity field of the wake might be important for various types of flight operations. This means that the physical modeling of the vortex core and its near-field induced velocity field must be considered in more detail.

The principle adopted here for the treatment of the viscous and strain terms is to consider sequential sub-processes in the solution of the various components of Eq. (2.59), and then to combine them together to give a consistent level of approximation to the rotor wake problem. These ideas follow the classical concepts introduced

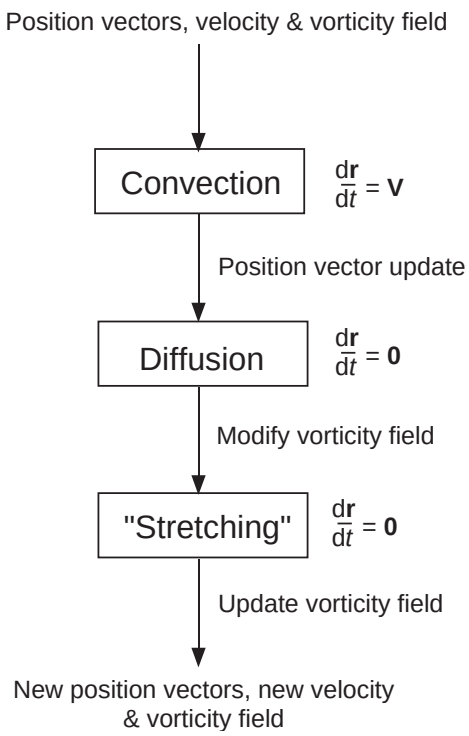


Figure 2.7: Principle of splitting the free-vortex wake solution into separate, sequential treatment of convection, viscous and stretching terms over one time step.

by Prandtl (Ref. 25) to distinguish viscous and inviscid phenomena. These concepts are also reviewed by Ashley & Landahl (Ref. 112), and similar principles applied to vortex methods have been followed by Chorin (Ref. 113). The concept of this "splitting" and recombinant process is shown schematically in Fig. 2.7. The approach is formulated as a time-marching process, which consists of three successive sub-steps where the convection, diffusion and stretching effects are considered sequentially.

The first sub-step in the process is a convection process, where the filaments are advanced to new positions under the influence of the local velocity field at the current time. In the second sub-step, viscous effects associated with diffusion of the filaments are calculated based on the age of the filaments relative to the time at which they

originated in the flow. The third sub-step implements filament strain or stretching effects, which uses the position vectors from the first sub-step and serves to modify the vorticity field. Combined with the new position vectors defined by the first sub-step, the second and third sub-steps allow the new velocity and vorticity fields to be calculated at the next time step. In the present application, the entire process has been implemented as a predictor-corrector sequence, so that the three sub-step updates are performed twice at each time-step, thereby improving the net accuracy and numerical stability of the solution process.

**Viscous Diffusion Model**

As mentioned previously in Section 1.2.3, viscous diffusion of the vortex filaments are usually included in free-vortex wake methods by incorporating a viscous core model into the solution for the induced velocity field through the right-hand side of Eq. (2.65). Because the tip vortices are the dominant vortical feature in the rotor wake, the viscous models are usually applied to the tip vortex alone, and will be based, in part, on empirical evidence. However, a "cut off" or other numerical desingularization will still be necessary for other vortical elements comprising the remainder of the flow, such as the vortex sheet.

While a variety of tip vortex models are possible, the simplest is the Lamb–Oseen model (Ref. 93). Here a solution to the one-dimensional, laminar, Navier–Stokes equation (i.e., a solution for velocity field with assumption that the axial/radial velocities are zero) gives the tangential or swirl velocity surrounding the vortex filament as

$$V_\theta(r) = \frac{\Gamma_v}{2\pi r_c}\left(\frac{1-e^{-\alpha(r/r_c)}}{r/r_c}\right) \tag{2.74}$$

where $r$ is the radial distance from the center of the vortex core and $\alpha = 1.25643$.

The radial location of the peak swirl velocity corresponds to the core radius $r = r_c$. Expanding the exponential term with a series expansion and ignoring the higher-order terms, it can be shown that

$$V_\theta(r) \approx \frac{\Gamma_v}{2\pi}\left(\frac{r}{r^2 + r_c^2}\right) \tag{2.75}$$

This is the Scully vortex model (Ref. 68). A series of general vorticity profiles for rectilinear vortices were suggested by Vatistas in Ref. 92, where the tangential velocity in a two-dimensional cross-sectional plane of the vortex was expressed as

$$V_\theta(r) = \frac{\Gamma_v}{2\pi}\left(\frac{r}{(r^{2n} + r_c^{2n})^{1/n}}\right) \tag{2.76}$$

Note that $n = 1$ in Eq. (2.76) gives the Scully vortex profile. However, it has been found that using $n = 2$ provides a better approximation to the velocity profile measurements (Refs. 92, 114) and has been used in the present approach.

Using the Lamb–Oseen results, the growth of the viscous core radius $r_c$ as a function of time is given by

$$r_c(t) = \sqrt{4\alpha\nu t} \tag{2.77}$$

Because $\psi = \zeta = \Omega t$, Eq. (2.77) is easily converted to a model that is a function of vortex or wake age $\zeta$.

The core growth given by Eq. (2.77) is found to be unrealistically slow in light of experimental evidence. This is because of the laminar flow assumption which considers only molecular diffusion. Squire (Ref. 94) proposed the inclusion of an average apparent or turbulent "eddy" viscosity parameter $\delta$ to account for the natural effects of turbulence on the net rate of viscous diffusion, effectively increasing the viscous core growth rates to values that are consistent with experimental observations of tip vortex growth. Furthermore, at $t = t_0$, the swirl velocity given by the Lamb-Oseen model

in Eq. (2.74) is singular at the origin of the tip vortex, and also unrealistically high velocities are obtained at young wake ages compared to measurements. Therefore, an effective origin offset was further proposed by Squire to give a finite core size and finite induced velocity field at the origin of the vortex filament.

Bhagwat & Leishman (Ref. 86) suggested a semi-empirical model which is a development of the Squire's approach, where the viscous core radius of a filament as a function of its age after it was left in the flow is given by

$$r_c(\zeta) = \sqrt{4\alpha\delta\nu\left(\frac{\zeta+\zeta_0}{\Omega}\right)} \equiv \sqrt{r_{c_0}^2 + \frac{4\alpha\delta\nu\zeta}{\Omega}} \tag{2.78}$$

The coefficients of this model ($\zeta_0$ and $\delta$) are defined empirically from an average of various tip vortex core growth measurements (Ref. 96). The apparent average eddy or turbulent eddy viscosity coefficient, $\delta$ is a function of the vortex Reynolds number, $\Gamma_v/\nu$, which is a complicating factor in the application of viscous corrected models to helicopter wake problems (Refs. 86, 88, 96). The factor $\delta$ is related to $\Gamma_v/\nu$ as

$$\delta = 1 + a_1\left(\frac{\Gamma_v}{\nu}\right) = 1 + a_1 Re_v \tag{2.79}$$

In the case of a purely laminar vortex, i.e., one where molecular diffusion alone exists, note that $\delta = 1$.

It appears that based on experimental observations and ongoing correlation studies, rotating-wing measurements at both full-scale and model-scale show a higher value of effective viscous diffusion with an average value of $a_1 = 2 \times 10^{-4}$, while fixed-wing experiments show a lower effective diffusion with an average value of $a_1 = 5 \times 10^{-5}$. Typically, this means that the value of $\delta$ for sub-scale rotors is about 10, which means that in a real vortex flow the actual viscous diffusion process occurs about 10 times faster than would be expected on the basis of molecular diffusion

alone. For full-scale rotors, which will have vortex Reynolds numbers that are an order of magnitude greater or more, the value of $\delta$ may be higher.

### Strain or "Stretching" Terms

While rotor wakes are formed in a predominantly incompressible flow fields (this is a rigorous assumption only for points far away from the vortex cores), the vortices themselves may have such high strengths and high local velocities that they may show some local compressibility effects (Ref. 114). However, assuming the flow is predominantly incompressible and that any local changes in density is small, Helmholtz's third law (Ref. 49) requires that, under such conditions, the net circulation strength of any vortex filament remains constant. Now the circulation associated with a vortex tube is given by

$$\Gamma = \int_S \vec{\omega} d\mathbf{S} \tag{2.80}$$

Positive strain, or stretching, of the vortex filament as it encounters the strain field produced by the induced velocity field, therefore, must increase the vorticity of that filament. This is because in an incompressible flowfield an increase in the length of the cylindrical filament must be accompanied with a corresponding decrease in the cross-sectional area of the filament — see Fig. 2.8. To find the effect of strain rate on the vorticity and velocity field, the vorticity in the filament is assumed to be concentrated inside a cylinder of length $l$, with an effective core radius $r_c$. Because the flow is considered to be incompressible, the principle of conservation can be applied to compute the effective change in core radius as a result of filament straining, $\varepsilon = \Delta l / l$

(a) "Unstrained" filament

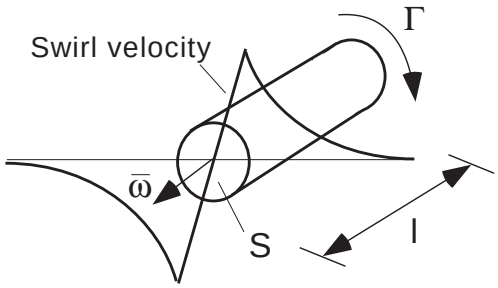


(b) "Strained" filament

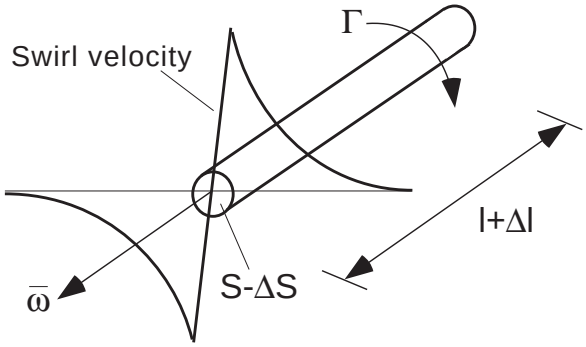


Figure 2.8: Schematic showing stretching of individual vortex filaments and vorticity intensification that results in an increase in swirl velocity surrounding the filament core.

over a time step $\Delta t = \Delta\zeta/\Omega$ and can be written as

$$\begin{aligned} \pi r_c^2 l &= \pi(r_c - \Delta r_c)^2 (l + \Delta l) \\ \left(\frac{r_c - \Delta r_c}{r_c}\right)^2 &= \frac{l}{l + \Delta l} \\ \Delta r_c &= r_c \left(1 - \frac{1}{\sqrt{1+\varepsilon}}\right) \end{aligned} \tag{2.81}$$

Combining Eqs. (2.78) and (2.81), the expression for the effective core at a given time $t = \zeta/\Omega$ can be written as

$$r_c(\zeta, \varepsilon) = \sqrt{r_{c_0}^2 + \frac{4\alpha\delta(Re_v)\nu}{\Omega} \int_0^\zeta (1+\varepsilon)^{-1} \, d\zeta} \tag{2.82}$$

The core radius calculated at any time includes the cumulative (or integral) effects of the strain field from the point of the origin of the vortex as it was convected through the flow field.

Note that a solution for the vortex core radius cannot be calculated independently of the wake geometry and the induced velocity field solution. The core radius obtained in Eq. (2.82) was used for the computation of the induced velocities from the vortex line segments in Eq. (2.76).

## 2.6 Rotor Trim Methodology

The strengths and the positions of the tip vortices are largely determined by the rotor operating conditions. Furthermore, the transient wake dynamics during a maneuver are highly sensitive to the initial conditions and the sequence of control pitch inputs used by the pilot to perform the maneuver. Therefore, it is very important to establish the initial wake geometry and filament strengths accurately before proceeding to simulate a maneuvering rotor problem. The maneuvers are generally initiated from a

steady state flight condition. The rotor controls must be trimmed appropriately to attain the necessary thrust and TPP orientation to fly the desired steady flight condition.

In the present work, a "wind-tunnel" trim methodology is implemented to trim the rotor to a specified thrust condition. This trim methodology assumes an isolated rotor, and ignores the effect of a tail rotor or the lateral aerodynamic forces acting on the rotor and the fuselage. The collective and cyclic pitch angles are adjusted such that the rotor operates at a specified thrust, and that the TPP is perpendicular to the rotor axis of rotation, effectively eliminating cyclic flapping. The approach for trimming both single and dual rotor configurations are discussed here. The procedure adopted is similar to the methodology described in Refs. 59, 82.

The rotor control input vector $\mathbf{x} = \{\theta_0 \; \theta_{1c} \; \theta_{1s}\}^T$ is updated during the trim procedure by solving a linearized system of coupled equations which relate the control inputs to the output vector which is denoted by

$$\mathbf{y} = \left\{ \begin{array}{ccc} C_T & \beta_{1s} & \beta_{1c} \end{array} \right\}^T \tag{2.83}$$

The change in the response vector for a perturbation in the input vector $\mathbf{x}$ can be written as a Taylor series expansion given by

$$\mathbf{y}(\mathbf{x}+\Delta\mathbf{x}) = \mathbf{y} + \frac{\partial \mathbf{y}}{\partial \mathbf{x}}\Delta\mathbf{x} + \ldots \tag{2.84}$$

The Jacobian matrix, $[J]$ of the dependent quantities with respect to the independent quantities can be written as

$$[J] = \frac{\partial \mathbf{y}}{\partial \mathbf{x}} = \left[ \begin{array}{ccc} \frac{\partial C_T}{\partial \theta_0} & \frac{\partial C_T}{\partial \theta_{1c}} & \frac{\partial C_T}{\partial \theta_{1s}} \\ \frac{\partial \beta_{1s}}{\partial \theta_0} & \frac{\partial \beta_{1s}}{\partial \theta_{1c}} & \frac{\partial \beta_{1s}}{\partial \theta_{1s}} \\ \frac{\partial \beta_{1c}}{\partial \theta_0} & \frac{\partial \beta_{1c}}{\partial \theta_{1c}} & \frac{\partial \beta_{1c}}{\partial \theta_{1s}} \end{array} \right] \tag{2.85}$$

Ignoring the higher-order terms in Eq. (2.84), the expression for the perturbation in

the control input vector $\Delta\mathbf{x}$ can be written as

$$\Delta\mathbf{x} = [J]^{-1}\left(\mathbf{y}(\mathbf{x}+\Delta\mathbf{x}) - \mathbf{y}\right) = [J]^{-1}\left\{\begin{array}{c} C_T - C_{T_{\text{req}}} \\ \beta_{1s} \\ \beta_{1c} \end{array}\right\} \longrightarrow 0 \tag{2.86}$$

With an initial guess for the control variables (usually values from the previous rotor revolution), Eq. (2.86) is solved iteratively until the correction vector is below the desired threshold level.

The above approach can be generalized to a system of an arbitrary number of rotors, all generating the same thrust such that the sum of the thrust vectors equals the weight of the helicopter. However, this approach is valid only for isolated rotor systems where there is minimal interference between the rotors.

This is definitely not the case with coaxial rotors, and even tandem rotors, where the rotors might overlap over a certain region of the disk or in forward flight where the wake of the front rotor might interact with the rear rotor. Under such conditions, two conditions must be satisfied for straight-and-level flight: 1. The net thrust generated by the multi-rotor system must counterbalance the components of weight and drag forces, and 2. A torque balance, i.e., the net torque acting on the helicopter must be zero. The formulation of the trim problem gets slightly more complicated for rotor systems with an odd number of rotors where the torque balance is dependent on the relative positions of the rotors to each other. Therefore, only dual rotor configurations are considered in the present work. Note that the approach can be easily extended to quad-rotor systems. For a dual rotor system, the control input vector and the response

vector can be written as

$$\mathbf{x} = \left\{ \begin{array}{cccccc} \theta_{0_1} & \theta_{1c_1} & \theta_{1s_1} & \theta_{0_2} & \theta_{1c_2} & \theta_{1s_2} \end{array} \right\}^T \tag{2.87}$$

$$\mathbf{y} = \left\{ \begin{array}{cccccc} \sum C_T & \sum C_Q & \beta_{1s_1} & \beta_{1c_1} & \beta_{1s_2} & \beta_{1c_2} \end{array} \right\}^T \tag{2.88}$$

Following the exact procedure adopted for single rotor systems in Eqs. (2.84)– (2.86), the perturbation in the control input vector $\Delta\mathbf{x}$ can be written as

$$\Delta\mathbf{x} = [J]^{-1} \left\{ \begin{array}{c} \sum C_T - C_{T_{\text{req}}} \\ \sum C_Q \\ \beta_{1s_1} \\ \beta_{1c_1} \\ \beta_{1s_2} \\ \beta_{1c_2} \end{array} \right\} \longrightarrow 0 \tag{2.89}$$

where the Jacobian matrix is given by

$$[J] = \left[ \begin{array}{cccc} \frac{\partial \sum C_T}{\partial \theta_{0_1}} & \cdots & \frac{\partial \sum C_T}{\partial \theta_{0_2}} & \cdots \\ \vdots & \ddots & \vdots & \ddots \\ \frac{\partial \sum C_Q}{\partial \theta_{0_1}} & \cdots & \frac{\partial \sum C_Q}{\partial \theta_{0_2}} & \cdots \\ \vdots & \ddots & \vdots & \ddots \end{array} \right] \tag{2.90}$$

## 2.7 Wave-Tracing for Acoustic Directivity Predictions

The main rotor is the primary noise source in helicopters. The adverse noise is generated, to a large extent, because of the unsteady, impulsive airloads generated by the interaction of the rotor blades with its own self-generated vortical wake. The computational mapping of the acoustic field requires a high degree of spatial and temporal resolution, so the computational efficiency is still at a premium. Various tools ranging

from analytical wake tracing concepts (Refs. 12, 115) to coupled blade-element unsteady aerodynamic models with Ffowcs–Williams Hawkins methods (Ref. 116) exist to predict the rotor noise directivity patterns (Ref. 13).

Determination of principal acoustic directivity patterns using wave tracing is an ideal option because the free-vortex wake solution provides details of the wake geometry and the blade positions at every timestep. Once the wake geometry is obtained, the positions of the blade-vortex interactions can be computed using simple analytical geometry concepts. These intersection points provide all potential locations for the BVI noise sources. The directivity of the noise propagation can then be solved using wave tracing and noise radiation principles.

Coalescence of wave fronts occur when the BVI source points have supersonic trace Mach numbers. It is, therefore, usually adequate to trace waves generated by sources that have supersonic trace Mach numbers because these contribute most to the net sound field. The trace Mach number is the effective velocity of the sound source in a fixed-frame of reference normalized by the speed of sound – see Fig. 2.9. The trace Mach number in a hub-fixed coordinate system can be defined by

$$M_{\mathrm{tr}} = \frac{|\mathbf{V} + \mathbf{V}_{\mathrm{v}}|}{a \sin\gamma} \tag{2.91}$$

where $\mathbf{V}_{\mathrm{v}}$ is the velocity of the vortex filament in the hub fixed frame of reference. Reference 12 defines trace Mach number as the relative velocity of the vortex filament along the blade and, therefore, Eq. (2.91) has $\tan\gamma$ in the denominator instead of $\sin\gamma$. This definition is only valid for very low Mach numbers or $\gamma \ll 1$ such that $\tan\gamma \approx \sin\gamma \approx \gamma$. For higher Mach numbers the approach adopted in Ref. 12 misses potential supersonic BVIs with moderate interaction angles. This is shown schematically in Fig. 2.10. The effect of using $\tan\gamma$ formulation is to reduce the magnitude of $M_{\mathrm{tr}}$ by a factor $\cos\gamma$. Notice that the trace Mach number can never be supersonic even for very

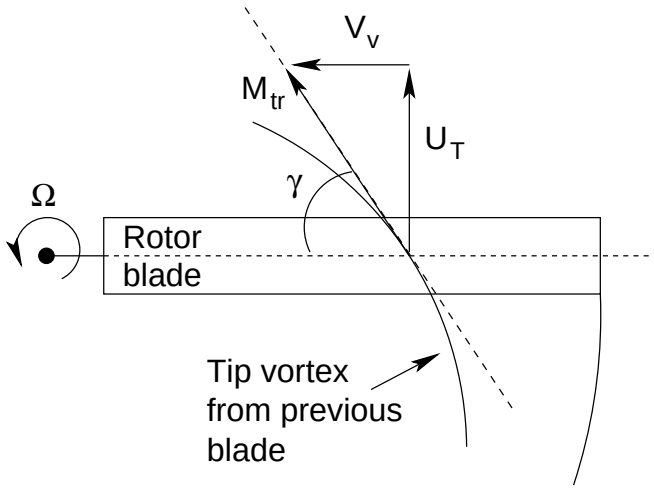


Figure 2.9: Schematic explaining the concept of trace Mach number for a BVI.

large blade Mach numbers for moderate interaction angles with the $\tan\gamma$ formulation. While such situations are rare in normal, steady flight conditions, this can become an issue during maneuvering flight where the magnitude of the instantaneous, transient velocities at the blade points can get very close to sonic speeds.

Figure 2.11 shows the schematic explaining how the sound wavelets from sources with supersonic trace Mach numbers accumulate along the cone with a semi-vertical angle $\mu$, called the Mach angle given by

$$\mu = \arcsin\left(\frac{1}{M_{\text{tr}}}\right) \tag{2.92}$$

$$\tag{2.93}$$

and propagate along a cone with a semi-vertical angle $\beta$ to the instantaneous trace velocity vector that is given by

$$\beta = \arccos\left(\frac{1}{M_{\text{tr}}}\right) \tag{2.94}$$

The noise signature at any observer plane can be obtained by tracing the locus of intersection of the acoustic cones with the observer plane. The locus is a series of hy-

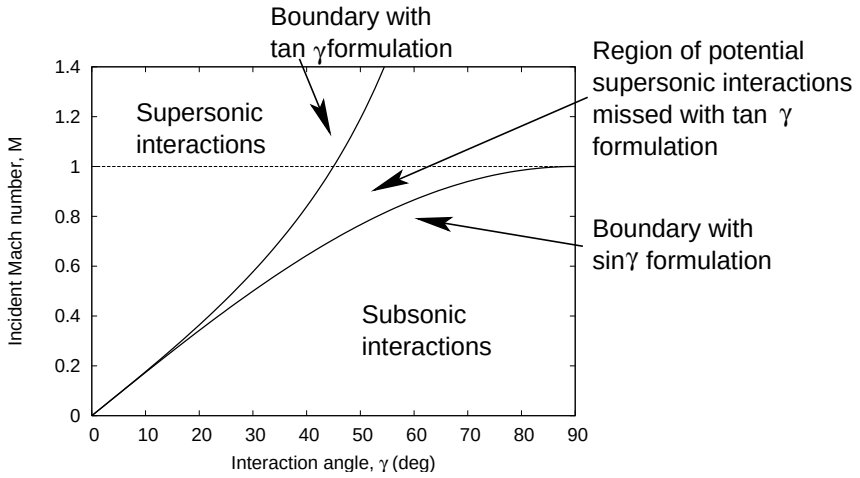


Figure 2.10: Plot showing the region of potential supersonic BVI locations missed by the tan$\gamma$ formulation in Eq. 2.91.

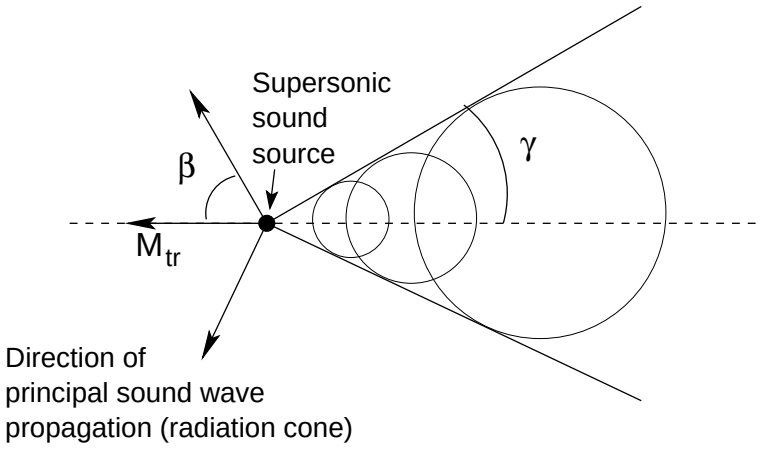


Figure 2.11: Schematic showing the coalescence of sound waves from a supersonic sound source and the direction of principal sound wave propagation.

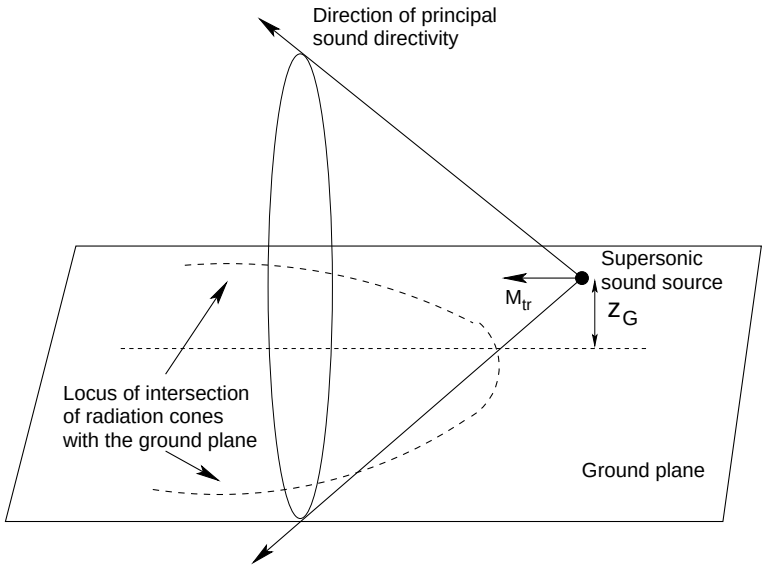


Figure 2.12: Schematic showing the locus of intersection of the radiation cones with an observer plane.

perbolas, as shown in Fig. 2.12. The acoustic lines might overlap over certain regions of the observer plane. These indicate the potential regions where strong focusing of noise can occur. The sound focusing occurs only if the wavelets from the sound sources actually coalesce at these points.

Direct wave tracing concepts (Ref. 12) can be used to determine the position of sound wavelets originating from the BVI sources. This approach is used in the present work. The computation of wavelet positions in the observer plane should be performed in a fixed reference plane moving with the rotor. In this coordinate system, the locus of the points on the wavelet for an outward moving source over a period $\Delta t$ can be written as

$$\begin{aligned} x &= x_b + (a\cos(\psi_b + \beta) + u)\,\Delta t \\ y &= y_b + (a\sin(\psi_b + \beta) + v)\,\Delta t \\ z &= z_b + (a + w)\,\Delta t \end{aligned} \tag{2.95}$$

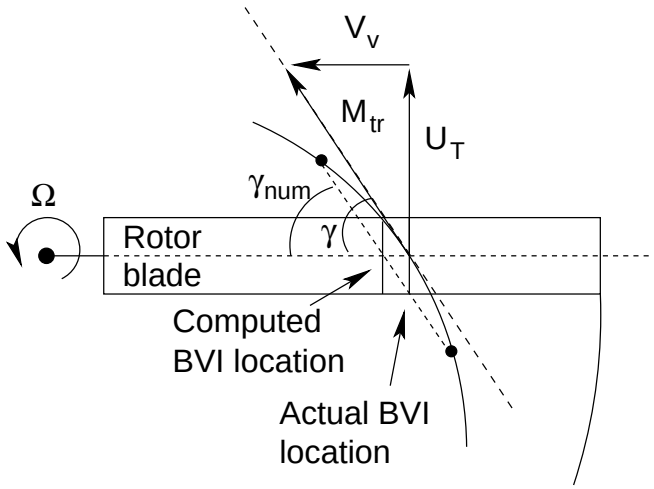


Figure 2.13: Schematic showing the errors introduced in the prediction of the BVI locations and trace Mach number from numerical discretizations.

By numerically "tracing" the positions of the wavelets at different instances in time, the pattern of wave fronts that intersect a defined reference plane can be determined.

## 2.8 Summary

This chapter focused on the development of a time-accurate, coupled rotor blade and wake computational model that can be used to predict the transient wake aerodynamics and the resulting unsteady airloads during maneuvering flight. The solution of the unsteady wake aerodynamic problem requires four different components, namely, the blade aerodynamic model, the blade flapping model, the free-vortex wake model and the viscous core growth model to capture the essential flow features critical to the proper estimation of transient blade airloads and rotor noise during flight maneuvers.

The rotor blade aerodynamic model uses a Weissinger-L model, which is a reduced-order lifting surface model with one chordwise panel and multiple spanwise segments, to estimate the blade circulation strengths to satisfy the flow tangency condition at the

blade control points. The boundary condition at the trailing edge is satisfied by using the Kutta condition, and the blade circulation strengths are related to the blade lift coefficients using the Kutta-Jukowski condition. The model is essentially invisicd and incompressible. Compressibility and other nonlinear effects are accounted for by using the Beddoes nonlinear airfoil model. The unsteady airloads are estimated using the Leishman–Beddoes indicial response functions, which accounts for the additional lift and drag produced because of the changes in angle of attack and the blade pitch rate. The contribution to the circulatory and non-circulatory forces are accounted for separately and the effects are combined to obtain the net lift and drag coefficients on the blade sections.

The equations for the rigid blade flapping model were developed to account for the inertial effects of the pitch and roll motion on the blade flapping response. The equations were written in a modified form as a system of first-order differential equations, which are then solved using the same numerical algorithms used for the wake calculations. The equations are solved at each time step consistently with the wake equations to obtain the coupled response.

The free-vortex wake methodology for the solution of the transient rotor wake dynamics was developed. The wake problem was solved using a splitting scheme where the three phenomena: 1. The convection, 2. Diffusion, and 3. The filament strain effects. These were modeled as sequential sub-processes, and their effects were coupled before marching to the next time step. A second-order, time-accurate, two-step backward, predictor-corrector algorithm was used to numerically solve the invisid, incompressible form of the governing equations for the convection of the wake markers. The viscous diffusion and the filament strain effects were accounted for by using a viscous core growth model that was corrected for filament strain effects. The modified

position vectors and the vorticity field were then marched to the next time step.

The rotor trim methodology for single and dual rotor systems were then presented. The change in the rotor thrust and the cyclic flapping to perturbations in the control pitch settings is formulated as a system of linearly dependent equations using the Taylor series approximation. The resulting equations are solved iteratively until a converged solution for the control pitch inputs is obtained for a desired net system thrust operating condition.

Finally, a brief overview of the wave-tracing algorithm to estimate the principal noise directivity patterns was presented. The wave-tracing algorithm provides information of the acoustic directivity patterns from the wake geometry and blade flapping solutions using simple analytical geometry concepts.

# Chapter 3

# Results & Discussion: Comparison With Experiments

The methodology described in the previous chapter has been developed to handle arbitrary, non-steady flight conditions and general rotor geometries. The numerical model is made up of various components, several of which have been validated extensively for steady flight conditions – see Ref. 82 for further details. However, previous studies using the time-accurate, free-vortex wake model did not include several modeling features that have been added in the new model, particularly the combined strain-viscous diffusion model in the rotor wake algorithm. Furthermore, the new model provides a more accurate treatment of the unsteady aerodynamic effects, which can be very important during rotor maneuvers. The modeling of additional flow physics makes the numerical algorithm more complicated, and the effectiveness of this new methodology needs to be established properly before it can be applied confidently to the study of helicopters under maneuvering flight conditions.

This chapter focuses on implementing the methodology that was developed to numerically simulate various existing experimental studies and validate the numerical model with the available experimental data. The emphasis of the validation efforts

will be primarily on flight conditions that have hitherto proven a challenge to existing aerodynamic models. Operations in ground effect and the analysis of coaxial rotors are good examples where the interaction of the wake with the ground or the mutual interaction of the wakes from the two rotors (in the case of coaxial rotors) have caused problems for most existing methods. The enhanced mutual interactions of the wake vorticity can cause local unsteady effects, which must be captured accurately to enable proper predictions of the induced velocity field.

This chapter is divided into two parts. The first part will analyze the transient wake aerodynamics to idealized maneuvers or control pitch perturbations. The emphasis in this part will be to comprehensively validate the wake geometries, the wake inflow, the sectional blade airloads, and the blade flapping response. This is done using the experiments of Taylor (Ref. 21), Carpenter & Friedovich (Ref. 22), Ellenrieder & Brinson (Ref. 23) and Jessurun et al. (Ref. 24). These simulations study the wake response to ramp changes in collective pitch and for harmonic oscillations of collective and cyclic pitch, mostly under hovering flight conditions. While in practice a flight maneuver would require the use of a combination of collective, cyclic pitch and tail rotor inputs, these initial idealized maneuvers are valuable because they provide considerable insight into the relationship between the wake dynamic response and the control pitch perturbations. Furthermore, these idealized maneuvers are performed under controlled conditions and are, therefore, easier to simulate using a stand-alone rotor model. The second part of this chapter will analyze in detail the wake geometry for rotors operating in ground effect, both in hover and forward flight conditions, and also for coaxial rotor configurations. The performance predictions for rotors operating in ground effect will be compared with the experimental measurements by Fradenburg (Ref. 117) and Sheridan & Weisner (Ref. 118).

## 3.1 Transient Wake Response to Time-Dependent Blade Pitch Inputs

The studies of the wake aerodynamics and the resulting induced velocity field for rotors operating IGE and for coaxial rotors provide valuable insight into the behavior of the rotor wake in response to local unsteady effects. However, the conditions are nominally steady, and provide no understanding of the wake response to changes in the rotor operating conditions or control pitch inputs. Very few laboratory experimental studies for the wake response to time-varying blade pitch control inputs are available in the literature. The documented experimental studies and the important observations have been discussed in detail in Section 1.1.3.

As mentioned previously, the primary wake response to perturbations from control pitch inputs is the bundling of the tip-vortices into a toroidal ring structure below the rotor. A similar behavior is observed in the transient wake simulations for changes in the collective pitch settings in the experiments of Carpenter & Friedovich – see Fig. 3.1.

Figure 3.2 shows the wake geometry and the streamlines along a vertical plane for an impulsive change in the collective pitch of the rotor blades. The bundling of the tip vortices is clearly visible in Fig. 3.2(a). Comparing Fig. 3.2(b) with Fig. 1.2, it is evident that the qualitative nature of the flowfield around the rotor is captured by the use of time-accurate free-vortex wake methodology. The following sections will compare in greater detail the quantitative predictions of the free-vortex wake simulations with measurements obtained from the experimental studies.

Figure 3.3 shows the comparison of wake boundary predictions with the flow visualization from the experiments of Carpenter & Friedovich (Ref. 22), for a ramp

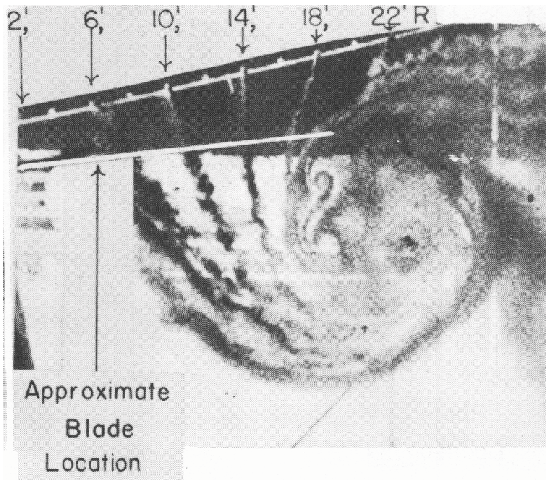


Figure 3.1: Flow visualization of the rotor wake from the experiments of Carpenter & Friedovich showing the characteristic bundling of tip vortices in response to impulsive change in the collective pitch input. (Photo from Carpenter & Friedovich (1953).)

change of collective pitch at 20°/s. The free-vortex wake methodology is capable of capturing the spatial evolution of the bundling of tip vortices. However, the images from the experiments do not provide adequate information to exactly determine the spatial location of the vortex bundle to perform a quantitative comparison of the wake geometry.

### 3.1.1 Ramp Changes in Collective Pitch

The simulations of the experiments of Carpenter & Friedovich (Ref. 22) were considered in some detail. In this experiment, the time dependent rotor response was studied subject to a rapid ramp increase in collective pitch. The three-bladed rotor had a radius of 5.8 m with solidity of 0.042. The rotor was operated at approximately 220 rpm ($\Omega = 23.04$ rad/s). The rotor collective pitch, $\theta_0$, was increased linearly from 0° to a maximum pitch angle of 12° at constant rates of 20, 48 and 200 degrees per second.

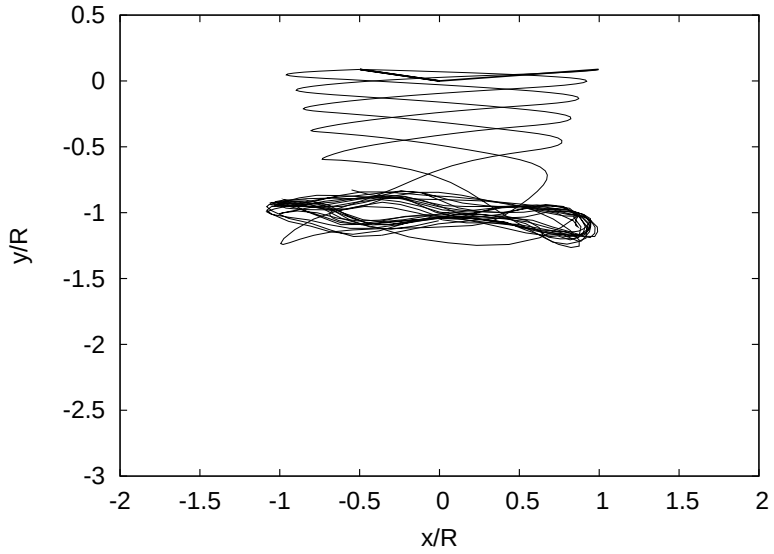


(a) Wake geometry

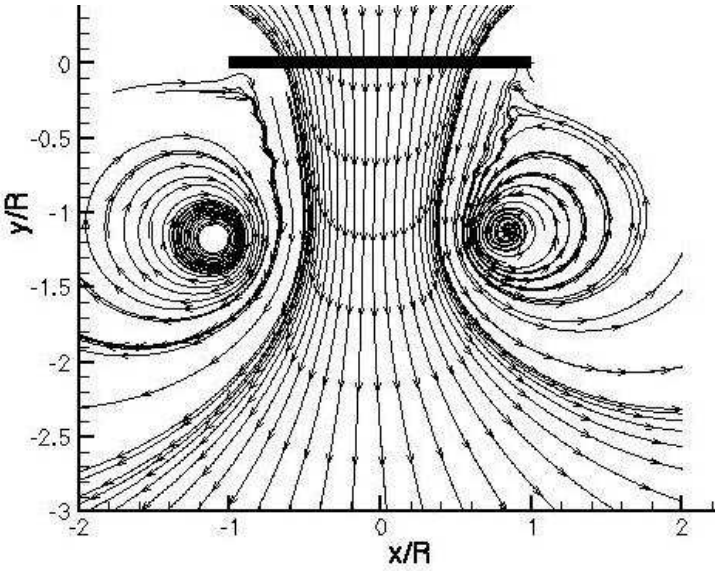


(b) Streamlines across a vertical plane

Figure 3.2: Wake geometry and time-averaged streamlines across a plane through the longitudinal centerline for an impulsive change in the collective pitch of the rotor. (a) Wake geometry, (b) Streamlines across a plane passing through longitudinal centerline.

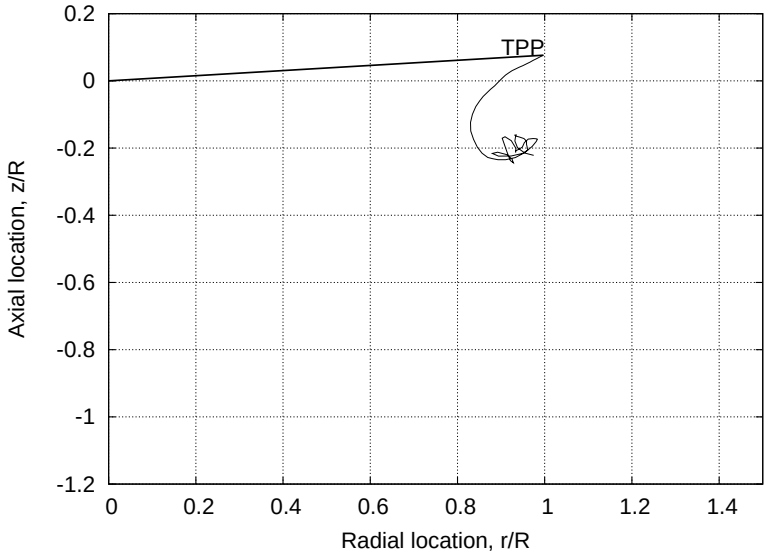


(a) Free-vortex wake

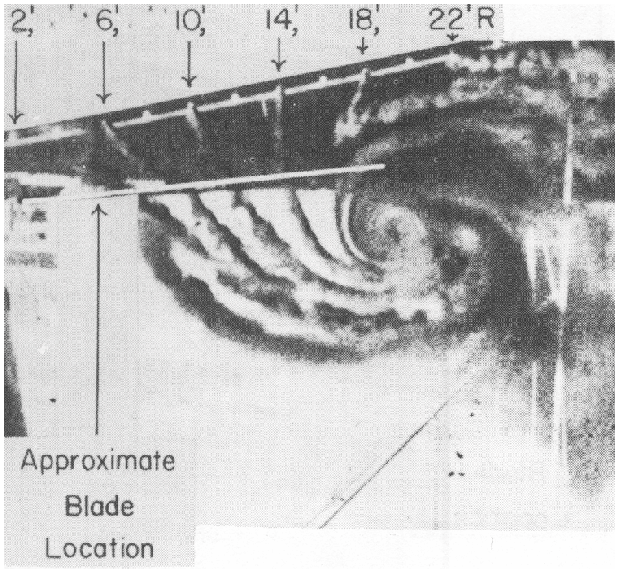


(b) Flow visualization from experiments

Figure 3.3: Comparison of the wake boundary with the flow visualization images for a ramp change of collective pitch at 20°/s three rotor revolutions after initiation of the maneuver. (a) Free-vortex wake predictions, (b) Flow visualization. (Photo from Carpenter & Friedovich (1953).)

In the experiments the blade flap angles, the rotor thrust, and the mean rotor inflow were measured as functions of time. Flow visualization was also performed in this experiment, complementing a valuable set of measurements for a relatively simple set of time-dependent blade pitch inputs.

**Rotor Wake Dynamics**

The computed evolution of the vortical wake structure is shown as a sequence of snapshots in Figs. 3.4 through 3.6 for three collective ramp rates of 200, 48 and 20 degrees per second, respectively. The geometry of the tip vortices trailing from the three blades is shown at selected times after the collective pitch input was applied. It is apparent that in each case the trailed vortices initially pair off and bundle up below the rotor to form a vortex ring. This is also shown by the flow-visualization images of Carpenter & Friedovich (Ref. 22). Immediately after the collective pitch input was applied, the vortices trailed from the blade tips can only convect relatively slowly away from the rotor because of the initially low thrust and low induced inflow. In fact by comparing the helicoidal pitch of the computed wake at early times versus later times in each case it is apparent that the net inflow through the rotor builds up only relatively slowly over several rotor revolutions. Initially, therefore, the tip vortices lie in close proximity to each other, and their respective induced velocities create a tendency for them to pair about each other. This pairing tendency is the main reason for the formation of a bundled vorticity immediately below the rotor plane. As previously alluded to, this vortex ring is analogous to the starting vortex system for a wing undergoing a sudden change in angle of attack (Ref. 25).

After the wake begins to develop and the inflow through the rotor increases, the newer trailed vortices begin to convect in a relatively higher wake induced velocity

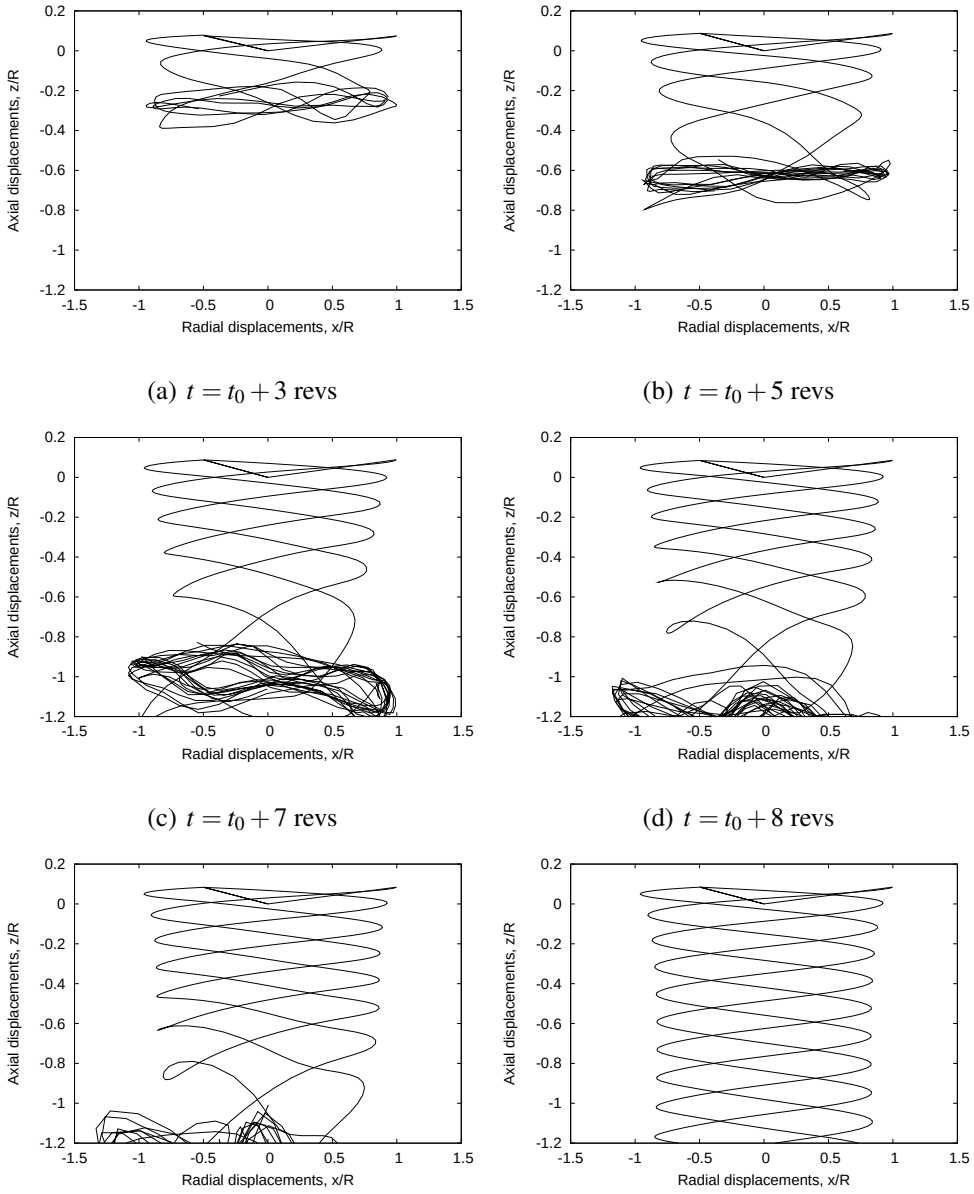


(a) $t = t_0 + 3$ revs

(b) $t = t_0 + 5$ revs

(c) $t = t_0 + 7$ revs

(d) $t = t_0 + 8$ revs

(e) $t = t_0 + 9$ revs

(f) $t = t_0 + 14$ revs

Figure 3.4: Snapshots of the wake geometries at different instances in time showing the bundling of the tip vortices for a ramp change in collective pitch at 200°/s.

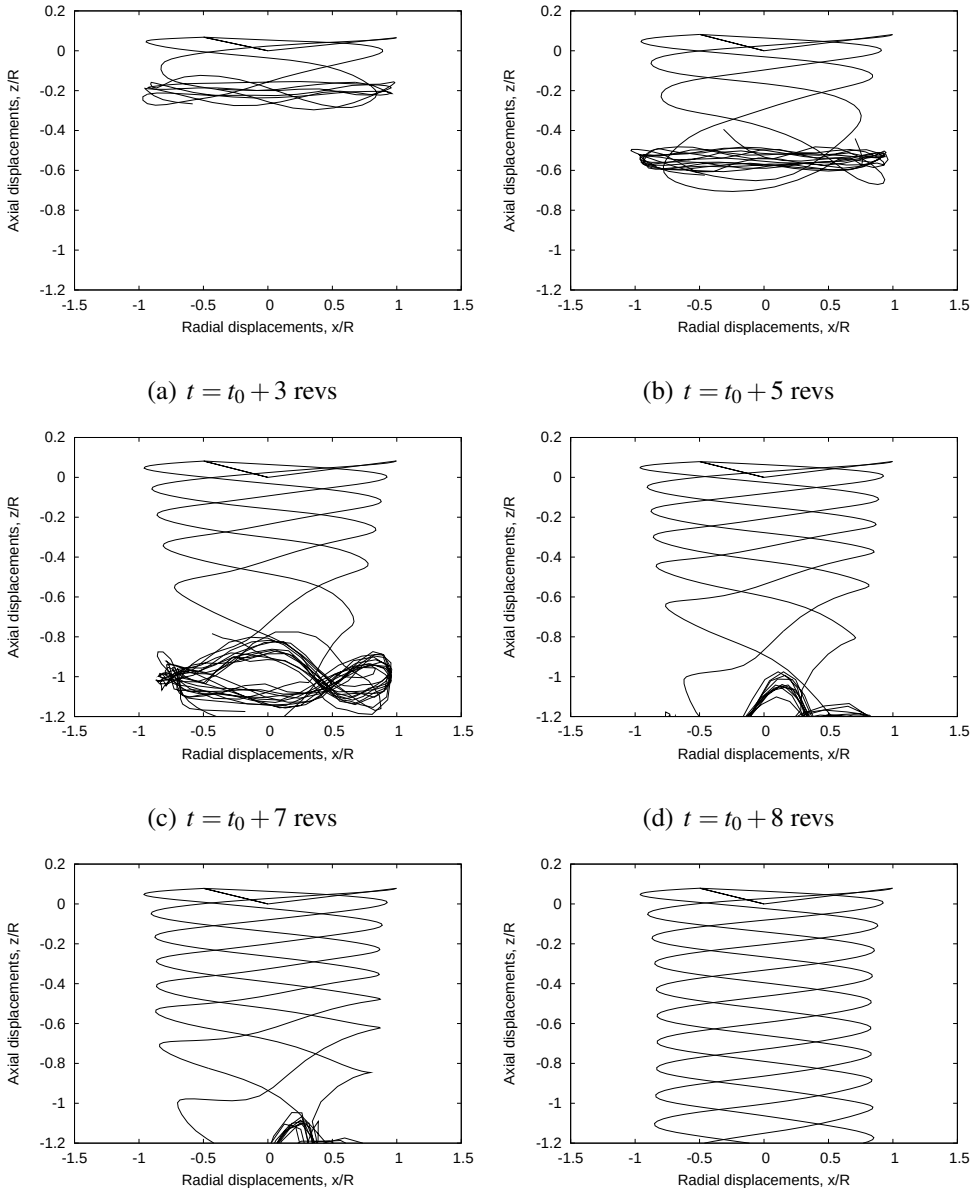


(a) $t = t_0 + 3$ revs

(b) $t = t_0 + 5$ revs

(c) $t = t_0 + 7$ revs

(d) $t = t_0 + 8$ revs

(e) $t = t_0 + 9$ revs

(f) $t = t_0 + 14$ revs

Figure 3.5: Snapshots of the wake geometries at different instances in time showing the bundling of the tip vortices for a ramp change in collective pitch at 48°/s.

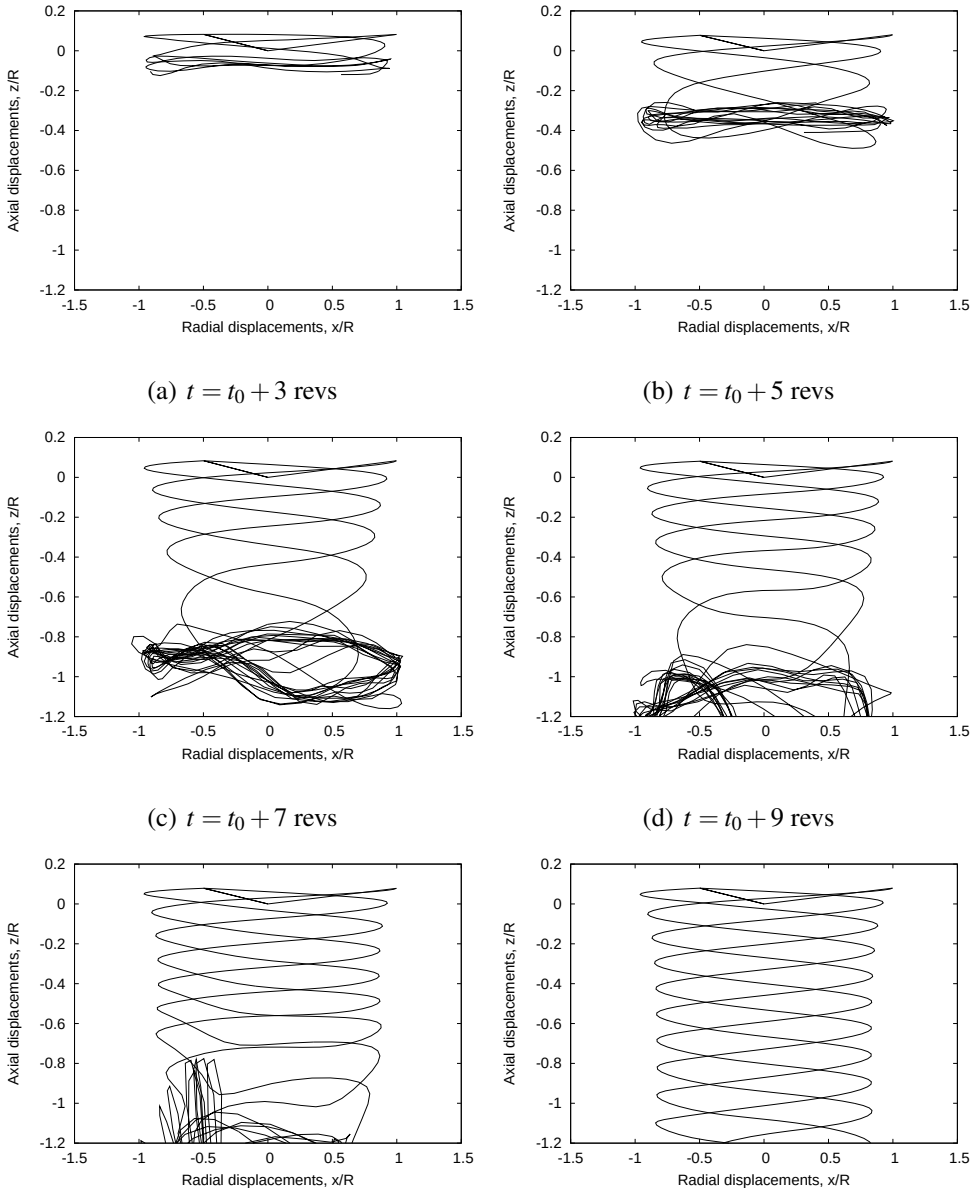


(a) $t = t_0 + 3$ revs

(b) $t = t_0 + 5$ revs

(c) $t = t_0 + 7$ revs

(d) $t = t_0 + 9$ revs

(e) $t = t_0 + 11$ revs

(f) $t = t_0 + 15$ revs

Figure 3.6: Snapshots of the wake geometries at different instances in time showing the bundling of the tip vortices for a ramp change in collective pitch at 20°/s.

field, and the starting ring is convected further down in the wake below the rotor. Notice that in each case the ring vortex structure is unstable and begins to show the presence of pronounced sinusoidal deformation modes or Kelvin waves (Ref. 85). These waves grow in amplitude with time and eventually cause the starting vortex system to break down as it convects into the far wake below the rotor.

As the rotor-induced inflow approaches a steady state value, the vorticity associated with the vortex ring has now been convected downstream well away from the rotor blades. After about four to six rotor revolutions (depending on the collective ramp rate), this starting wake has been convected about one and a half rotor radii below the rotor. At this point, any further instability has a small influence on the rotor aerodynamics. The wake then approaches a steady-state (periodic) condition with the tip vortices taking on a more characteristic helicoidal form.

**Rotor Thrust and Blade Flapping Response**

Figures 3.7 through 3.9 show the predicted results of the rotor thrust and blade flapping response time-histories for the three collective pitch ramp rates of 20°/s, 48°/s and 200°/s, respectively, along with measurements from the experiments. In each case, the predicted time-history of the rotor thrust response and build up in the blade flapping show good agreement with the measured values. Notice that there is a lag in the development of the rotor thrust, which builds up and reaches its final value in about two to four rotor revolutions, depending on the collective pitch input rate. The intermediate values of thrust show significant overshoots before settling down to their final values. For the highest ramp rate of 200°/s, the thrust overshoot is about twice the steady-state value, confirming the significant effects of transient blade pitch inputs on overall rotor wake evolution, blade airloads, and rotor flapping response.

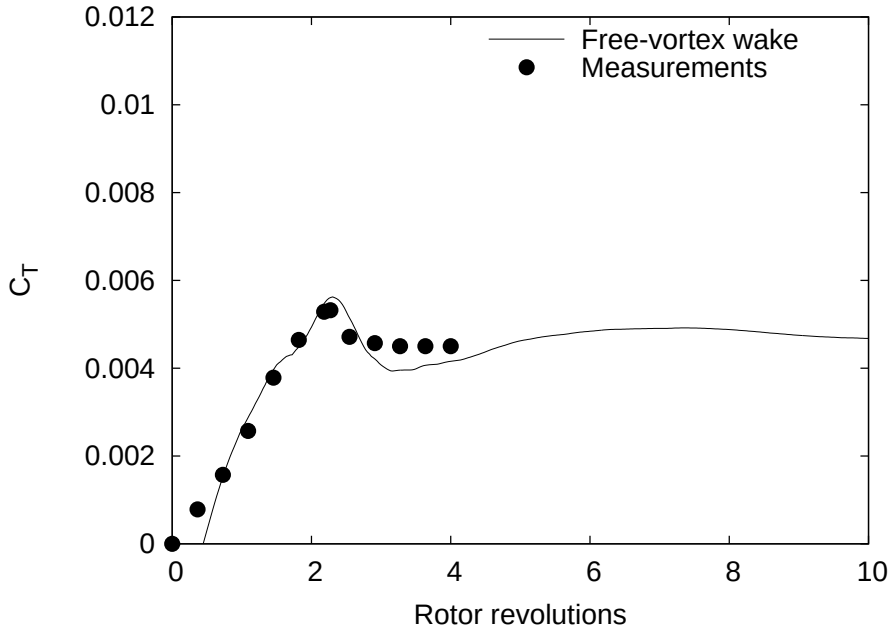


(a) Thrust response

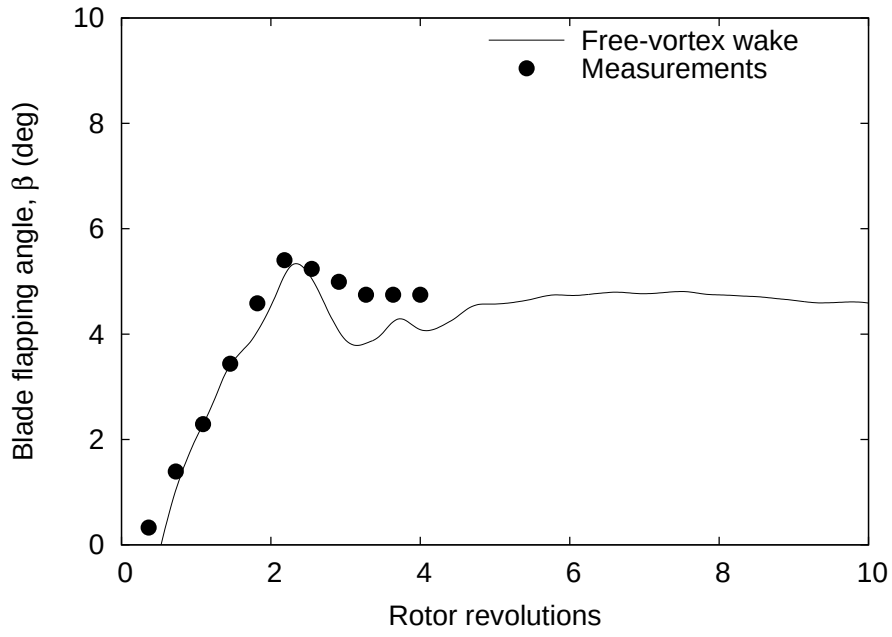


(b) Blade flapping response

Figure 3.7: Time-histories of the rotor thrust and the blade flapping response for a ramp change in collective pitch from 0° to 12° at 20°/s: (a) Thrust response, (b) blade flapping response. Measurements from Carpenter & Friedovich (1950).

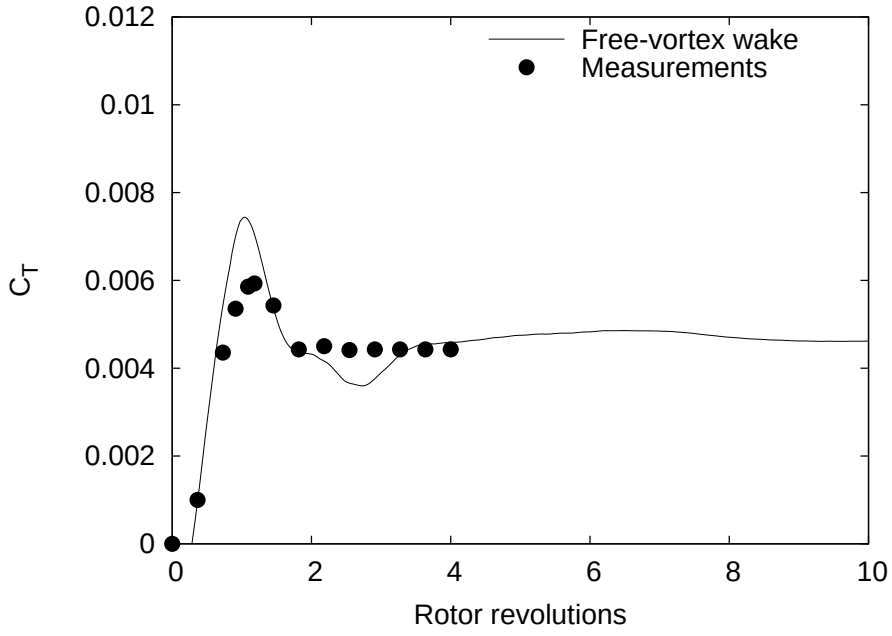


(a) Thrust response

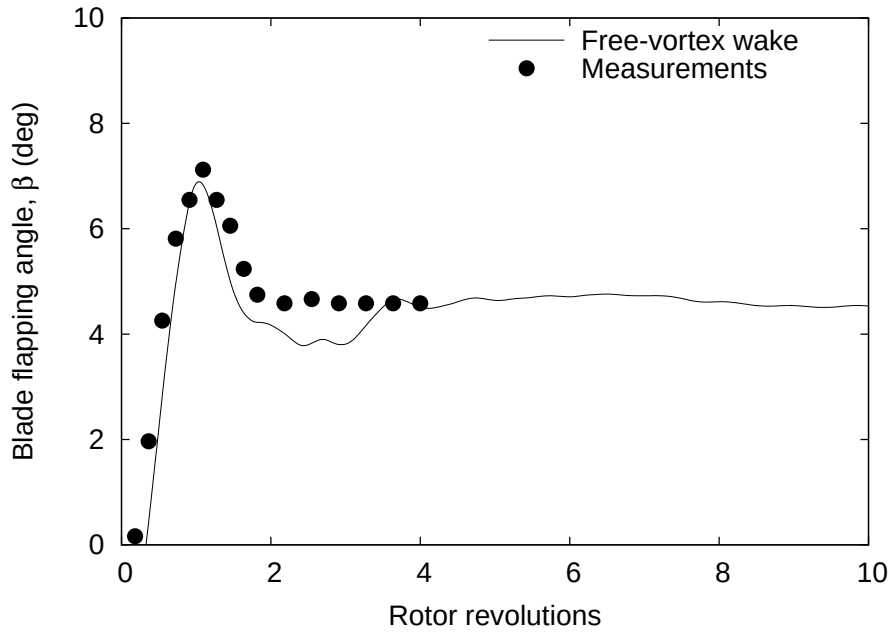


(b) Blade flapping response

Figure 3.8: Time-histories of the rotor thrust and the blade flapping response for a ramp change in collective pitch from 0° to 12° at 48°/s: (a) Thrust response, (b) blade flapping response. Measurements from Carpenter & Friedovich (1950).

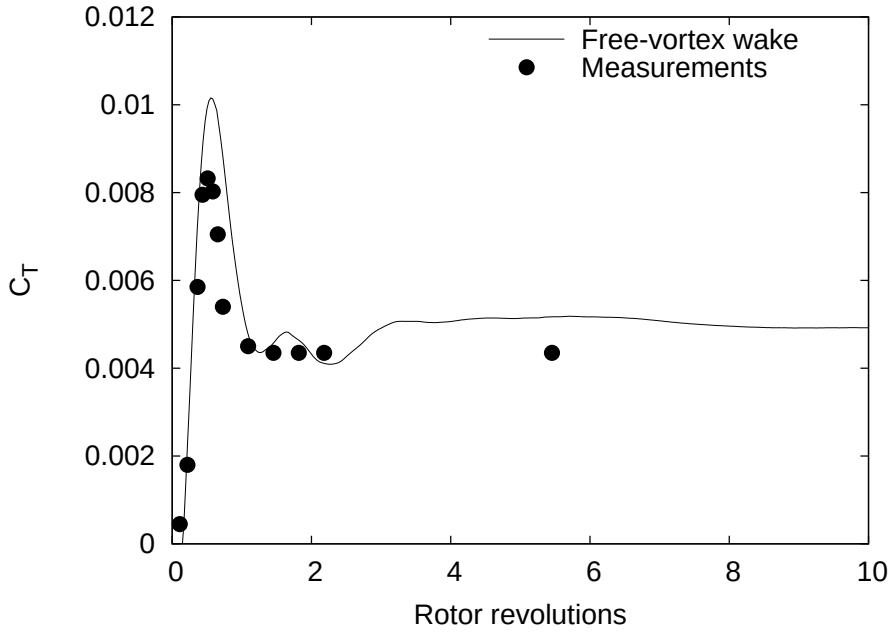


(a) Thrust response

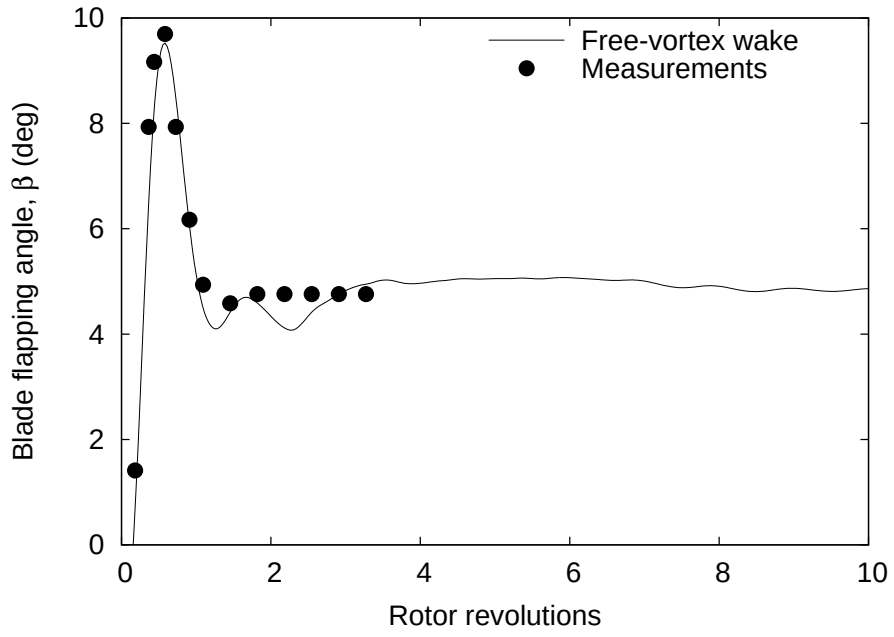


(b) Blade flapping response

Figure 3.9: Time-histories of the rotor thrust and the blade flapping response for a ramp change in collective pitch from 0° to 12° at 200°/s: (a) Thrust response, (b) blade flapping response. Measurements from Carpenter & Friedovich (1950).

The lag in the mean rotor inflow and thrust overshoots in these experiments were attributed by Carpenter & Friedovich to flow inertia effects, i.e., a noncirculatory or apparent mass effect. This was the first documented instance of the development of a so-called dynamic inflow equation. In view of the present results, however, it can be concluded that the problem is dominated by the temporal evolution of the vorticity trailed into the rotor wake, and therefore, it is predominantly a circulatory effect.

### 3.1.2 Oscillatory Pitch Inputs

The dynamic response of the rotor wake to a step or ramp change in collective pitch can be idealized by a combination of responses to a series of inputs at several different frequencies. In this section, the behavior of the inflow induced by the rotor wake to oscillatory blade pitch excitation is examined. This problem has been studied experimentally (Ref. 23) to provide validation of various dynamic inflow models (Refs. 119, 120). The rotor-wake dynamic response at low and intermediate ranges of frequencies below the rotational frequency is of particular interest from the perspective of helicopter flight dynamics and handling qualities. This is also important for rotor acoustics, the resulting wake evolution and changes in the tip vortex positions being closely correlated with rotor noise fluctuations.

Ellenrieder & Brinson (Ref. 23) have conducted a series of experiments to measure the time-dependent inflow of a hovering rotor in response to sinusoidal excitations of the collective and cyclic pitch. The experiments used a four-bladed model rotor with rectangular blades which were torsionally soft. Under normal operating conditions these blades had an elastic twist of approximately $-6^\circ$ (information provided by Ellenrieder to the author and not documented in Ref. 23). The rotor radius was 0.77 m, the blade chord was 0.06 m, and the rotor was operated at a nominal rotational speed

of 1200 rpm ($\Omega = 125.66$ rad/s). The rotor thrust coefficient $C_T$ was 0.013, although the thrust was not measured directly and only estimated. The blade pitch inputs for both collective and cyclic excitations consisted of changes of 1.5° in magnitude. The measurement of inflow velocities was made using hot-wire anemometers at 10 stations along the radius and $0.2R$ below the rotor at the 90° azimuth location. A Fourier frequency analysis was used to find the amplitude and phase of the spatial and temporal inflow response, although results for only the first harmonic have been made available.

### Collective Pitch Excitation

Collective pitch excitation was accomplished by changing the time-varying pitch of all four rotor blades exactly in phase. An example of the computed rotor wake evolution is shown in Fig. 3.10 for an excitation of 12.5 Hz (0.625/rev). It is apparent that in this case the perturbations to the blade pitch inputs manifest as waves of alternating regions of axial expansion and contraction between adjacent groups of tip vortices. The axial contraction of the wake is qualitatively similar to that observed for an impulsively started rotor, with the bundled filaments closely resembling the formation of vortex rings. However, because of the continuous oscillations in the collective blade pitch, the regions of contraction is followed by a region of expansion where the wake vortices have a larger axial separation. This sequence occurs over the whole extent of the wake as the perturbations travel through the wake system as long as the excitations in the blade pitch persist.

The induced inflow at the rotor disk also showed an oscillatory behavior as a result of these periodic waves of contraction and expansion inside the rotor wake. Figures 3.11 and 3.12 show the first harmonic measured and predicted amplitude and

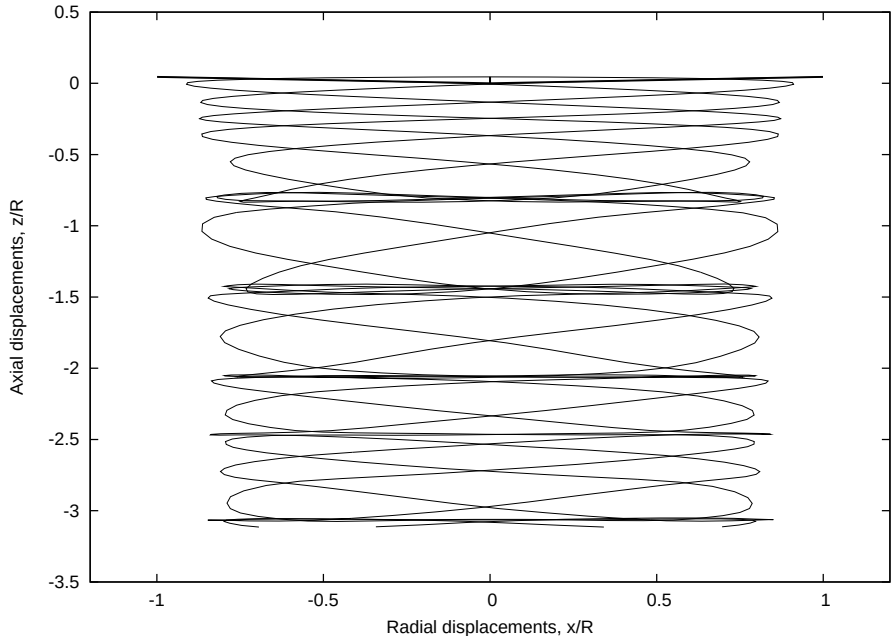


(a) $\psi = \psi_b$

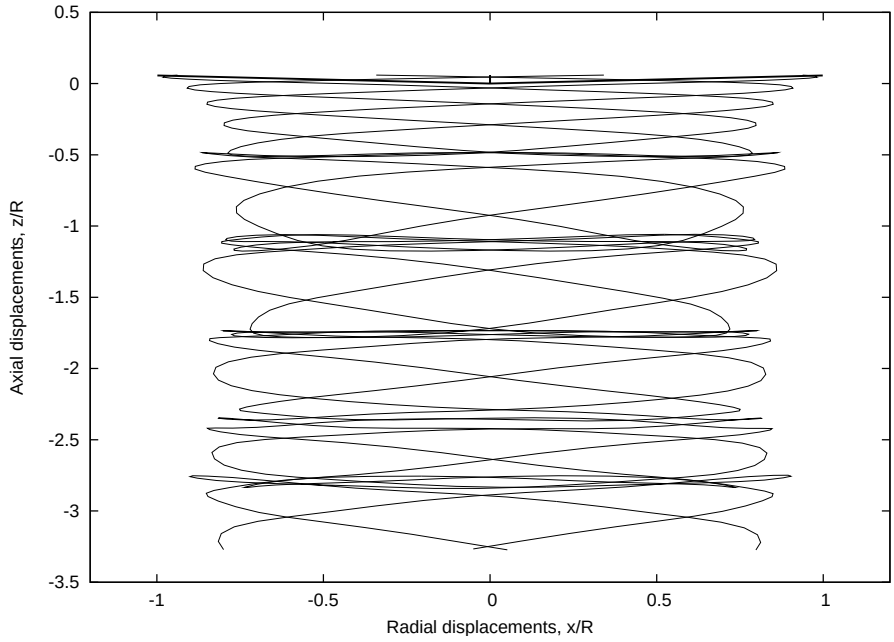


(b) $\psi = \psi_b + 380^\circ$

Figure 3.10: Side views of wake geometry showing the vortex bundling for collective pitch excitation at two different instances in time.

corresponding phase of the inflow response across the span of the blade. The inflow values are shown relative to the values obtained in the hovering state. Clearly, the results in Fig. 3.11 show that the inflow response varies significantly with both the excitation frequency and the radial blade station. For low excitation frequencies, the inflow response is nominally constant over the span. As the excitation frequency increases, however, the unsteady inflow response appears to be concentrated more in the tip region, which is also the trend observed in the experiments. This is an interesting observation because the maximum inflow response corresponds approximately to the spanwise location of the maximum in the blade lift. The results also show that at the low excitation frequencies the inflow is much more in phase with the collective pitch excitation. As the excitation frequency is increased, however, the phase lag increases quickly over the inboard portion of the blades. This trend observed in the experiments was well modeled by the present analysis.

### Cyclic Pitch Excitation

The experiments of Ellenrieder & Brinson (Ref. 23) also included results for cyclic pitch excitations, although these data were more limited in scope and phase data are unavailable. In this case, the time-varying pitch of the four blades were excited with a successive phase lag of 90°, thereby constituting a cyclic excitation. An example of the wake evolution for a cyclic excitation at 12 Hz (0.6/rev) is shown in Fig. 3.13. As noted for the case with collective inputs, the wake structure showed a wave-like behavior, with alternate regions of axial contraction and expansion between successive groups of tip vortices. However, because in this case the blade pitch was excited in a cyclic manner these wave structures propagate through the rotor wake in the form of a helicoid.

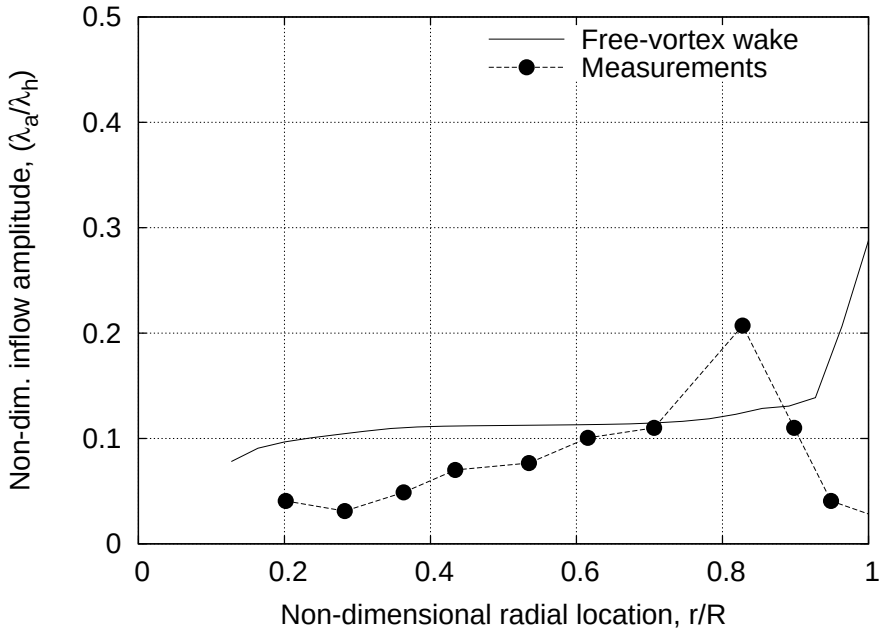


(a) 5 Hz (0.25/rev)

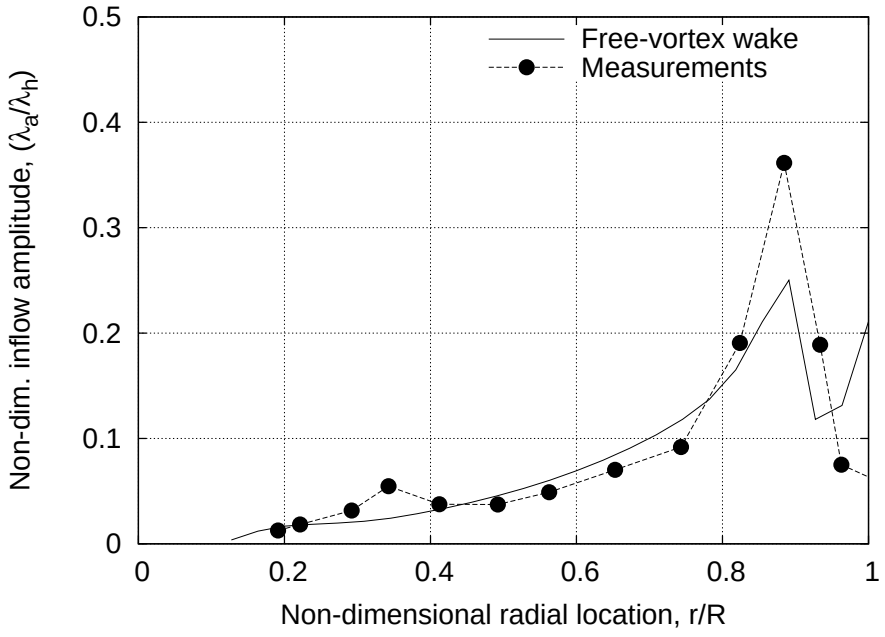


(b) 12.5 Hz (0.625/rev)

Figure 3.11: Amplitude response of the induced inflow along the blade span for collective pitch excitation at different frequencies: (a) 5 Hz (0.25/rev), (b) 12.5 Hz (0.625/rev). Experimental data from Ellenrieder & Brinson (1998).

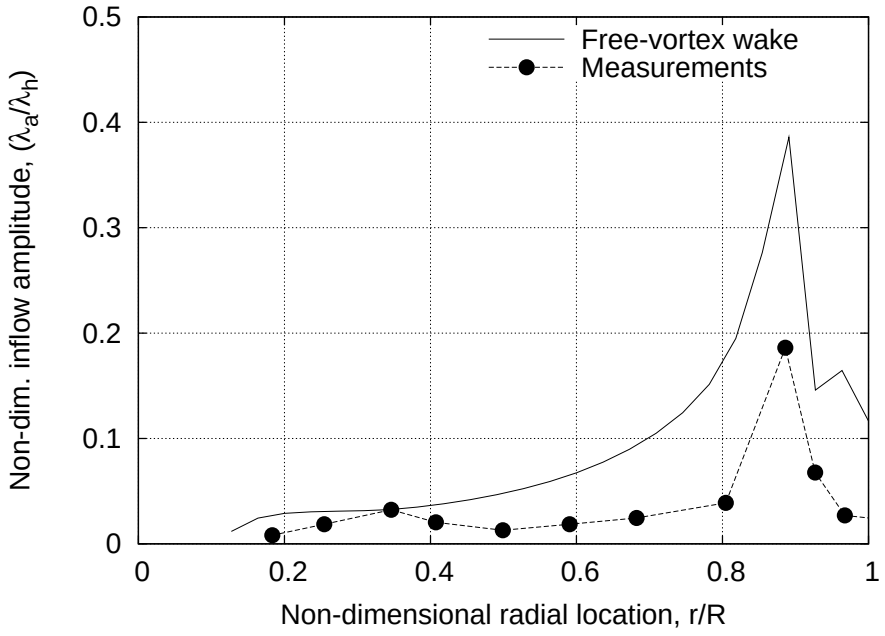


(c) 17.2 Hz (0.86/rev)

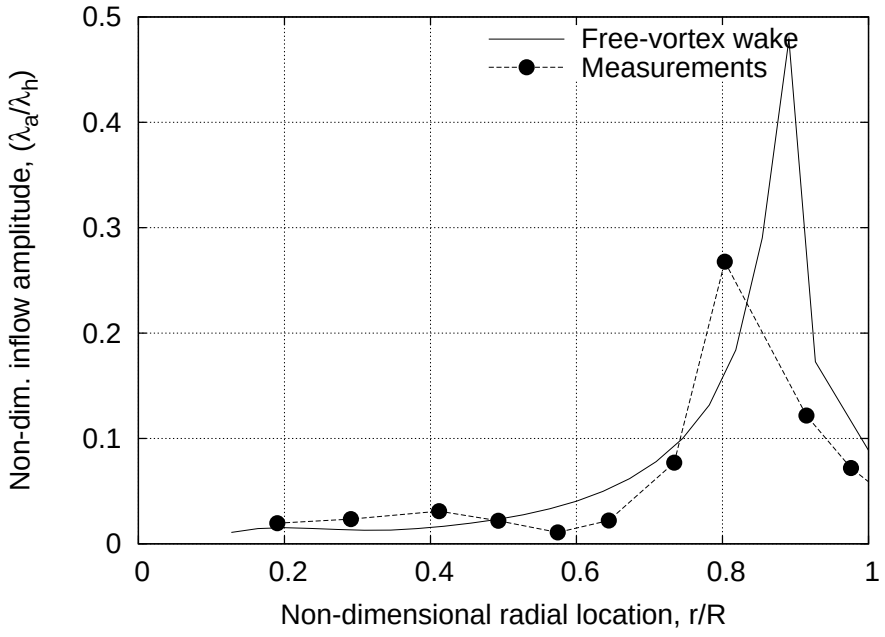


(d) 21.7 Hz (1.085/rev)

Figure 3.11: (Cont'd.) Amplitude response of the induced inflow along the blade span for collective pitch excitation at different frequencies: (c) 17.2 Hz (0.86/rev), (d) 21.7 Hz (1.086/rev). Experimental data from Ellenrieder & Brinson (1998).

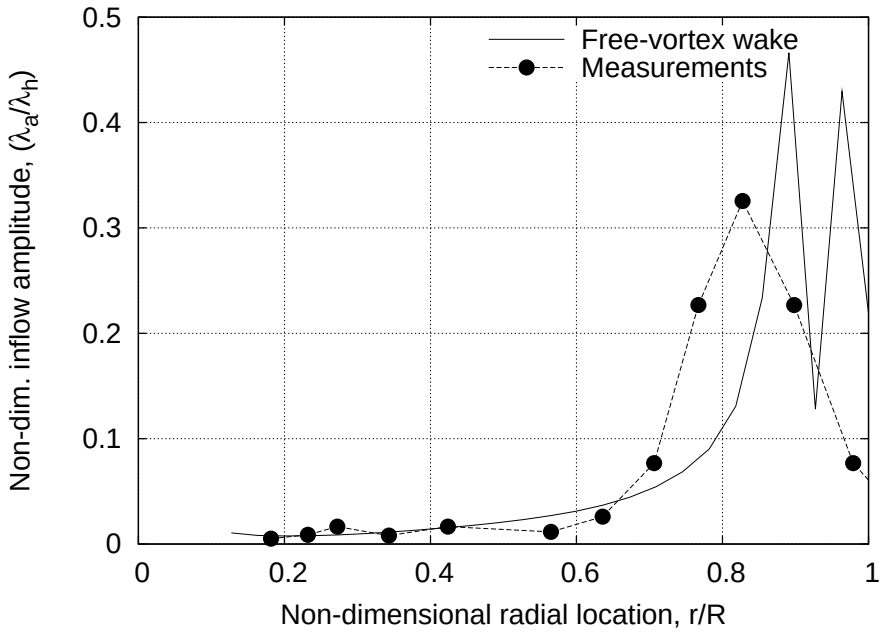


(e) 27 Hz (1.35/rev)

Figure 3.11: (Cont'd.) Amplitude response of the induced inflow along the blade span for collective pitch excitation at different frequencies: (e) 27 Hz (1.35/rev). Experimental data from Ellenrieder & Brinson (1998).

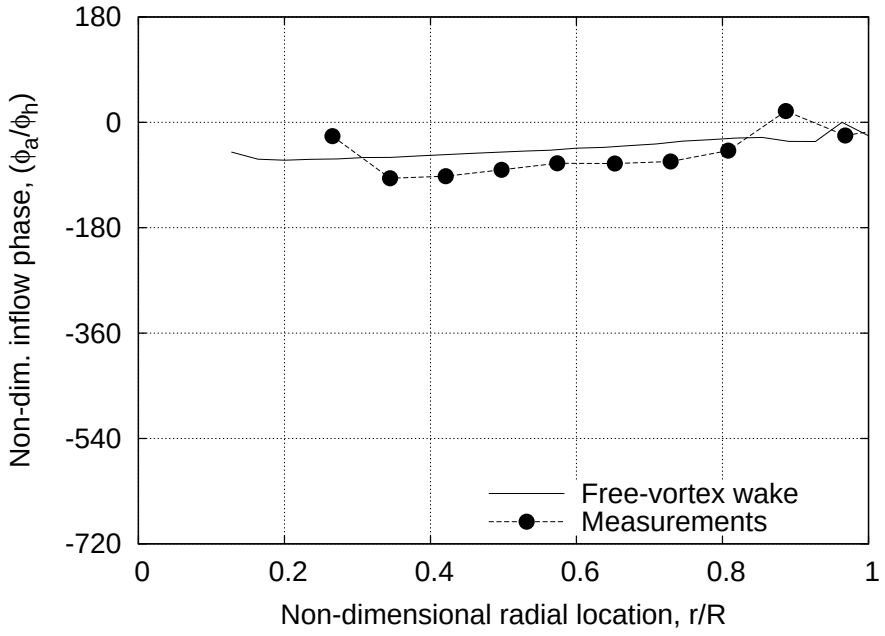


(a) 5 Hz (0.25/rev)

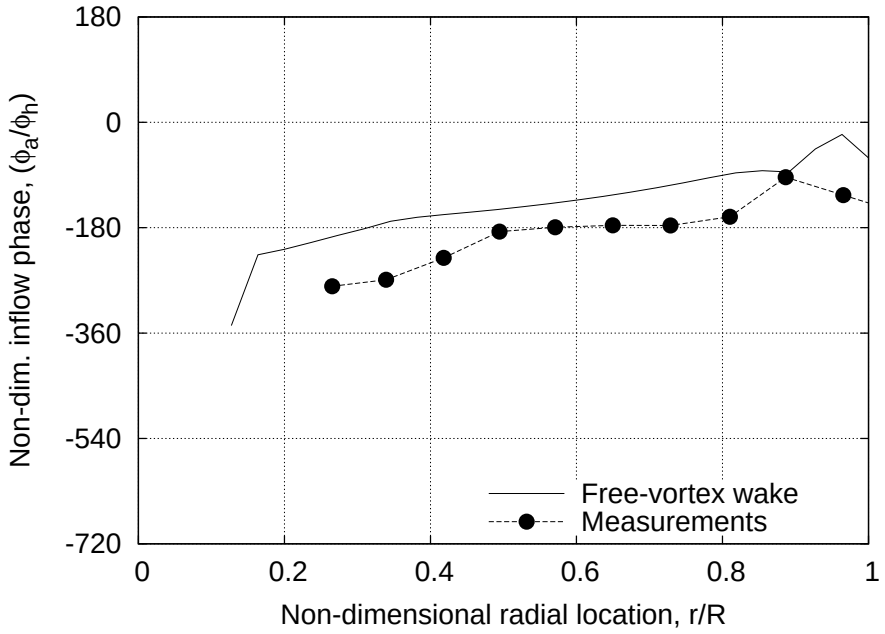


(b) 12.5 Hz (0.625/rev)

Figure 3.12: Phase response of the induced inflow along the blade span for collective pitch excitation at different frequencies: (a) 5 Hz (0.25/rev), (b) 12.5 Hz (0.625/rev). Experimental data from Ellenrieder & Brinson (1998).

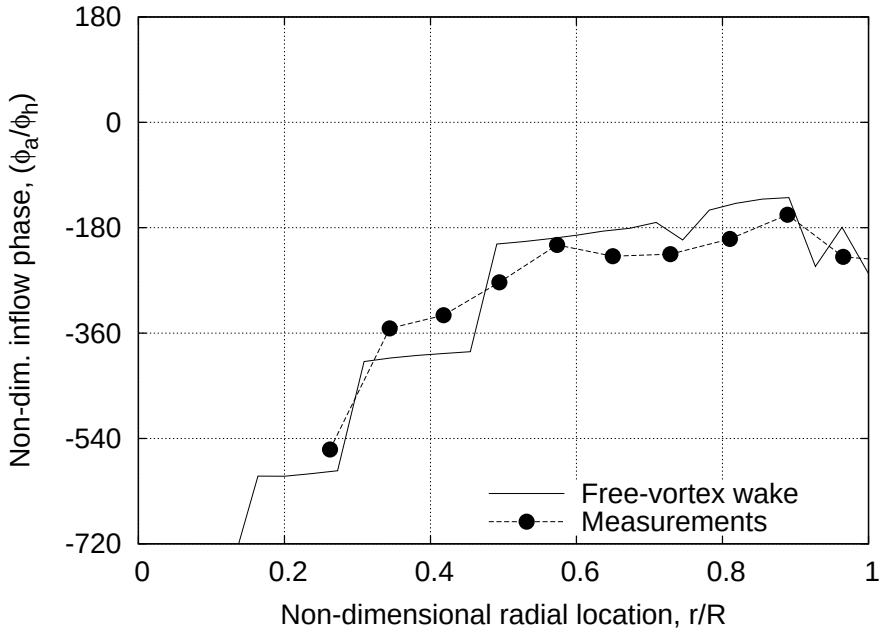


(c) 17.2 Hz (0.86/rev)

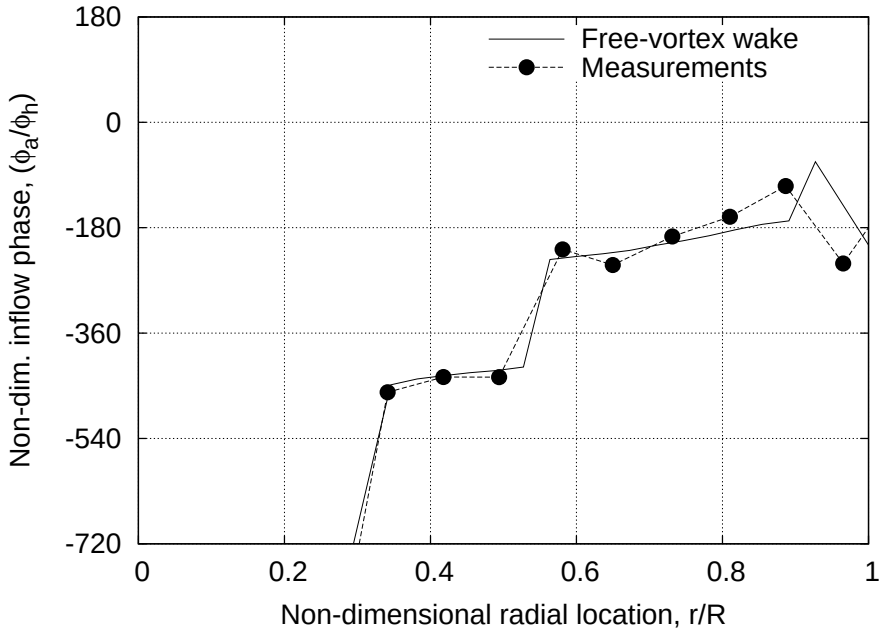


(d) 21.7 Hz (1.085/rev)

Figure 3.12: (Cont'd.) Phase response of the induced inflow along the blade span for collective pitch excitation at different frequencies: (c) 17.2 Hz (0.86/rev), (d) 21.7 Hz (1.086/rev), (e) 27 Hz (1.35/rev). Experimental data from Ellenrieder & Brinson (1998).

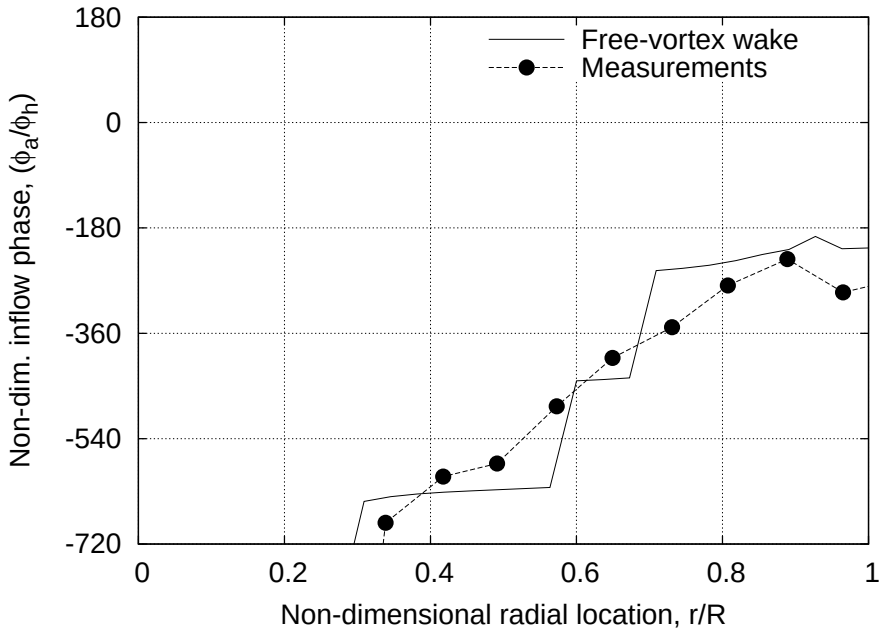


(e) 27 Hz (1.35/rev)

Figure 3.12: (Cont'd.) Phase response of the induced inflow along the blade span for collective pitch excitation at different frequencies: (e) 27 Hz (1.35/rev). Experimental data from Ellenrieder & Brinson (1998).

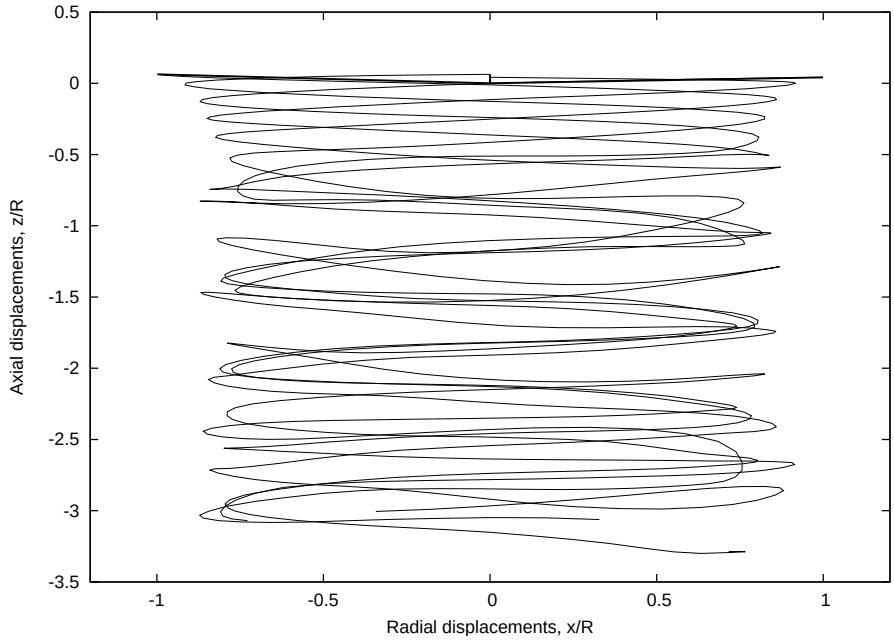


(a) $\psi = \psi_b$

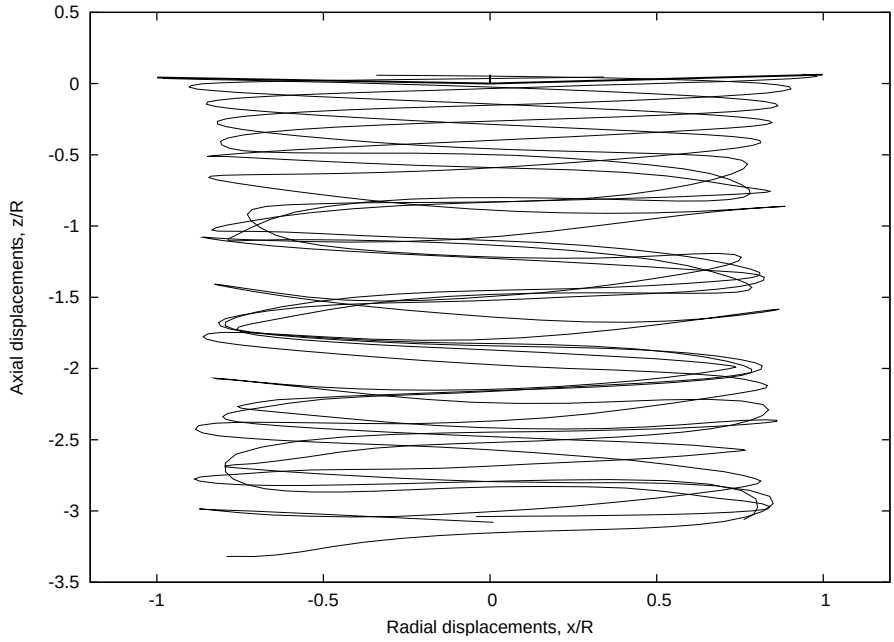


(b) $\psi = \psi_b + 380^\circ$

Figure 3.13: Side views of wake geometry showing the vortex bundling for cyclic pitch excitation at two different instances in time.

The first harmonic magnitude of the rotor-induced inflow across the span of the blade to cyclic pitch excitation is shown in Fig. 3.14 for several excitation frequencies. Overall, the predictions showed good agreement with the experimental results. As found for the collective inputs, the inflow response with increasing excitation frequency was more significant near the blade tips. The high inflow amplitude in the region of maximum blade lift was even more pronounced than the corresponding results for the inflow response to collective pitch excitation (see Fig. 3.11). However, the overall inflow response to cyclic pitch excitation was found to be significantly different from the response to the collective pitch excitation. The diminishing amplitude in the intermediate frequencies below half the rotational frequency is especially interesting because this frequency range determines the basic handling qualities and control characteristics of the helicopter. The results for the radial variation in the corresponding phase of the first harmonic in the predicted inflow response are shown in Fig. 3.15. No experimental data are available in this case. The phase response was also found to be different from the phase response to the collective pitch excitation. The phase lag was found to be greater on the inboard parts of the rotor. The results suggest that the tip vortices are the primary features influencing the temporal evolution of the overall rotor wake.

Figure 3.16 shows a comparison the time histories of the normalized rotor thrust and power for periodic excitations of collective pitch at 12.5 Hz and the cyclic pitch at 12 Hz. Notice that even though the collective pitch and the cyclic pitch were perturbed by the same amplitude and approximately the same frequencies, the cyclic pitch excitation does not have a significant effect on the integrated thrust and power values, even while affecting the wake geometries and the wake induced inflow at the rotor plane. While excitations of collective pitch seem more important, it is erroneous to conclude

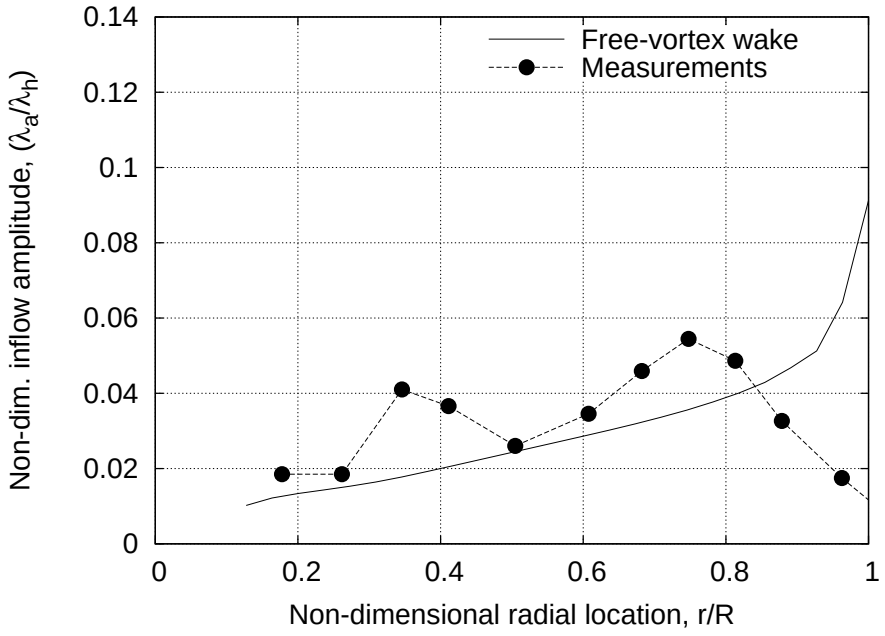


(a) 5 Hz (0.25/rev)

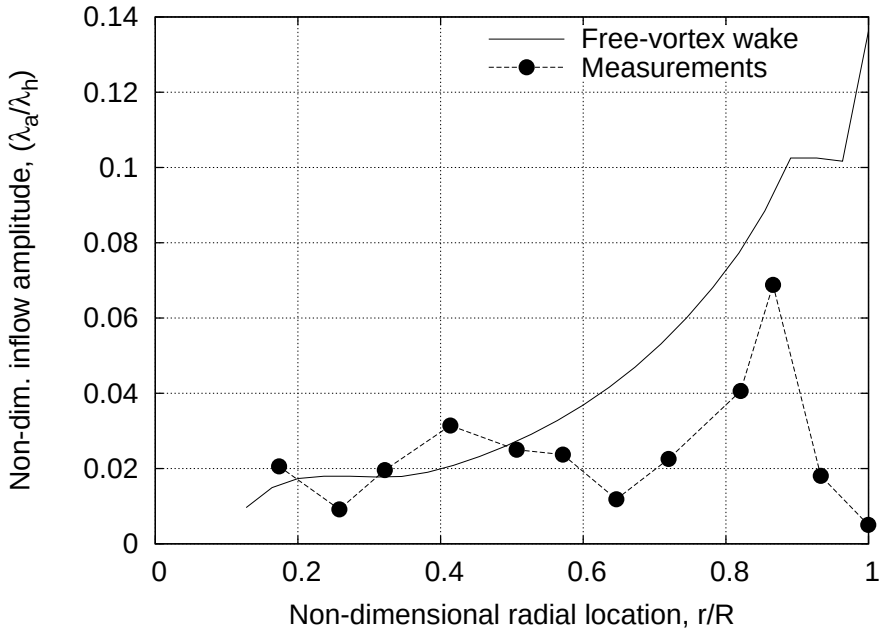


(b) 12 Hz (0.6/rev)

Figure 3.14: Amplitude response of the induced inflow along the blade span for cyclic pitch excitation at different frequencies: (a) 5 Hz (0.25/rev), (b) 12 Hz (0.6/rev). Experimental data from Ellenrieder & Brinson (1998).

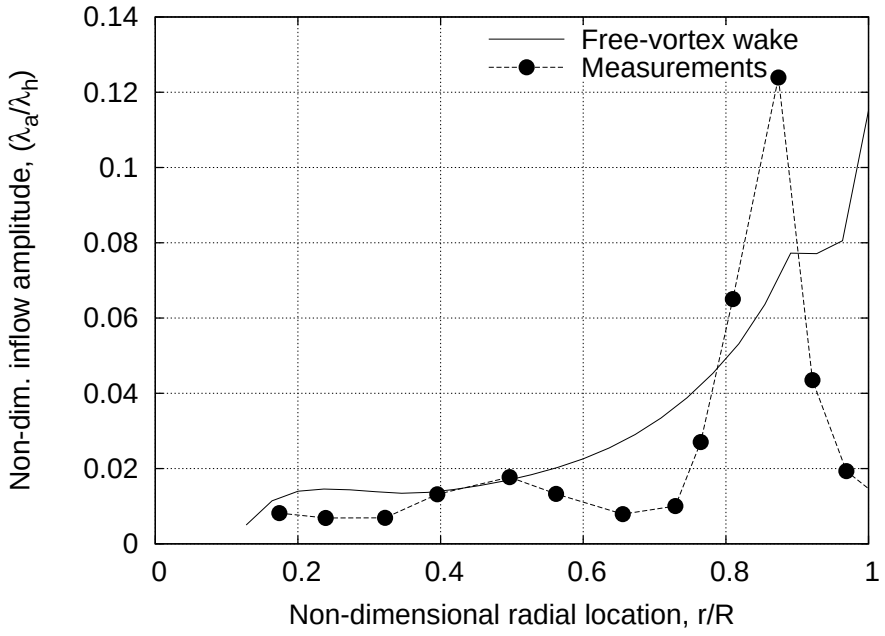


(c) 17 Hz (0.85/rev)

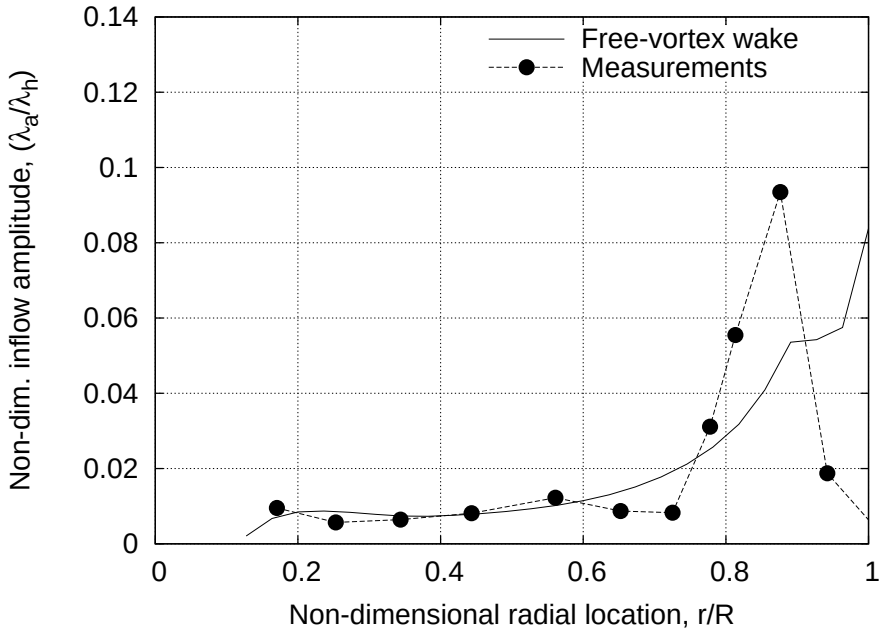


(d) 22 Hz (1.1/rev)

Figure 3.14: (Cont'd.) Amplitude response of the induced inflow along the blade span for cyclic pitch excitation at different frequencies: (c) 17 Hz (0.85/rev), (d) 22 Hz (1.1/rev). Experimental data from Ellenrieder & Brinson (1998).

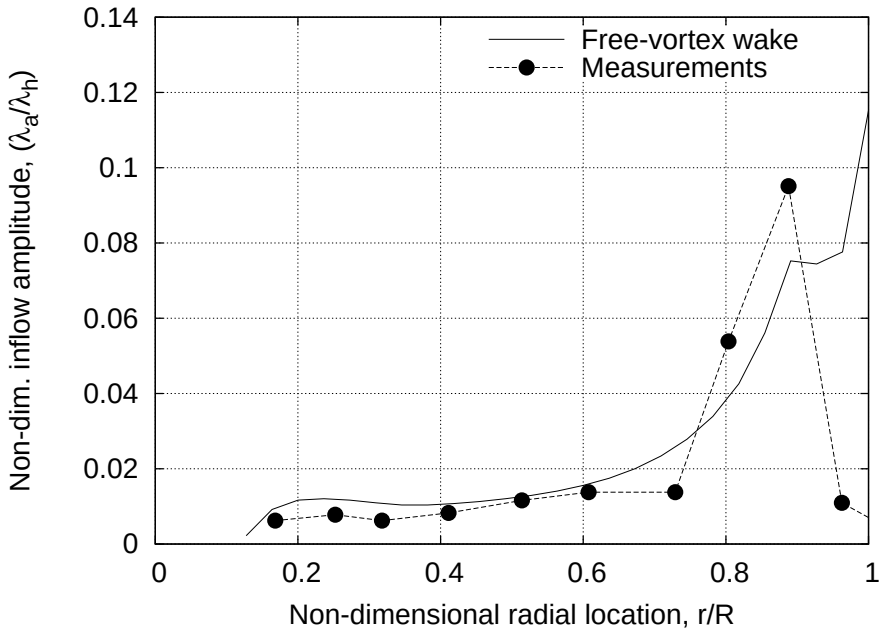


(e) 27 Hz (1.35/rev)

Figure 3.14: (Cont'd.) Amplitude response of the induced inflow along the blade span for cyclic pitch excitation at different frequencies: (e) 27 Hz (1.35/rev). Experimental data from Ellenrieder & Brinson (1998).

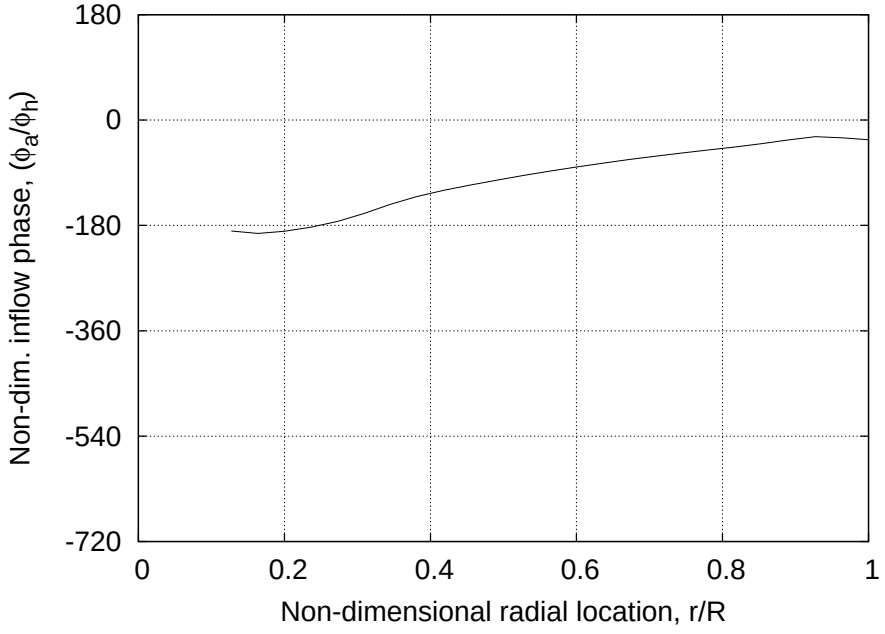


(a) 5 Hz (0.25/rev)

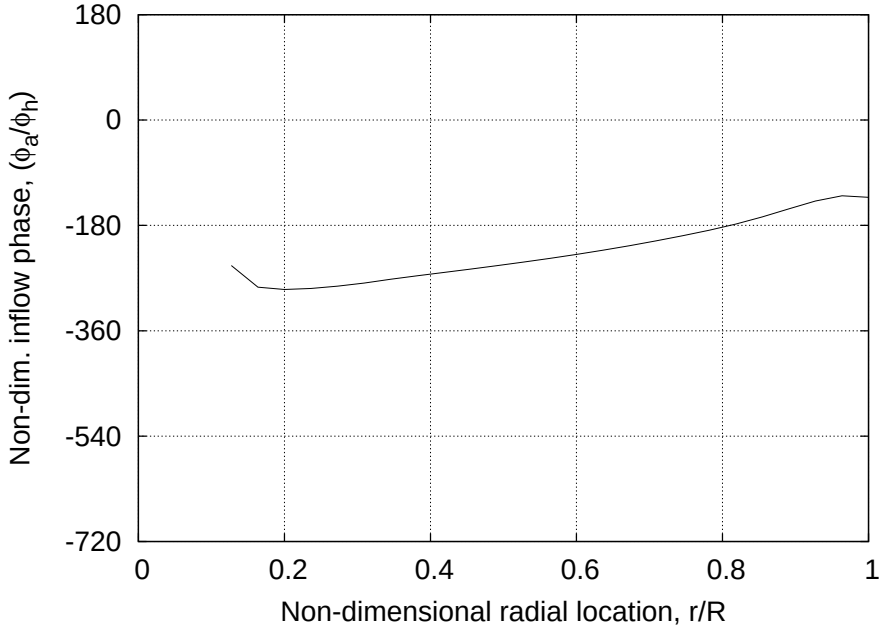


(b) 12 Hz (0.6/rev)

Figure 3.15: Phase response of the induced inflow along the blade span for cyclic pitch excitation at different frequencies. (a) 5 Hz (0.25/rev), (b) 12 Hz (0.6/rev).

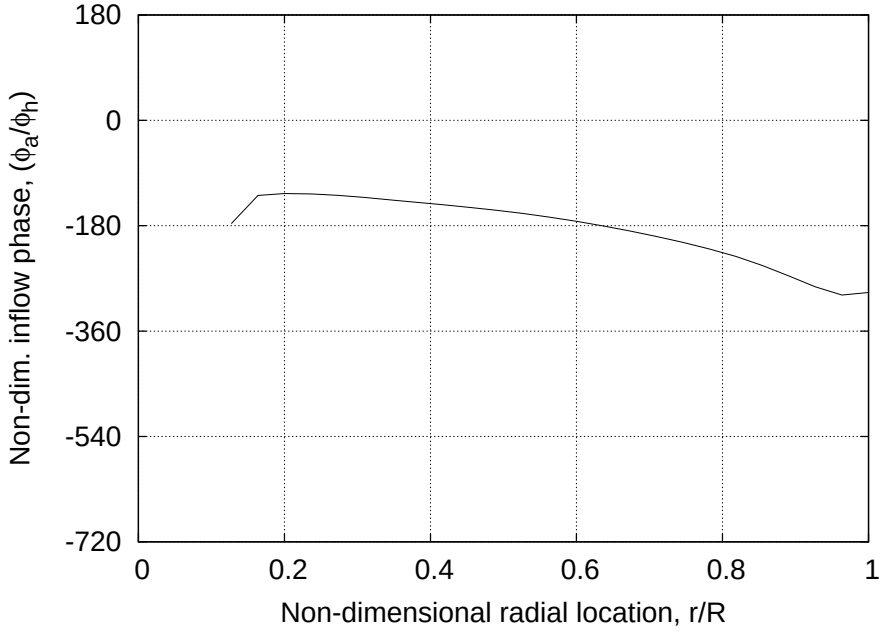


(c) 17 Hz (0.85/rev)

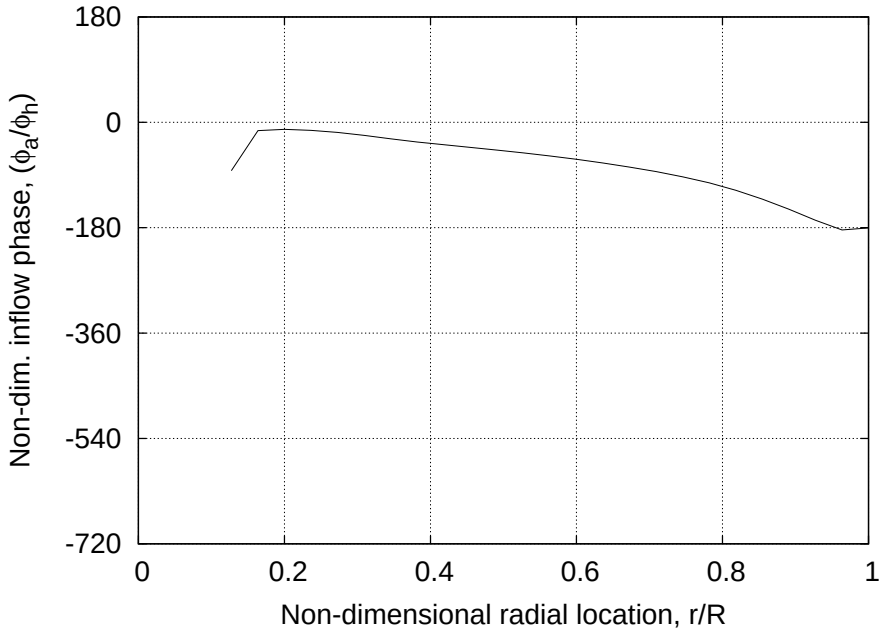


(d) 22 Hz (1.1/rev)

Figure 3.15: (Cont'd.) Phase response of the induced inflow along the blade span for cyclic pitch excitation at different frequencies: (c) 17 Hz (0.85/rev), (d) 22 Hz (1.1/rev).

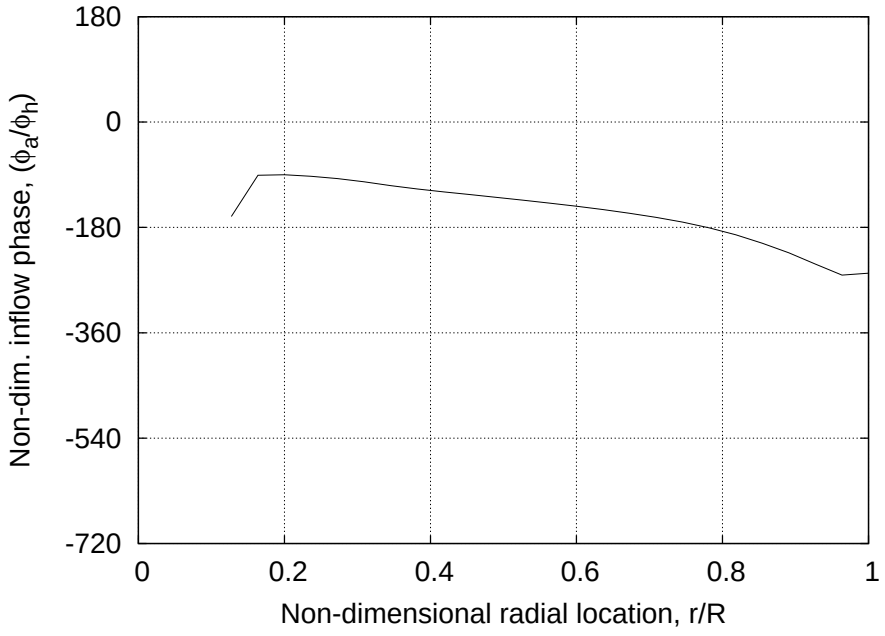


(e) 27 Hz (1.35/rev)

Figure 3.15: (Cont'd.) Phase response of the induced inflow along the blade span for cyclic pitch excitation at different frequencies: (e) 27 Hz (1.35/rev).

that the perturbations of the cyclic pitch are not important. Excitations of cyclic pitch affects the tip vortex trajectories and, therefore, the interactions of the vortices with the blades. This can affect the distribution of the airloads across the rotor disk and thereby the rotor acoustics.

## 3.2 Operations In Ground Effect (IGE)

Predicting the rotor wake geometry and the rotor performance in ground effect using numerical models has been difficult because of the inability of the existing models to accurately capture the nonlinear interactions of the vortical rotor wake with the ground plane. It has been experimentally observed that when a hovering rotor operates close to the ground, the rotor wake impinges on the ground and is convected radially outward, analogous to the classical Hiemenz flow (Ref. 121). The interaction of the wake vortices with the ground plane also affects the inflow at the rotor TPP. For constant rotor thrust, the inflow at the rotor decreases and, therefore, produces a reduced power requirement.

While operating in ground effect seems beneficial as far as power requirements are concerned, these benefits disappear if the wake recirculates and is reingested by the rotor (Ref. 20). Such conditions can be found during transition to forward flight in ground effect. Experiments by Sheridan and Weisner (Ref. 118) show the formation of a ground vortex upstream of the rotor, which can result in flow recirculation near the leading edge of the rotor disk. This increases the power requirements during transition to forward flight; this is be considered as a form of "power settling."

The present calculations were performed on a generic three-bladed rotor with a solidity $\sigma = 0.075$ and a linear twist rate of $-13^\circ$ per radius. The rotor was trimmed

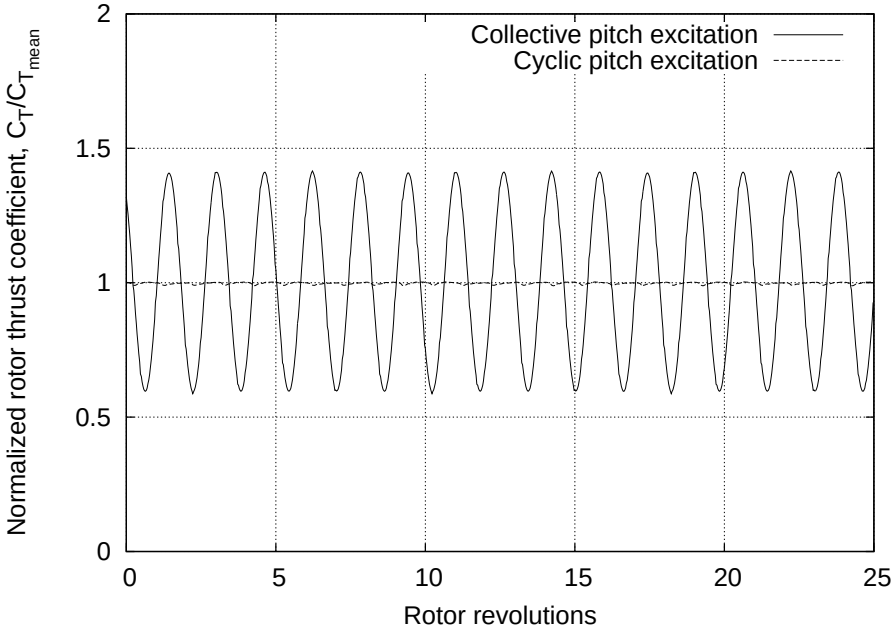


(a) Non-dimensional thrust time-history

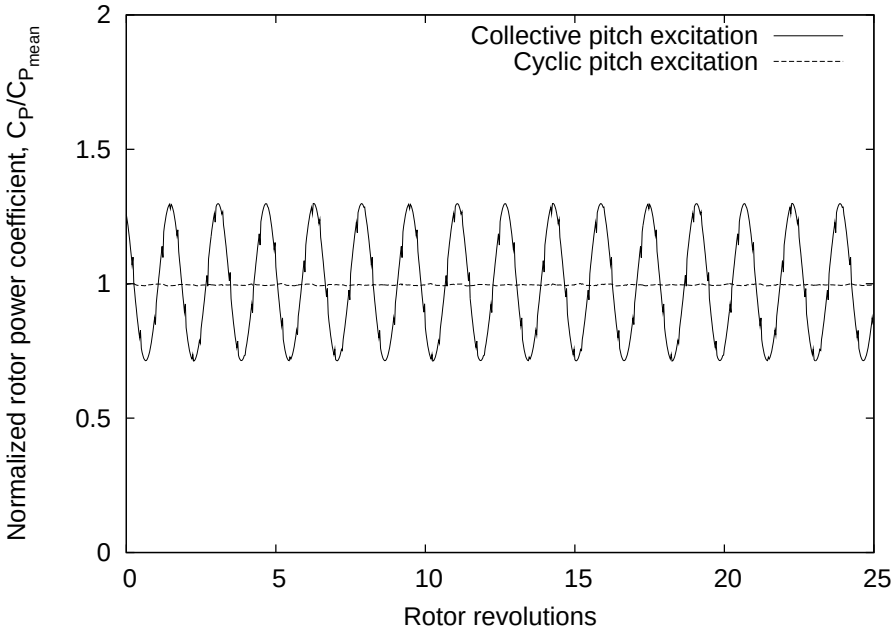


(b) Non-dimensional power time-history

Figure 3.16: Comparison of the thrust and power time histories for periodic excitaiton of the collective pitch (at 12 Hz) and the cyclic pitch (at 12.5 Hz). (a) Nondimensional rotor thrust, (b) non-dimensional rotor power ratio.

to a constant thrust of $C_T = 0.008$, unless mentioned otherwise. The ground effect simulations were simulated using the method of images (Ref. 35).

### 3.2.1 Hover In Ground Effect

Figure 3.17(a) shows an example of the rotor wake geometries for the rotor and its image, as predicted by the free-vortex methodology using the method of images. It is observed that the wake spreads radially outward as it approaches the ground. However, the radial convection does not continue indefinitely, and the wake starts rolling up beyond a certain distance for the rotor.

The rollup is seen more clearly in Fig. 3.17(b), which shows the wake boundary for a hovering rotor operating near ground at a height $h = 1.5R$. Notice that the wake contracts immediately below the rotor, but then begins to expand radially outward as it approaches the ground. The radial expansion vigorously stretches the tip vortices, and modifies the local induced velocity field. The high positive strain imposed on the filaments counteracts viscous diffusion effects decreasing the core size, and the vortices persist in the flowfield for a longer duration, a result supported by experimental observations (Ref. 88).

Figure 3.18 shows the predicted wake geometries for hovering rotors operating at different heights above the ground, ranging from $h = 3R$ (essentially "out of ground" effect) to as close as $h = 0.5R$. Notice that rotor wake and its image is symmetric about the ground plane and the wake filaments do not intersect the ground plane. This can be a problem encountered when using the method of images with a relaxation wake model when the rotor operates very close to the ground (Ref. 20). However, operations at heights less than half a rotor radius are uncommon, except perhaps for human powered helicopters.

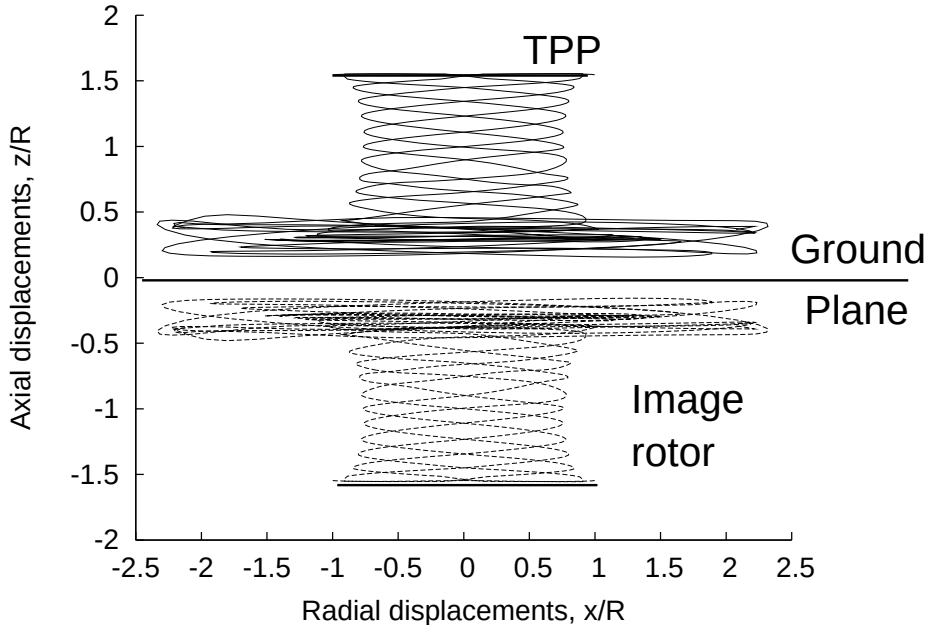


(a) Wake geometry

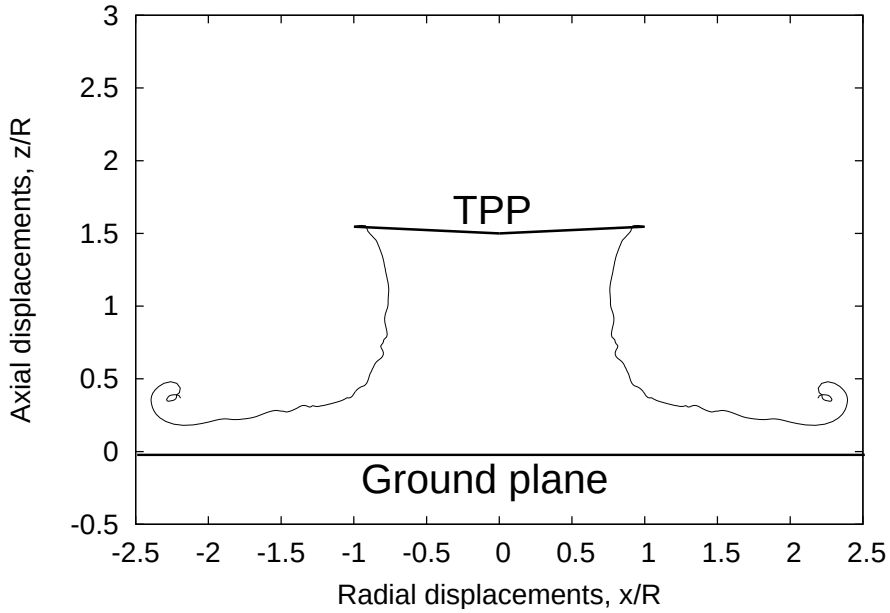


(b) Wake boundary

Figure 3.17: Wake geometry of a hovering rotor in ground effect predicted using the method of images. $C_T = 0.008$, $h/R = 0.15$: (a) Wake geometry showing the rotor wake and its image, (b) wake boundary showing the rollup in the far wake.

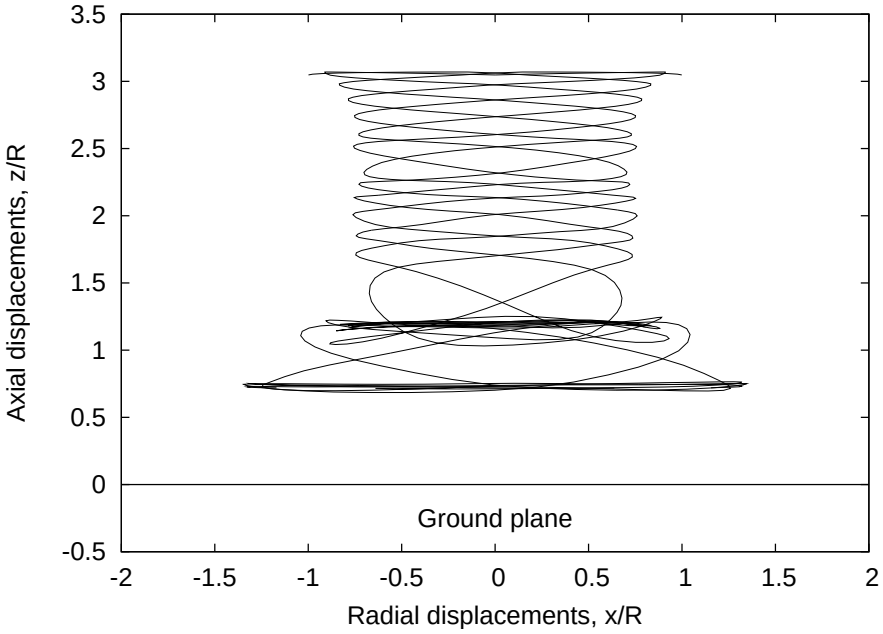


(a) $h/R = 3.0$

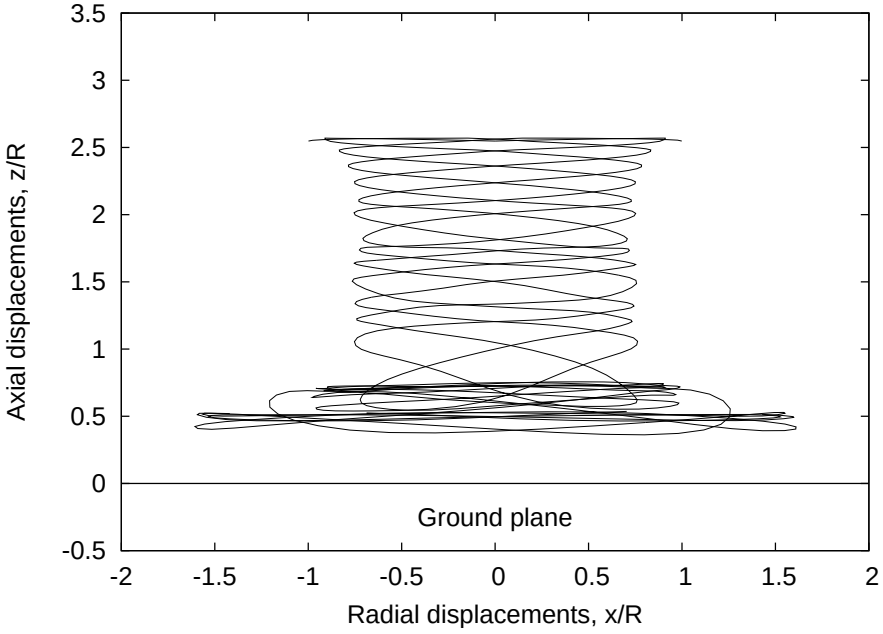


(b) $h/R = 2.5$

Figure 3.18: Wake geometries for a three-bladed rotor operating at different heights above the ground in hover for $C_T = 0.008$: (a) $h/R = 3.0$, (b) $h/R = 2.5$.

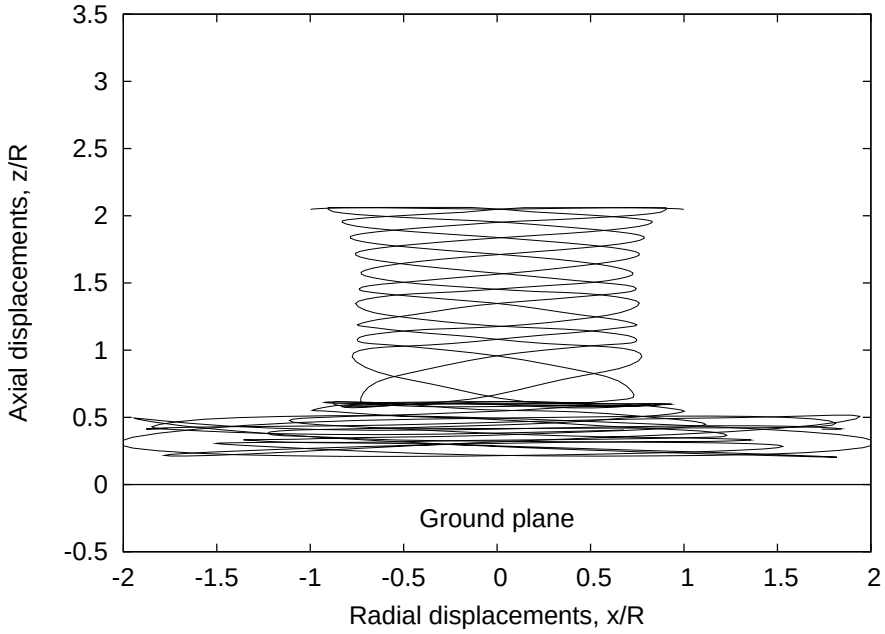


(c) $h/R = 2.0$

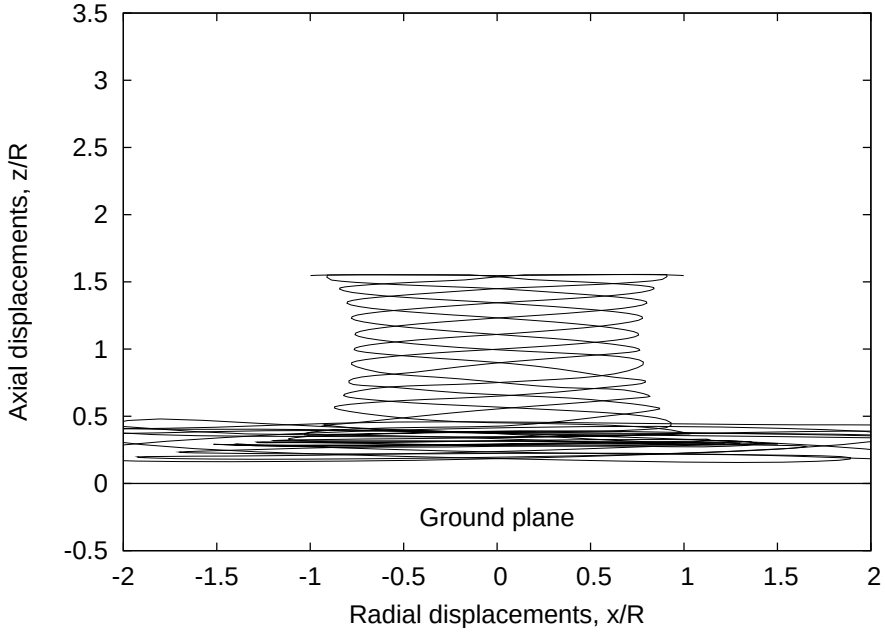


(d) $h/R = 1.5$

Figure 3.18: (Cont'd.) Wake geometries for a three-bladed rotor operating at different heights above the ground in hover for $C_T = 0.008$: (c) $h/R = 2.0$, (d) $h/R = 1.5$.

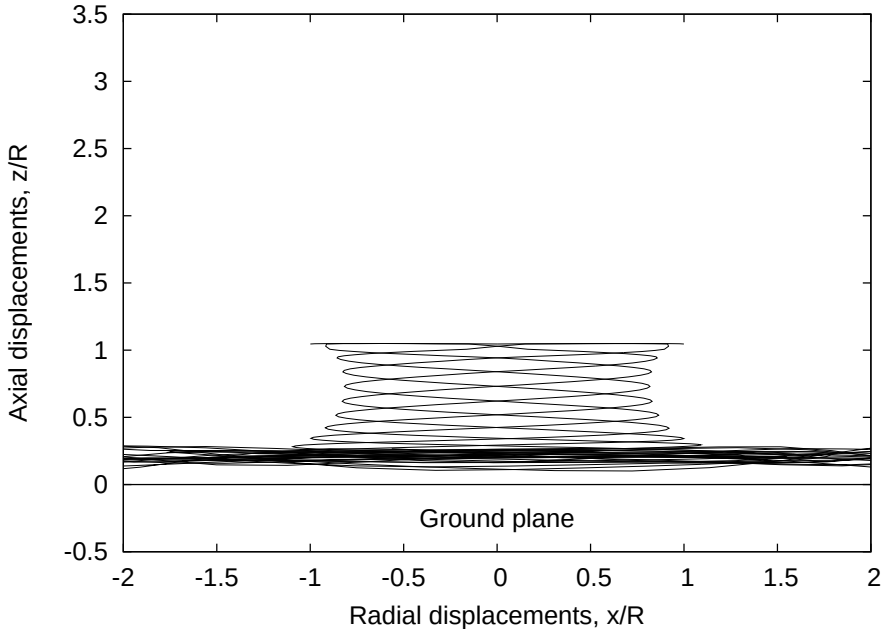


(e) $h/R = 1.0$

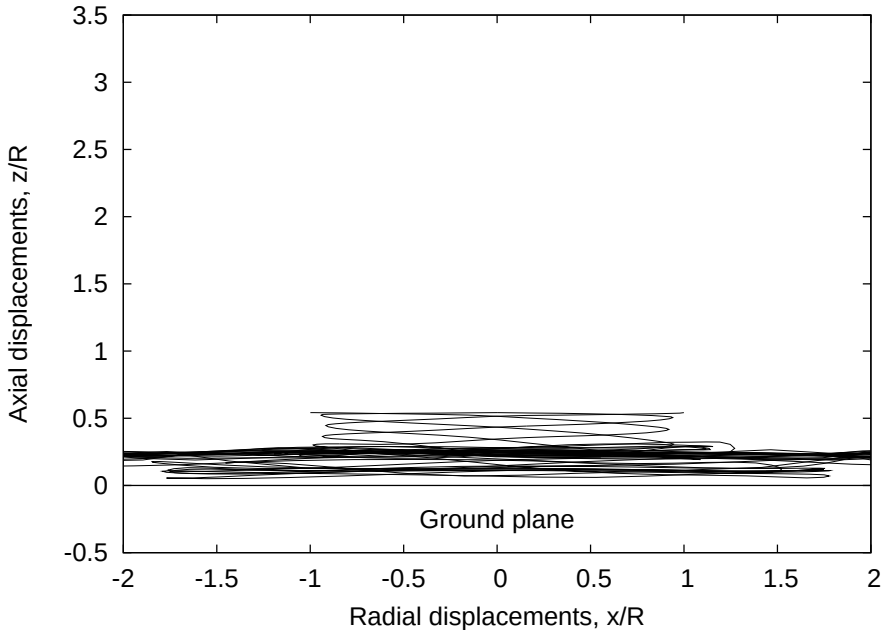


(f) $h/R = 0.5$

Figure 3.18: (Cont'd.) Wake geometries for a three-bladed rotor operating at different heights above the ground in hover for $C_T = 0.008$: (e) $h/R = 1.0$, (f) $h/R = 0.5$.

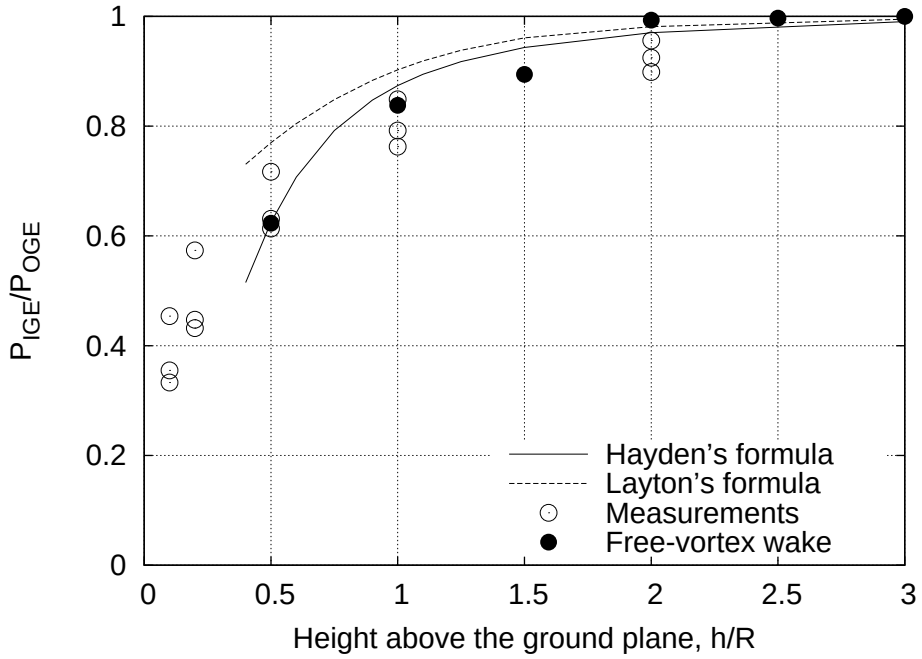


(a) Total power requirements

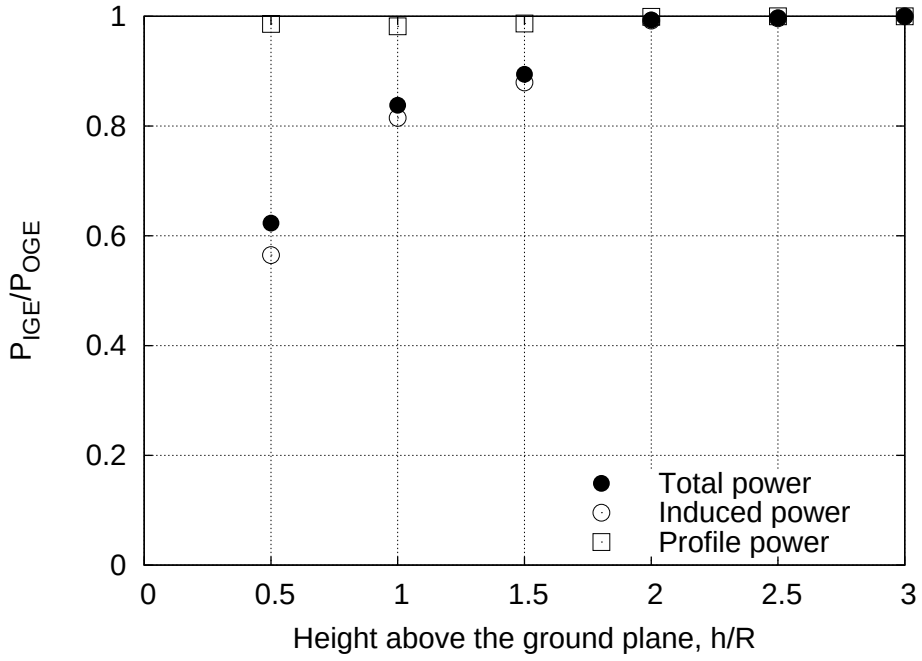


(b) Component breakdown of power requirements

Figure 3.19: Predictions of total power requirements during operation in ground effect as a function of the height of the rotor plane above the ground.

Figure 3.19(a) shows the predictions of the power required for a rotor operating IGE in comparison to the power required OGE as a function of the rotor height above the ground. The predictions are in good agreement with the performance measurements made by Fradenburgh (Ref. 117). These predictions are also in good agreement with the empirical curves suggested by Hayden (Ref. 122) and by Layton (Ref. 123) based on curve-fits to actual helicopter rotor power measurements. Notice that for heights $h/R > 2.5$, the ratio $P_{IGE}/P_{OGE}$ approaches unity. This is expected because the wake geometry in Fig. 3.18(a) shows no effect of the ground on the wake at these heights. As the rotor height above the ground is decreased, the power required drops considerably below the OGE power requirements.

Figure 3.19(b) shows the breakdown of the required power into induced and profile power components as a function of the height about the ground. Notice that the profile power component decreases only slightly as the rotor operates closer to the ground whereas the induced power decreases quickly as height between the rotor and the ground plane is reduced. The reduction in the net inflow through the rotor implies that the rotor can now operate at a lower collective pitch to generate the desired thrust. Operating at a lower collective pitch setting also leads to a slight decrease in the profile power requirements.

### 3.2.2 Forward Flight In Ground Effect

The interactions between the wake vortices are enhanced as the rotor transitions into forward flight (see Figs. 3.20 and 3.21). The tip vortices start bundling in the advancing and retreating side forming a "horseshoe" shaped vortex bundle near the ground. This bundled ring structure is washed away quickly as the forward flight speed increases, and the wake structure at higher advance ratios is found to be similar to that

observed OGE. The bundled vortex structure affects the induced velocity at the rotor plane, and this reduces the overall rotor power requirements at these low advance ratios, as seen in Fig. 3.22. Notice that the power requirements are not affected by the presence of the ground plane at higher advance ratios. The predictions from the free-vortex wake methodology show excellent agreement with the estimates from experiments of Sheridan & Weisner (Ref. 118).

The flow field velocities from the free-vortex wake simulations IGE were calculated over a grid of points along the longitudinal and lateral centerline planes. From the time-averaged velocity field over one revolution the streamline patterns can be determined. Figure 3.23(a) and (b) show the time-averaged streamlines around the rotor IGE for an advance ratio $\mu = 0.02$ across the longitudinal and lateral centerlines. The rotor was operating at a height $h = R$ above the ground. The results show clear evidence of the leading edge ground vortex, which is also observed in experiments (Ref. 118). This flow recirculation region is essentially a ground vortex that is wrapped under the leading edge of the rotor disk and forms just after the rotor transitions into forward flight from hovering flight. This recirculation is responsible, in part, for the small increase in power requirements shown in Fig. 3.22.

As the forward flight increases, as shown in Fig. 3.23(c), the recirculation region diminishes in extent and is swept under the rotor. As already described, however, as forward flight speed increases, the most substantial effects in the rotor induced power requirements is the enhanced proximity of the vortex bundles that trail from the lateral edges of the rotor disk. This can be seen in Fig. 3.23(d) where the vortex bundles move laterally away from the rotor, but are also closer vertically to the disk because of the influence of the ground.

These results show the usefulness of the free-vortex wake method for predicting

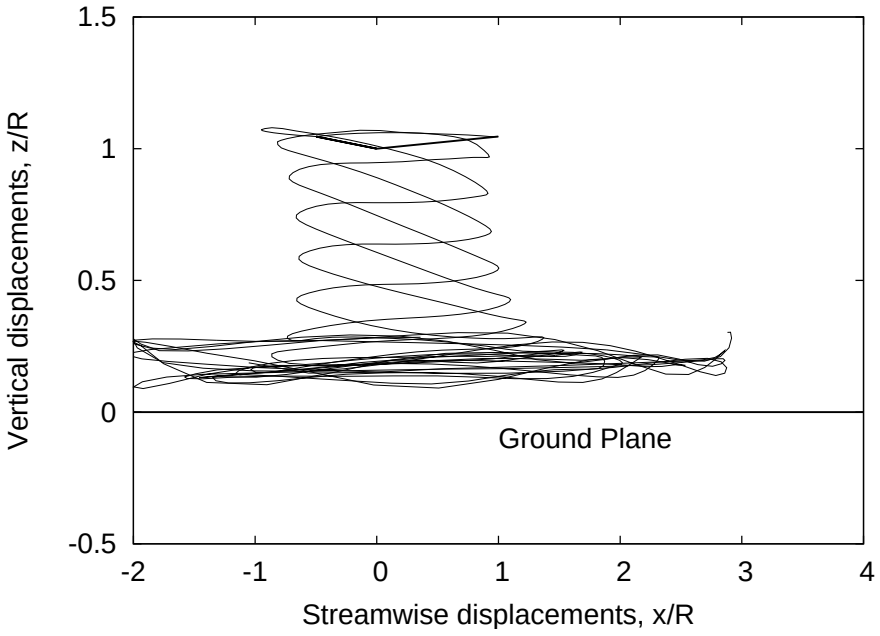


(a) $\mu = 0.02$

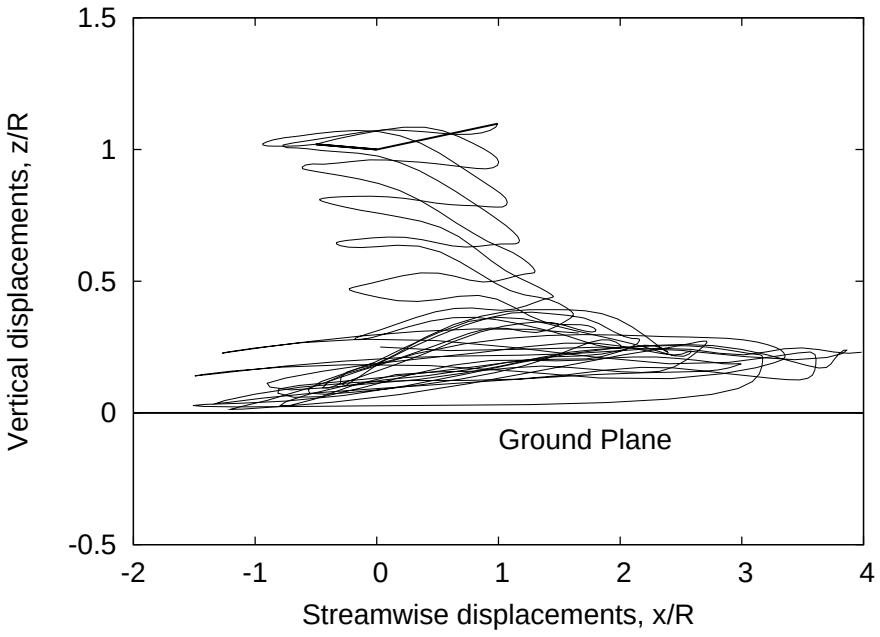


(b) $\mu = 0.05$

Figure 3.20: Side views of the wake geometries for rotor operating at different advance ratios IGE at a height $h = R$ above the ground, $C_T = 0.008$: (a) $\mu = 0.02$, (b) $\mu = 0.05$.

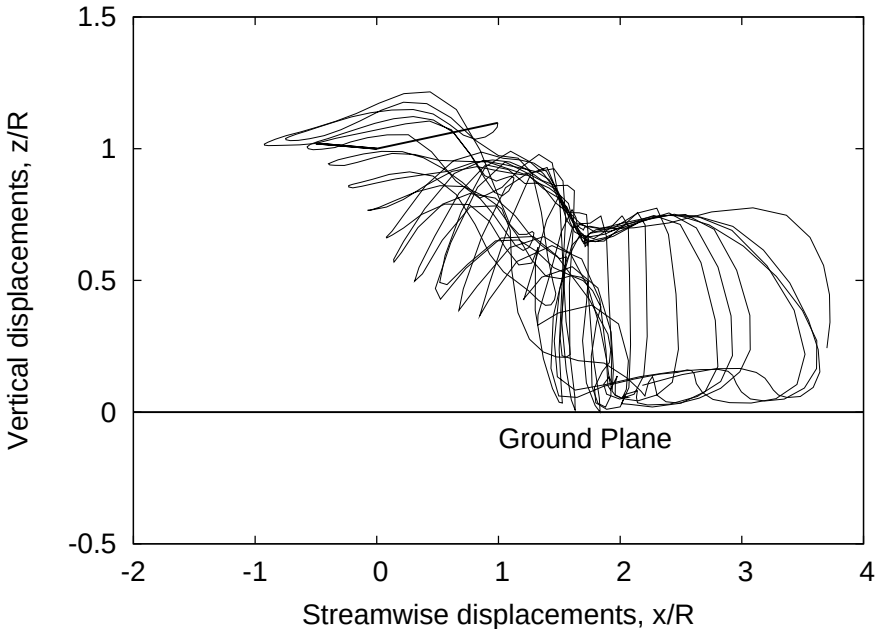


(c) $\mu = 0.08$

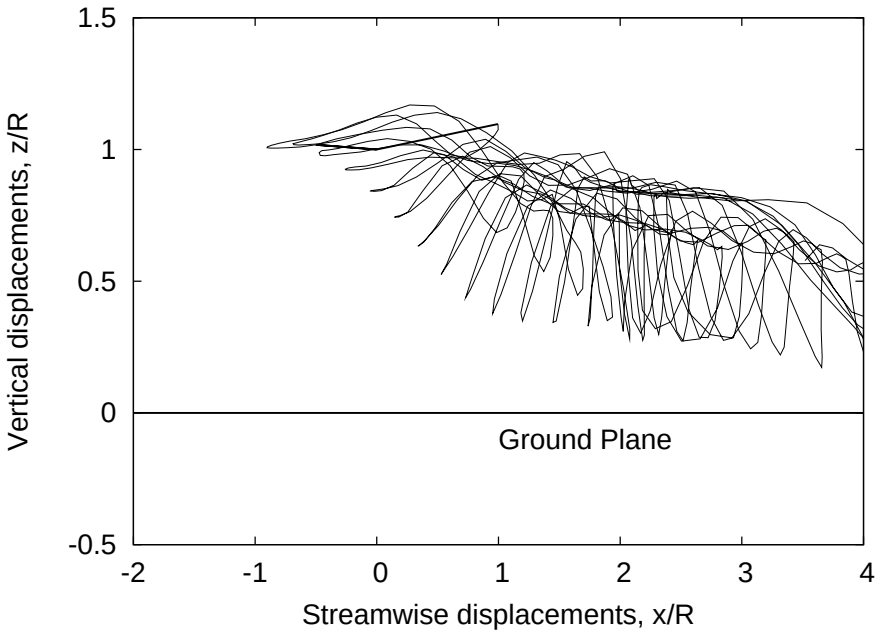


(d) $\mu = 0.1$

Figure 3.20: (Cont'd.) Side views of the wake geometries for rotor operating at different advance ratios IGE at a height $h = R$ above the ground, $C_T = 0.008$: (c) $\mu = 0.08$, (d) $\mu = 0.1$.

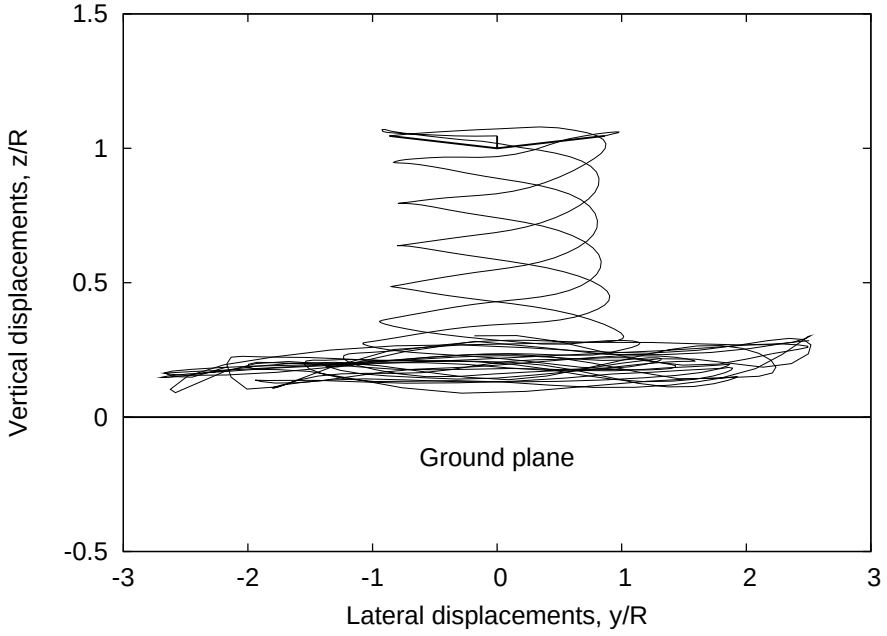


(a) $\mu = 0.02$

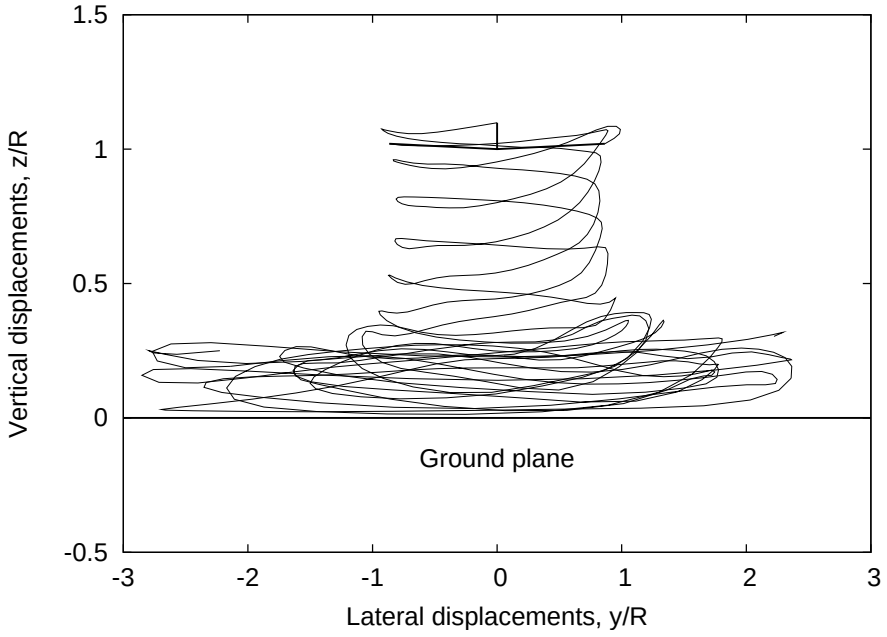


(b) $\mu = 0.05$

Figure 3.21: Rear views of the wake geometries for rotor operating at different advance ratios IGE at a height $h = R$ above the ground, $C_T = 0.008$: (a) $\mu = 0.02$, (b) $\mu = 0.05$.

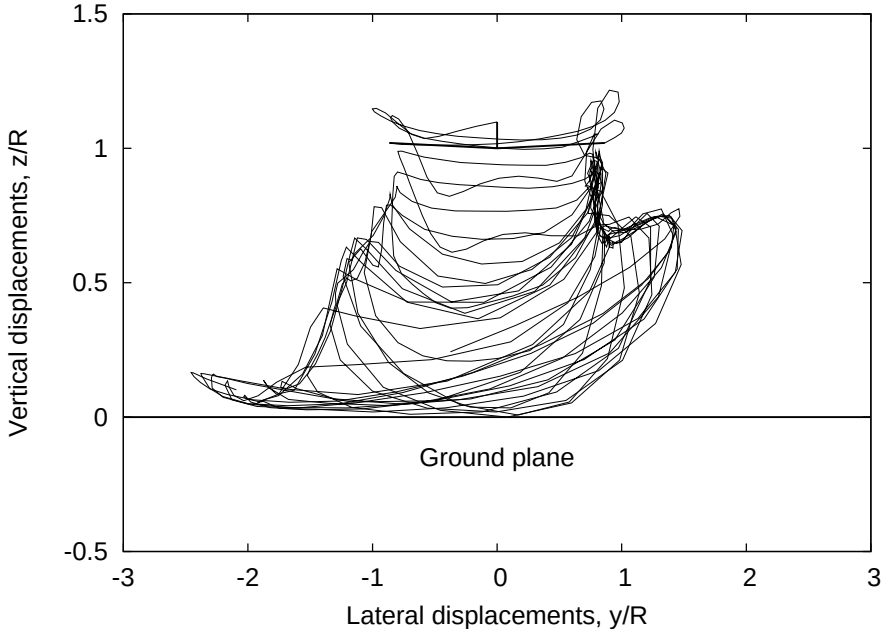


(c) $\mu = 0.08$

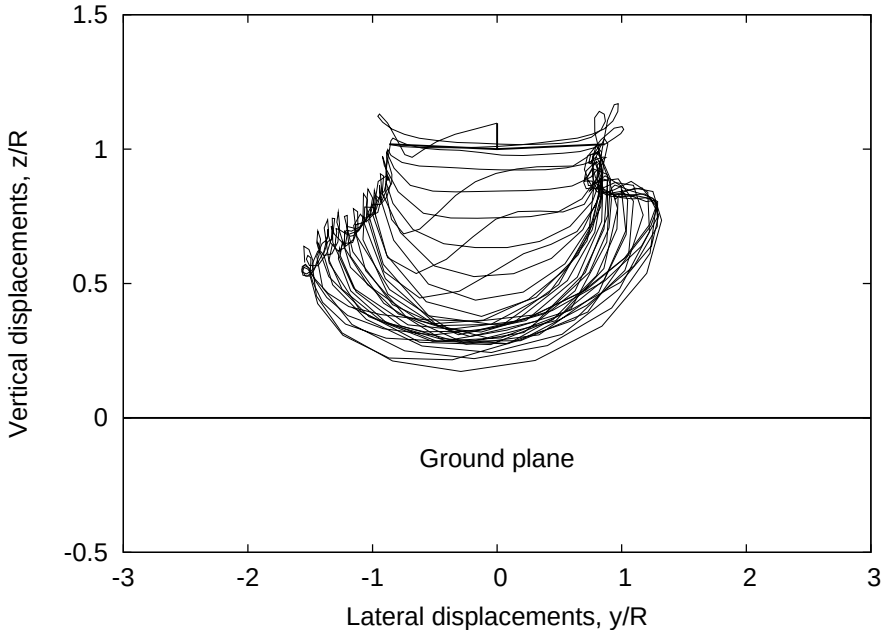


(d) $\mu = 0.1$

Figure 3.21: (Cont'd.) Rear views of the wake geometries for rotor operating at different advance ratios IGE at a height $h = R$ above the ground, $C_T = 0.008$: (c) $\mu = 0.08$, (d) $\mu = 0.1$.

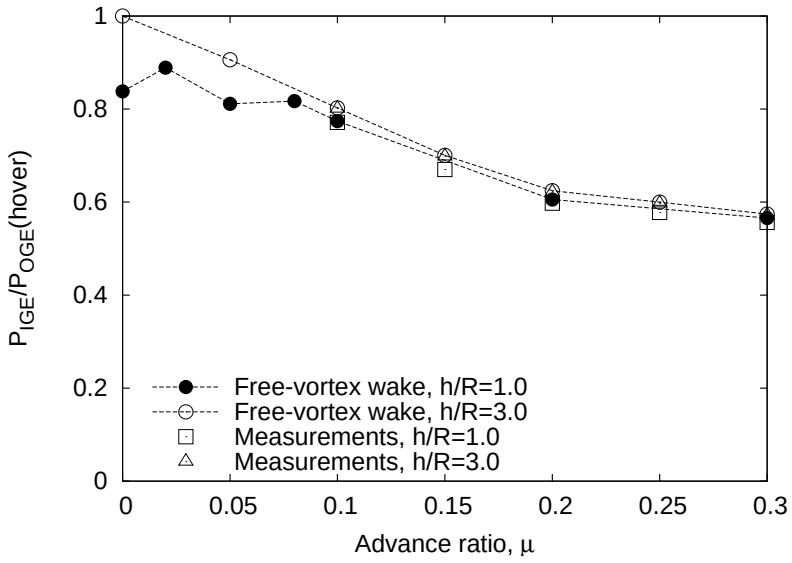


Figure 3.22: Power requirements for a rotor operating IGE as a function of the advance ratio at two different heights, $h = R$ and $h = 3R$.

the essential features of the rotor wake near the ground, and for identifying the primary mechanisms that affect rotor performance. This can also be done at a reasonable computing cost, so the method is useful for a variety of practical studies of rotors operating IGE. The quantitative validity of the approach, however, needs further work, especially for other types of rotors. Comparisons against detailed flowfield measurements for rotors operating IGE are needed; unfortunately these experimental data do not yet exist and are difficult to acquire.

## 3.3 Coaxial Rotors

Coaxial rotor configurations are being considered for the design of heavy lift helicopters (Ref. 124). The flowfield surrounding a coaxial rotor is particularly complicated even for hovering flight conditions, mainly because a large part of the lower

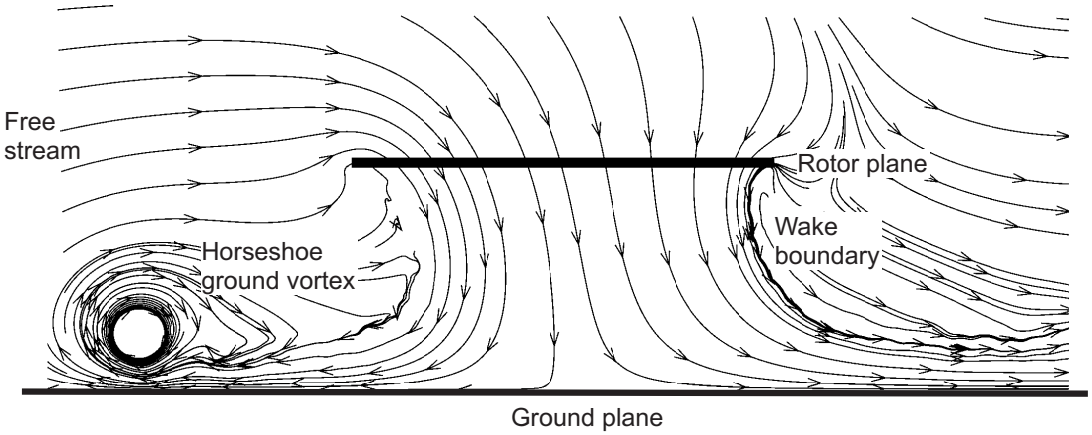


(a) Plane through longitudinal centerline

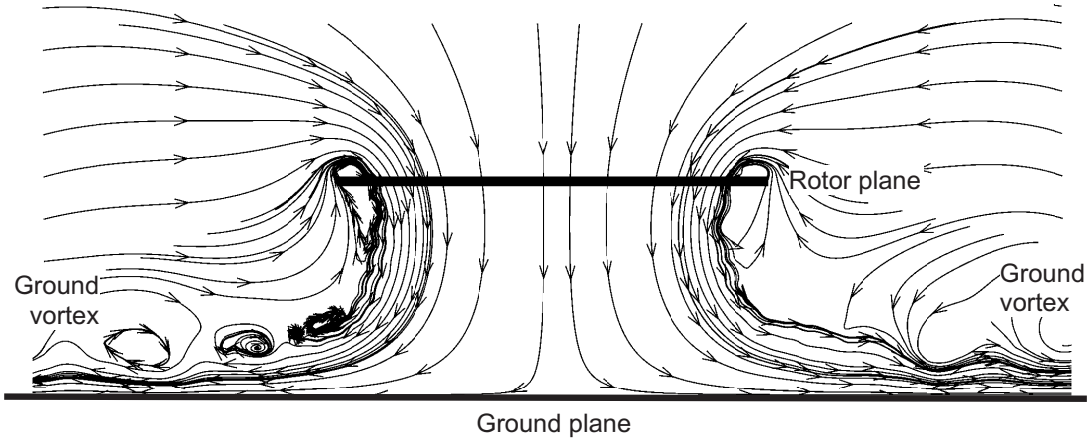


(b) Plane through lateral centerline

Figure 3.23: Streamlines showing the formation of the ground vortex for a rotor operating IGE at very low advance ratios. $C_T = 0.008$, $\mu = 0.02$.

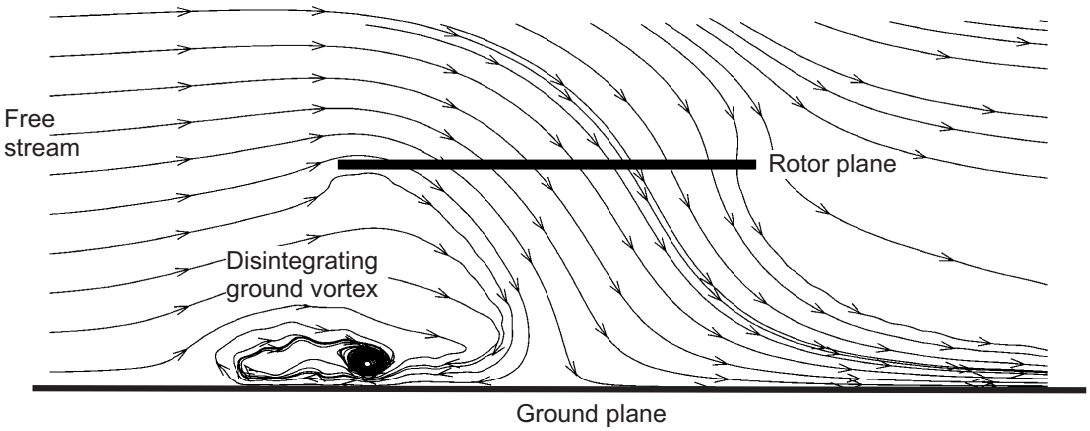


(c) Plane through longitudinal centerline

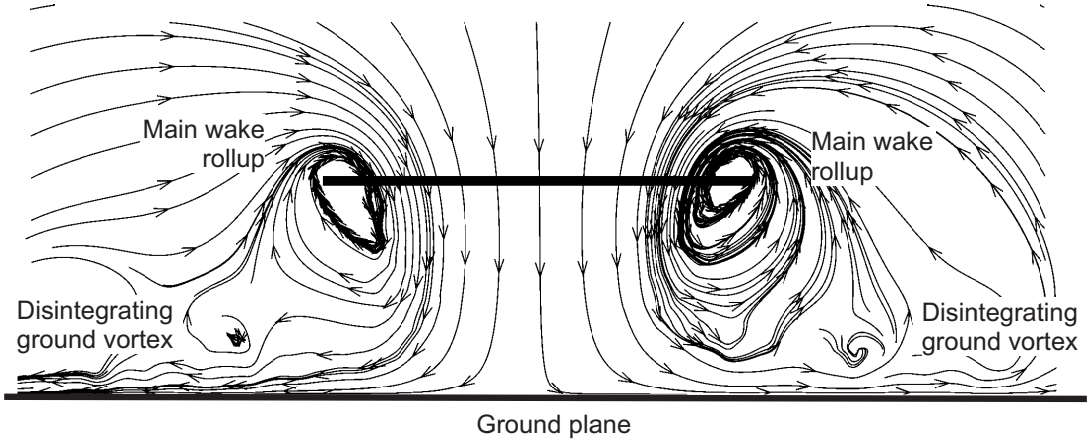


(d) Plane through lateral centerline

Figure 3.23: (Cont'd.) Streamlines showing the breakdown of the ground vortex for a rotor operating IGE increasing advance ratios. $C_T = 0.008$, $\mu = 0.05$.

rotor disk operates under the influence of the vortical wake of the upper rotor. The interaction of the tip vortices trailing from the edges of the blade tips of the upper rotor with the blades of the lower rotor needs to be captured accurately to estimate the spanwise blade loading on the upper and lower rotors.

For a trimmed flight, the two rotors must generate an equal and opposite torque. The lower rotor is under an apparent climb condition (arising from the downwash of the upper rotor) and, therefore, has higher induced power requirements. This means that for a torque balance, the two rotors must operate at different thrust conditions such that the net thrust produced is equal to balance the vertical forces.

The wake structure, the induced velocity field and the rotor performance are a function of the net rotor thrust, the blade shape, and the separation distance between the two rotors. A thorough study of the variation in induced velocity field with respect to these parameters is essential in designing an optimal coaxial rotor configuration for application to heavy-lift helicopters.

Figure 3.24 shows the predicted wake geometries for a generic, four-bladed utility helicopter configuration at two different inter-rotor separation distances, $h = 0.1R$ and $h = R$. The rotors were trimmed for a torque balance and net thrust criteria, as described in Section 2.6. Notice in Fig. 3.24(a), that the lower rotor operates almost completely in the wake of the upper rotor. The separation distance is comparable to the pitch of the helical wake, and the wake of the upper rotor does not have enough time to develop fully before interacting with the lower rotor. There is also evidence of strong interaction and pairing between the tip vortices of the upper and lower rotors in the far wake, i.e., beyond one rotor radius below the rotors.

In contrast, when the rotor separation distance is increased (see Fig. 3.24(b)), the wake of the upper rotor is fully developed and it interacts with a much smaller region

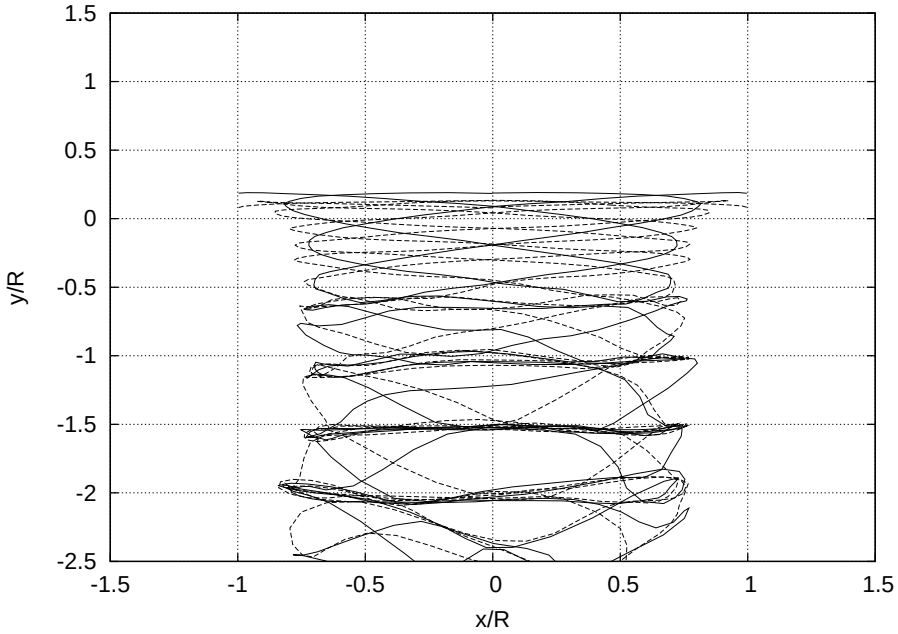


(a) $h/R = 0.1$

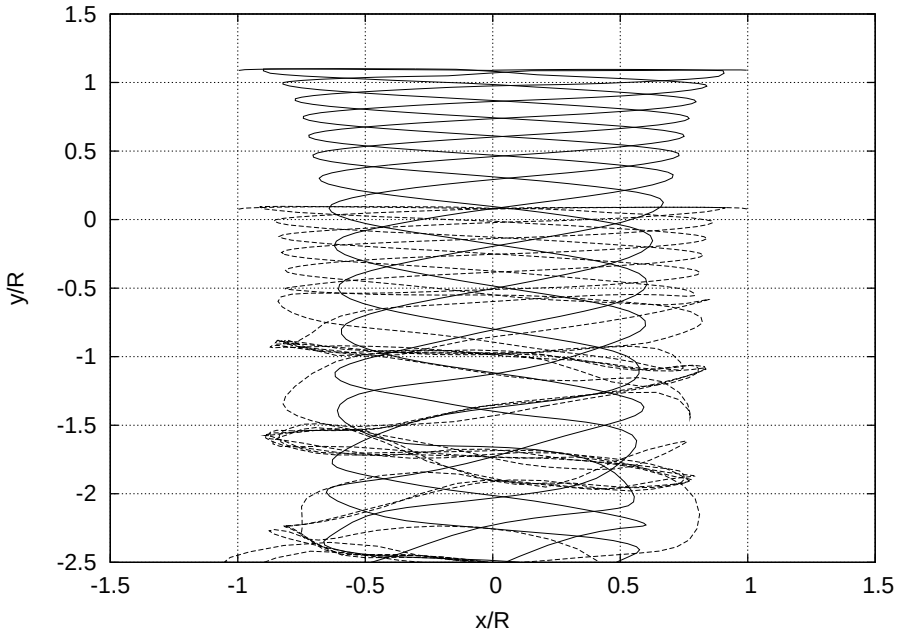


(b) $h/R = 1.0$

Figure 3.24: Wake geometry predictions for a generic coaxial rotor configuration at two different inter-rotor separation distances. (a) $h/R = 0.1$, (b) $h/R = 1.0$.

of the lower rotor. The wakes of the two rotors are clearly distinguishable in the far wake, unlike those shown in Fig. 3.24(a). Also notice that the helical pitch of the tip vortices trailed from the upper rotor increases as it is convected within the wake of the lower rotor. This is because the tip vortices experience a higher induced velocity field arising from the wake of the lower rotor. There is some evidence of pairing of tip vortices in the outer wake (the wake of the lower rotor). The interaction of the lower rotor blades with the tip vortices trailed from the upper rotor introduces a spanwise as well as an azimuthal variation in the blade loads on the lower rotor. This perturbation seems to be responsible for the pairing phenomena observed in the wake of the lower rotor. The "helicoidal" pairing, in this case, is very similar to that observed in Fig. 3.13 (discussed in more detail in Section 3.1.2) where the wake responds to excitations in cyclic pitch.

Figure 3.25 compares the spanwise distribution of the induced velocity at the rotor blade for rotors operating at constant thrust to the case where the rotors are operating in a torque balance condition. Notice that for small inter-rotor separation distances (see Figs. 3.25(a) and (b)) there is not a significant difference in the distribution of the induced inflow, except close to the blade tips. The differences observed near the blade tips of the lower rotor are primarily because of the strong interactions with the tip vortices from the upper rotor, which have different strengths in these two conditions. As the rotor separation distance is increased, considerable differences are observed in the spanwise distribution of the induced velocities for the two cases – see Figs. 3.26(a) and (b). This is because, for a torque trim condition, the two rotors operate at different thrust levels as the separation distance increases, as shown in Table 3.1. The differences in the induced velocity field further affect the bound circulation associated with the rotor blades, as is evident from the results shown in Figs. 3.27 and 3.28.

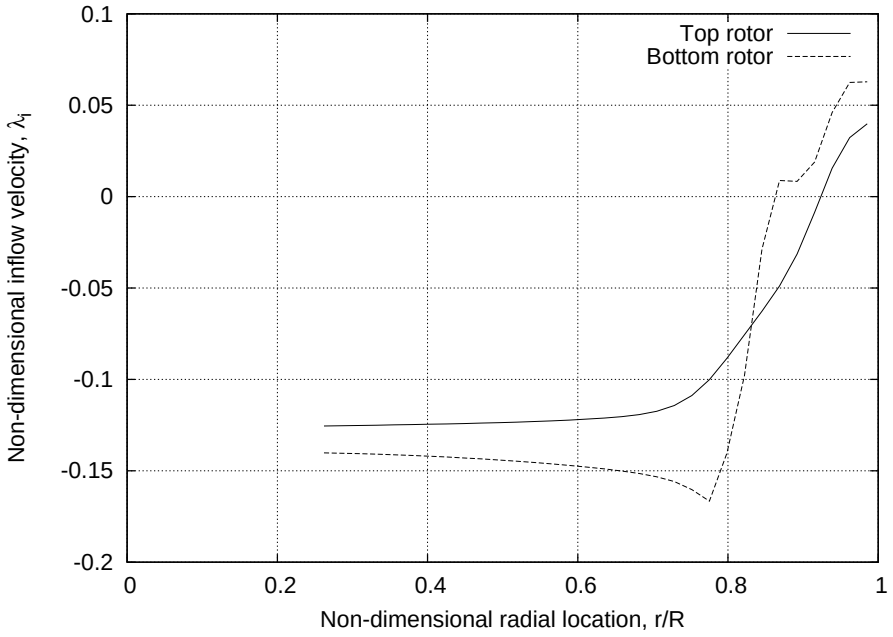


(a) $C_{T_u} = C_{T_l}$

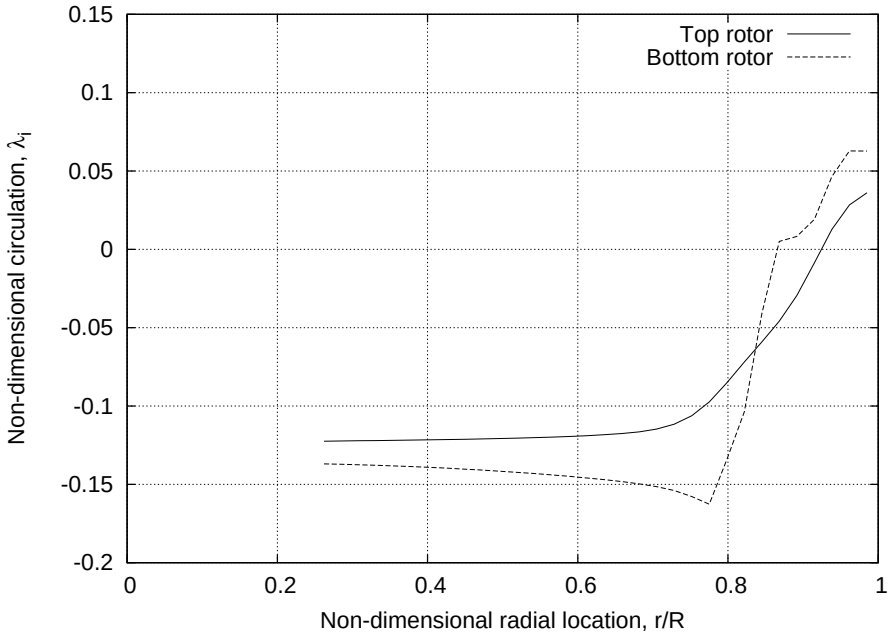


(b) $C_{Q_u} = C_{Q_l}$

Figure 3.25: Time-averaged spanwise variations of the induced velocity at the rotor blade for rotors operating at different separation distances for constant thrust versus a torque balance condition, $h/R = 0.1$.

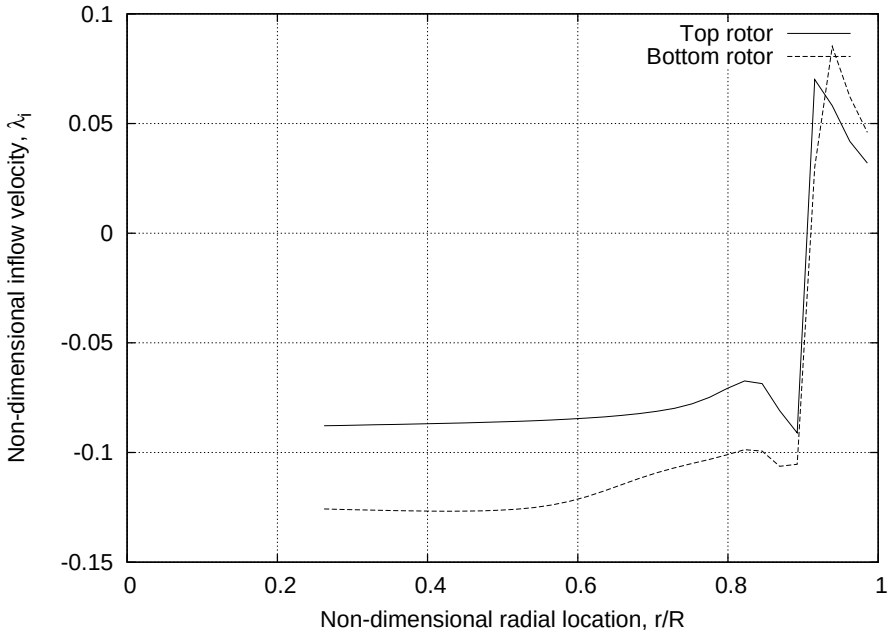


(a) $C_{T_u} = C_{T_l}$

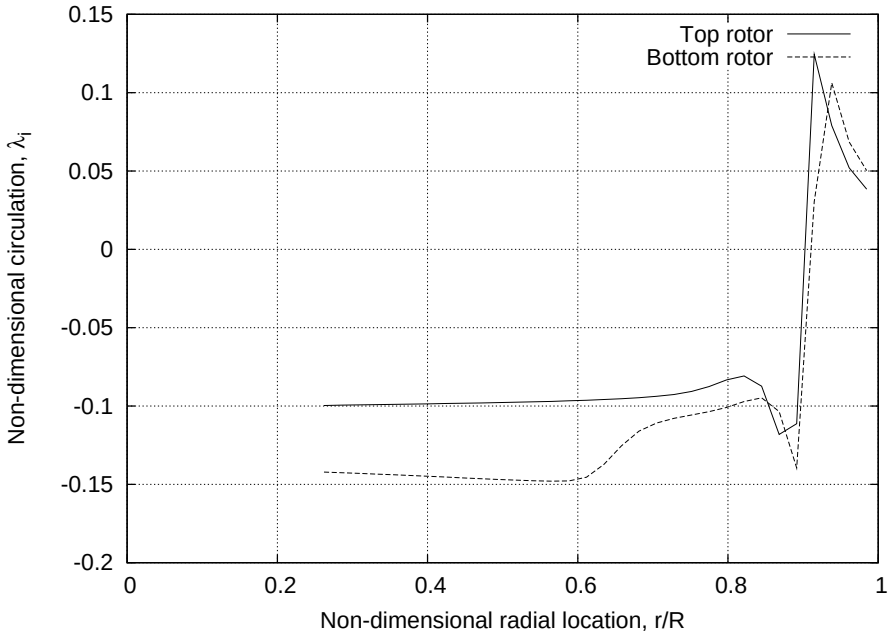


(b) $C_{Q_u} = C_{Q_l}$

Figure 3.26: Time-averaged spanwise variations of the induced velocity at the rotor blade for rotors operating at different separation distances for constant thrust versus a torque balance condition, $h/R = 1.0$.

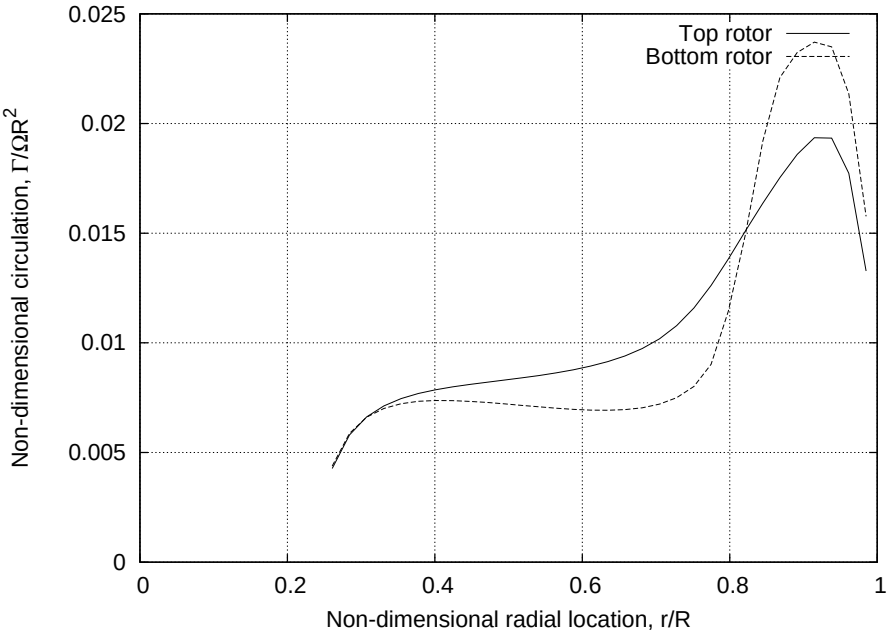


(a) $C_{T_u} = C_{T_l}$

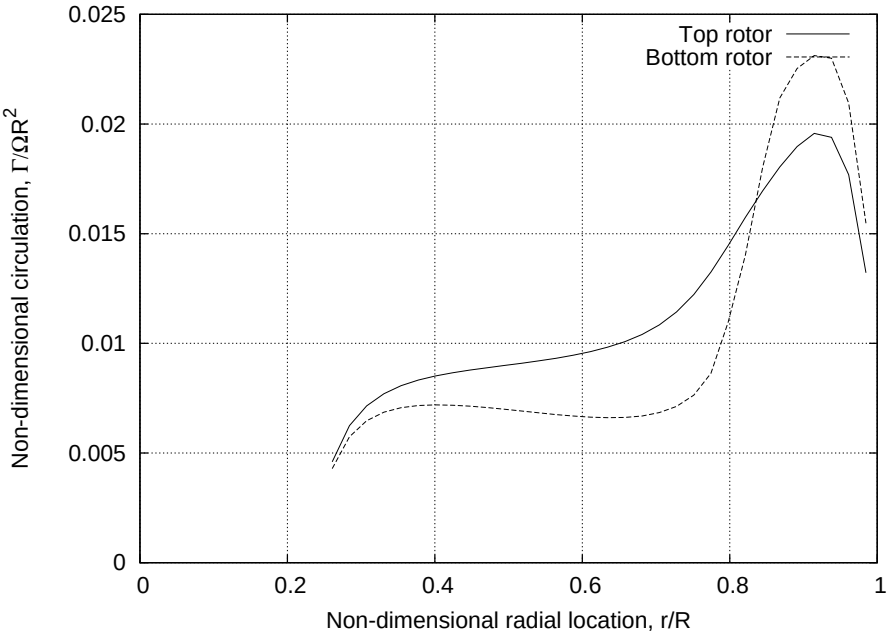


(b) $C_{Q_u} = C_{Q_l}$

Figure 3.27: Time-averaged spanwise variations of the bound circulation at the rotor blade for rotors operating at different separation distances for constant thrust versus a torque balance condition, $h/R = 0.1$.

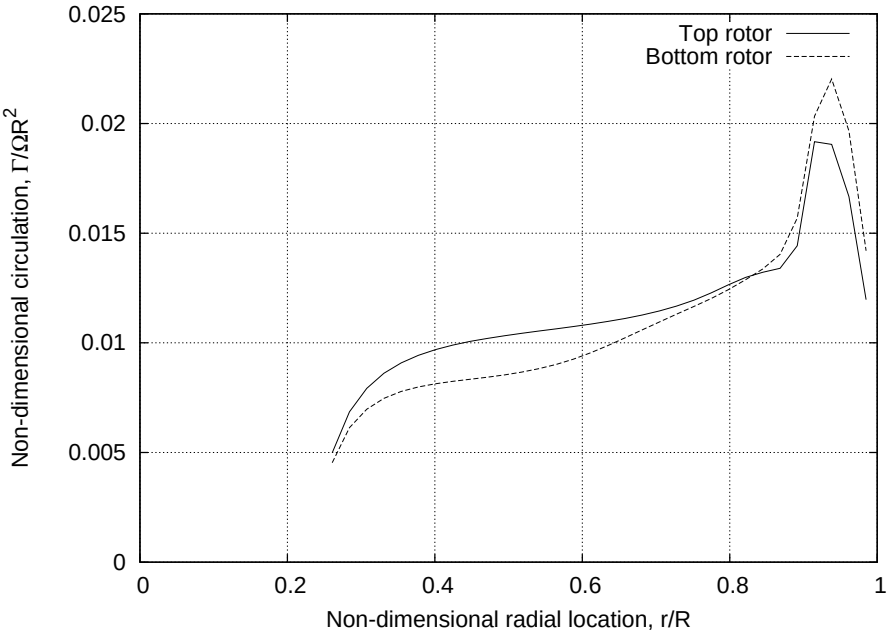


(a) $C_{T_u} = C_{T_l}$

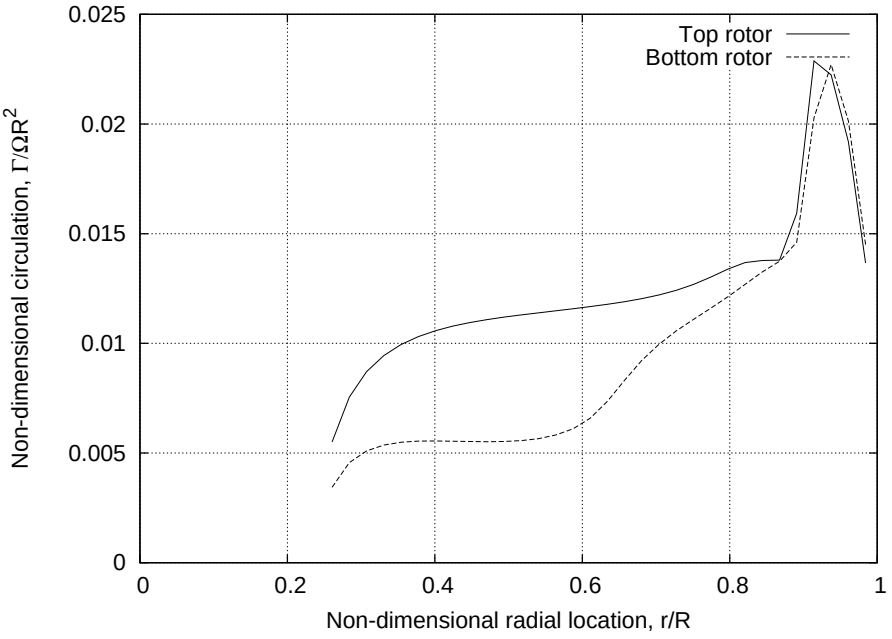


(b) $C_{Q_u} = C_{Q_l}$

Figure 3.28: Time-averaged spanwise variations of the bound circulation at the rotor blade for rotors operating at different separation distances for constant thrust versus a torque balance condition, $h/R = 1.0$.

Table 3.1: Rotor performance parameters for coaxial rotors operating in a torque balance condition for two different rotor separation distances .

| | | $h/R = 0.1$ | $h/R = 1.0$ |
|---|---|---|---|
| Thrust ($C_T = 0.016$) | $C_{T_u}$ | 0.0083 | 0.0088 |
| | $C_{T_l}$ | 0.0077 | 0.0072 |
| Induced power | $C_{P_{iu}}$ | 0.0009657 | 0.0009052 |
| | $C_{P_{il}}$ | 0.0009455 | 0.0009075 |
| Profile power | $C_{P_{0u}}$ | 0.0001093 | 0.0001144 |
| | $C_{P_{0l}}$ | 0.0001258 | 0.0001079 |
| Total power | $C_{P_u}$ | 0.0010750 | 0.0010196 |
| | $C_{P_l}$ | 0.0010713 | 0.0010154 |

The performance of coaxial rotor configurations was studied in detail by Harrington (Ref. 125). Identical rotors with two, untwisted blades were used in this experiment. The rotor blades had a radius $R = 3.81$ m and a solidity $\sigma = 0.048$. The blades had a tapered planform such that $c_t/c_r = 0.39$. The rotational speed of the rotor was 40 rad/s, and the separation distance between the rotors was $h = 0.18R$. The power measurements were made for a range of net system thrust levels from $C_T = 0.0005$ to $C_T = 0.008$ and a torque balance condition.

Figure 3.29 shows the predictions of the required power as a function of the net system thrust for the Harrington rotor along with the measured values. The results from the free-vortex wake method show excellent agreement with the measurements. It has been mentioned previously that a torque balance condition requires the rotors to operate at different thrust levels. It is noticed that the differences in the thrust generated by the rotors increase as the net system thrust increases – see Fig. 3.30. This

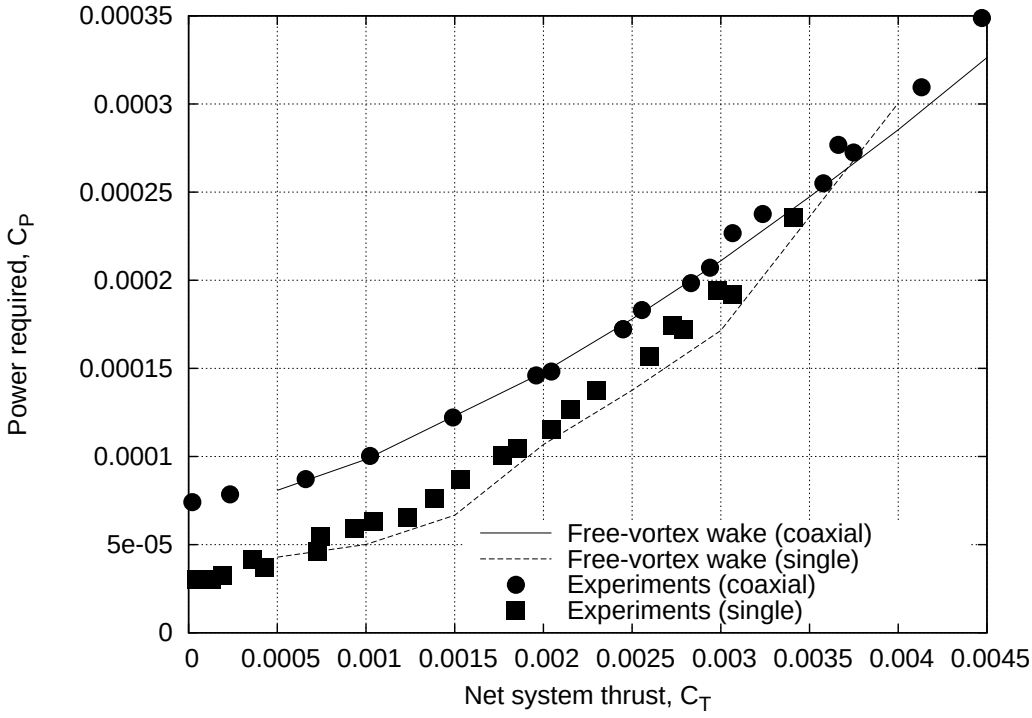


Figure 3.29: Predictions of the power requirements of for a coaxial rotor configuration as a function of the system thrust. Measurements from Harrington (1951).

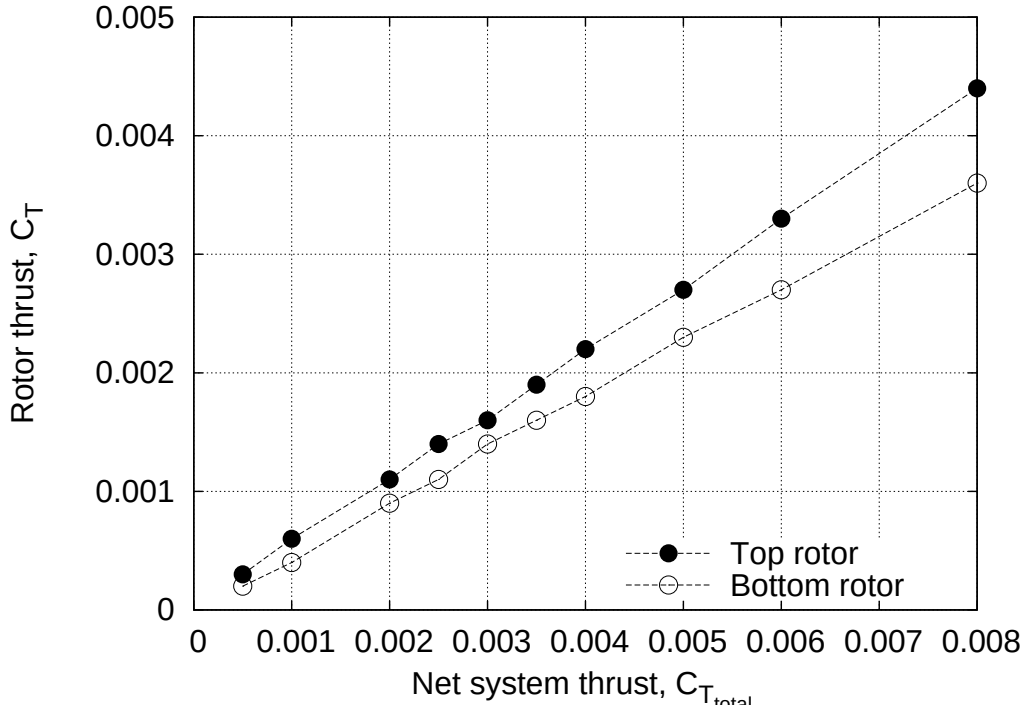


Figure 3.30: Rotor trim solutions showing the individual rotor thrust as a function of the net system thrust.

is because, as the net system thrust is increased, the overall inflow through the lower rotor increases and, therefore, the upper rotor must generate a greater percentage of the net thrust to achieve torque balance.

The free-vortex methodology is capable of predicting the rotor performance accurately for the coaxial rotor configurations. While similar results are possible using simple analysis tools like BEMT, there are several issues with these momentum theory based methods that need some empirical inputs to solve the problem. For example, the wake contraction must be prescribed to obtain the influence of the wake of the upper rotor on the lower rotor. However, in the free-vortex methodology the wake boundaries are obtained as a solution to the wake problem.

## 3.4 Summary

The emphasis of this first chapter of results has been to demonstrate the capability of the free-vortex wake methodology to accurately predict the rotor wake dynamics, the resulting induced inflow response along with the rotor performance parameters for a wide variety of steady and non-steady flight conditions. The wake aerodynamics for time-varying blade control pitch inputs was studied in detail to better understand the characteristic wake response to control pitch perturbations. It was observed that the blade tip vortices had a tendency to pair up and bundle into a toroidal ring structure below the rotor, an observation supported by experimental flow visualization. These rings were observed to be unstable and break down as they are convected downstream. The intensity and the aerodynamics of the bundled wake structure are dependent on the type and magnitude of the blade pitch inputs. For example, periodic excitations of collective pitch resulted in a series of axial contractions and expansions of the wake structure with the bundles parallel to the rotor TPP. However, for excitations of the cyclic pitch the successive bundles took on a more helicoidal shape. Comparisons of quantitative predictions of thrust, blade flapping and inflow response with available experimental data showed excellent agreement. This provides considerable confidence in the capability of the present methodology to capture the wake response and its influence on the blade airloads under arbitrary, unsteady flight conditions. The methodology can be used as a computational tool in the analysis of free-flight maneuvers to better understand the aerodynamics of the rotor during maneuvers, and more importantly the effect of the pilot control inputs on the rotor aerodynamic loads and noise levels.

The flow field surrounding the rotor for operations IGE and for coaxial rotor systems were analyzed in detail. It was seen that for hover IGE conditions the wake

first contracts, but then quickly expands radially outward as it approaches the ground. The radial convection does not occur indefinitely because of the propensity of the tip vortices to pair up and form bundles. Transition into forward flight showed evidence of the leading-edge ground vortex, a phenomena observed in flow visualization experiments. The rotor power performance estimates were in good agreement with the measured values for all flight regimes.

The problem of coaxial rotors were analyzed for two conditions, both rotors operating at the same thrust, and the rotors operating in a torque balance condition. It was observed that for a torque balance the two rotors can operate at very different thrust levels depending on the separation between the rotors. The inter-rotor separation distance also influenced the evolution of the wake from the upper rotor. It was seen that for small separation distances the tip vortices trailed from the blades of the two rotors interacted closely and paired to form concentric bundles. With the increase in the separation distance, the wake from the upper rotor was completely engulfed within the wake of the lower rotor. The helical pitch of the wake vortices increased as the wake from the upper rotor convected downstream. The wake from the lower rotor exhibits helicoidal bundling akin to that observed with periodic excitation of the cyclic pitch. This can be attributed to the spanwise as well as azimuthal variation of the blade loading in the lower rotor because of its interaction with the wake from the upper rotor.

# Chapter 4

# Results & Discussion: Maneuvering Flight

The validation efforts discussed in the previous chapter provide sufficient confidence in the capabilities of the free-vortex wake methodology to predict the time-varying wake aerodynamics during non-steady flight conditions. The objective of the current chapter is twofold. First, to demonstrate the applicability and numerical robustness of the free-vortex method in computing the rotor aerodynamics for large displacement flight maneuvers. And second, to apply the numerical algorithm developed to study various flight maneuvers and gain a deeper insight into the physical features of the wake dynamics associated with these maneuvers, as well as their potential influence on the blade airloads and resulting rotor acoustics.

The maneuvers analyzed in this chapter can be broadly categorized into two classes: idealized and free-flight maneuvers. In idealized maneuvers, only one of the pilot's control inputs is perturbed to perform the maneuver. This neglects the effects of cross-coupling and might cause an imbalance in the forces along the primary axes. The final orientation and the flight path of the helicopter are arbitrary, and depend very much on the type of control inputs used to perform the maneuver. While such maneuvers are unrealistic in practice, these idealized maneuvers serve as a good starting point in

the study of non-steady, transient flight conditions. In contrast, free-flight maneuvers are performed using a combination of collective, cyclic pitch and pedal inputs, and the primary objective is to fly the helicopter along a desired flight path. This is a more realistic simulation of actual piloted maneuvers.

Maneuvers initiated both from hover and forward flight conditions are studied in the subsequent sections. Popup and popdown maneuvers, initiated from a hovering flight condition, are considered first. This is followed by a study of idealized maneuvers initialized from a steady, forward flight condition. Arrested descent, starboard and port rolls and roll reversals are simulated using idealized, one-degree-of-freedom control pitch inputs. These idealized maneuvers will help in the identification of the primary wake features associated with different flight maneuvers. Finally, a thorough investigation of the starboard and port roll, roll reversal, and quickstop (a variation of arrested descent maneuver) in piloted, free-flight conditions is presented. The additional complexities introduced by the cross-coupling effects can be better understood by comparing the free-flight maneuvers with the idealized maneuvers.

## 4.1 Determination of the Optimum Wake Resolution

The fidelity with which the acoustic computations can be performed are highly dependent on the spatial and temporal resolution of the predicted wake geometry. High resolution wake solutions are computationally very expensive. Therefore, an optimum resolution of the wake needs to be decided to keep the computational costs down to a practical level, but without losing the capability to predict important acoustic phenomena. Many rotor design analyses use very coarse spatial and temporal resolutions in wake predictions; in some cases the resolution is as coarse as $\Delta\psi = 15^\circ$ (Ref. 7).

Many BVI interactions, especially parallel interactions that are acoustically most significant, occur over much smaller spatial domains, i.e., less than 15°. At such coarse resolutions it is highly probable that these acoustically critical interactions will not be captured accurately, or even completely missed.

Figure 2.13 shows a schematic of the error introduced by coarse resolutions. The curved tip vortices are approximated using straight line segments. At coarser resolutions, these line segments will not approximate the curvature at the point of intersection accurately. This introduces errors in the exact position of the BVI, the effective trace Mach number and the interaction angle. Therefore, the sensitivity of the BVI prediction process on the wake resolution needs to be investigated thoroughly before proceeding with the actual acoustic analyses of flight maneuvers.

A discretization study was conducted for a rotor in forward flight with an advance ratio $\mu = 0.1$. The free-vortex wake solution was computed at three different discretization levels, $\Delta\psi = 2.5^\circ,\ 5^\circ,$ and $10^\circ$ respectively. Figure 4.1 shows the BVI locations predicted by the free-vortex wake method and the corresponding principal acoustic directivity patterns at the three levels of discretization. The potential BVI locations with supersonic trace Mach numbers are shown with filled circles. Notice that the wake geometries with coarser resolutions fail to provide a complete map of the intersection points. The coarsest resolution ($\Delta\psi = 10^\circ$) fails to capture the parallel interactions in the advancing side, which are extremely important from the rotor acoustics point of view.

Failure to predict the proper BVI locations lead to very poor acoustic directivity predictions, as shown in the right hand side plots in Fig. 4.1. The coarsest resolution does not predict the primary directivity of the acoustic field, which is observed only with the finest resolutions. A discretization level of 5° captures the key acoustic fo-

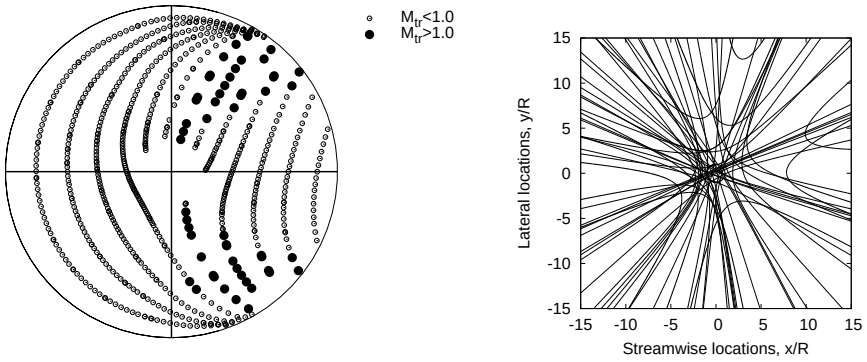


(a) $\Delta\psi = 2.5^\circ$

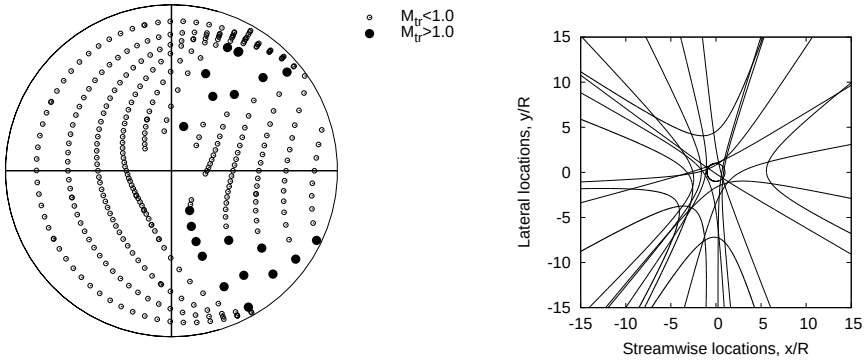


(b) $\Delta\psi = 5^\circ$

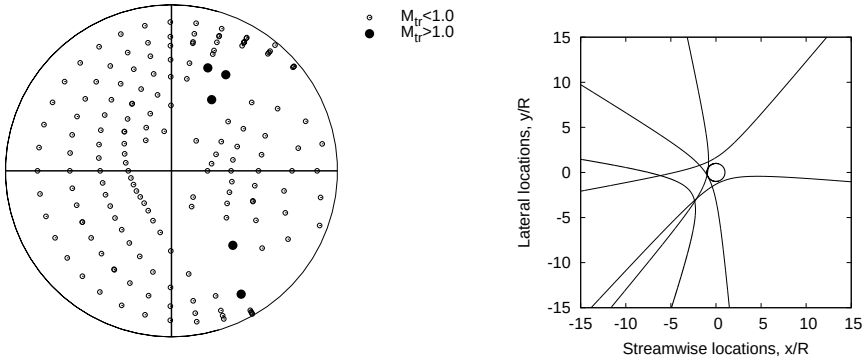


(c) $\Delta\psi = 10^\circ$

Figure 4.1: Predictions of BVI locations over the rotor disk and the corresponding principal acoustic directivity cones along an observer plane at a distance $3R$ below the rotor TPP for three different discretization levels for a rotor in forward flight with advance ratio $\mu = 0.1$. (a) $\Delta\psi = 2.5^\circ$, (b) $\Delta\psi = 5^\circ$, (c) $\Delta\psi = 10^\circ$.

cusing directions, however, it is still lacking in detail. It is, therefore, obvious that any reliable predictions of rotor aeroacoustics will require grid resolutions of $\Delta\psi = 2.5^\circ$ or even finer grids. However, the computational penalty imposed, when computing wake dynamics over several rotor revolutions is high. A compromise between the resolution and computational expense is necessary. Based on the discretization study, one can conclude that a resolution of $\Delta\psi = 2.5^\circ$ seems to provide reasonable predictions of the BVI locations and the acoustic directivity.

As mentioned previously, the transient wake dynamics in response to control input perturbations persist for several rotor revolutions. It must be noted that even for modest resolutions of $\Delta\psi = 2.5^\circ$, the simulations of maneuvering flight can take up to several days on a high end computer workstation. A computational cost breakdown of the various components of the free-vortex algorithm immediately shows that the Biot–Savart computations of the mutually induced velocity field of the rotor wake is the most expensive step. The number of Biot–Savart calculations required per timestep in a free-vortex wake simulation is given by

$$\mathrm{N_{BS}} = (N_b N_\zeta)^2 \tag{4.1}$$

It is obvious that the Biot–Savart computation for the free-vortex wake structure is an $O(N^2)$ operation. The computational efficiency of the free-vortex method can be enhanced greatly by reducing the number of Biot–Savart computations, while still retaining the overall accuracy of the method.

Among the existing techniques for optimizing Biot–Savart computations, the velocity field interpolation technique (Ref. 126), and fast multipole methods (Ref. 79) offer great promise in reducing computational costs. While fast multipole concepts can reduce the computational costs from $O(N^2)$ to $O(N)$, its application to vortex filaments is not entirely clear. Therefore, the present method uses the velocity field

interpolation technique (Ref. 126) to keep computational costs down to an acceptable level. In this technique, the positions of all collocation points in the wake are still determined by applying the principles vorticity transport, however, the self and the mutually induced velocities are only calculated at the free collocation points; linear interpolation of the induced velocity field is used at the pseudo-free points. Interpolation of the velocity field is equivalent to interpolation based on the first-order derivatives of the vortex filament positions and, therefore, results in a higher order solution accuracy.

## 4.2 Idealized Maneuvers

Idealized maneuvers are a mathematical abstraction where only the primary response of the wake aerodynamics to any one of the control inputs is studied. These maneuvers might not be realizable in actual piloted flight because the cross-coupling effects will introduce additional forces and moments that need to be balanced using appropriate control inputs for controlled flight along the desired trajectory. For example, consider the helicopter's response to a pure collective pitch input. Increasing the collective pitch will increase the thrust generated by the rotor and, therefore, the helicopter will ascend vertically and/or accelerate into forward flight, depending also on the disk tilt angle. However, the increase in the rotor thrust is also accompanied by an increase in the rotor torque, and the tail rotor must generate a higher thrust to balance the rotor torque, i.e., the pilot must also apply appropriate pedal inputs to achieve enough anti-torque moment.

The situation becomes even more complicated when there is an asymmetry in the flow field across the rotor disk, such as during forward flight. The time-varying

incident and inflow velocities cause a cyclic blade flapping response, which must be further offset using appropriate cyclic pitch inputs. While it is essential to study the maneuvering wake aerodynamics as the sum of responses to all the control inputs necessary for a controlled flight, it might not be possible to analyze in detail the wake dynamics associated with different control pitch inputs. Therefore, it is beneficial to study idealized, albeit abstract mathematical maneuvers to isolate the effects of individual control pitch inputs and to analyze them in detail. This will help in gaining a better understanding of additional complexities introduced when simulations of free-flight maneuvers are performed.

The UH-60 rotor geometry was used as a baseline in the computations. The rotor radius was 8.177 m and the rotational tip speed was 220.9 m/s. All calculations were carried out for a helicopter weight coefficient of $C_W = 0.00575$, unless mentioned otherwise. The wake computations were carried out using relatively fine spatial and temporal resolutions. While this imposes a significant penalty on the computational overhead, the wake geometry and airloads time-histories at such resolutions are necessary for the computation of aeroacoustics associated with BVI (see Section 4.1 and Ref. 9). The discretizations used in the present simulation were $\Delta\psi = 2.5^\circ$ and $\Delta\zeta = 5.0^\circ$. The velocity field interpolation technique (Ref. 126) was used to compute velocity fields at intermediate $\zeta$ locations when using unequal discretizations.

### 4.2.1 Popup & Popdown Maneuvers

In a popup maneuver, a military pilot performs a near vertical ascent to look over terrain or tree tops by quickly pulling up on the collective pitch. In the present simulation, a positive collective pitch input was applied in the form of a half-doublet over a period of approximately five rotor revolutions, as shown in Fig. 4.2. The time-

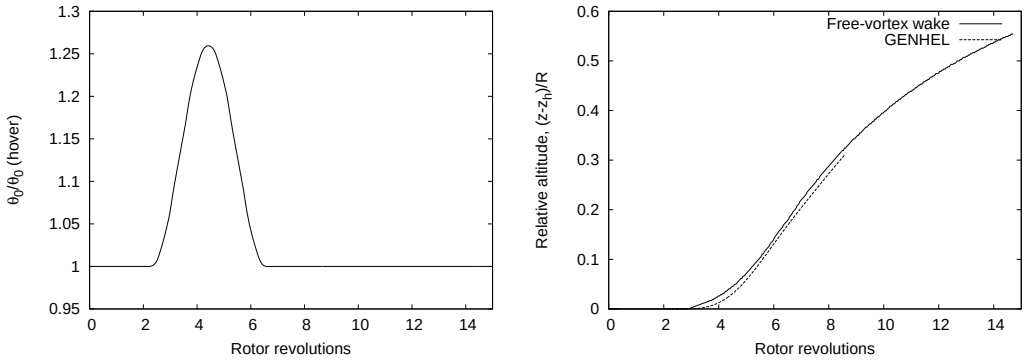


(a) Collective pitch

(b) Change in altitude

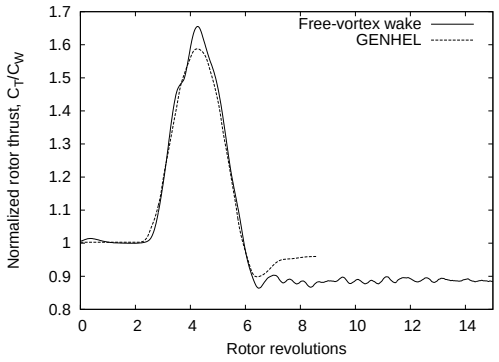


(c) Normalized rotor thrust

Figure 4.2: Collective pitch perturbation, change in the vertical position and the time-history of the rotor thrust during a popup manueuver: (a) Collective pitch relative to hover value, (b) altitude, (c) normalized rotor thrust coefficient.

histories of the rotor control inputs and the free stream conditions were obtained by simulating the popup maneuver using the GENHEL model (Ref. 32). These control time-histories were then prescribed as inputs to the free-vortex based rotor aerodynamics simulation.

Figures 4.2(b) and (c) show the time-histories of the altitude and the thrust ratio of the rotor. In an axial flight condition the rate of climb produced depends not only on excess rotor thrust, but also on the vertical drag of the fuselage caused by the

rotor downwash and the additional climb velocity. The effects of fuselage drag was accounted by using an equivalent flat plate area (Ref. 1).

$$D_v = \frac{1}{2}\rho V_z^2 f_v \tag{4.2}$$

In the present study an equivalent flat plate area, $f_v = 30$ ft$^2$ was used in the simulations. The expression for the vertical acceleration of the helicopter as a system can then be written as

$$a_z = \frac{T - D_V}{W} \tag{4.3}$$

where $\mathbf{a} = a_z\mathbf{k}$ is the acceleration at any given time instant, and $V_z$ was evaluated in this case as the sum of the average induced velocity in the rotor wake below the rotor. The drag on the fuselage causes a decrease in the rate of climb (albeit a slow one) after the controls are restored to their initial state. This is evident from the time-history of altitude, see Fig. 4.2(b).

For the popup maneuver, the results obtained from the free-vortex wake simulations were compared with those obtained from the GENHEL simulations. Notice that both the GENHEL results and the free-vortex wake method are in good agreement in terms of the overall behavior of the rotor thrust and also the climb response (altitude). The differences in the rotor thrust during the maneuver arise from the differences in modeling of the wake induced effects between the two methods. Notice that the rotor thrust at the end of the free-vortex wake simulation does not return to its original state. This is because the rotor controls in the vortex wake simulation were adjusted to the values prescribed by GENHEL and, therefore, the trim conditions are not the same before and after the maneuver.

The predicted wake dynamics during the popup maneuver are shown in Fig. 4.3, which are snapshots of the side view of the wake geometry at various instances in time.

Notice that the wake evolution is characterized by the bundling of tip vortices into a toroidal vortical ring type structure below the rotor disk. The bundled ring structure is similar to the characteristic wake response to abrupt control pitch inputs that were observed experimentally by Carpenter & Friedovich (Ref. 22) — see Section 3.1.1.

As the collective pitch is increased a concentration of tip vortices first occurs immediately below the rotor disk. The vortex bundle is then convected downstream rapidly below the rotor as a wave — see Figs. 4.3(b) and (c). As the collective pitch is brought back to its initial state another bundling in the wake occurs. This time a vortical ring is formed further downstream below the rotor — see Fig. 4.3(d). This is because a decrease in collective pitch reduces the rotor thrust and the wake circulation is reduced near the rotor plane. This situation is less conducive to the bundling of wake vorticity. A rarefaction wave in this case originates at the rotor plane. The more tightly packed tip vortices further downstream (which originated when the rotor was operating at a higher thrust) now bundle in the far wake. This ring is convected downstream rapidly below the rotor and normal conditions are only established approximately seven rotor revolutions after the control settings are brought back to their initial state.

While this maneuver is relatively simple from a piloting perspective, the results show the rich physics of the wake structure under these conditions, the behavior of which is certainly not intuitive.

The popdown maneuver is essentially the opposite of a popup maneuver. Here the pilot decreases the collective pitch in a hovering flight condition and performs a near vertical descent to quickly reach a lower altitude. This can be done at various rates, although because this maneuver is usually performed near the ground, the descent rates are relatively mild. However, in this case the rotor descends into its own wake.

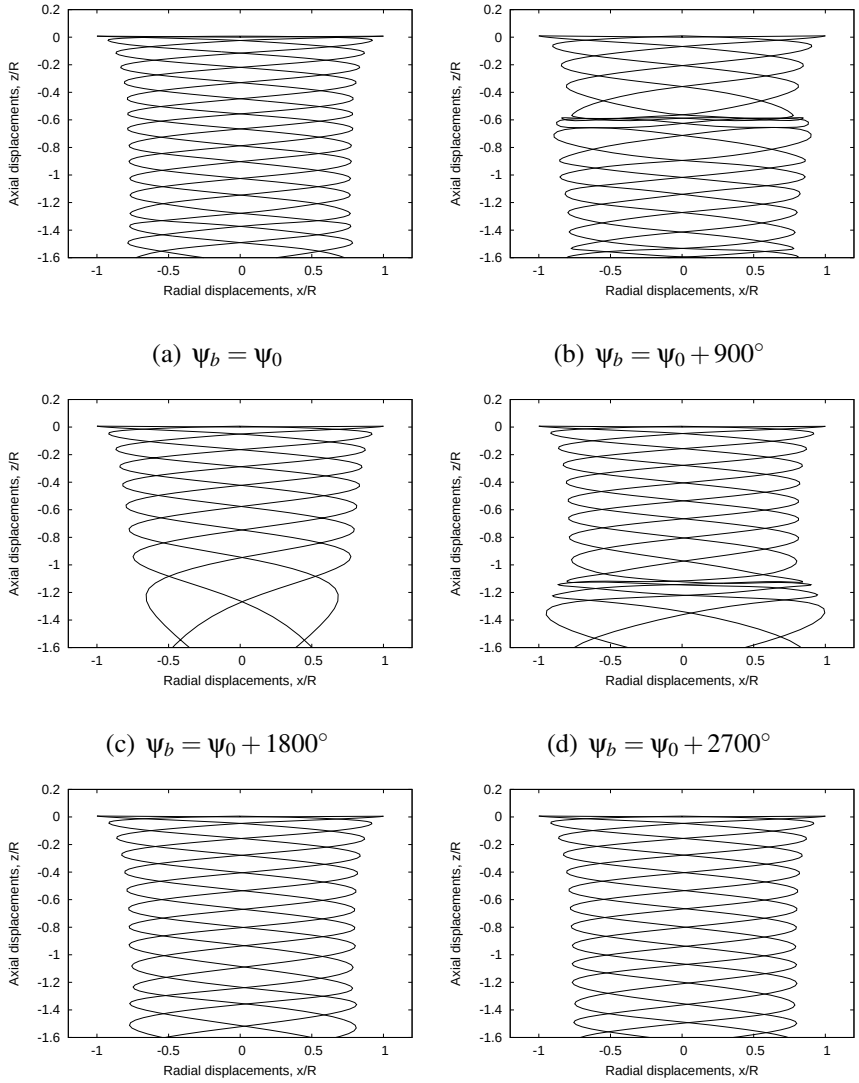


(a) $\psi_b = \psi_0$

(b) $\psi_b = \psi_0 + 900^\circ$

(c) $\psi_b = \psi_0 + 1800^\circ$

(d) $\psi_b = \psi_0 + 2700^\circ$

(e) $\psi_b = \psi_0 + 3600^\circ$

(f) $\psi_b = \psi_0 + 4500^\circ$

Figure 4.3: Side views of the wake geometry during a popup maneuver at various instances in time: (a) Steady hovering flight, (b) maximum collective pitch, (c) collective pitch restored to the initial value, (d) 7.5 rotor revolutions after the maneuver, (e) 10 rotor revolutions after initiating the maneuver, and (f) wake returns to the hovering state.

In the present simulation, a negative collective pitch was applied in form of a half-doublet over a period of approximately five rotor revolutions, as shown in Fig. 4.4(a). As in the popup maneuver simulation the collective pitch was prescribed as an input to the free-vortex based rotor wake simulation.

Figures 4.4(b) and (c) show the variations of the altitude and the rotor thrust ratio over time. Again the predictions from the GENHEL simulation and the free-vortex model show similar overall results for the rotor thrust and sink rate, but there were slight differences in the rotor thrust time-history. These differences, as in the case of a popup maneuver, can be attributed mostly to the effects of the rotor wake dynamics and to how the nonlinear wake dynamics affect the inflow through the rotor disk.

Figure 4.5 shows snapshots of the side views of the rotor wake geometry for this case. In this maneuver the rotor descends and begins to encounter its own self generated wake — see Fig. 4.5(b). Again a change in the blade pitch control settings is accompanied by the formation of a characteristic vortical ring structure in the rotor wake. However, unlike in the popup case, the vortical ring first forms downstream away from the rotor plane. This behavior is consistent with the latter part of the popup maneuver where the collective pitch is lowered from its maximum value.

The descent rates in the present simulation are not very high relative to the induced velocity through the rotor and, therefore, the net vertical velocities are still high enough to convect away any wake disturbances downstream away from the rotor TPP. As the collective pitch is restored to its nominal operating condition, however, there is evidence of strong bundling of the tip vortices near the rotor plane — see Fig. 4.5(c). This ring again propagates downward through the rotor wake causing a second saddle in the rotor thrust time-history. The effects of this phenomenon are not present in GENHEL simulation and can be attributed to the inability of the lower fi-

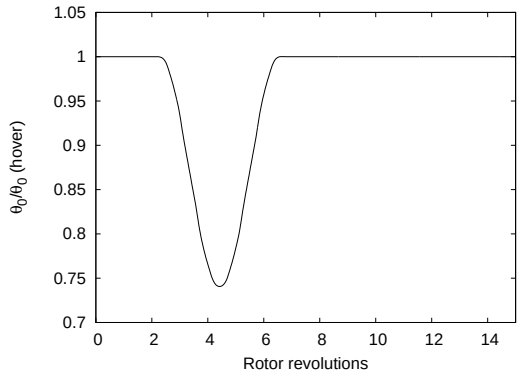


(a) Collective pitch

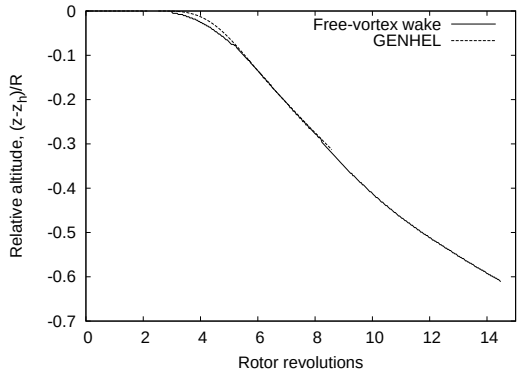


(b) Change in altitude

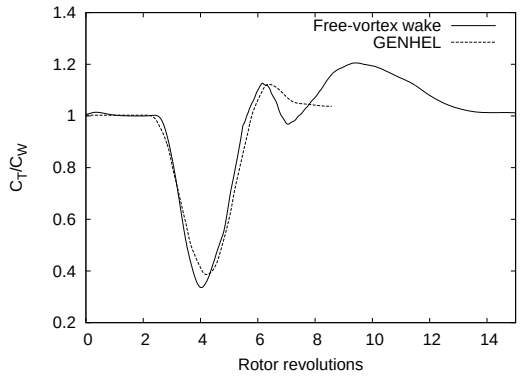


(c) Normalized rotor thrust

Figure 4.4: Collective pitch perturbation, change in the vertical position and the time-history of the rotor thrust during a popdown manueuver: (a) Collective pitch relative to hover value, (b) altitude, (c) normalized rotor thrust coefficient.

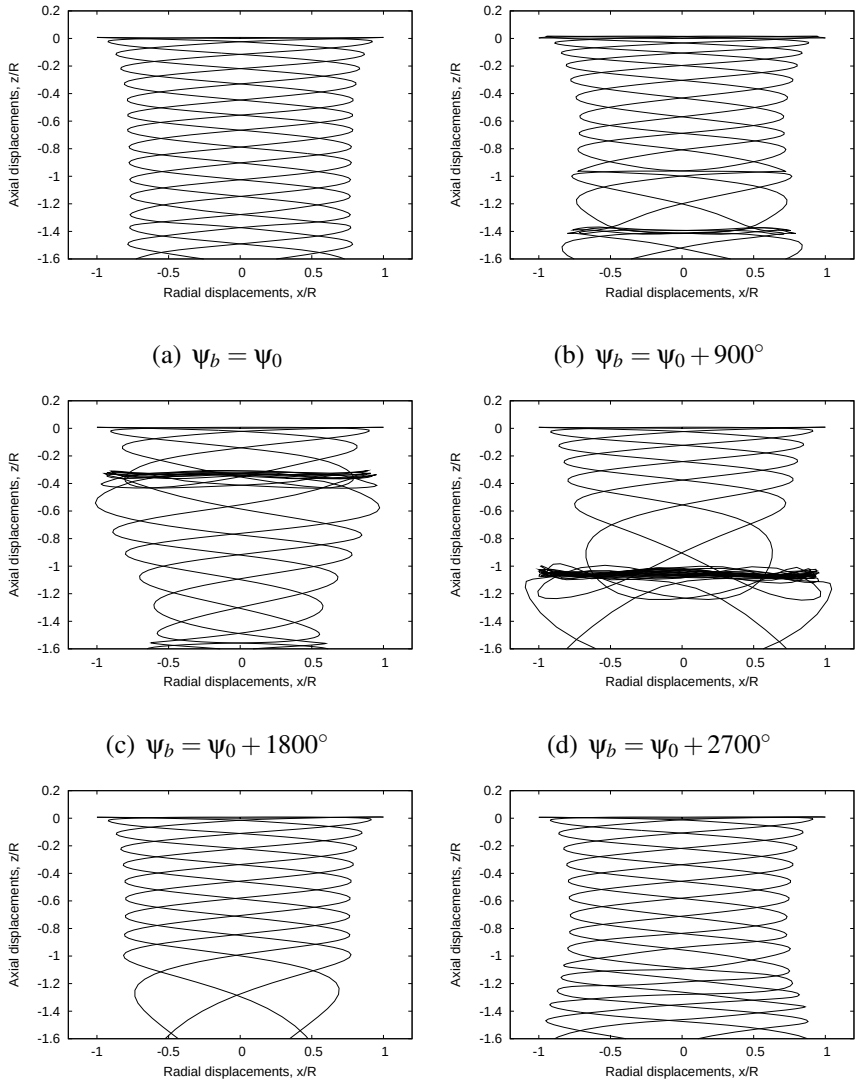


(a) $\psi_b = \psi_0$

(b) $\psi_b = \psi_0 + 900^\circ$

(c) $\psi_b = \psi_0 + 1800^\circ$

(d) $\psi_b = \psi_0 + 2700^\circ$

(e) $\psi_b = \psi_0 + 3600^\circ$

(f) $\psi_b = \psi_0 + 4500^\circ$

Figure 4.5: Side views of the wake geometry during a popdown maneuver at various instances in time: (a) Steady hovering flight, (b) minimum collective pitch, (c) collective pitch restored to the initial value, (d) 7.5 rotor revolutions after the maneuver, (e) 10 rotor revolutions after initiating the maneuver, and (f) wake returns to the hovering state.

delity dynamic inflow model to suitably model such highly nonlinear wake dynamics.

It is evident that in the present simulation the descent rates were mild and were insufficient to convect the accumulated vortex bundle up and through the rotor TPP; this would produce a condition resembling the vortex ring state. However, for larger control input perturbations and larger descent rates, vortex ring state conditions are more likely to be encountered in response to control inputs, a problem that has been previously considered using vortex theory in Ref. 87.

From the pilot's point of view, the popup and the popdown maneuvers are relatively simple flight maneuvers to perform, but aerodynamically these maneuvers clearly demonstrate the rich details of wake dynamics and also the sensitivity of wake dynamics to perturbations in blade pitch inputs. The formation of a toroidal ring in the rotor wake, its propagation and its influence on the rotor airloads is non-intuitive. Neither the popup or the popdown cases are acoustically significant because the interactions between the blades and their tip vortices are nearly perpendicular (Ref. 9).

### 4.2.2 Port and Starboard Roll Maneuvers

In a roll maneuver the pilot banks the helicopter in one direction by applying appropriate cyclic control inputs and maintains altitude by using collective pitch. Such situations occur in practice when the helicopter enters into a coordinated turn from a steady forward flight condition, or while circling tightly to approach a landing zone.

The roll maneuvers were initiated from a nominally steady descending flight condition at an advance ratio $\mu = 0.186$ and a descent flight path angle $\gamma = -6^{\circ}$. The steady, descending flight condition was used as the baseline for all the idealized flight maneuvers. Figure 4.6 shows the rear view of the wake geometry, the non-dimensional lift distribution over the rotor disk and the principal acoustic directivity

patterns for this steady flight condition. Notice how the flight path angle brings the tip vortices close to the TPP. The wake roll up on the advancing side is found to be above the TPP. The strong interactions between the wake vortices and the rotor blades manifest as steep gradients in the lift on the retreating side of the rotor disk — see Fig. 4.6(b). The noise directivity is more focused in the second quadrant, however, the noise is generally omnidirectional for this flight condition, as shown in Fig. 4.6(c).

The desired roll rates and angles for the maneuvers were obtained using a linear, single degree of freedom model of roll dynamics, analogous to the equation for pitch dynamics described in Ref. 127. The governing equation for roll dynamics (with the usual simplifications) can be written as

$$\dot{p} + L_p p = L_{\delta_{\text{lat}}} \delta_{\text{lat}} \tag{4.4}$$

The solution to Eq. (4.4) for a step input of lateral cyclic is given by the following expressions

$$p = -\frac{L_{\delta_{\text{lat}}}}{L_p} \delta_{\text{lat}} \left(1 - \exp(L_p t)\right) \tag{4.5}$$

$$\phi = \int_0^t p\,dt = -\frac{L_{\delta_{\text{lat}}}}{L_p} \delta_{\text{lat}} \left[t + \frac{1}{L_p}\left(1 - \exp(L_p t)\right)\right] \tag{4.6}$$

For the present simulation only representative trajectories were required. It is therefore not necessary to know the exact values of the control and stability derivatives (Ref. 127). The desired trajectory can then be simulated by setting parameters such as the desired maximum roll rate or the maximum bank angle. The control inputs for the maneuvers were generated by imposing a rectangular step input for a given duration. In this case the asymptotic value of Eq. (4.5) is given by

$$\Delta\phi = -\frac{L_{\delta_{\text{lat}}}}{L_p} \delta_{\text{lat}} \Delta t \tag{4.7}$$

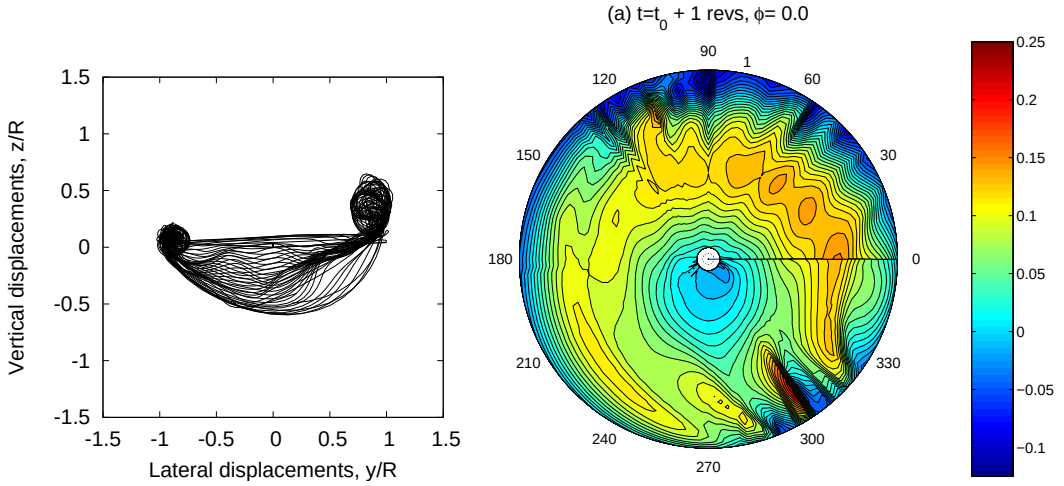


(a) Wake geometry – rear view




(b) Lift distribution

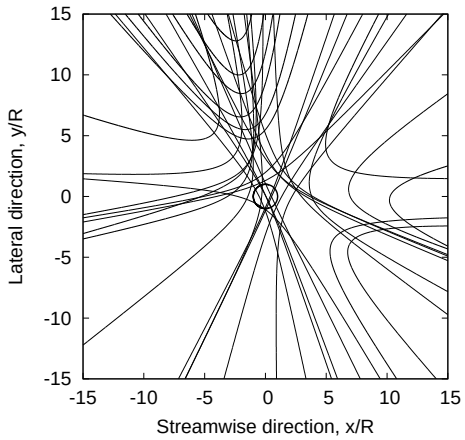


(c) Principal acoustic directivity patterns

Figure 4.6: Rear view of the wake geometry, the non-dimensional lift distribution and the principal acoustic directivity patterns for a representative, four-bladed rotor in steady descending forward flight condition. $C_W = 0.00575$, $\mu = 0.186$, $\gamma = -6^\circ$.

In the following calculations, the maximum roll rate was set to $p = 45°/s$ and the maximum bank angle was restricted to $\phi = 60°$ (a 2g turn). The only other unknown is the time period over which the maneuver is performed. Based on flight test data (Ref. 128) the time periods for typical banking maneuvers for UH-60 was determined to be approximately ten rotor revolutions. The vehicle orientation during the maneuver can then be determined using Eq. (4.4).

Figure 4.7 shows the time-histories of the roll rate $p$ and the corresponding bank angle $\phi$ used to simulate the starboard and port roll maneuvers. The rotor was also continuously trimmed to a higher thrust using collective pitch inputs which is required to satisfy vertical force equilibrium during the banking maneuver.

Figure 4.8 shows the rear views of the wake snapshots for a rotor executing a starboard roll maneuver at different instants in time. The roll towards the starboard side delays the roll up of the wake vortices along the retreating side of the rotor disk. Notice that the final wake geometry, with maximum bank angle orientation, is considerably different from that observed in steady, descending flight condition — see Fig. 4.6(a). However, the maneuver brings the blade tip vortices closer to the rotor TPP in the first quadrant, thereby enhancing the potential of BVIs here. This is also apparent in the rotor lift distribution at the end of the roll maneuver, as shown in Fig. 4.9. Notice the high impulsive loads on the rear advancing side (see Fig. 4.9(f)) which is again caused by the increased numbers of BVIs.

Figure 4.10 shows the snapshots of the rear views of the wake geometries for a rotor executing roll to port. The behavior is similar to that observed during the starboard roll, except that now the wake passes up more through the retreating side of the rotor disk. This maneuver also causes a lag in the roll up of the wake on the advancing side of the rotor disk.

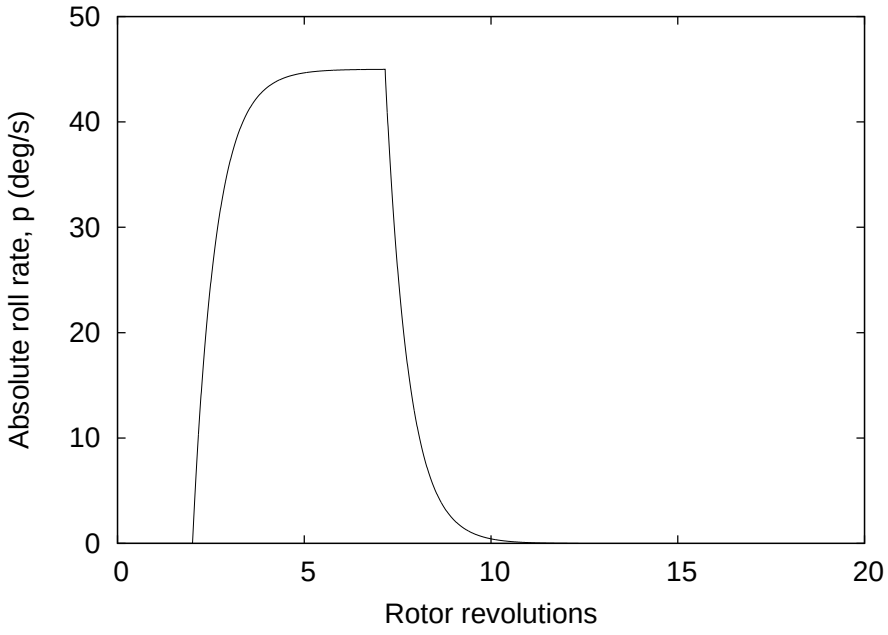


(a) Roll rate, $p$

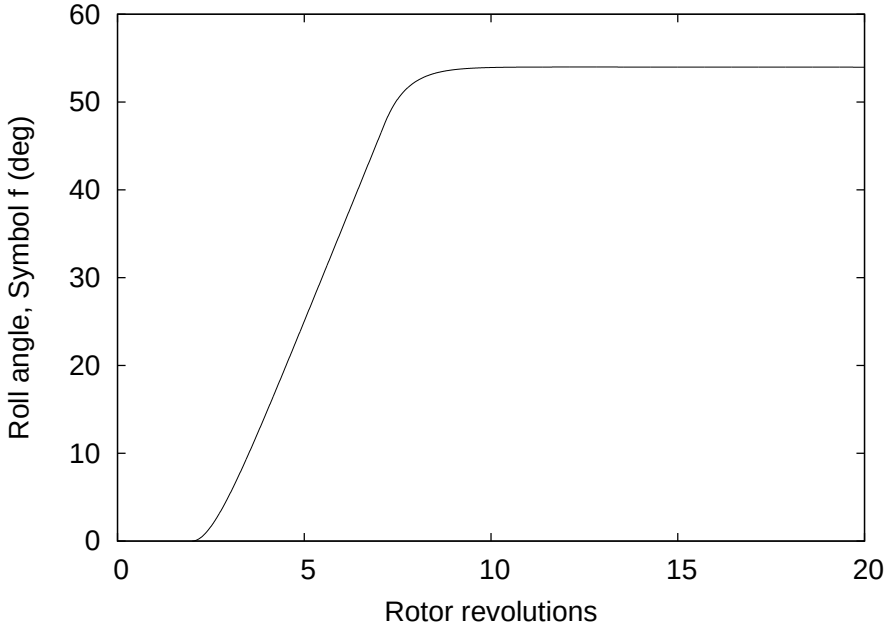


(b) Roll angle, $\phi$

Figure 4.7: Time-histories of the absolute roll rate $p$ and the corresponding bank angle $\phi$ used to simulate the idealized roll maneuver: (a) Roll rate, (b) roll angle.

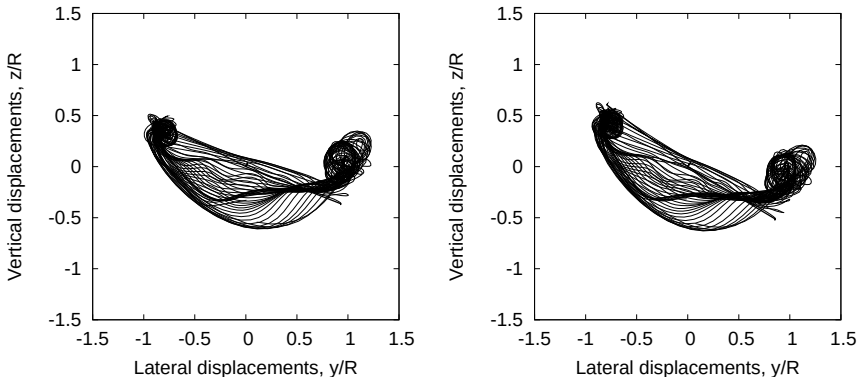


(a) $t = t_0$+5 revs, $\phi = 25^\circ$




(b) $t = t_0$+6 revs, $\phi = 35^\circ$

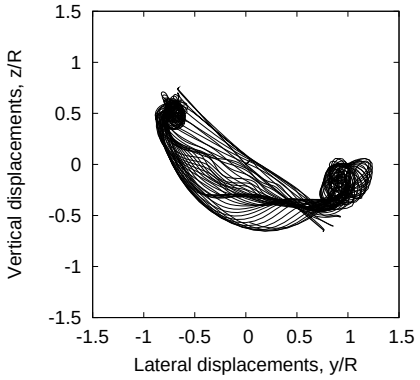


(c) $t = t_0$+7 revs, $\phi = 45^\circ$

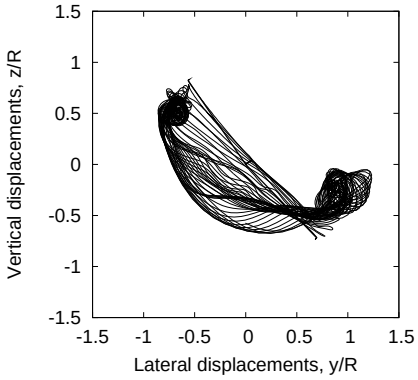


(d) $t = t_0$+8 revs, $\phi = 50^\circ$

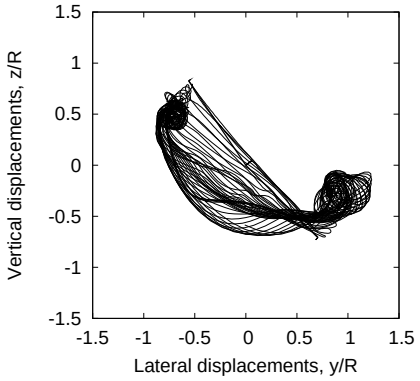


(e) $t = t_0$+9 revs, $\phi = 52^\circ$

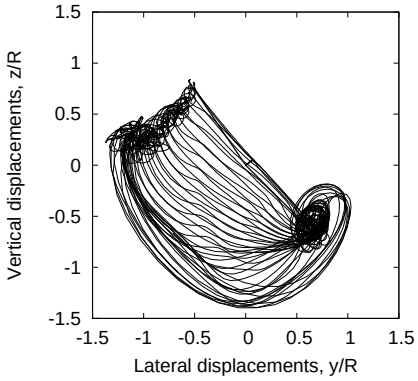


(f) $t = t_0$+20 revs, $\phi = 55^\circ$

Figure 4.8: Snapshots of the rear view of the wake geometry for a representative, four-bladed rotor excecuting a starboard roll at various instances in time.

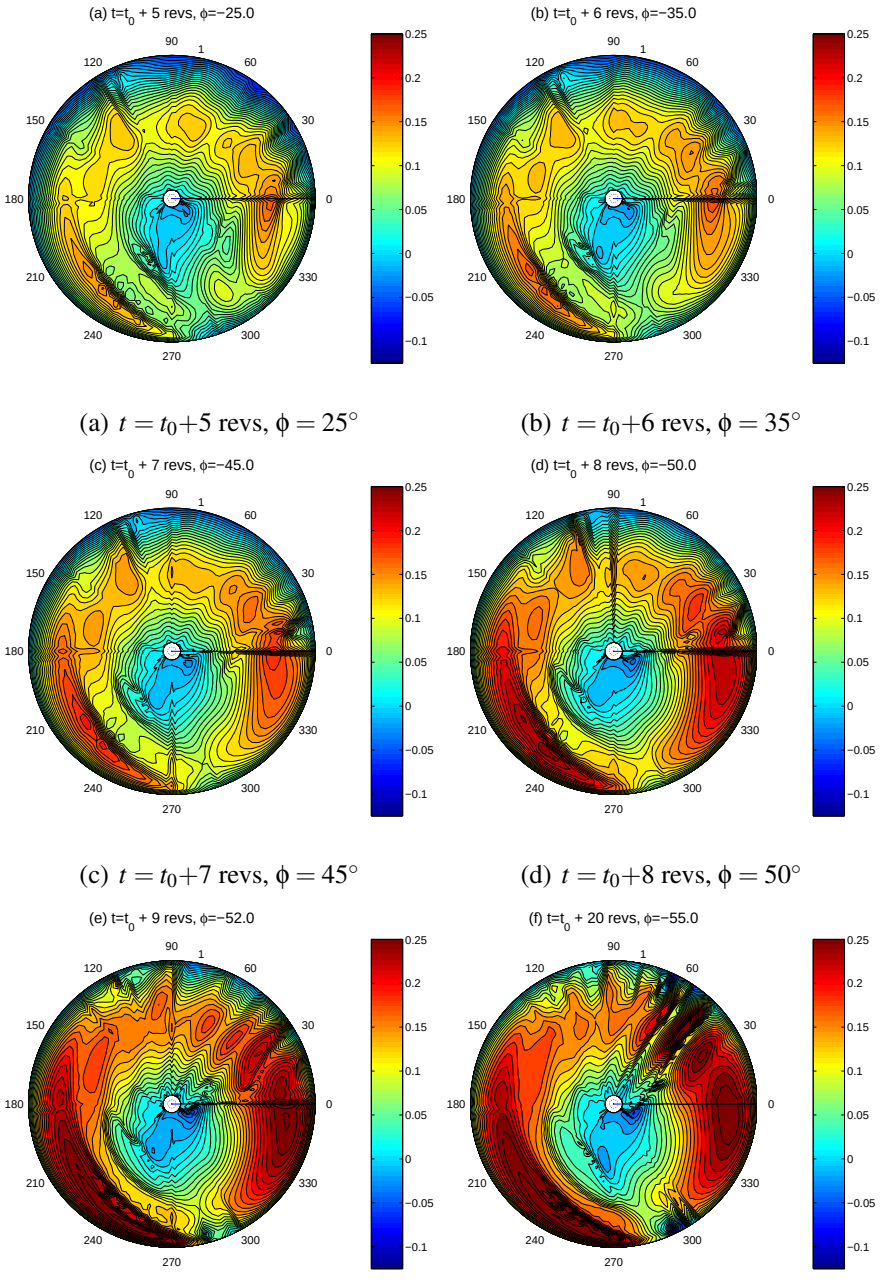


(a) $t = t_0$+5 revs, $\phi = 25°$

(b) $t = t_0$+6 revs, $\phi = 35°$

(c) $t = t_0$+7 revs, $\phi = 45°$

(d) $t = t_0$+8 revs, $\phi = 50°$

(e) $t = t_0$+9 revs, $\phi = 52°$

(f) $t = t_0$+20 revs, $\phi = 55°$

Figure 4.9: Contours of the non-dimensional lift distribution $C_l M^2$ for a representative, four-bladed rotor excecuting a starboard roll at various instances in time.

Figure 4.11 shows the contours of the non-dimensional lift distribution across the rotor during this maneuver. In this case, however, the rolled-up bundle of tip vortices on the advancing side moves down through the rotor disk. This interaction is responsible for the steep gradients in the lift distribution on the advancing side during the maneuver (see Figs. 4.11(b)–(e)). When the rotor reaches the maximum bank angle it is observed that the BVIs on the retreating side intensify, as shown in Fig. 4.11(f).

The rotor lift distribution for both starboard roll and the port roll (Figs. 4.9 and 4.11) cases were found to be considerably different from each other. The magnitudes of lift are higher during the maneuver because the rotor is operating at a higher thrust. However, the more interesting aspect is the distribution of the lift and BVI locations over the rotor disk. During the starboard roll maneuver the lift distribution is biased toward the retreating side. The opposite is true in the case of the port roll maneuver. Overall there is evidence of high impulsive blade loads during the roll maneuvers resulting from enhanced numbers and intensities of BVI, which can also have a significant impact on the intensity of rotor noise.

Figures 4.12 and 4.13 show snapshots of the acoustic directivity patterns at various instances in time for a rotor executing starboard and port roll maneuvers, respectively. The directivity patterns are clearly sensitive to the sign of the roll maneuver. This is not surprising because the wake dynamics is particularly sensitive to the manuever state — see Figs. 4.8 and 4.10. As the rotor enters the roll maneuver from a steady flight condition, the noise radiation pattern is omnidirectional. However, as the rotor progresses through the maneuver the noise radiation pattern starts to focus more strongly in a particular direction, the actual direction depending on whether a starboard or a port roll is performed. The primary focusing of the wave fronts occurs in the second and fourth quadrants during the port roll, while in case of a starboard roll

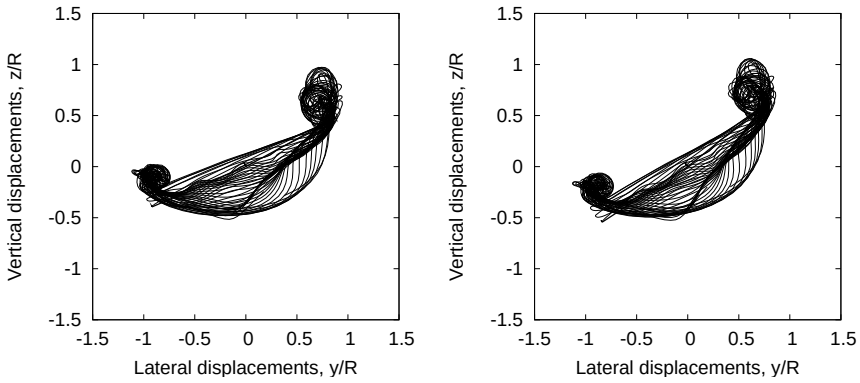


(a) $t = t_0$+5 revs, $\phi = -25^\circ$ (b) $t = t_0$+6 revs, $\phi = -35^\circ$

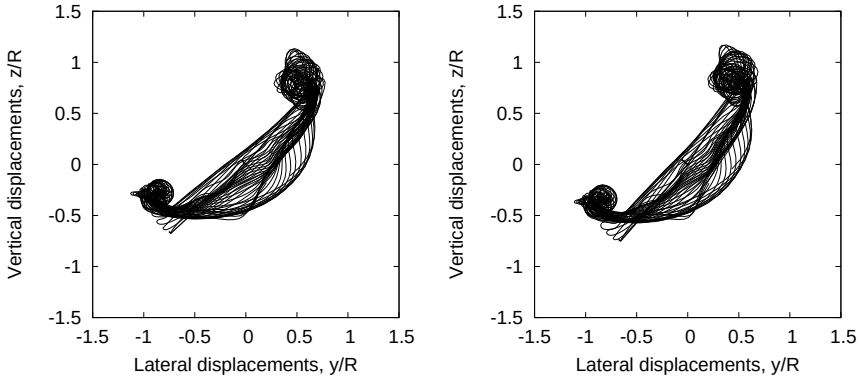


(c) $t = t_0$+7 revs, $\phi = -45^\circ$ (d) $t = t_0$+8 revs, $\phi = -50^\circ$

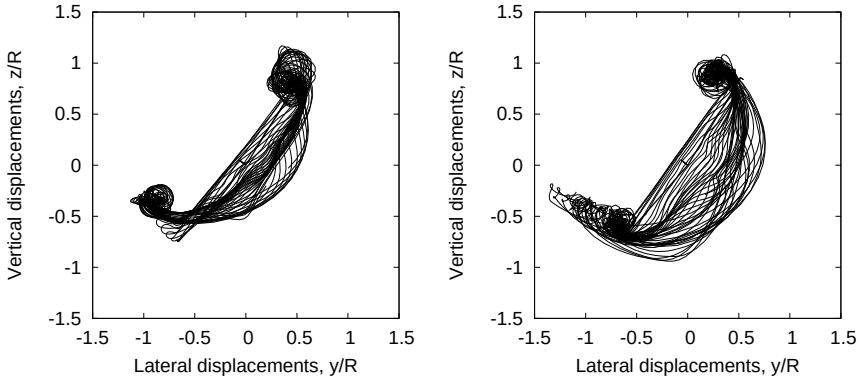


(e) $t = t_0$+9 revs, $\phi = -52^\circ$ (f) $t = t_0$+20 revs, $\phi = -55^\circ$

Figure 4.10: Snapshots of the rear view of the wake geometry for a representative, four-bladed rotor excecuting a port roll at various instances in time.

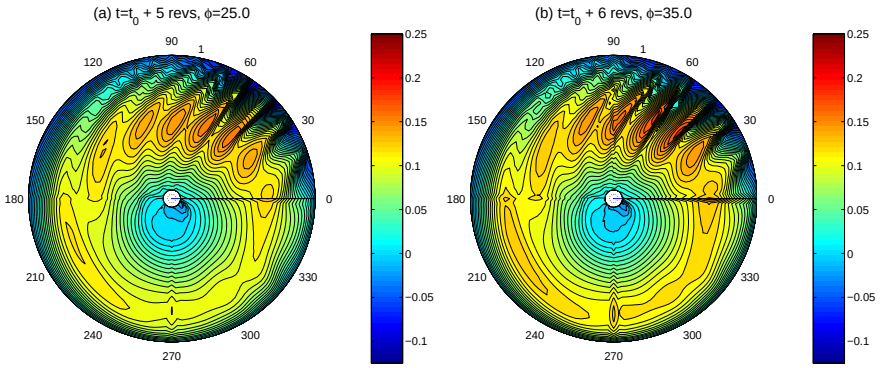


(a) $t = t_0 + 5$ revs, $\phi = -25°$ (b) $t = t_0 + 6$ revs, $\phi = -35°$

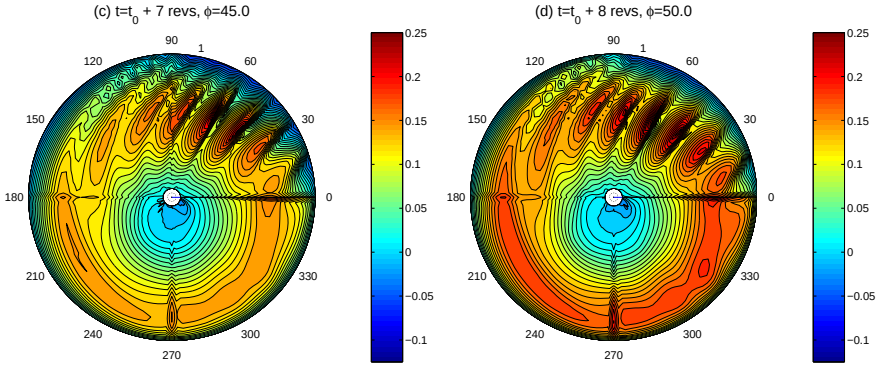


(c) $t = t_0 + 7$ revs, $\phi = -45°$ (d) $t = t_0 + 8$ revs, $\phi = -50°$

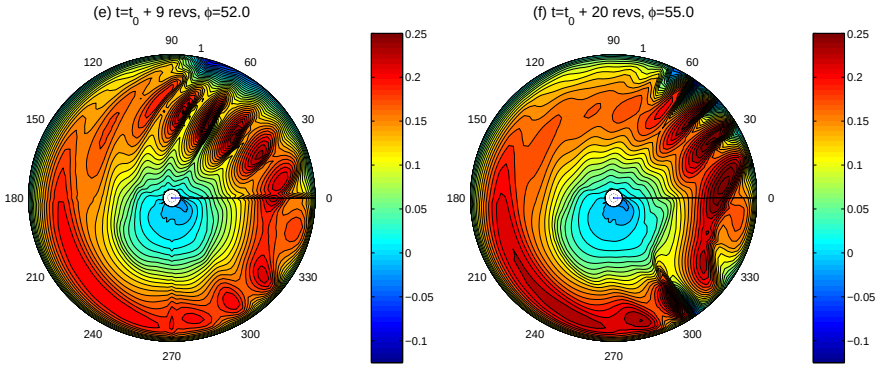


(e) $t = t_0 + 9$ revs, $\phi = -52°$ (f) $t = t_0 + 20$ revs, $\phi = -55°$

Figure 4.11: Contours of the non-dimensional lift distribution $C_l M^2$ for a representative, four-bladed rotor excecuting a port roll at various instances in time.

they occur in the first and second quadrants. Based on the changes in the intensity of the lift distribution, differences in the intensity of the noise generated can also be expected in these flight conditions.

Observe the sequence of the directivity patterns over rotor revolutions 8 to 20 — see Figs. 4.12(d) through (f) and Figs. 4.13(d) through (f). The change in the bank angle of the rotor is almost negligible. However, the acoustic radiation patterns still show considerable changes over time. This can be attributed almost entirely to the temporal lag in the wake dynamics; the wake is still adapting to the change in rotor position (bank angle and roll rates) over the first eight rotor revolutions. The differences in the directivity patterns after the ninth rotor revolution indicates that there has been further reorganization of the wake structure during this time interval.

Finally, Fig. 4.14 shows the time-histories of the power predictions for the starboard and port roll maneuvers predicted by the free-vortex wake methodology. As expected, the power requirements increase as the rotor banks sideways mainly because the rotor is generating a higher thrust. Notice that the power increase during the roll to port has a greater time lag when compared to the roll to starboard. However, the final power requirement is higher when the rotor is banked to port, emphasizing the asymmetries in the wake geometries during starboard and port rolls.

As mentioned previously, the rotor was trimmed during the maneuver to achieve vertical force balance. During the trim process the cyclic flapping of the rotor blades was also eliminated and the so rotor TPP remained perpendicular to the rotor shaft, i.e., the rotor behaved as a solid disk and there was no lag in the blade flapping response. The absence of rotor flapping is the reason why the maximum lift occurs on the retreating side for a starboard roll and on the advancing side for a port roll. The discontinuities in the contours of lift distribution during the maneuvers is also an arti-

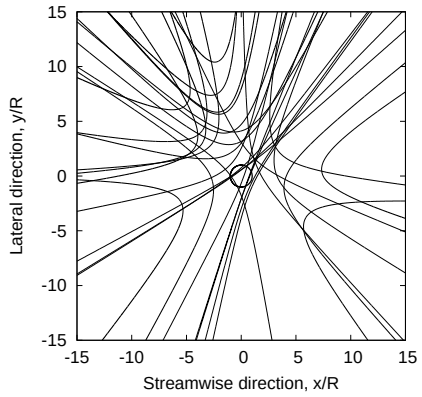


(a) $t = t_0$+5 revs, $\phi = 25^\circ$

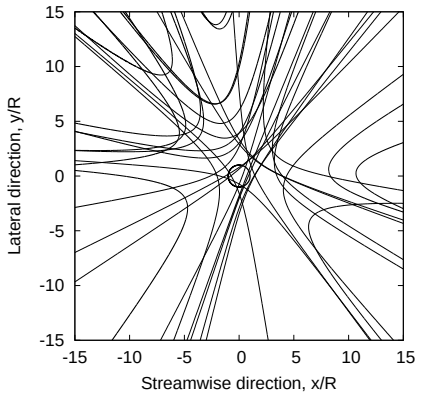


(b) $t = t_0$+6 revs, $\phi = 35^\circ$

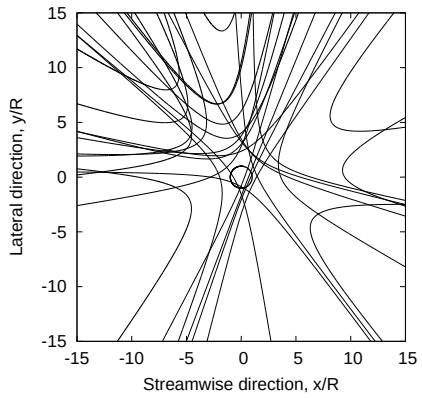


(c) $t = t_0$+7 revs, $\phi = 45^\circ$

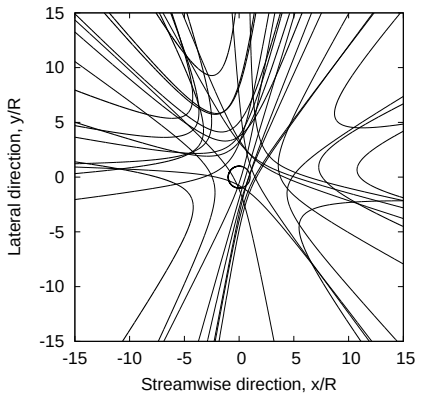


(d) $t = t_0$+8 revs, $\phi = 50^\circ$

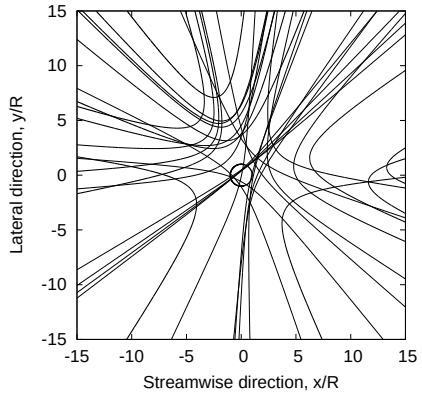


(e) $t = t_0$+9 revs, $\phi = 52^\circ$

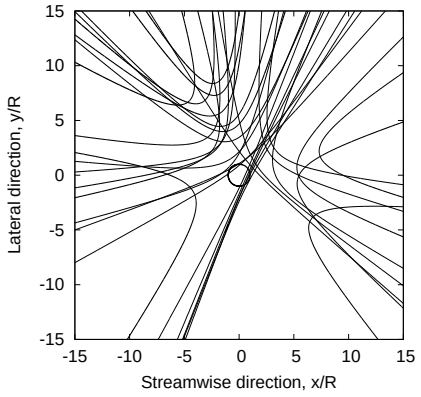


(f) $t = t_0$+20 revs, $\phi = 55^\circ$

Figure 4.12: Principal sound radiation directions for a representative, four-bladed rotor executing starboard roll at a plane $z = 3R$ below the rotor TPP.

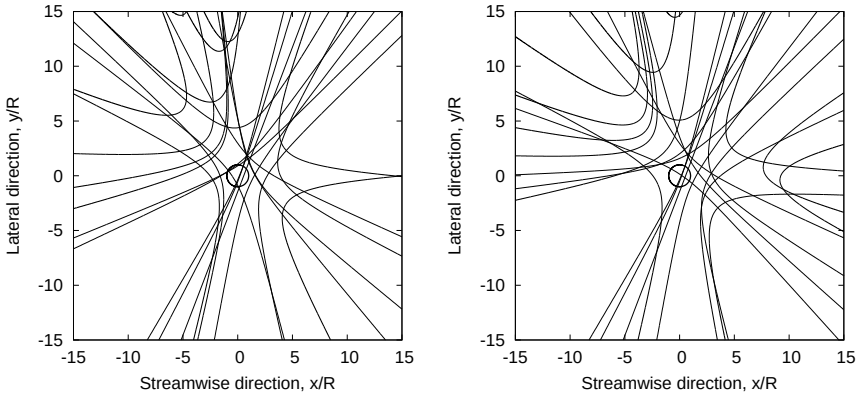


(a) $t = t_0$+5 revs, $\phi = -25^\circ$




(b) $t = t_0$+6 revs, $\phi = -35^\circ$

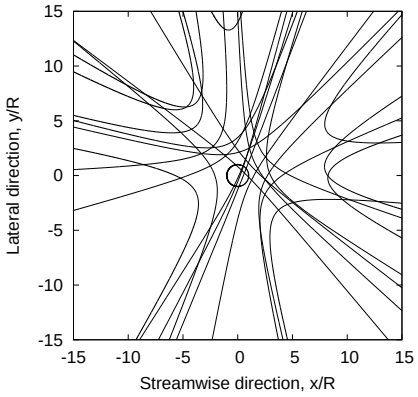


(c) $t = t_0$+7 revs, $\phi = -45^\circ$

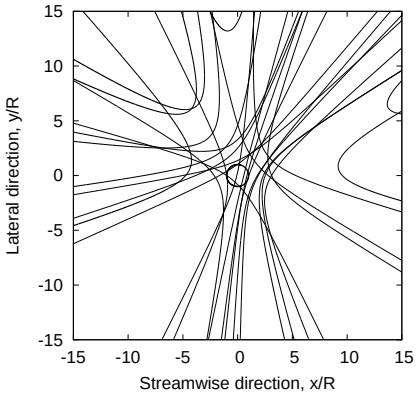


(d) $t = t_0$+8 revs, $\phi = -50^\circ$

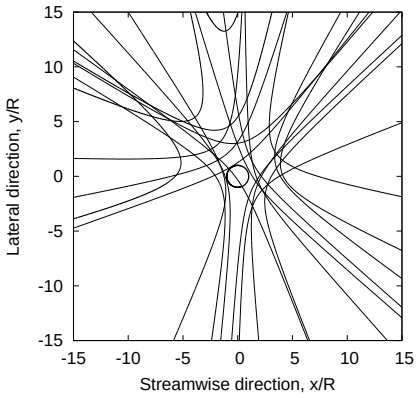


(e) $t = t_0$+9 revs, $\phi = -52^\circ$

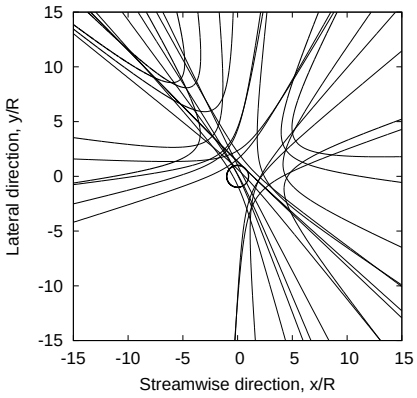


(f) $t = t_0$+20 revs, $\phi = -55^\circ$

Figure 4.13: Principal sound radiation directions for a representative, four-bladed rotor excecuting a port roll at various instances in time.

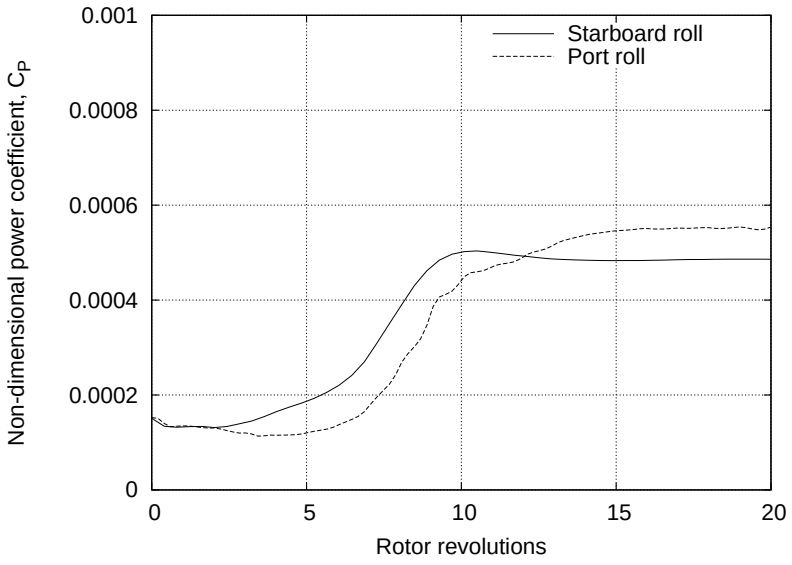


Figure 4.14: Time-history of the rotor power during the idealized starboard and port roll maneuvers.

fact of rotor trim. In the present simulation the rotor was trimmed every quarter of a revolution. The abrupt change in the collective pitch during trim is accompanied by a sudden change in the lift distribution and, therefore, trim procedure during a maneuver is not fully realistic. However, the study still provides valuable insight into the wake dynamics, especially the asymmetries in the wake evolution during the starboard and port roll.

### 4.2.3 Roll Reversal Maneuvers

Consider now a roll reversal maneuver where the helicopter banks to one side and then rolls to the other side at twice the rate, and then banks to its original flight condition. This simulation is representative of an evasive combat maneuver. In the present simulations, the roll reversal maneuver was performed in such a manner that the time taken for the roll reversal is same as the time taken for the helicopter to roll to the

maximum bank angle; this means that the roll rates during the roll reversal are twice that of the initial roll to one side.

The pilot control inputs were a series of rectangular step inputs with appropriate signs. Figure 4.15 shows the time histories of the roll rate $p$ and the corresponding bank angle $\phi$ used to simulate the roll reversal maneuver. During the maneuver the rotor was continuously trimmed to a higher thrust using collective inputs to maintain vertical force equilibrium.

It has already been shown how the wake reacts to the changes in the flight conditions with a relatively long aerodynamic lag. In this case, with the relatively quick reversal in the roll rate and roll angles, the wake does not have enough time to adjust to the more rapid changes taking place. It is clear from the simulations in this case that the rotor moves well into its self-generated wake, greatly enhancing the number of BVIs. Based on the previously described analysis of pure rolls to starboard and port, the wake response in the roll reversal can be expected to depend on the manner in which it is performed, i.e., whether a port-starboard-port (PSP) or a starboard-port-starboard (SPS) maneuver is performed. Therefore, both PSP and SPS maneuvers were simulated to better understand the rotor wake dynamics. The rotor orientation and rates were again input to the free-vortex wake method.

Figure 4.16 shows the snapshots of the rear view of the wake geometry for a rotor executing an SPS roll reversal. As the rotor banks toward starboard — see Figs. 4.16(a) and (b)) the wake response was found to be similar to that found during a starboard roll; the roll up on the advancing side was delayed, and the wake moves up through the rotor over the advancing side of the rotor disk.

Figure 4.16(b) shows the rotor wake geometry when the rotor attains the maximum starboard bank angle. At this point, the rotor starts rolling towards port. Here the

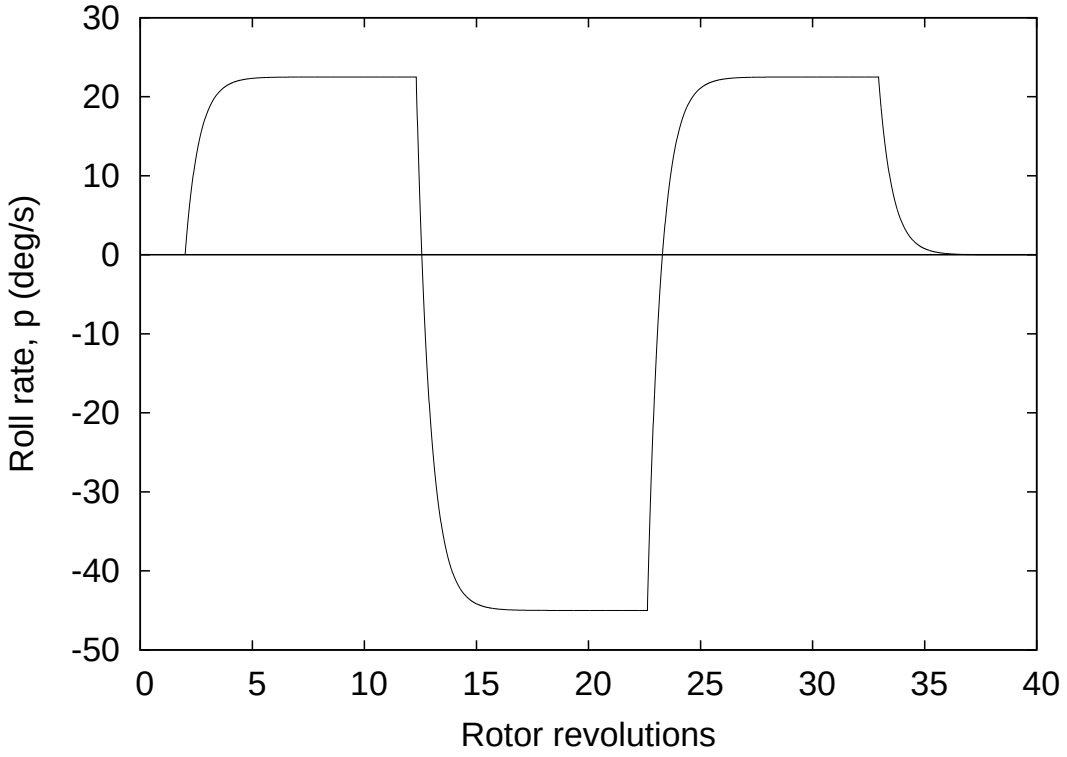


(a) Roll rate, $p$

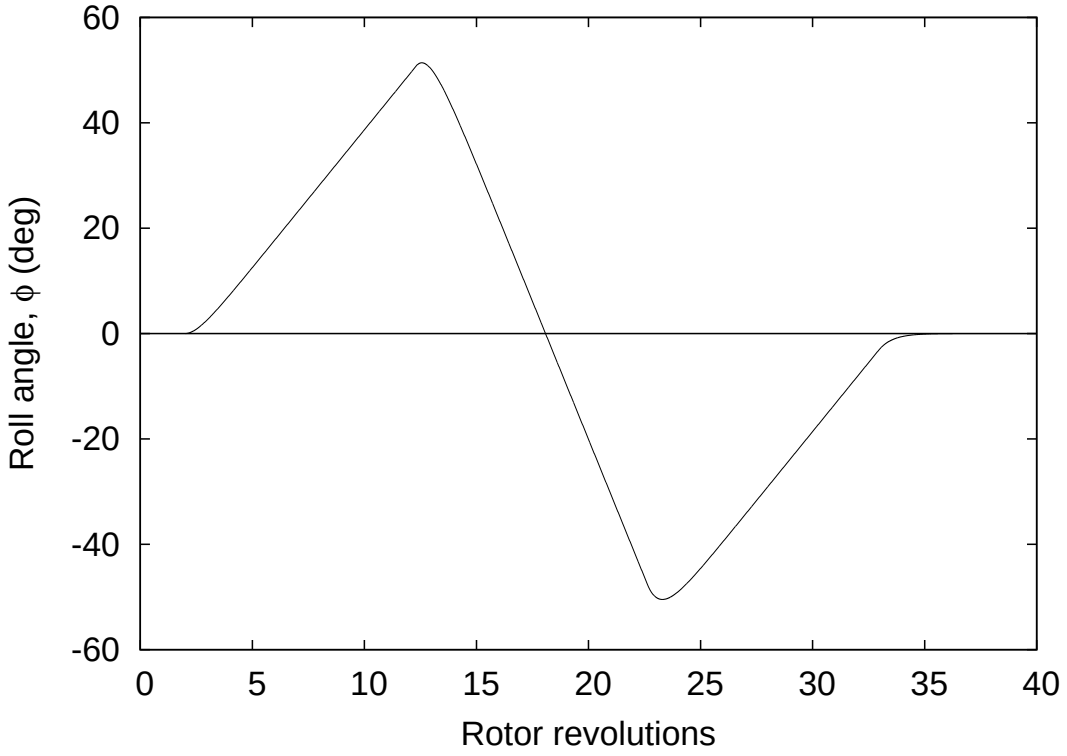


(b) Roll angle, $\phi$

Figure 4.15: Time-histories of the roll rate $p$ and the corresponding bank angle $\phi$ used to simulate the idealized roll reversal maneuver: (a) Roll rate, (b) roll angle.

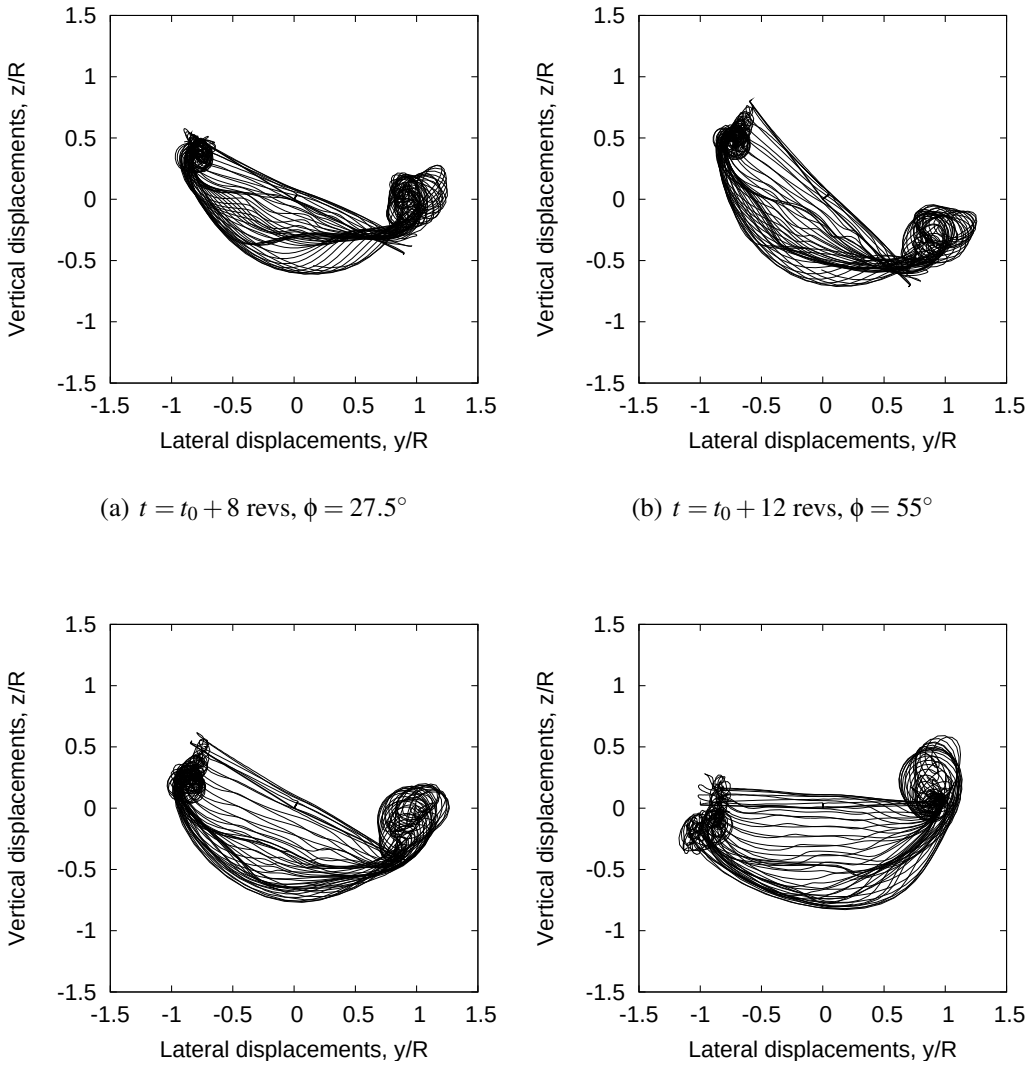


(a) $t = t_0 + 8$ revs, $\phi = 27.5^\circ$

(b) $t = t_0 + 12$ revs, $\phi = 55^\circ$

(c) $t = t_0 + 15$ revs, $\phi = 27.5^\circ$

(d) $t = t_0 + 18$ revs, $\phi = 0^\circ$

Figure 4.16: Rear views of the predicted wake geometries for a representative, four-bladed rotor undergoing an SPS roll reversal, $\mu = 0.186$, $\gamma = -6^\circ$: (a) Halfway into starboard roll, (b) rotor operating at maximum bank angle toward starboard, (c) rotor commencing roll to port, (d) rotor at zero bank angle.

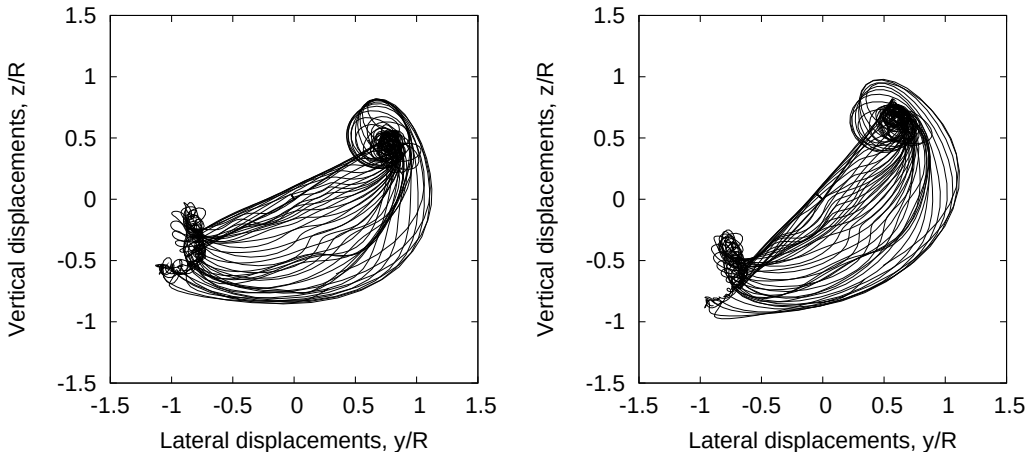


(e) $t = t_0 + 21$ revs, $\phi = -27.5°$




(f) $t = t_0 + 23$ revs, $\phi = -55°$

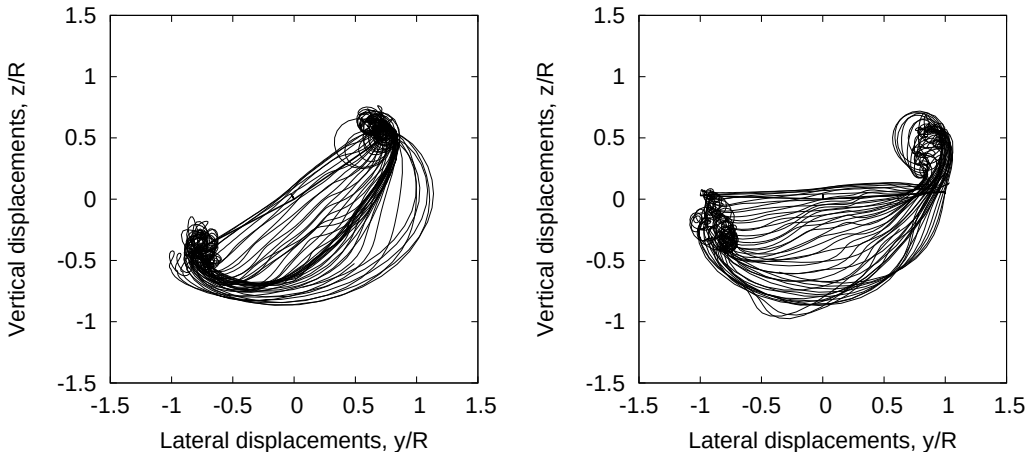


(g) $t = t_0 + 28$ revs, $\phi = -27.5°$




(h) $t = t_0 + 36$ revs, $\phi = 0°$

Figure 4.16: (Cont'd.) Rear views of the predicted wake geometries for a rotor undergoing an SPS roll reversal, $\mu = 0.186$, $\gamma = -6°$. (e) Rotor rolling toward port, (f) rotor at maximum bank angle toward port, (g) rotor returning to straight and level flight condition, (h) rotor operating at steady descending flight condition.

rotor disk starts moving into its own wake over the advancing side. Also the roll up on the advancing side occurs nearer to the rotor disk, and the tip vortices here are now bundled much tighter. These rolled up vortices interact more strongly with the blades on the advancing side of the rotor disk — see Figs. 4.16(c) through (e).

Notice that the blades continuously interact with the vortices on the advancing side of the disk. The bundled tip vortices move further inboard as the rotor attains its maximum bank angle on the port side and starts returning to the initial operating state. The wake only slowly returns to its initial state after these conditions are restored, emphasizing yet again the relatively long timescales involved in the rotor wake adjustments during maneuvering flight conditions.

Figure 4.17 shows the contours of the lift over the rotor disk for the SPS maneuver. It is immediately apparent that the roll reversal maneuver introduces considerable fluctuations in the lift distribution over time. When the rotor rolls initially to starboard, the lift distribution (Figs. 4.17(a) and (b)) is very similar to that observed during a starboard roll (c.f., Fig. 4.9). After the rotor reaches its maximum bank angle to the starboard and starts rolling to the port, the rolled up wake vortices trailed from the advancing side interact strongly with the blades producing an impulsive load in the first quadrant of the rotor disk. The BVIs on the advancing side continue to cause high impulsive loads over the port side of the rotor disk, as shown in Figs. 4.17(d) through (f). After the rotor returns to its original flight condition, the lift distribution then becomes very similar to that observed in steady descending flight conditions.

Figure 4.18 shows the sound directivity patterns for a rotor executing an SPS roll reversal at various instances in time. As the rotor rolls towards starboard the acoustic directivity — see Figs. 4.18(a) and (b) is found to be similar to the effects obtained during the transient conditions in the starboard roll case — see Figs. 4.12(e and (f)).

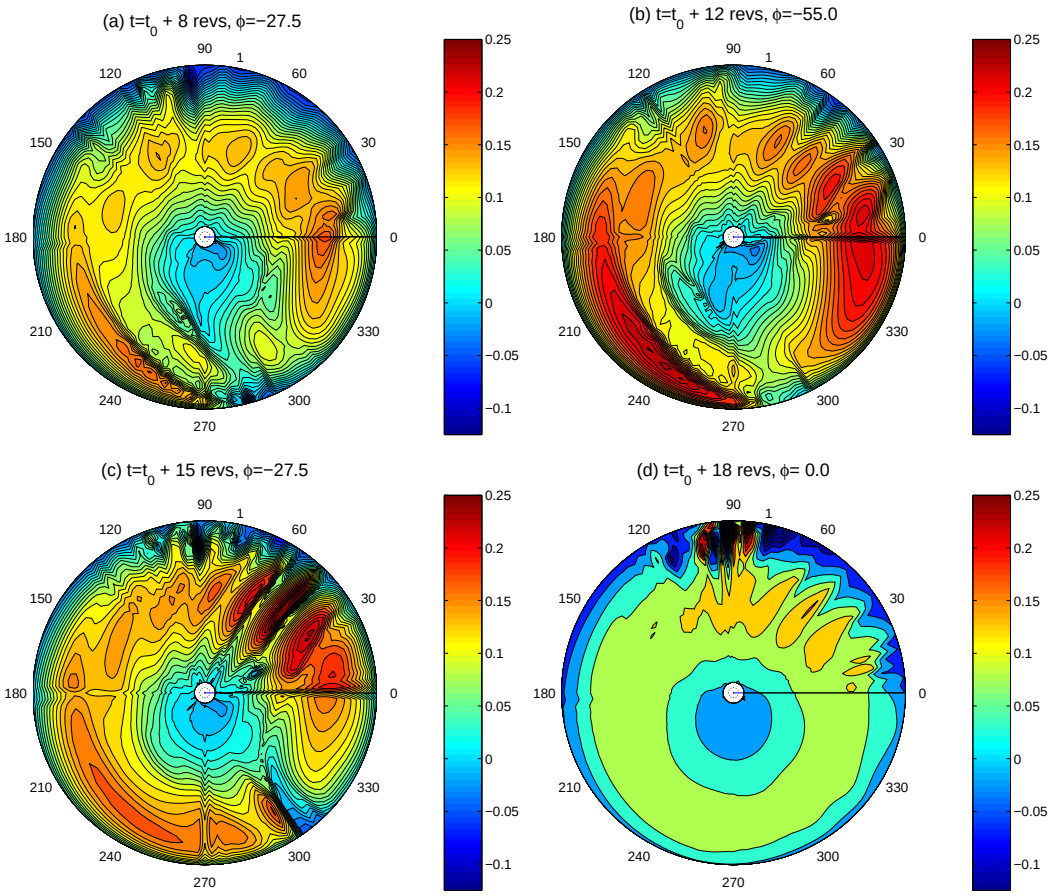


Figure 4.17: Contours of the non-dimensional lift, $C_l M^2$, distribution for a representative, four-bladed rotor undergoing an SPS roll reversal, $\mu = 0.186$, $\gamma = -6°$: (a) Halfway into starboard roll, (b) rotor operating at maximum bank angle toward starboard, (c) rotor commencing roll to port, (d) rotor at zero bank angle.

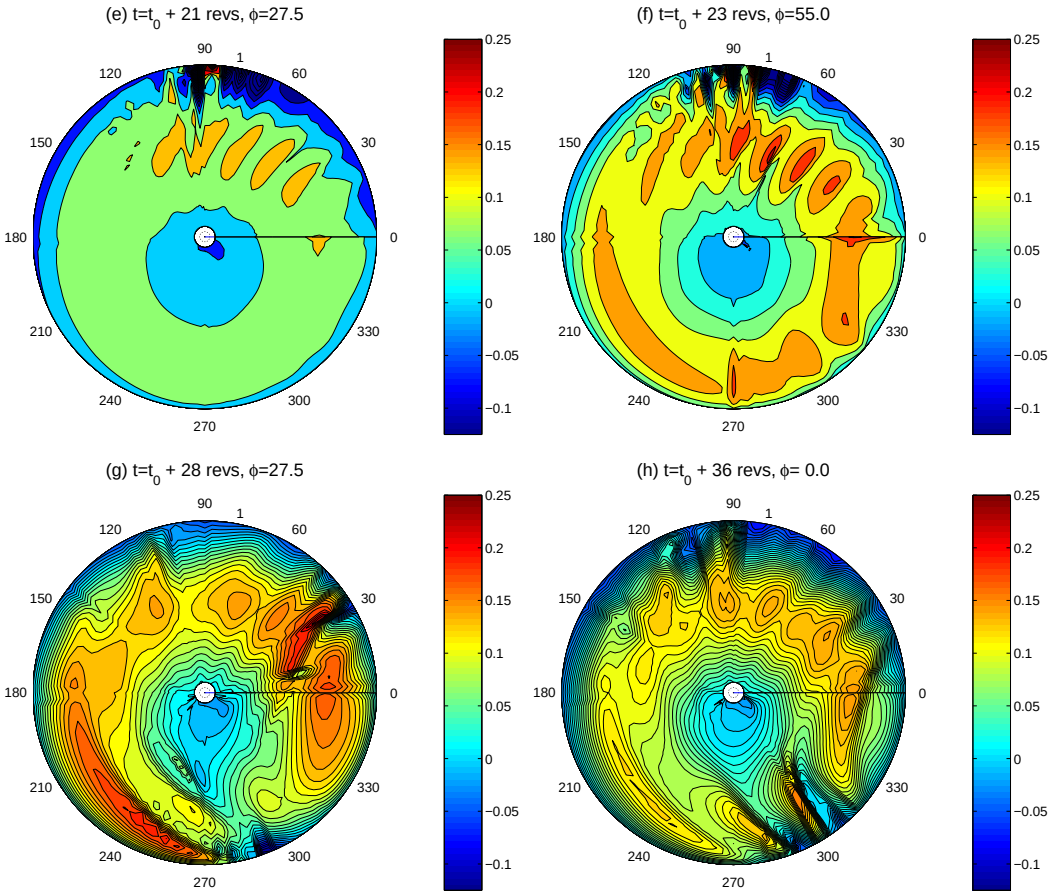


Figure 4.17: (Cont'd.) Contours of the non dimensional lift, $C_l M^2$, distribution for a representative, four-bladed rotor undergoing an SPS roll reversal, $\mu = 0.186$, $\gamma = -6^\circ$. (e) Rotor rolling toward port, (f) rotor at maximum bank angle toward port, (g) rotor returning to straight and level flight condition, (h) rotor operating at steady descending flight condition.

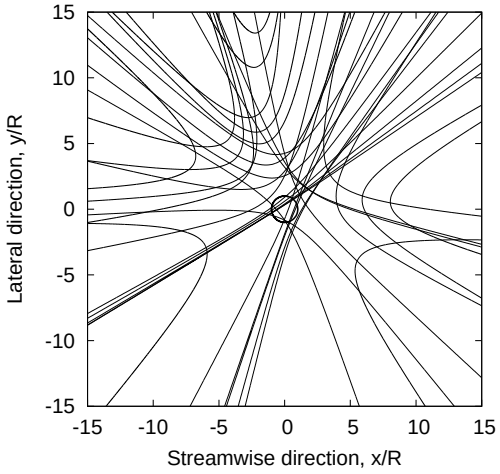


(a) $t = t_0 + 8$ revs, $\phi = 27.5^\circ$

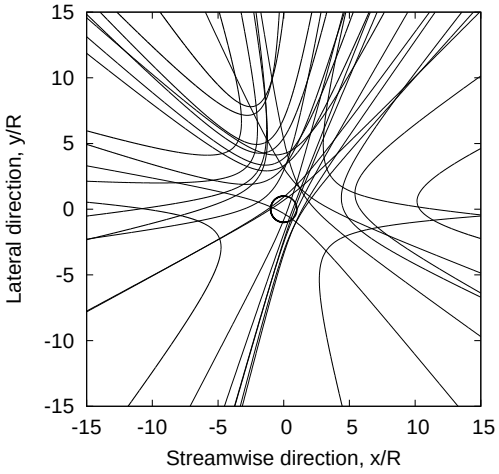


(b) $t = t_0 + 12$ revs, $\phi = 55^\circ$

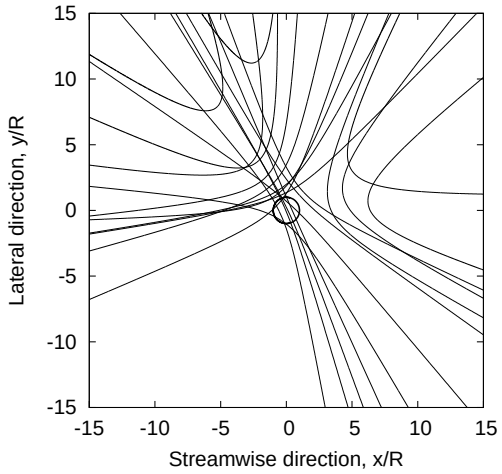


(c) $t = t_0 + 15$ revs, $\phi = 27.5^\circ$

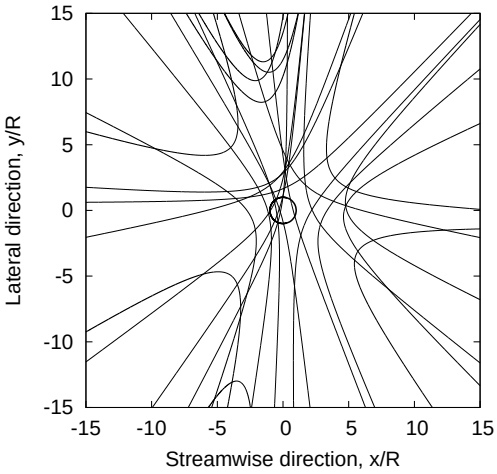


(d) $t = t_0 + 18$ revs, $\phi = 0^\circ$

Figure 4.18: Snapshots of the principal directions of sound propagation for a representative, four-bladed rotor undergoing an SPS roll reversal, $\mu = 0.186,\ \gamma = -6^\circ$: (a) Halfway into starboard roll, (b) rotor operating at maximum bank angle toward starboard, (c) rotor commencing roll to port, (d) rotor at zero bank angle.

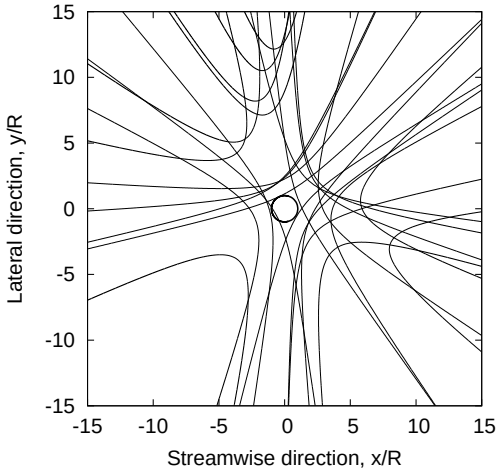


(e) $t = t_0 + 21$ revs, $\phi = -27.5^\circ$

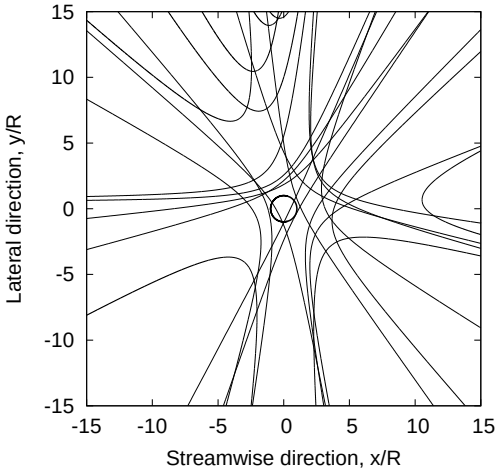


(f) $t = t_0 + 23$ revs, $\phi = -55^\circ$

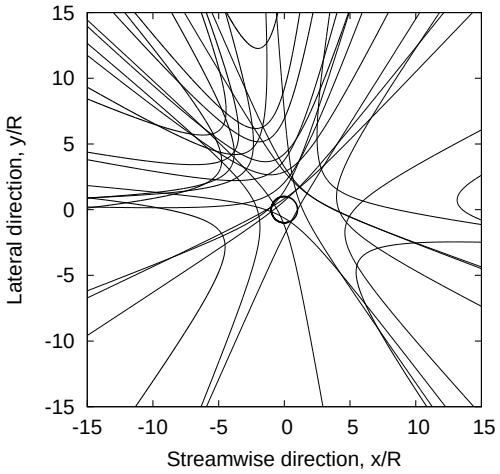


(g) $t = t_0 + 28$ revs, $\phi = -27.5^\circ$

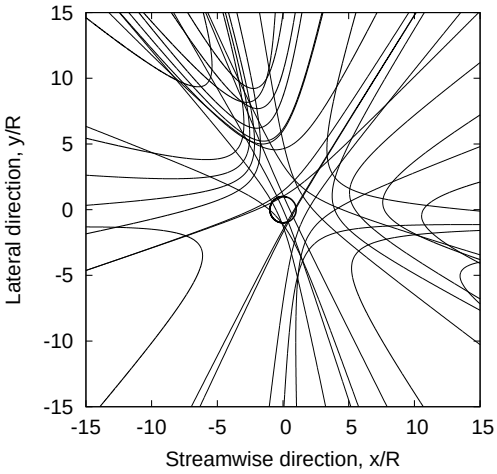


(h) $t = t_0 + 36$ revs, $\phi = 0^\circ$

Figure 4.18: (Cont'd.) Snapshots of the principal directions of sound propagation for a representative, four-bladed rotor undergoing an SPS roll reversal, $\mu = 0.186$, $\gamma = -6^\circ$. (e) Rotor rolling toward port, (f) rotor at maximum bank angle toward port, (g) rotor returning to straight and level flight condition, (h) rotor operating at steady descending flight condition.

The directivity patterns, however, change quickly as the rotor reverses the roll rate, as shown in Figs. 4.18(b) through (f). There is considerable defocusing of sound as the rotor exits the maneuver and returns to steady flight conditions. The final sound radiation pattern shown in Fig. 4.18(h) is very similar to that observed in the steady flight condition, shown previously in Fig. 4.6(c).

Figure 4.19 shows the wake snapshots at different instants in time for a rotor executing the PSP roll reversal. The wake response in the initial stages of the maneuver is comparable to that observed for a roll to port. The wake roll up on the advancing side interacts closely with the rotor blades on the advancing side as it moves through the rotor disk — see Figs. 4.19(a and (b)). Notice that the bulk of the wake is in the plane of the rotor during the port roll. As the rotor reverses the roll direction and begins its starboard roll motion, the wake roll up on the advancing side moves through the disk and the wake starts to expand below the plane of the rotor — see Figs. 4.19(c through (e)). A lag in the wake roll up on the advancing side is also observed. This mollifies the effects of the BVIs that occur over the advancing side of the disk. After steady state conditions are established the wake geometries were found to be similar to those observed in steady, descending flight condition.

Figure 4.20 shows the corresponding contour plots of the lift distribution over the rotor disk. The interactions between the tightly rolled up vortex bundle trailed from the advancing side of the disk and the rotor blades manifest as strong impulsive loads on the advancing side — see Fig. 4.20(a) through (c). However, after the rotor starts rolling toward the starboard side, the tip vortex bundling is weakened and the wake expands away from the rotor disk. This is also reflected in the lift distribution (see Figs. 4.20(d) through (f)) which does not show any changes in the gradients. The impulsive loads briefly return on the advancing side as the rotor rolls to port yet again

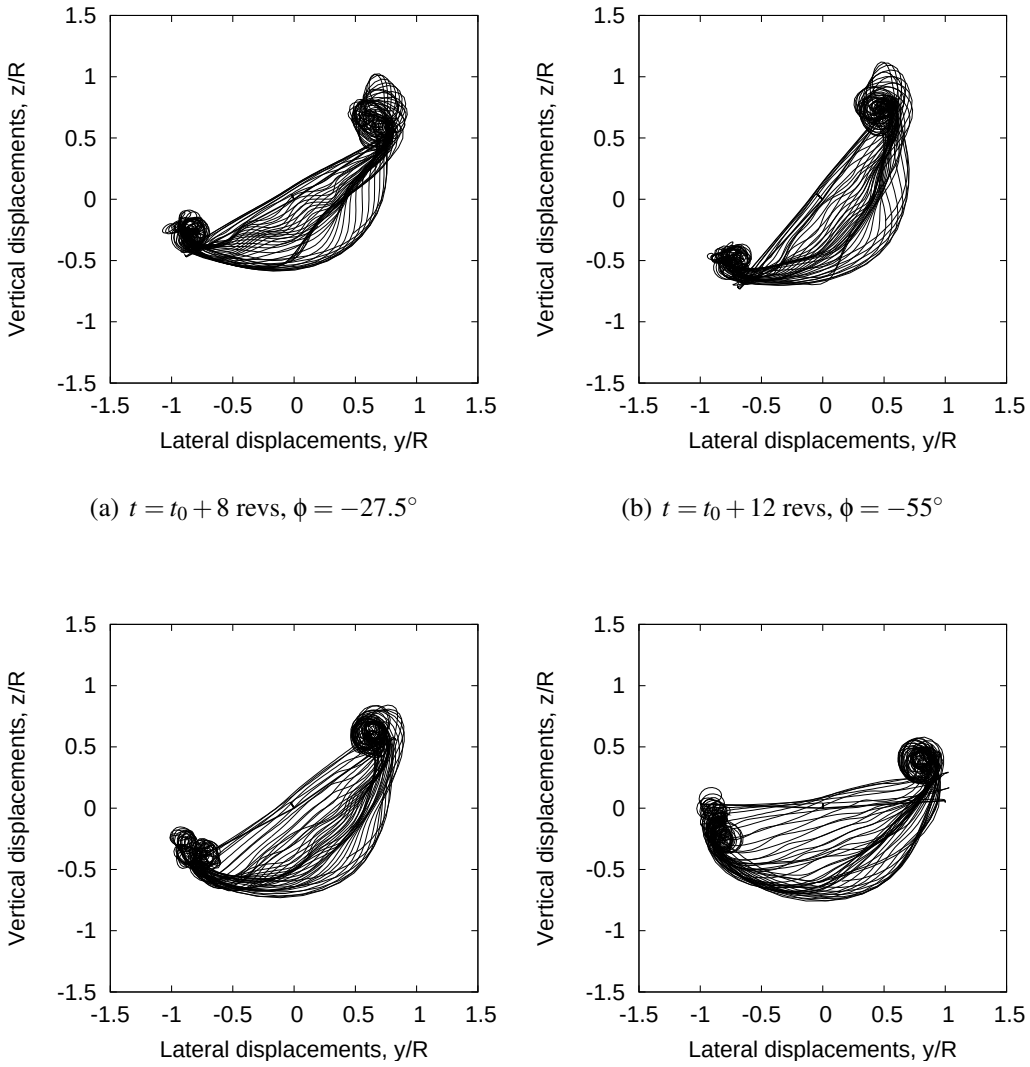


(a) $t = t_0 + 8$ revs, $\phi = -27.5^\circ$

(b) $t = t_0 + 12$ revs, $\phi = -55^\circ$

(c) $t = t_0 + 15$ revs, $\phi = -27.5^\circ$

(d) $t = t_0 + 18$ revs, $\phi = 0^\circ$

Figure 4.19: Rear views of the predicted wake geometries for a representative, four-bladed rotor undergoing a PSP roll reversal, $\mu = 0.186$, $\gamma = -6^\circ$: (a) Halfway into port roll, (b) rotor operating at maximum bank angle toward port, (c) rotor commencing roll to starboard, (d) rotor at zero bank angle.

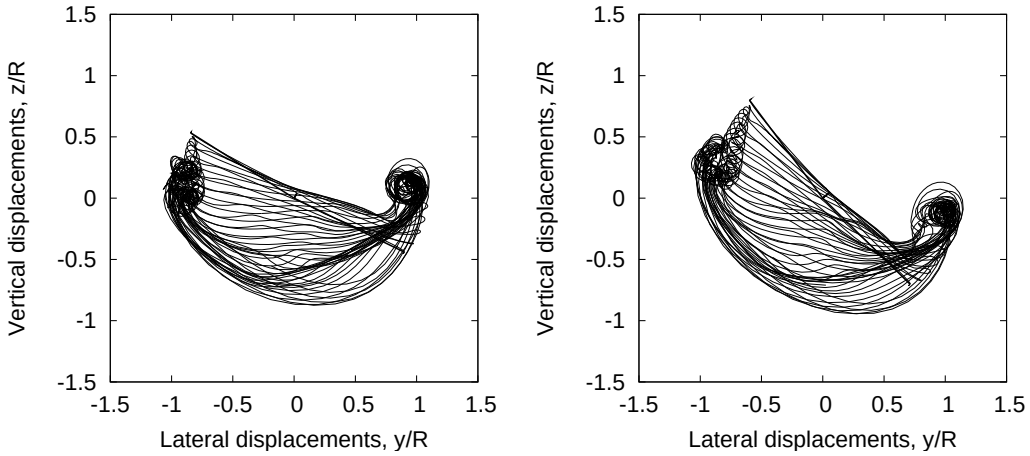


(e) $t = t_0 + 21$ revs, $\phi = 27.5^\circ$




(f) $t = t_0 + 23$ revs, $\phi = 55^\circ$

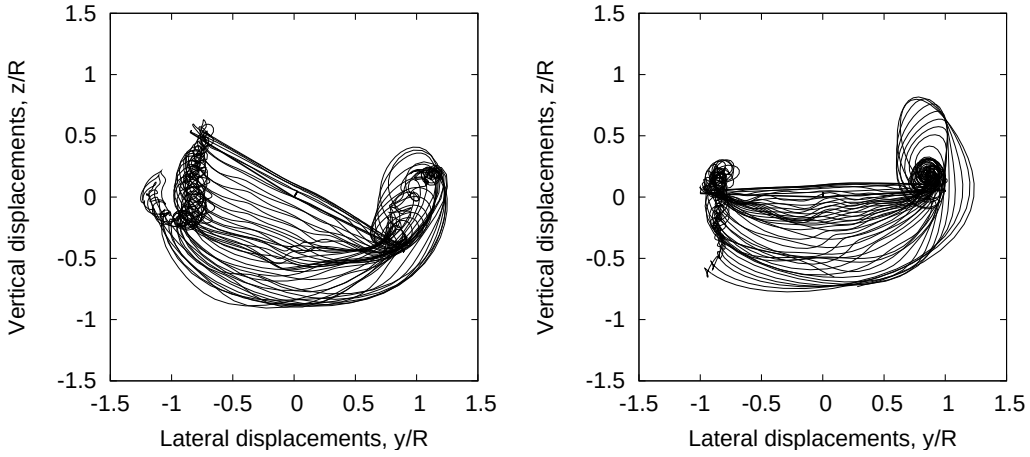


(g) $t = t_0 + 28$ revs, $\phi = 27.5^\circ$




(h) $t = t_0 + 36$ revs, $\phi = 0^\circ$

Figure 4.19: (Cont'd.) Rear views of the predicted wake geometries for a representative, four-bladed rotor undergoing a PSP roll reversal, $\mu = 0.186$, $\gamma = -6^\circ$. (e) Rotor rolling toward starboard, (f) rotor at maximum bank angle toward starboard, (g) rotor returning to straight and level flight condition, (h) rotor operating at steady descending flight condition.

before attaining its final equilibrium orientation.

Figure 4.21 shows snapshots of the noise directivity patterns for the PSP roll reversal. As the rotor rolls toward port notice that the noise is dominated by the near parallel interactions on the advancing side of the rotor disk. As the rotor enters the roll reversal, the noise directivity changes quickly, as found with the SPS maneuver. It is interesting to note that the defocusing of noise occurs when the rotor is at its maximum bank angle to starboard. The acoustic directivity patterns then change back to those observed in Fig. 4.6(c) as the rotor returns to steady, descending flight.

Figure 4.22 shows the power predictions during the roll reversal maneuver predicted by the free-vortex wake methodology. The behavior is similar to that observed during the starboard and port rolls, however, the maximum transient power requirements are considerably smaller than the final steady power requirements observed in the roll maneuvers. This is because of the lags associated with the wake aerodynamics. The tip vortices do not have enough time to adjust to the control pitch inputs during the roll reversal.

## 4.3 Free Flight Maneuvers

For the aerodynamic simulation of free flight maneuvers, the motion of the helicopter about all the principal coordinate axes must be considered. This requires some form of helicopter flight dynamics model that is capable of predicting the various forces acting on the helicopter and calculating the helicopter's position, orientation, and velocities. The time-histories of the helicopter motion must then be coupled to the free-vortex wake model to capture the transient wake aerodynamics during such maneuvers. The coupling between the helicopter flight dynamics model and the free-

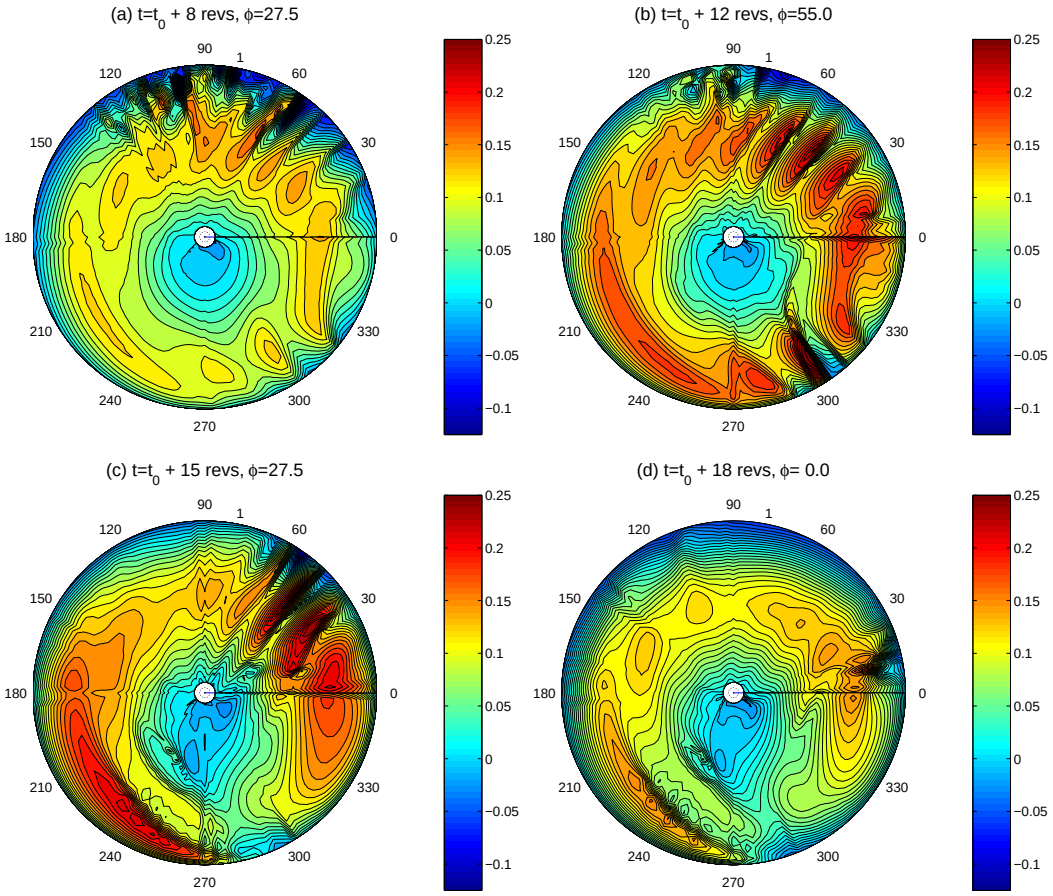


Figure 4.20: Contours of the non dimensional lift, $C_l M^2$, distribution for a representative, four-bladed rotor undergoing a PSP roll reversal, $\mu = 0.186$, $\gamma = -6°$: (a) Halfway into port roll, (b) rotor operating at maximum bank angle toward port, (c) rotor commencing roll to starboard, (d) rotor at zero bank angle.

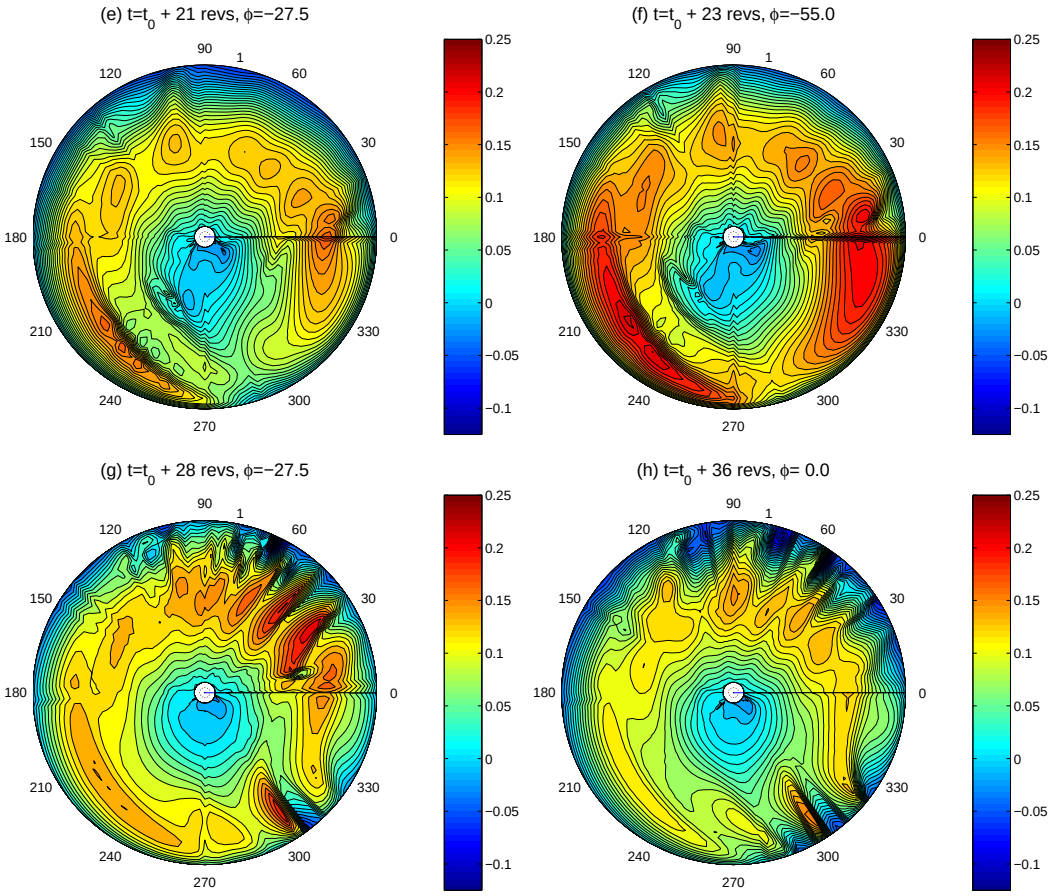


Figure 4.20: (Cont'd.) Contours of the non dimensional lift, $C_l M^2$, distribution for a representative, four-bladed rotor undergoing a PSP roll reversal, $\mu = 0.186,\ \gamma = -6^\circ$. (e) Rotor rolling toward starboard, (f) rotor at maximum bank angle toward starboard, (g) rotor returning to straight and level flight condition, (h) rotor operating at steady descending flight condition.

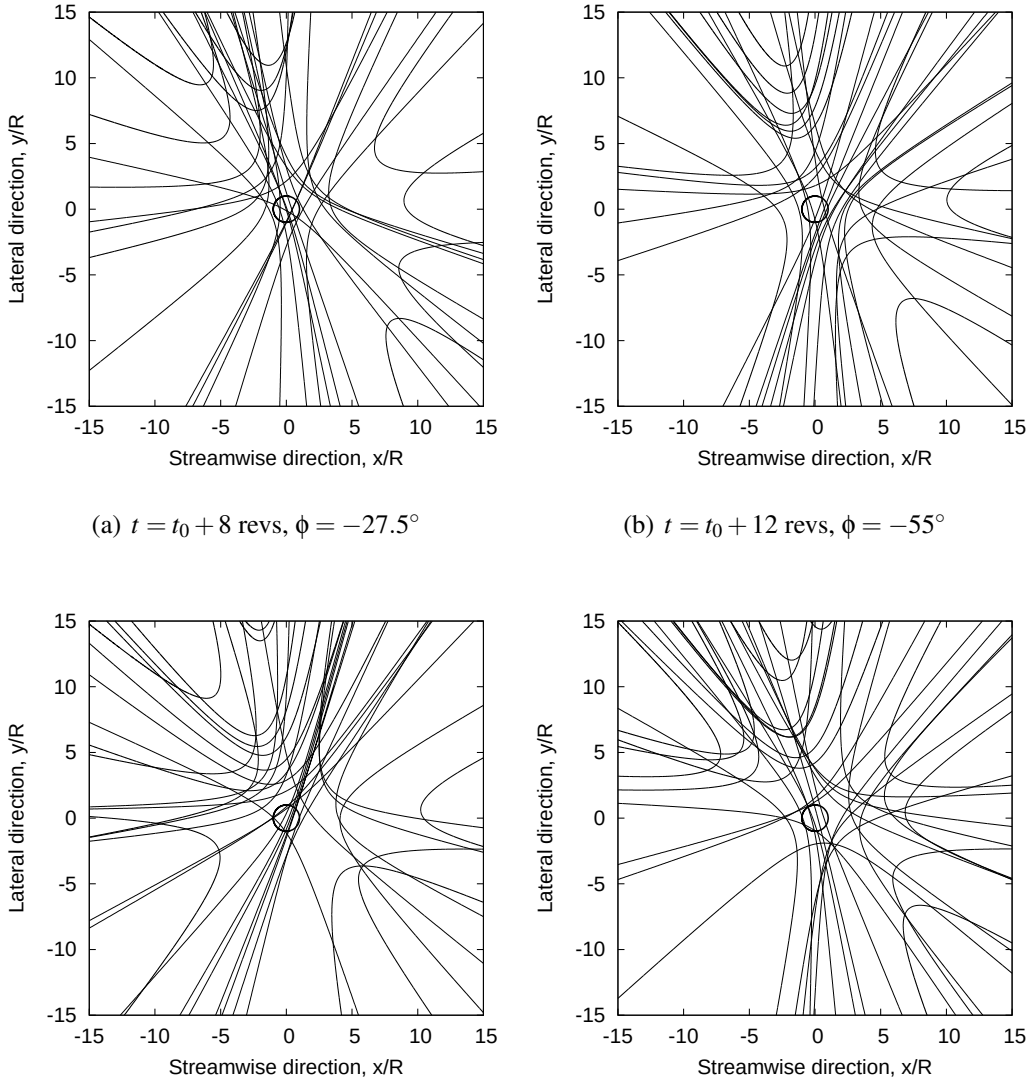


(a) $t = t_0 + 8$ revs, $\phi = -27.5^\circ$

(b) $t = t_0 + 12$ revs, $\phi = -55^\circ$

(c) $t = t_0 + 15$ revs, $\phi = -27.5^\circ$

(d) $t = t_0 + 18$ revs, $\phi = 0^\circ$

Figure 4.21: Snapshots of the principal directions of sound propagation for a representative, four-bladed rotor undergoing a PSP roll reversal, $\mu = 0.186$, $\gamma = -6^\circ$: (a) Halfway into port roll, (b) rotor operating at maximum bank angle toward port, (c) rotor commencing roll to starboard, (d) rotor at zero bank angle.

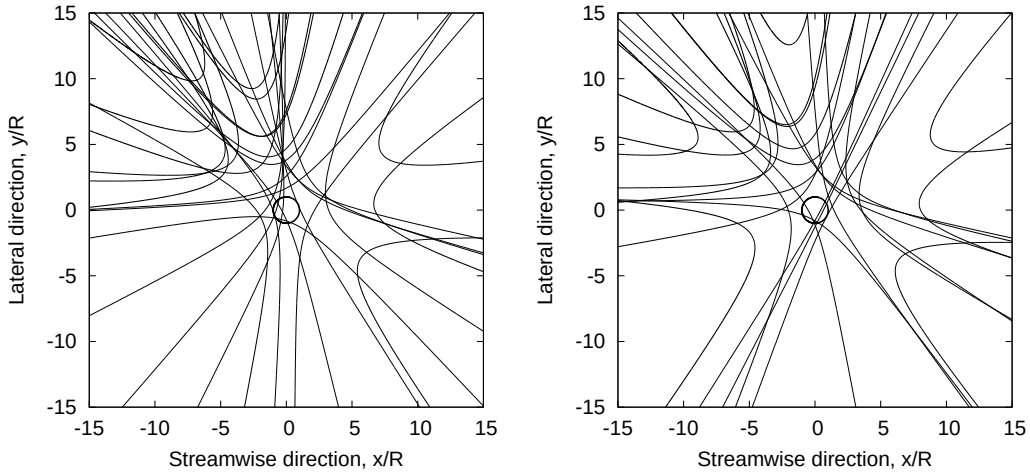


(e) $t = t_0 + 21$ revs, $\phi = 27.5^\circ$

(f) $t = t_0 + 23$ revs, $\phi = 55^\circ$

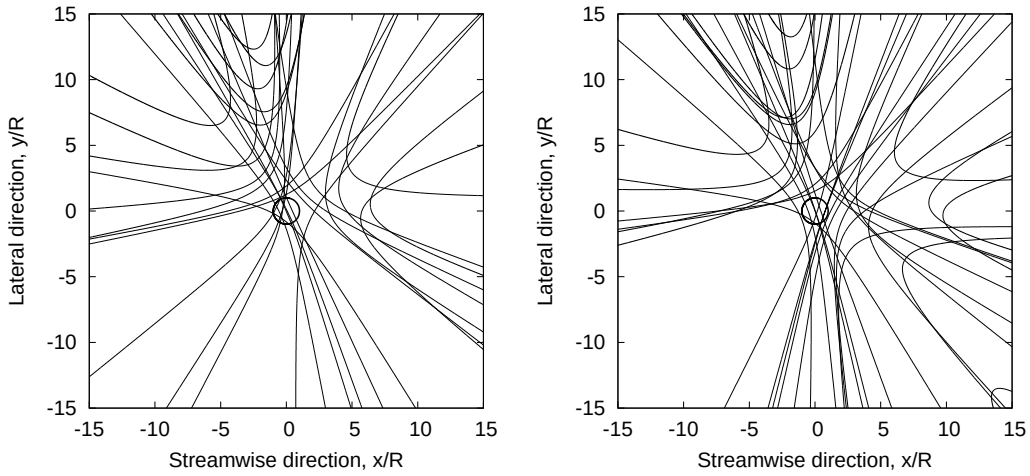


(g) $t = t_0 + 28$ revs, $\phi = 27.5^\circ$

(h) $t = t_0 + 36$ revs, $\phi = 0^\circ$

Figure 4.21: (Cont'd.) Snapshots of the principal directions of sound propagation for a representative, four-bladed rotor undergoing a PSP roll reversal, $\mu = 0.186$, $\gamma = -6^\circ$. (e) Rotor rolling toward starboard, (f) rotor at maximum bank angle toward starboard, (g) rotor returning to straight and level flight condition, (h) rotor operating at steady descending flight condition.

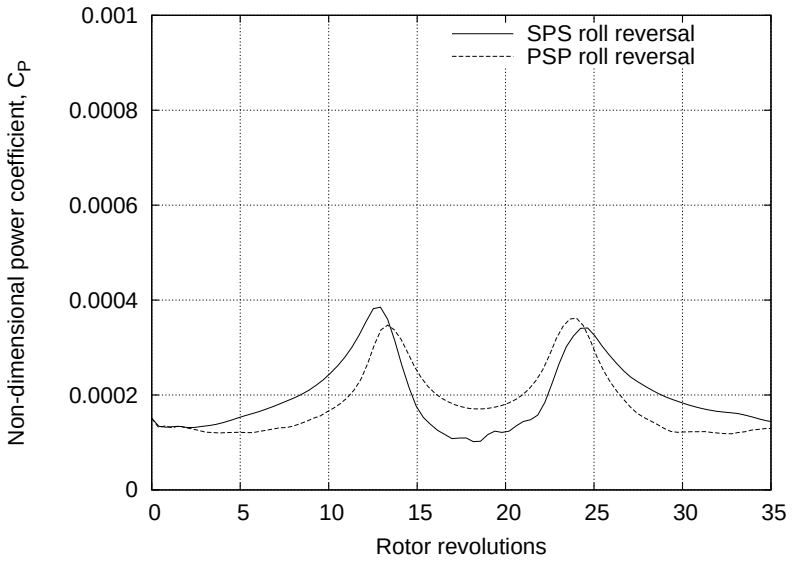


Figure 4.22: Time-history of the power requirements during the SPS and the PSP roll reversal maneuvers.

vortex wake model can be performed using two approaches: an uncoupled strategy or a coupled strategy, which are shown schematically in Fig. 4.23.

In an uncoupled simulation the flow of information is unidirectional, i.e., only the output from the flight dynamics simulation is prescribed to the free-vortex wake model to analyze the wake aerodynamics. The flight dynamics model must resort to a lower-order model (usually the dynamic inflow model) to obtain the induced velocity field at the blades during the maneuver. The disadvantage of this approach is that the flight dynamics simulation cannot account for the nonlinearities in the inflow distribution at the rotor disk arising from bundling of tip vortices during maneuvers. These nonlinearities can change the net forces and moments acting on the helicopter (see discussion in Section 4.2.1) and, therefore, the time-history of the control inputs and the resulting helicopter response might be different from the one obtained using a dynamic inflow model.

In a coupled simulation, the nonlinear inflow across the rotor disk obtained from the free-vortex wake calculations is fed back to the flight dynamics simulation model (Ref. 34). The coupling allows the flight dynamics model to account for the nonlinear evolution of the rotor wake during maneuvers and, therefore, the time-histories of the control inputs predicted will be, in theory, closer to reality.

However, a coupled flight dynamics, free-vortex wake simulation at resolutions necessary to properly resolve BVIs can quickly become computationally prohibitive. Furthermore, the emphasis of this dissertation is to gain a better understanding of the wake response to control pitch perturbations. For this purpose, it is desirable to study just the wake aerodynamic response to a combination of control pitch perturbations in isolation and to ignore the effects of the nonlinear wake induced inflow on the helicopter flight dynamics response. This is the logical extension of the idealized maneuvers studied in the previous section. Therefore, the present study adopts an open-loop strategy for the simulation of free flight maneuvers. As with the idealized maneuvers, the UH-60 rotor geometry was used as a baseline in all the calculations.

### 4.3.1 Starboard and Port Roll Maneuvers

Previously, in Section 4.2.2, the starboard and port roll maneuvers were analyzed using 1-DOF roll equations. It was shown that the wake aerodynamics is complicated and considerably different for the two cases even without the consideration of cross coupling effects. Therefore, one can expect further differences in the wake aerodynamics and possible BVIs when the maneuver is performed using a combination of real pilot control inputs necessary to perform these maneuvers. While the differences between rolls to starboard and port respectively are of particular interest, it is also desirable to study the sensitivity of the wake dynamics and the resulting rotor airloads

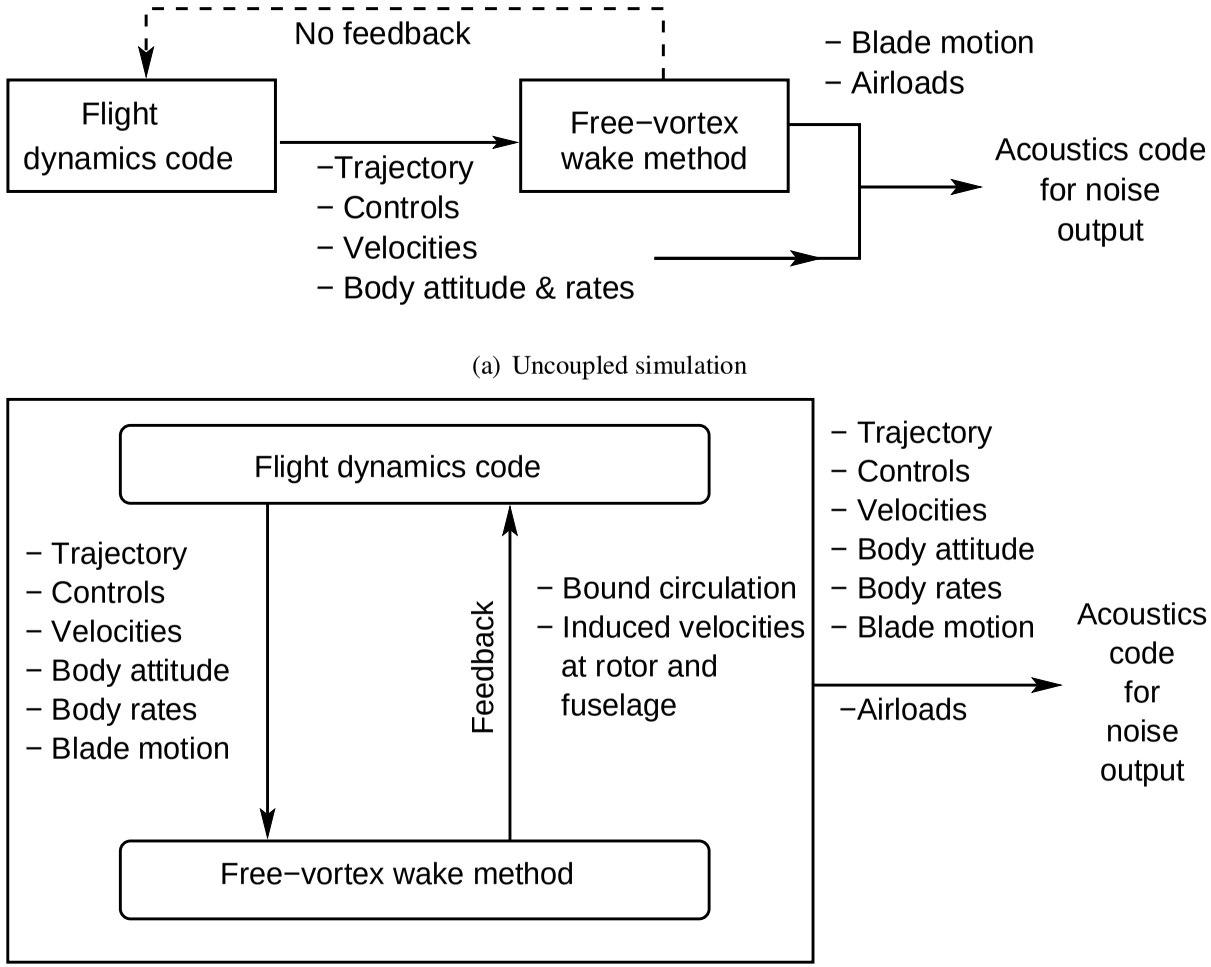


(a) Uncoupled simulation

(b) Coupled simulation

Figure 4.23: Schematic showing the transfer of information between the flight dynamics module and the free-vortex wake aerodynamics module for open-loop and closed-loop strategies: (a) Uncoupled strategy, (b) coupled strategy.

to roll rates. Therefore, the roll maneuver simulations performed over three different durations 0.5s, 1s and 5s, corresponding to maximum transient roll rates of approximately 50°/s, 35°/s and 6°/s respectively, were studied.

**Roll to Starboard**

Figure 4.24 shows the time-histories of the collective, cyclic and pedal pilot control inputs prescribed to the free-vortex wake to simulate roll to starboard over a duration of 0.5 seconds. Notice that the lateral pitch input in this case is not a step function as was previously assumed. Furthermore, notice that there are considerable changes in the collective and longitudinal cyclic pitch inputs during the maneuver. Figures 4.24(e) and (f) show the time-history of the roll rate, $p$, and the roll attitude, $\phi$, that were imposed on the rotor during a starboard roll maneuver. Notice that instantaneous roll rates of over 60°/s are experienced. Notice also that the pilot overshoots the target bank angle (at the end of 11 rotor revolutions) and has to bank slightly to port to reach the desired target bank angle. This correction turns out to a significant effect on the rotor airloads.

Figures 4.25 and 4.26 show the top and rear wake snapshots for a rotor executing a starboard roll at various instances in time. As the maneuver progresses the rotor rolls starboard, bringing the tip vortices closer to the advancing blade — see Fig. 4.26. The tip vortices trailed on the advancing side (starboard) of the rotor disk are tightly wound up during the course of this maneuver. Notice that there is a concentrated vortex bundle that originates when the pilot rectifies the overshoot in roll attitude. The slight roll to port causes the bundled wake to move through the rotor disk, as shown in Fig. 4.26(d). Because the wake responds with a certain time lag, it is not entirely clear if the bundling of tip vortices was caused by the rectification of the overshoot in

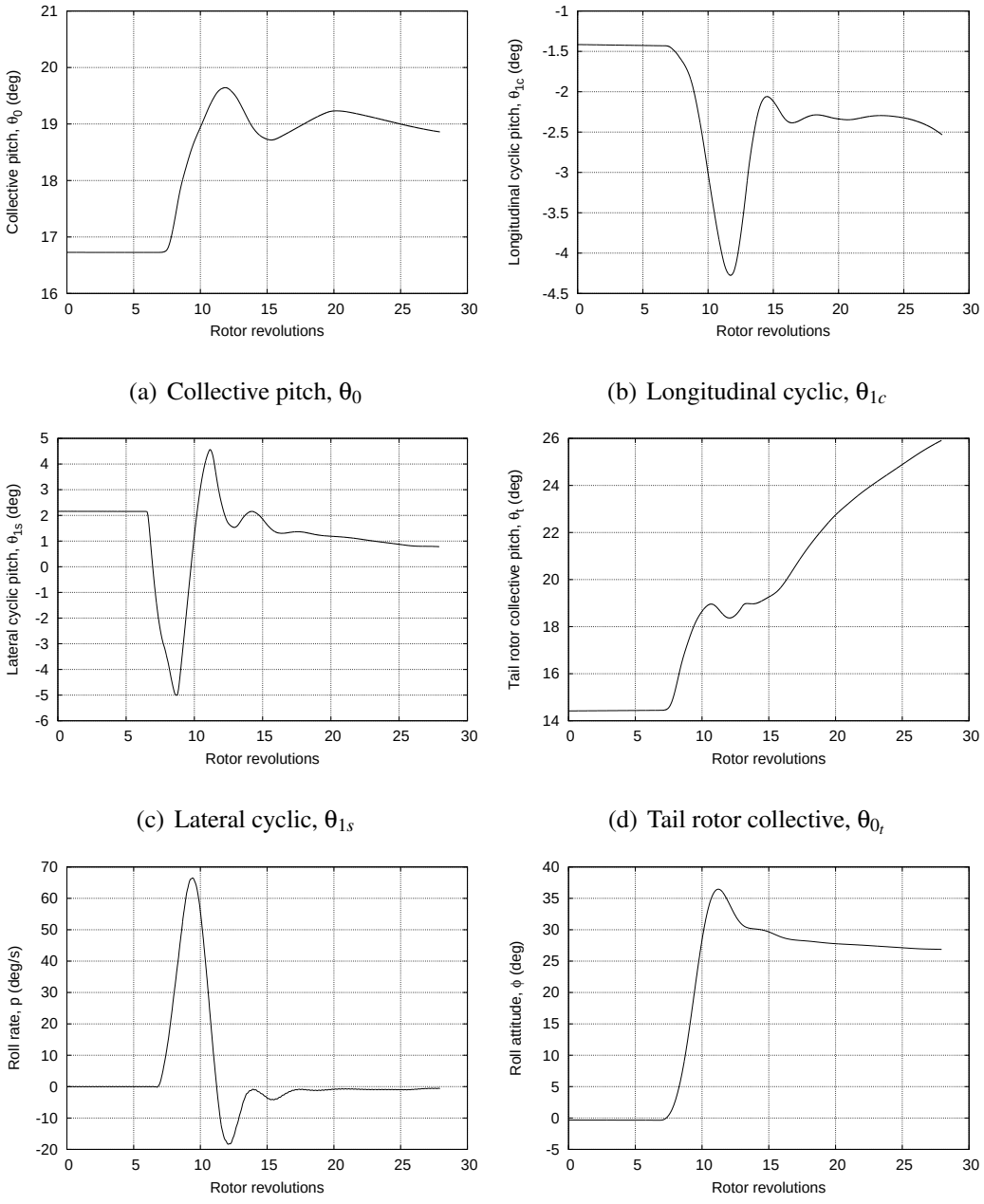


(a) Collective pitch, $\theta_0$

(b) Longitudinal cyclic, $\theta_{1c}$

(c) Lateral cyclic, $\theta_{1s}$

(d) Tail rotor collective, $\theta_{0_t}$

(e) Roll rate, $p$

(f) Roll attitude, $\phi$

Figure 4.24: Time-histories of pilot control inputs used to perform a starboard roll maneuver over 0.5 second and the resulting roll response: (a) Collective pitch, (b) longitudinal cyclic, (c) lateral cyclic, (d) tail rotor collective, (e) roll rate, and (f) roll attitude.

roll attitude. It is possible that high transient roll rates (greater than 60°/s in this case) were responsible for the vortex bundling and the slight roll to port merely caused the blades to move into the wake. However, no such strong bundling was observed in the idealized starboard roll maneuver, where only the effect of roll rates was studied. Therefore, it can be concluded that the bundling was induced by a combination of pilot actions and was not just a pure roll rate effect.

In Fig. 4.25(f) it is seen that the tip vortices follow a curved trajectory after the coordinated turn is established. The bundled structure is quickly convected away and below the rotor TPP and steady state conditions are soon established.

Figure 4.27 shows the non-dimensional lift contours, $C_l M^2$, over the rotor disk for a reference blade at various instances in time. Notice the intensification of BVIs on the advancing side of the rotor disk during the starboard roll. Interestingly, the steepest gradients in the lift distribution (representative of BVIs) do not occur during periods when the rotor experiences high roll rates, rather it occurs after the pilot corrects for the overshoot in the bank angle from the desired orientation (see Fig. 4.27(e)). The piloting correction initiates a bundling of the tip vortices, which is more prominent on the advancing side of the rotor — see Figs. 4.25(d) and (e). The relative positions of the rotor blades and the bundled vortices are such that the rotor moves through this ring structure causing a "super-BVI," which is evident in Fig. 4.27(e).

Figure 4.28 shows the time-histories of the thrust and the power predictions during the maneuver. The behavior is considerably different from that observed during the idealized maneuver (c.f., Fig. 4.14). Notice that there is a slight decrease in the power requirements as the maneuver is initiated. The BVI associated with the pilot's correction of the overshoot in the bank attitude is seen to have a significant impact in the thrust and power requirements.

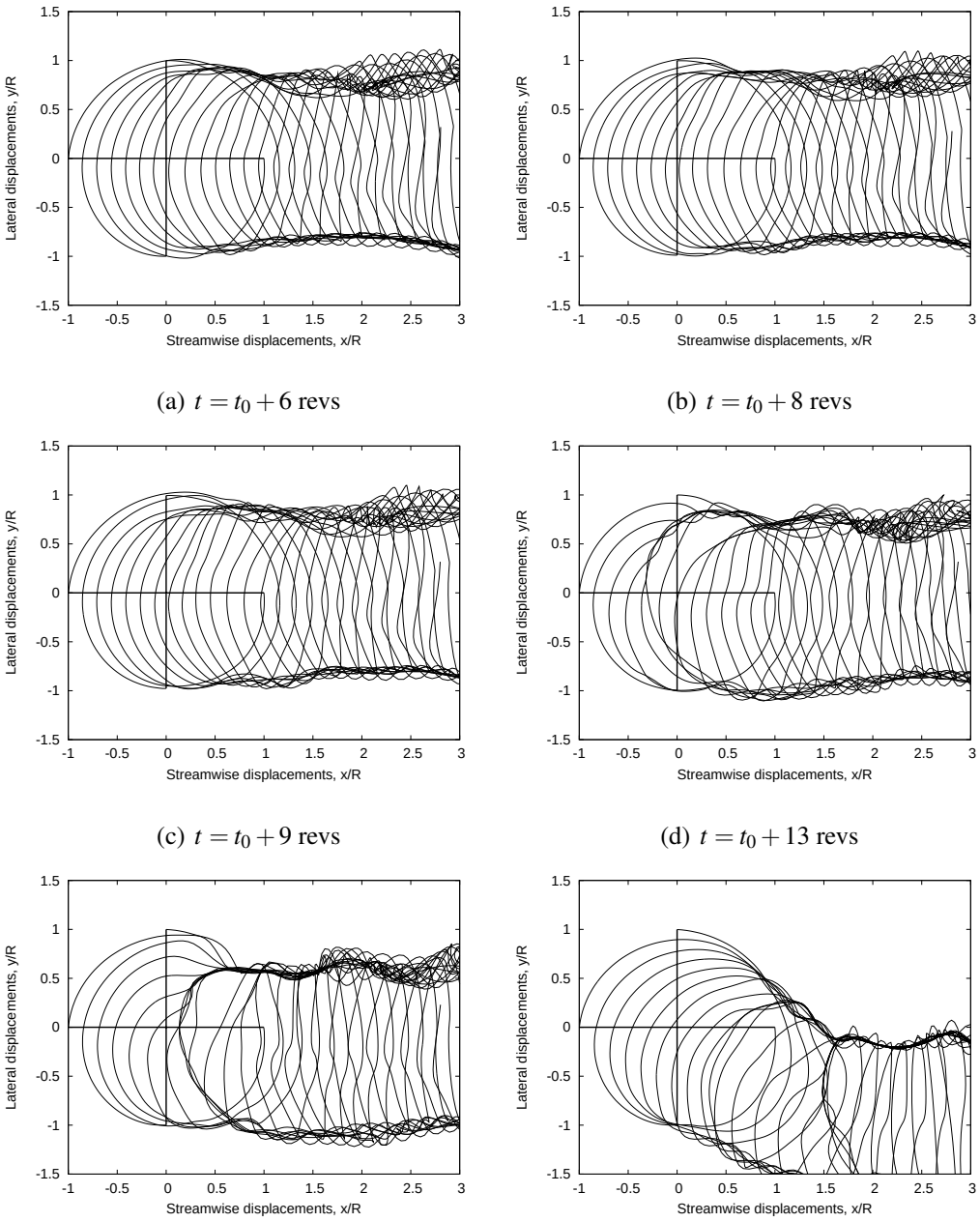


(a) $t = t_0 + 6$ revs

(b) $t = t_0 + 8$ revs

(c) $t = t_0 + 9$ revs

(d) $t = t_0 + 13$ revs

(e) $t = t_0 + 15$ revs

(f) $t = t_0 + 22$ revs

Figure 4.25: Top views of the predicted wake geometries for a representative, four-bladed rotor undergoing a starboard roll, $\mu = 0.093$: (a) Before initiation of the maneuver, (b) after 2 revolutions, (c) after 3 revolutions, (d) after 7 revolutions, (e) after 9 revolutions, (f) rotor operating at desired bank angle.

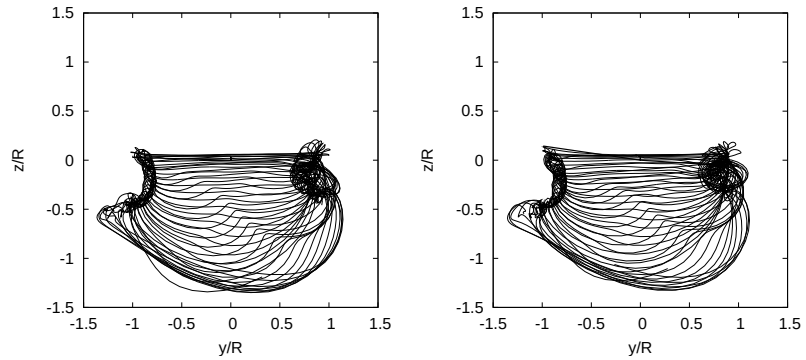


(a) $t = t_0 + 6$ revs




(b) $t = t_0 + 8$ revs

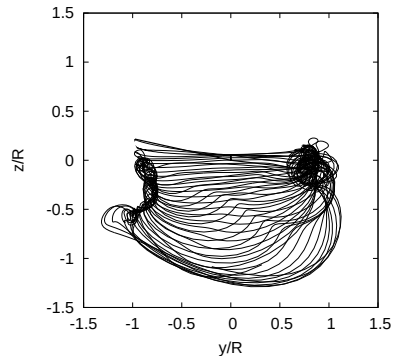


(c) $t = t_0 + 9$ revs

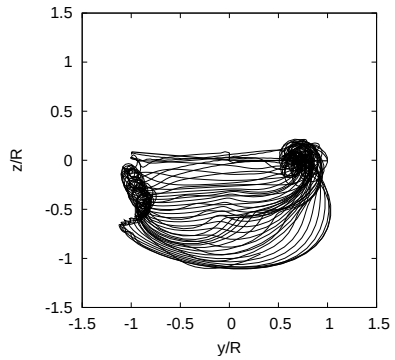


(d) $t = t_0 + 13$ revs

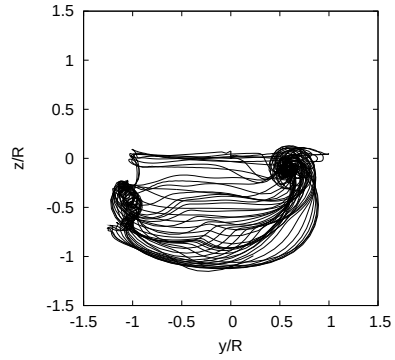


(e) $t = t_0 + 15$ revs

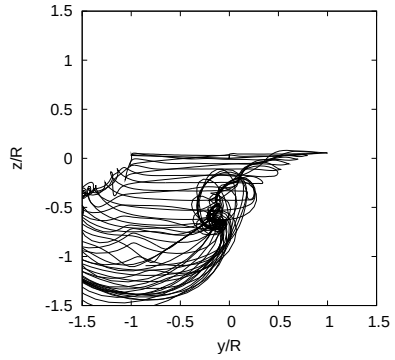


(f) $t = t_0 + 22$ revs

Figure 4.26: Rear views of the predicted wake geometries for a representative, four-bladed rotor undergoing a starboard roll, $\mu = 0.093$: (a) Before initiation of the maneuver, (b) after 2 revolutions, (c) after 3 revolutions, (d) after 7 revolutions, (e) after 9 revolutions, (f) rotor operating at desired bank angle.

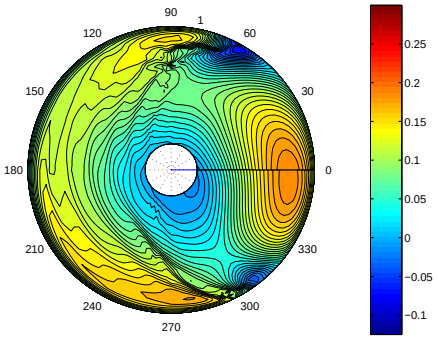


(a) $t = t_0 + 6$ revs

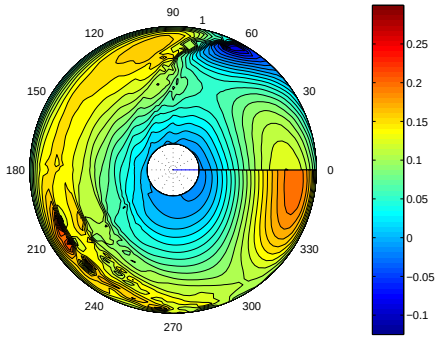


(b) $t = t_0 + 8$ revs

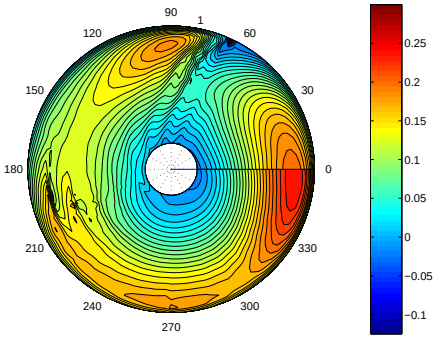


(c) $t = t_0 + 9$ revs

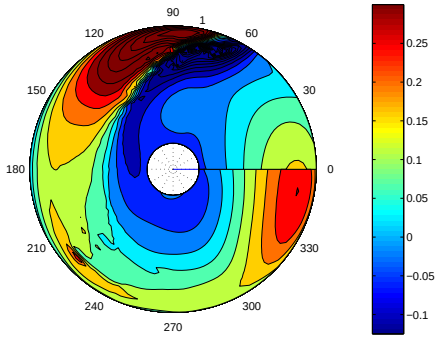


(d) $t = t_0 + 13$ revs

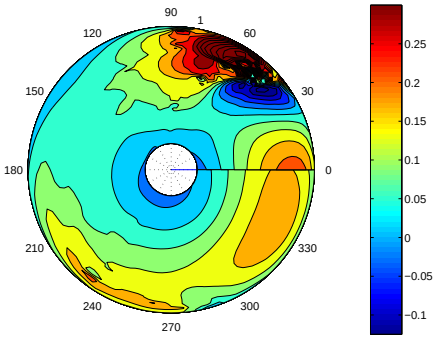


(e) $t = t_0 + 15$ revs

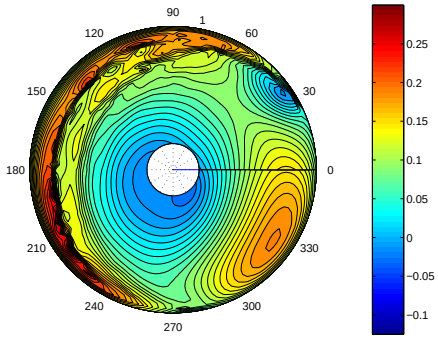


(f) $t = t_0 + 22$ revs

Figure 4.27: Contours of the non-dimensional lift distribution for a representative, four-bladed rotor undergoing a starboard roll over a duration of 0.5 seconds, $\mu = 0.093$: (a) Before initiation of the maneuver, (b) after 2 revolutions, (c) after 3 revolutions, (d) after 7 revolutions, (e) after 9 revolutions, (f) rotor operating at desired bank angle.

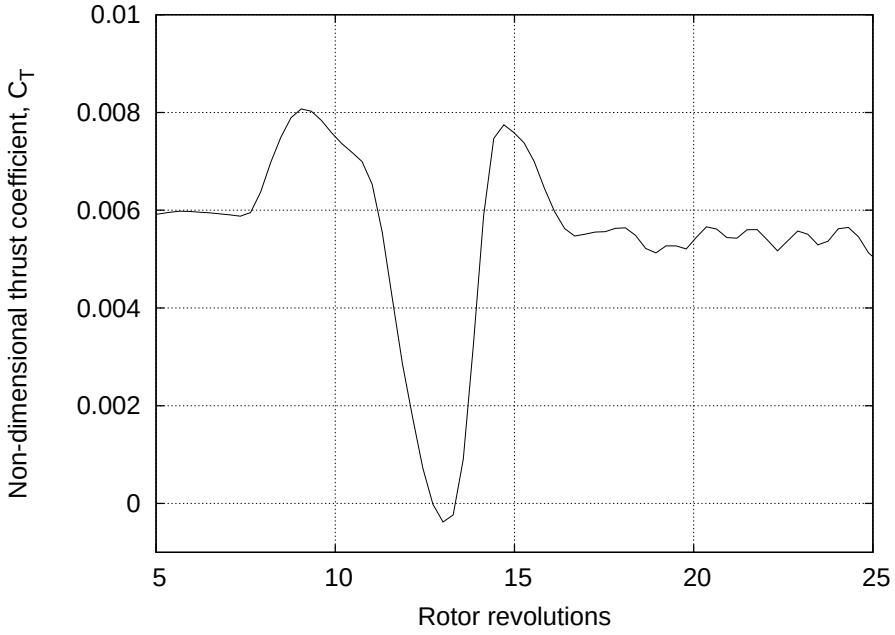


(a) Non-dimensional thrust coefficient

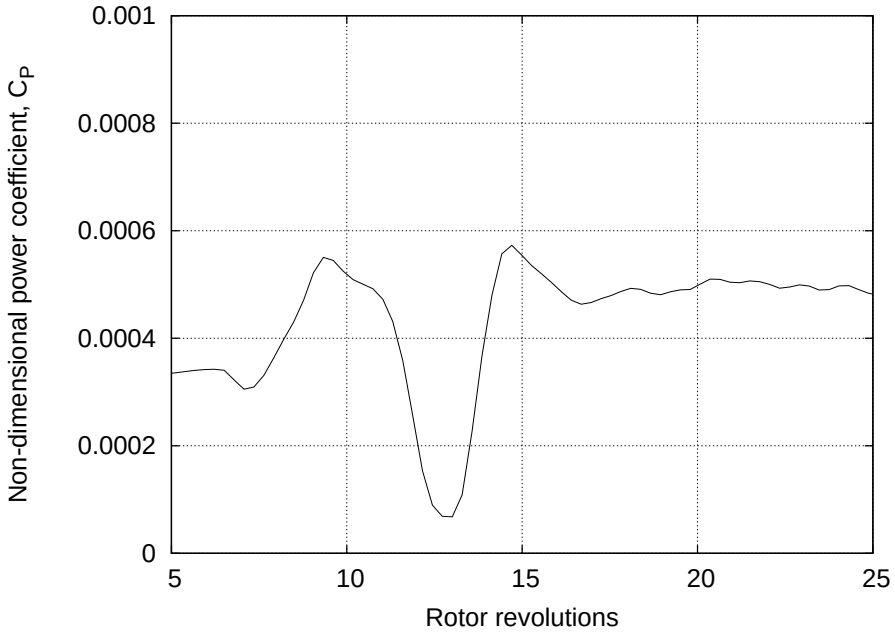


(b) Non-dimensional power coefficient

Figure 4.28: Time-histories of the thrust and power for a four-bladed rotor executing a starboard roll maneuver over a duration of 0.5 seconds: (a) Thrust, (b) Power.

Finally, Fig. 4.29 shows the BVI sound pressure levels (BVISPL) at various instances of time predicted by PSU-WOPWOP (Ref. 8) based on the predictions of the airloads from the free-vortex wake methodology. The plots shown are reproduced from Ref. 10. The strong gradients on the advancing side is seen to produce an intense omnidirectional sound as the pilot corrects for the overshoot in the roll attitude.

Figure 4.30 shows the time-histories of the pilot control inputs and the resulting roll response for a rotor executing a starboard roll maneuver over a duration of one second. The magnitudes of control input perturbations necessary to perform this maneuver are considerably smaller in comparison to the aggressive roll maneuver considered previously — see Fig. 4.24. Notice that there is a slight overshoot in roll attitude (Fig. 4.30(f)) and the roll rate necessary to rectify this overshoot is only half of that required in the previous case — see Fig. 4.24(e). It can, therefore, be expected that the bundling in this case will not be as intense as was observed in the previous maneuver.

Figures 4.31 and 4.32 show the snapshots of the top and rear views of the wake geometry at various instances in time. The qualitative behavior of the wake aerodynamics is similar to that observed for the maneuver taking place over 0.5 second duration (c.f. Fig. 4.25). The roll to starboard brings the trailed vortices closer to the blades on the advancing side of the disk and the tip vortices are also wound up tightly on the advancing side. The wake exhibits a tendency to bundle (see Fig. 4.31(e)), however the bundling is not as intense as was observed in Fig. 4.25(e).

Figure 4.33 shows the contours of the non-dimensional lift distribution over the rotor disk as the rotor executes the roll to starboard. As the maneuver progresses the BVIs on the advancing side intensify. Once again the steepest gradients in lift distribution occur when the pilot rectifies the overshoot in the roll attitude. However, the

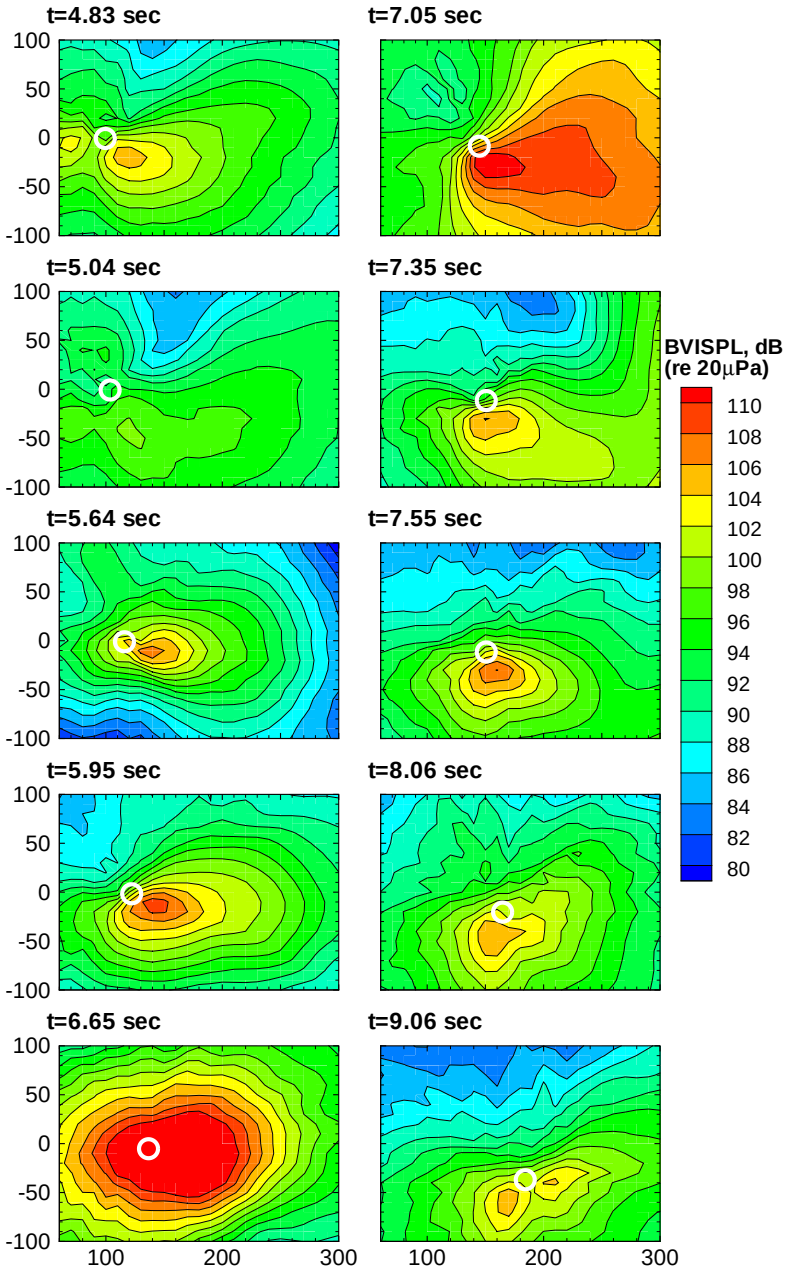


Figure 4.29: BVI sound pressure levels obtained from PSU-WOPWOP showing the acoustic intensity at an observer plane below the rotor at various instances of time for a rotor executing a starboard roll maneuver over a duration of 0.5 seconds, $\mu = 0.093$.

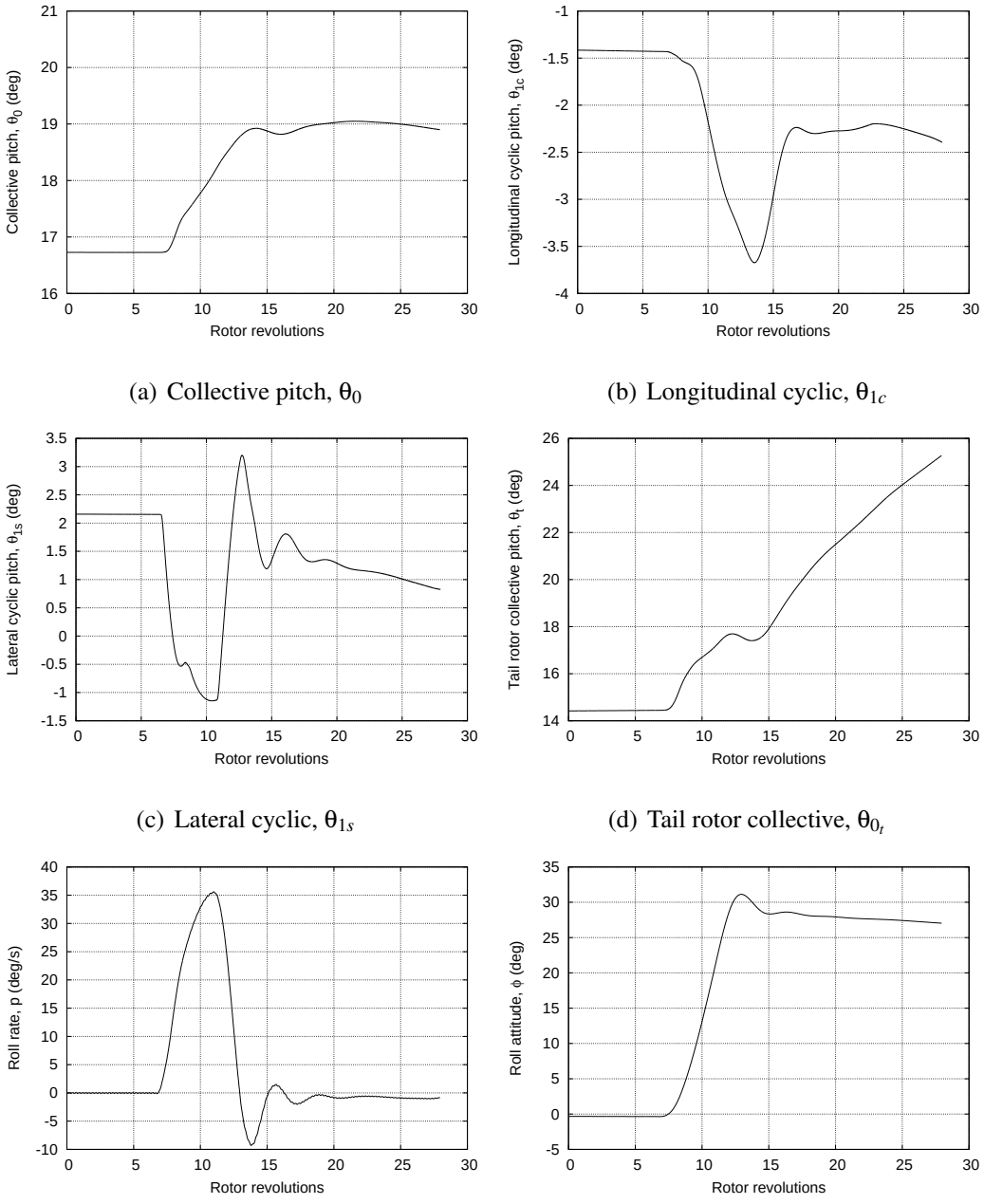


(a) Collective pitch, $\theta_0$

(b) Longitudinal cyclic, $\theta_{1c}$

(c) Lateral cyclic, $\theta_{1s}$

(d) Tail rotor collective, $\theta_{0_t}$

(e) Roll rate, $p$

(f) Roll attitude, $\phi$

Figure 4.30: Time-histories of pilot control inputs used to perform a starboard roll maneuver over 1 second and the resulting roll response: (a) Collective pitch, (b) longitudinal cyclic, (c) lateral cyclic, (d) tail rotor collective, (e) roll rate, and (f) roll attitude.

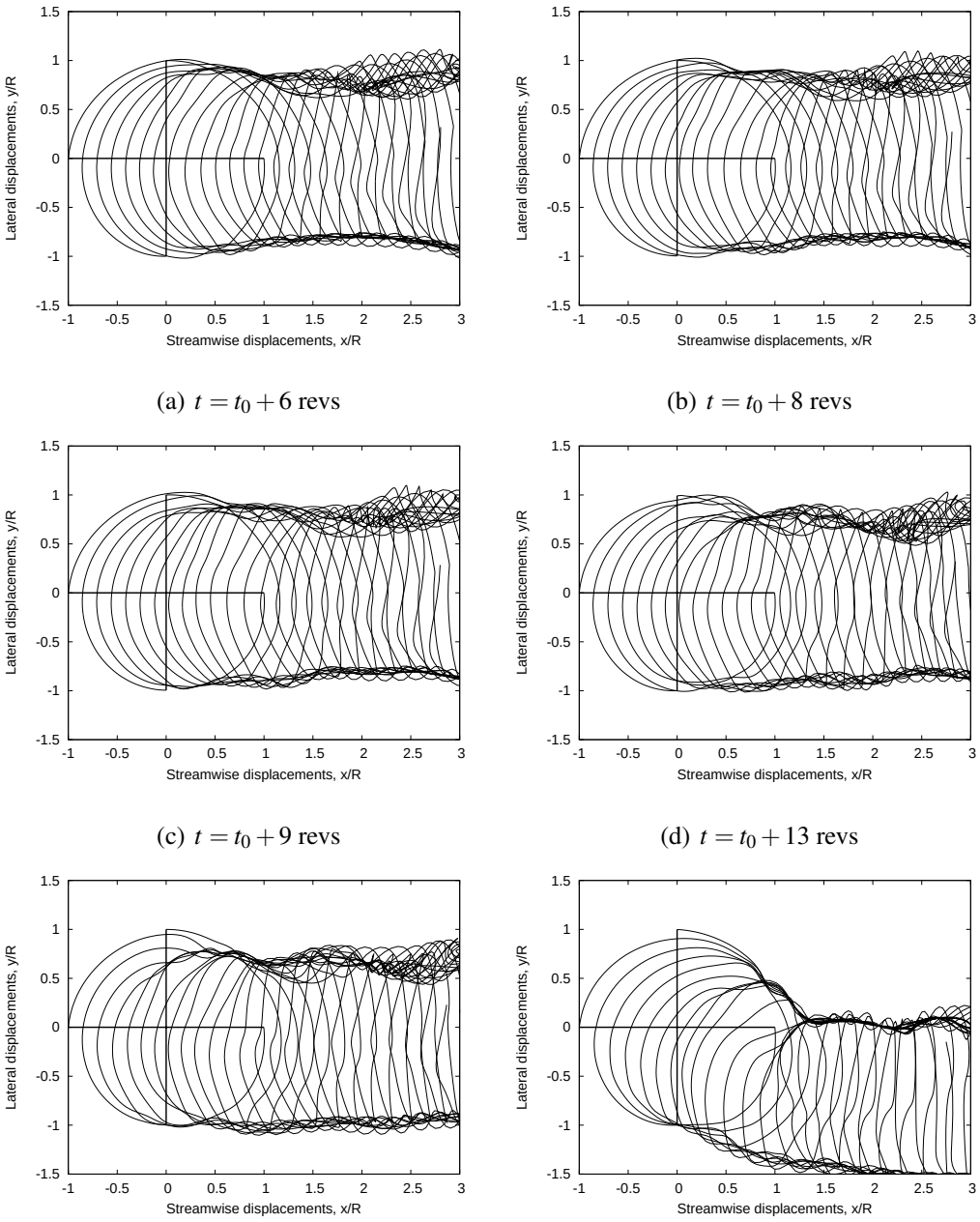


(a) $t = t_0 + 6$ revs

(b) $t = t_0 + 8$ revs

(c) $t = t_0 + 9$ revs

(d) $t = t_0 + 13$ revs

(e) $t = t_0 + 15$ revs

(f) $t = t_0 + 22$ revs

Figure 4.31: Top views of the predicted wake geometries for a representative, four-bladed rotor undergoing a starboard roll over a duration of one second, $\mu = 0.093$: (a) Before initiation of the maneuver, (b) after 2 revolutions, (c) after 3 revolutions, (d) after 7 revolutions, (e) after 9 revolutions, (f) rotor operating at desired bank angle.

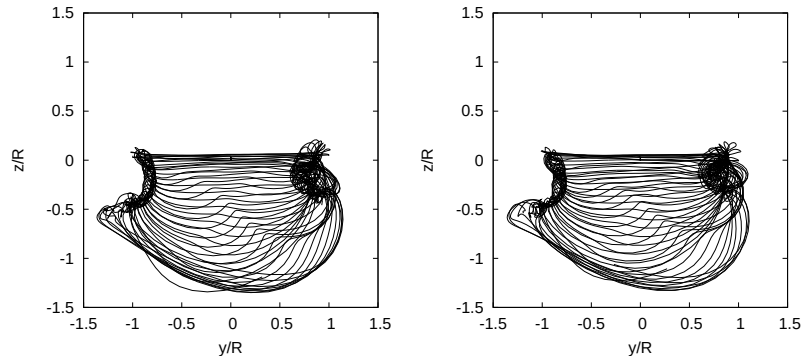


(a) $t = t_0 + 6$ revs




(b) $t = t_0 + 8$ revs

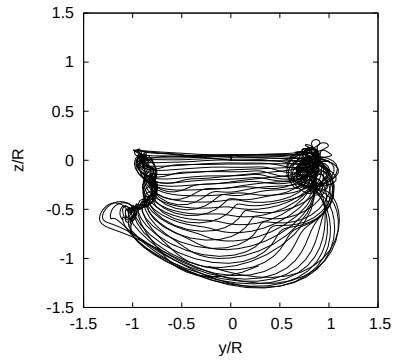


(c) $t = t_0 + 9$ revs

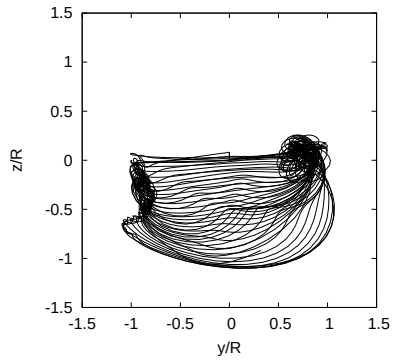


(d) $t = t_0 + 13$ revs

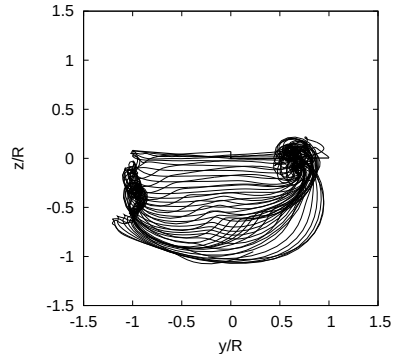


(e) $t = t_0 + 15$ revs

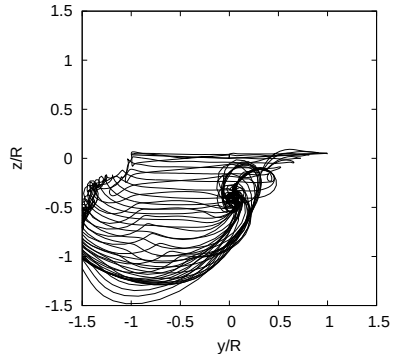


(f) $t = t_0 + 22$ revs

Figure 4.32: Rear views of the predicted wake geometries for a representative, four-bladed rotor undergoing a starboard roll over a duration of one second, $\mu = 0.093$: (a) Before initiation of the maneuver, (b) after 2 revolutions, (c) after 3 revolutions, (d) after 7 revolutions, (e) after 9 revolutions, (f) rotor operating at desired bank angle.

intensity of the "super-BVI" in this case is much less in comparison to that observed in the previous case (c.f., Fig. 4.33(e) with Fig. 4.27(d)).

Figure 4.34 shows the thrust and power time-histories predicted by the free-vortex wake methodology. The fluctuation associated with the pilot's correction of the overshoot in the bank attitude is considerably mitigated in comparison to the previous case.

The BVI sound level pressure predictions from PWU-WOPWOP is shown in Fig. 4.35. It is seen that the intensity of noise generated is not as severe compared to the previous maneuver – see Fig. 4.29

Finally, Fig. 4.36 shows the control inputs and the corresponding roll response for the slowest starboard roll manuever considered in the present study, over a duration of 5 seconds with a maximum transient roll rate of only 6°/s. In this case there is no overshoot of the desired bank angle and the maneuver is very benign compared to the two previous cases.

Figures 4.37 and 4.38 show the snapshots of the top and rear views of the wake respectively for this case. The transient wake dynamics show no tendency to form bundles throughout the maneuver. The wake geometry looks very similar to that during steady flight condition for most of the maneuver.

The contours of lift distribution — see Fig. 4.39 show no evidence of a "super-BVI" for the slowest starboard roll maneuver. This is not surprising because the wake dynamics (see Fig. 4.37) are essentially quasi-steady throughout the maneuver, and do not interact closely with the rotor blades. There is a slight intensification of the BVIs over the advancing side of the disk, similar to those observed with the more aggressive roll maneuvers considered previously. Finally, Fig. 4.34 shows the time-histories of the thrust and power. The thrust and power show no fluctuations as was

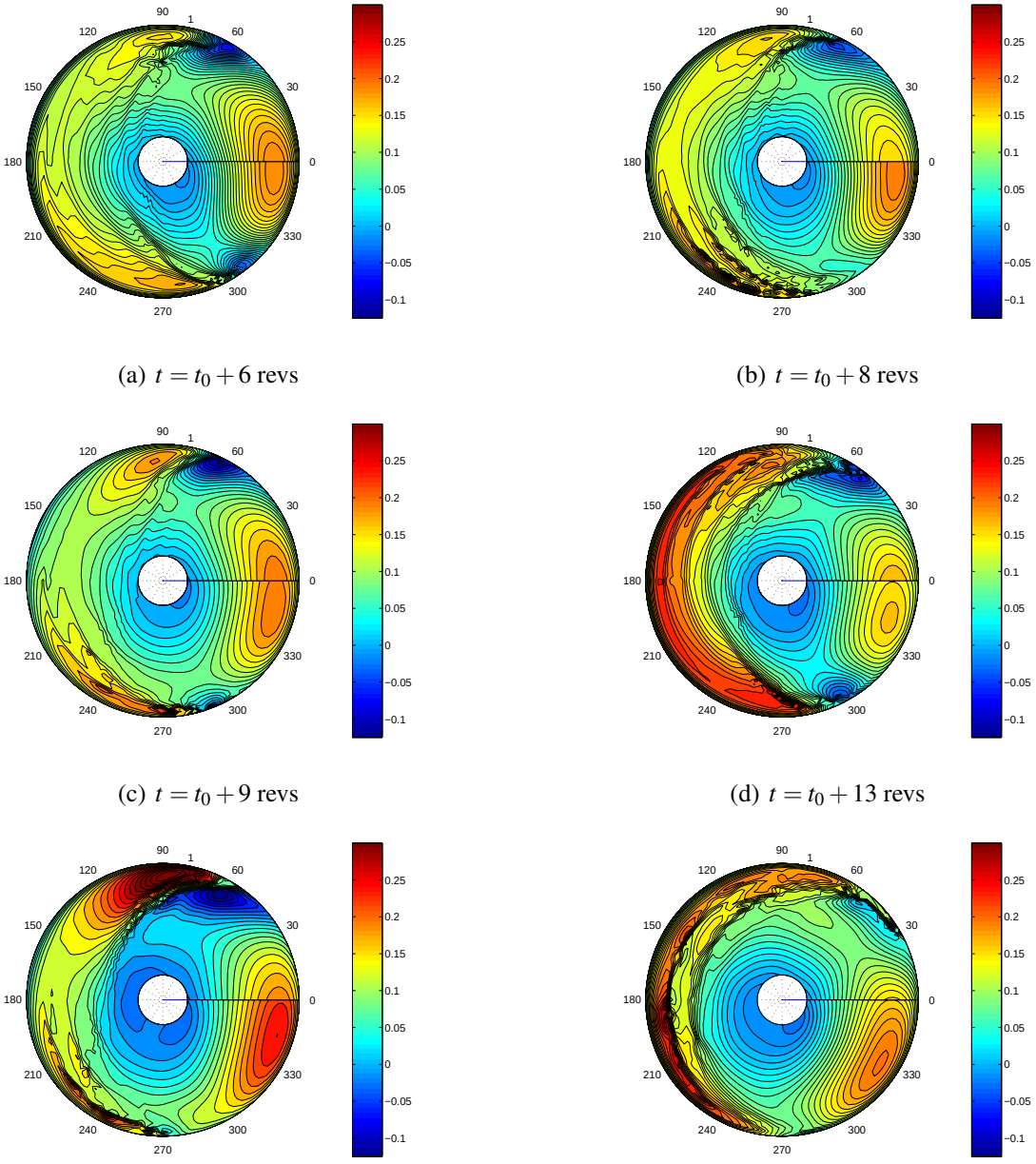


(a) $t = t_0 + 6$ revs

(b) $t = t_0 + 8$ revs

(c) $t = t_0 + 9$ revs

(d) $t = t_0 + 13$ revs

(e) $t = t_0 + 15$ revs

(f) $t = t_0 + 22$ revs

Figure 4.33: Contours of the non-dimensional lift distribution for a representative, four-bladed rotor undergoing a starboard roll over a duration of 1 second, $\mu = 0.093$: (a) Before initiation of the maneuver, (b) after 2 revolutions, (c) after 3 revolutions, (d) after 7 revolutions, (e) after 9 revolutions, (f) rotor operating at desired bank angle.

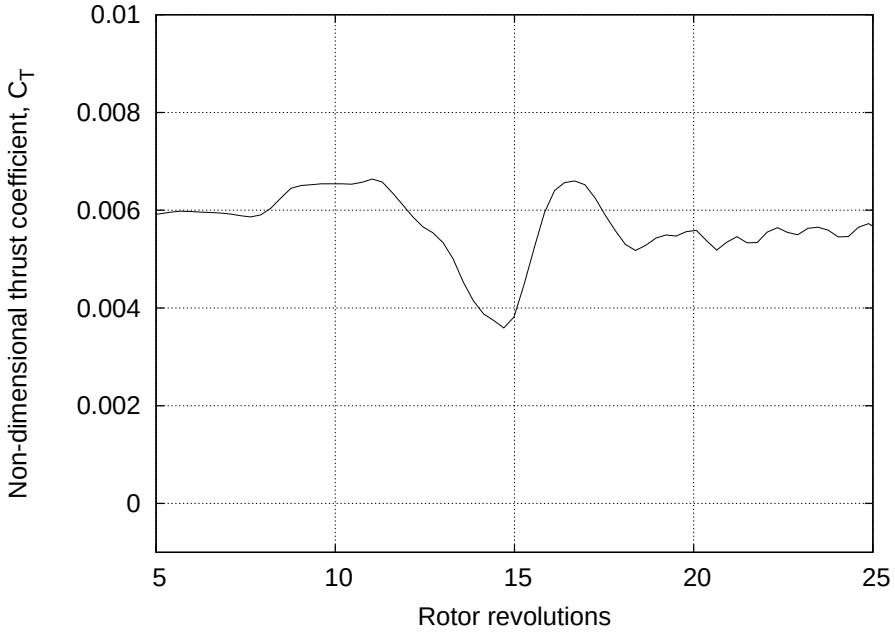


(a) Non-dimensional thrust coefficient

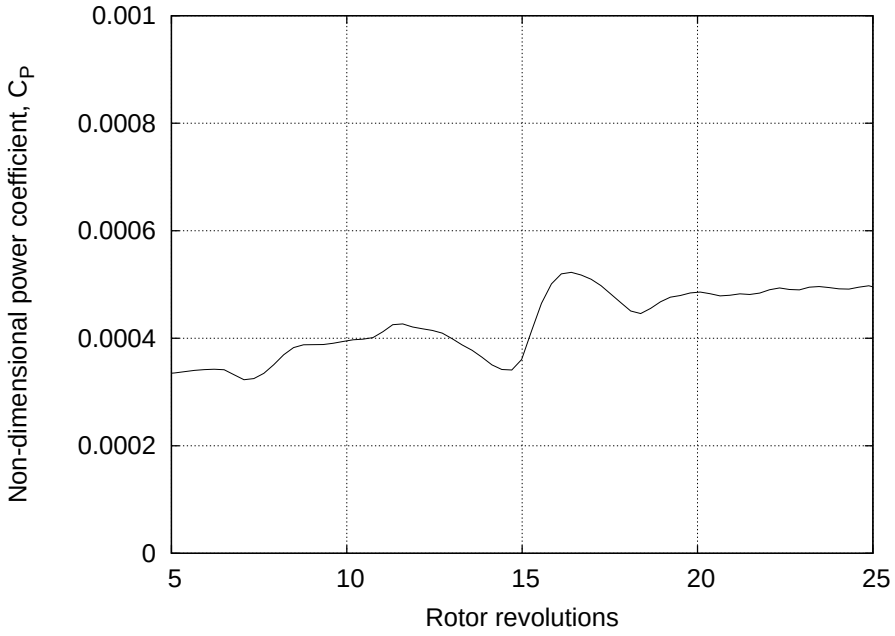


(b) Non-dimensional power coefficient

Figure 4.34: Time-histories of the thrust and power predictions for a rotor executing a starboard roll over a duration of 1 second: (a) Thrust, and (b) Power.

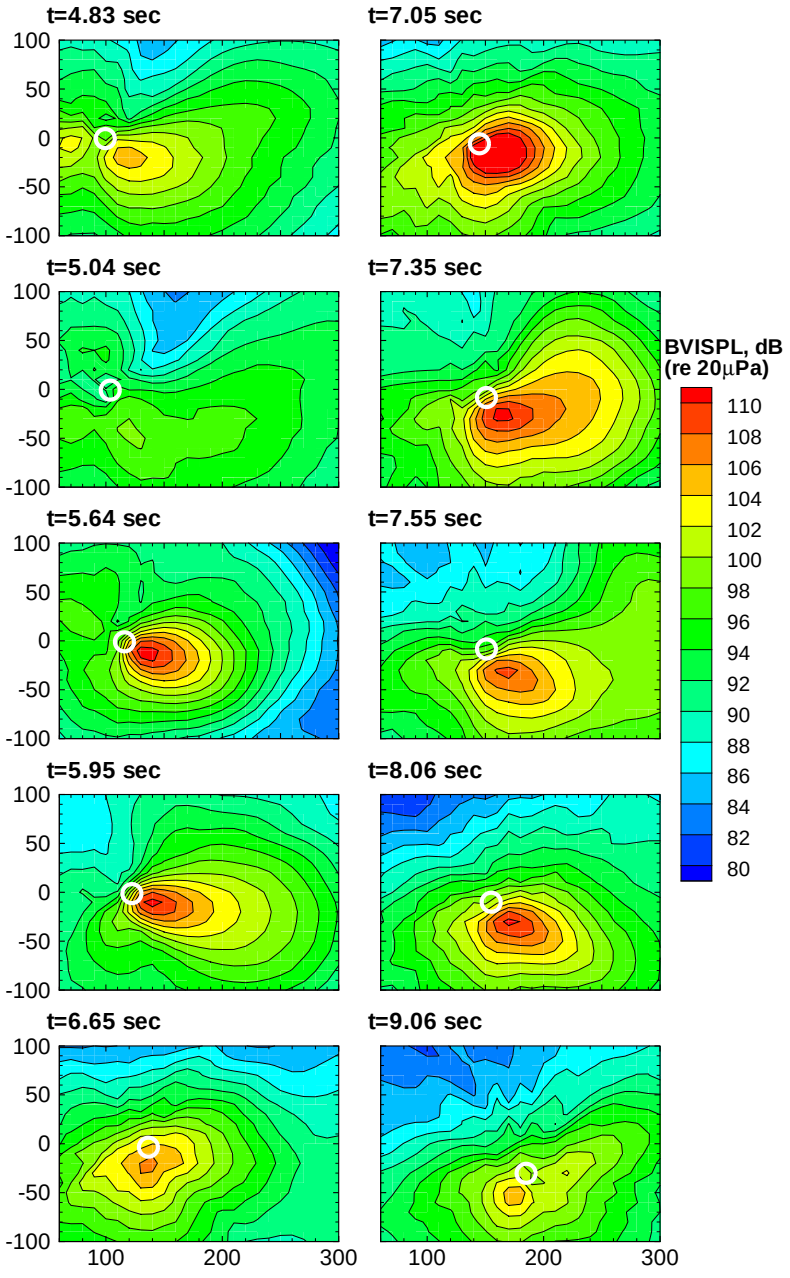


Figure 4.35: Plot showing the BVI sound pressure levels predicted by PSU-WOPWOP for a rotor executing a starboard roll maneuver over a duration of 1 second, $\mu = 0.093$.

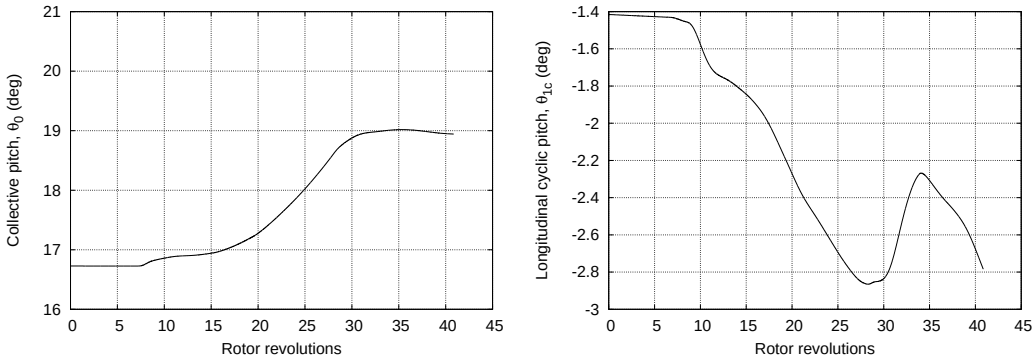


(a) Collective pitch, $\theta_0$




(b) Longitudinal cyclic, $\theta_{1c}$

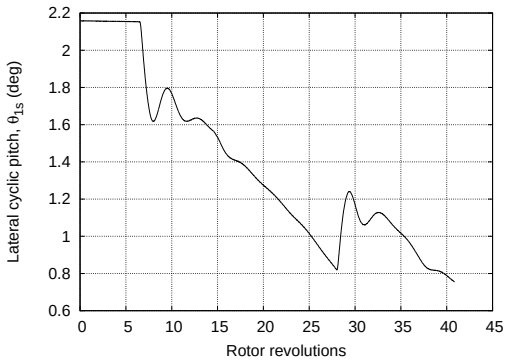


(c) Lateral cyclic, $\theta_{1s}$

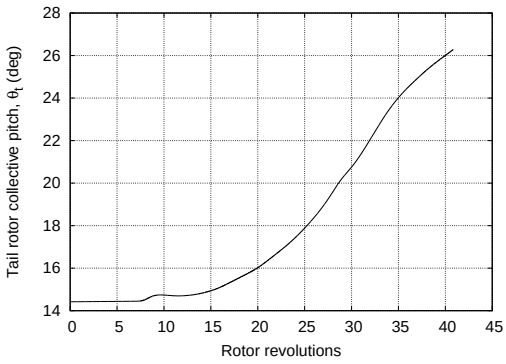


(d) Tail rotor collective, $\theta_{0_t}$

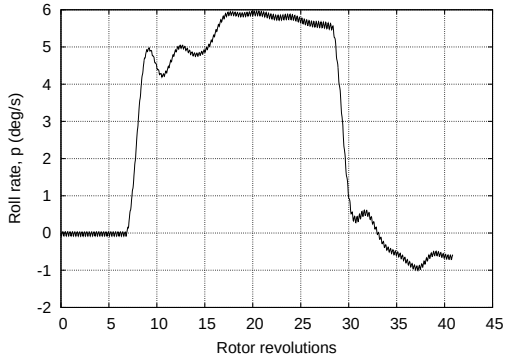


(e) Roll rate, $p$

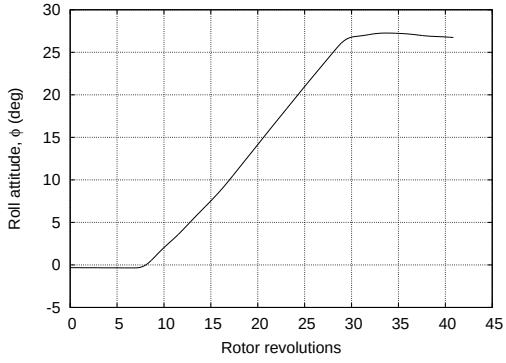


(f) Roll attitude, $\phi$

Figure 4.36: Time-histories of pilot control inputs used to perform a starboard roll maneuver over 5 seconds and the resulting roll response: (a) Collective pitch, (b) longitudinal cyclic, (c) lateral cyclic, (d) tail rotor collective, (e) roll rate, and (f) roll attitude.

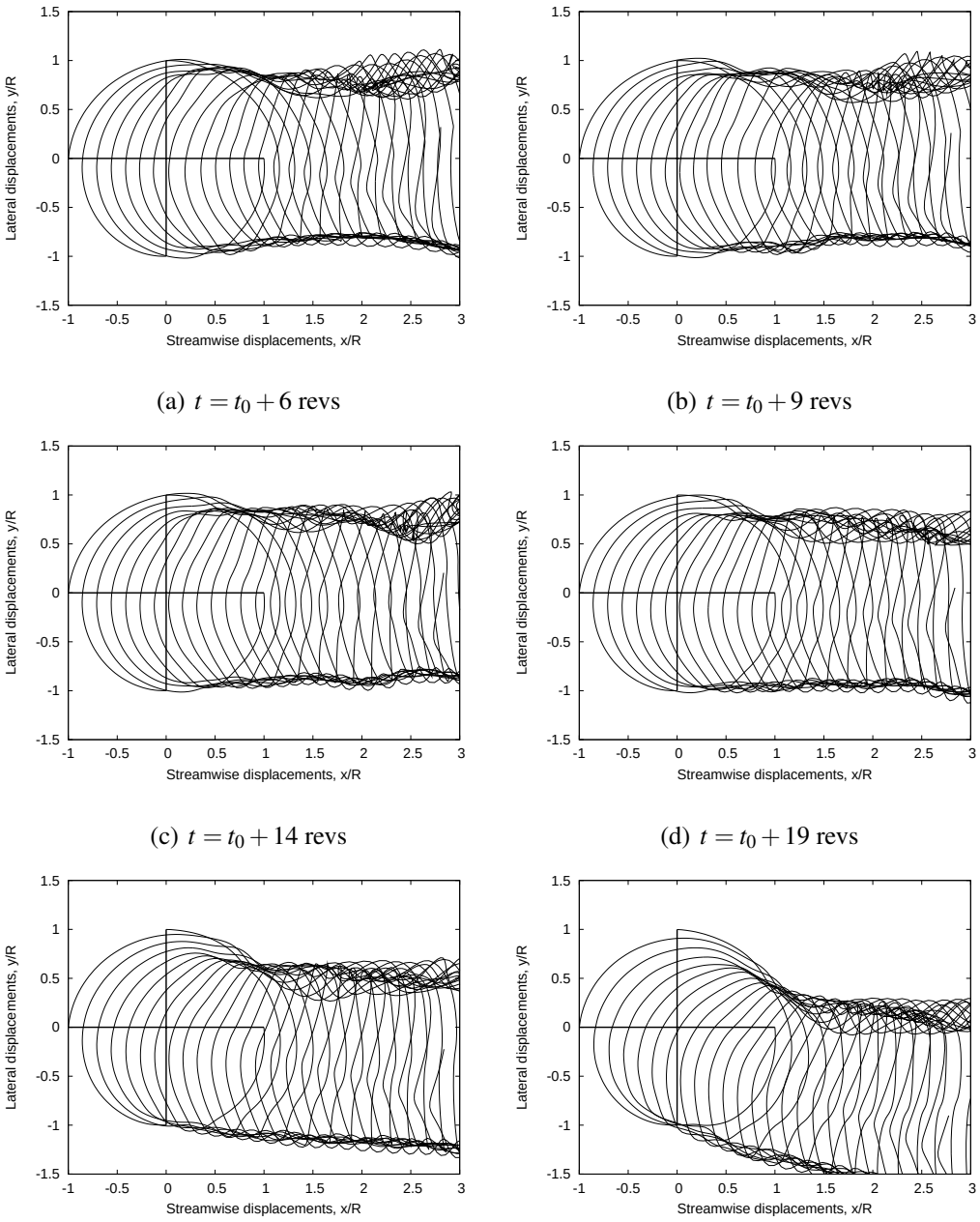


(a) $t = t_0 + 6$ revs

(b) $t = t_0 + 9$ revs

(c) $t = t_0 + 14$ revs

(d) $t = t_0 + 19$ revs

(e) $t = t_0 + 26$ revs

(f) $t = t_0 + 32$ revs

Figure 4.37: Top views of the predicted wake geometries for a representative, four-bladed rotor undergoing a starboard roll over a duration of 5 seconds, $\mu = 0.093$: (a) Before initiation of the maneuver, (b) after 3 revolutions, (c) after 9 revolutions, (d) after 14 revolutions, (e) after 21 revolutions, (f) rotor operating at desired bank angle.

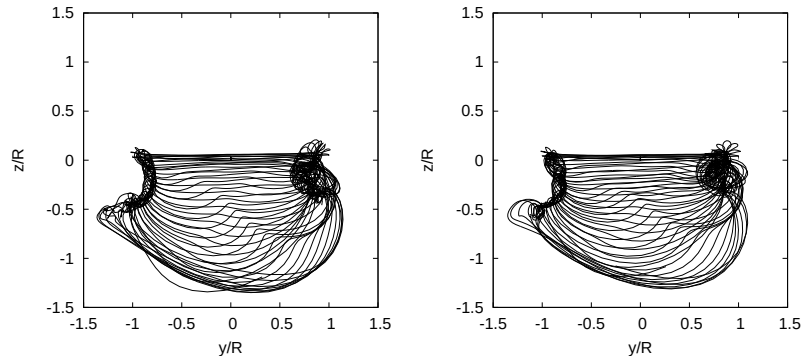


(a) $t = t_0 + 6$ revs




(b) $t = t_0 + 9$ revs

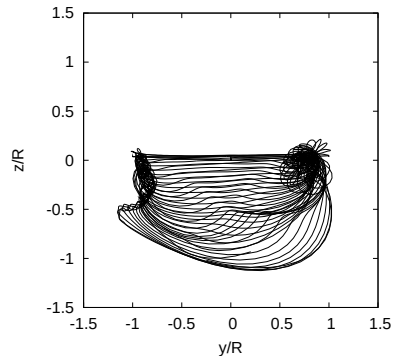


(c) $t = t_0 + 14$ revs

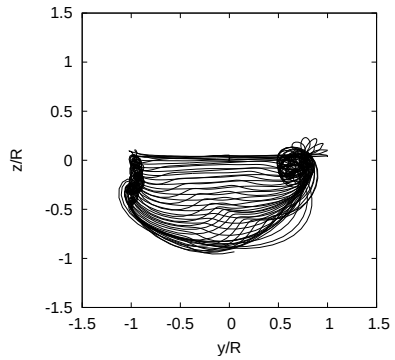


(d) $t = t_0 + 19$ revs

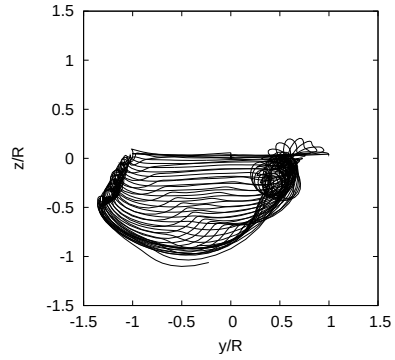


(e) $t = t_0 + 26$ revs

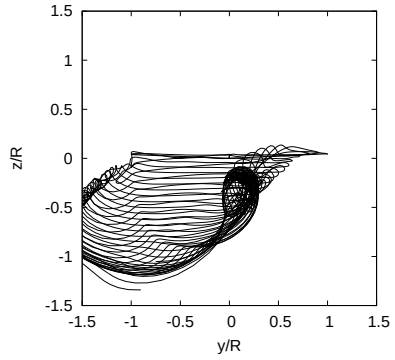


(f) $t = t_0 + 32$ revs

Figure 4.38: Rear views of the predicted wake geometries for a representative, four-bladed rotor undergoing a starboard roll over a duration of 5 seconds, $\mu = 0.093$: (a) Before initiation of the maneuver, (b) after 3 revolutions, (c) after 9 revolutions, (d) after 14 revolutions, (e) after 21 revolutions, (f) rotor operating at desired bank angle.

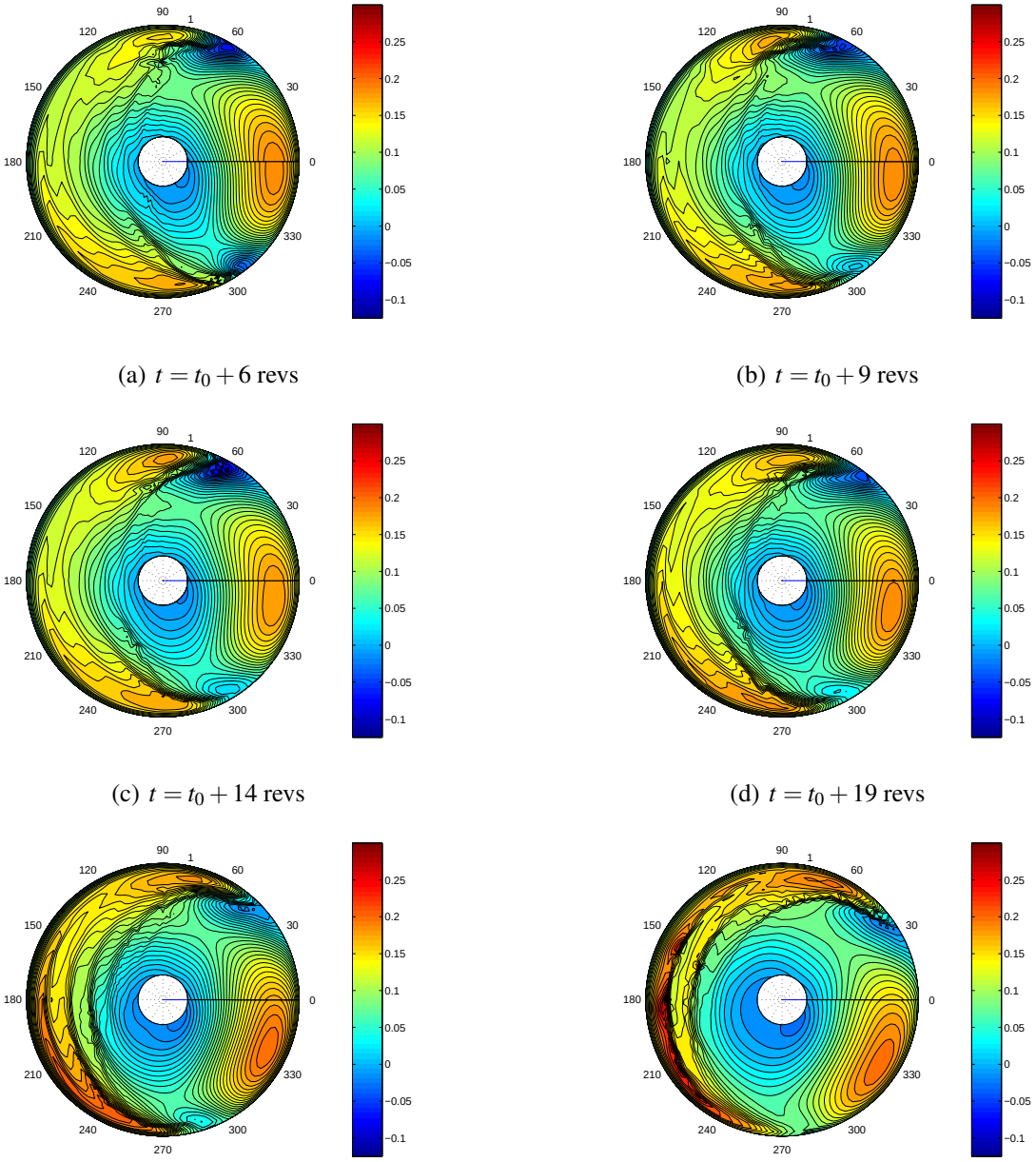


(a) $t = t_0 + 6$ revs

(b) $t = t_0 + 9$ revs

(c) $t = t_0 + 14$ revs

(d) $t = t_0 + 19$ revs

(e) $t = t_0 + 26$ revs

(f) $t = t_0 + 32$ revs

Figure 4.39: Contours of the non-dimensional lift distribution for a representative, four-bladed rotor undergoing a starboard roll over a duration of 5 seconds, $\mu = 0.093$: (a) Before initiation of the maneuver, (b) after 2 revolutions, (c) after 3 revolutions, (d) after 7 revolutions, (e) after 9 revolutions, (f) rotor operating at desired bank angle.

observed in the previous cases. The variation in thrust and power values are essentially quasi-steady for this maneuver.

The three starboard roll maneuvers considered highlight the sensitivity of the rotor wake aerodynamics to the roll rates imposed on the rotor. Furthermore, it emphasizes the importance of taking into account the human pilot for helicopter flight dynamic simulations. It is evident from the most aggressive starboard roll maneuver that even slight perturbations of the control pitch inputs by pilots to rectify attitude and/or trajectory errors can lead to intense BVIs, which can have a significant impact on the rotor noise signature.

**Roll to Port**

A roll to port was considered to study the differences in the wake evolution and its effect on the transient airloads compared to the starboard roll maneuver considered previously. Figure 4.41 shows the time-histories of the control inputs and the resulting roll rate, $p$, and the roll attitude, $\phi$, imposed on the rotor to perform this maneuver. The maneuver was again performed such that helicopter finally entered a constant radius,banked turn. As with the starboard roll there is an overshoot of the target bank angle, which is corrected by rolling slightly to starboard.

While the qualitative nature of maneuver is very similar to the starboard roll considered previously, there are subtle differences. The final bank angle when the helicopter enters the coordinated turn is approximately $32^\circ$ (as compared to $\phi \approx 27^\circ$ in the starboard roll case). While the final bank angle is slightly greater than that for the starboard roll case, the maximum roll rate during the roll to port is only $45^\circ$/s. The differences can be attributed to the asymmetries in the rotor loads in the forward flight condition and the presence of a tail rotor in the GENHEL simulation; the latter

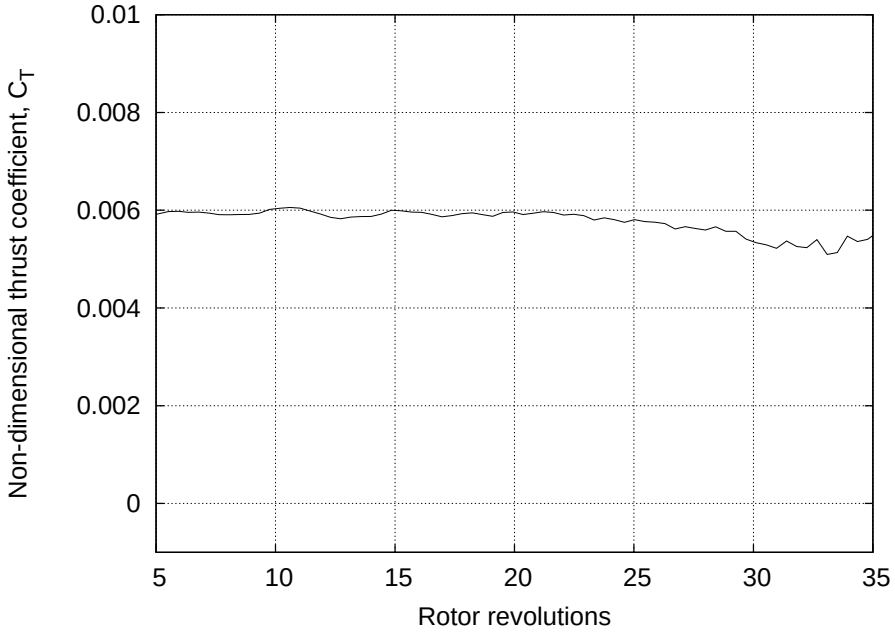


(a) Non-dimensional thrust coefficient

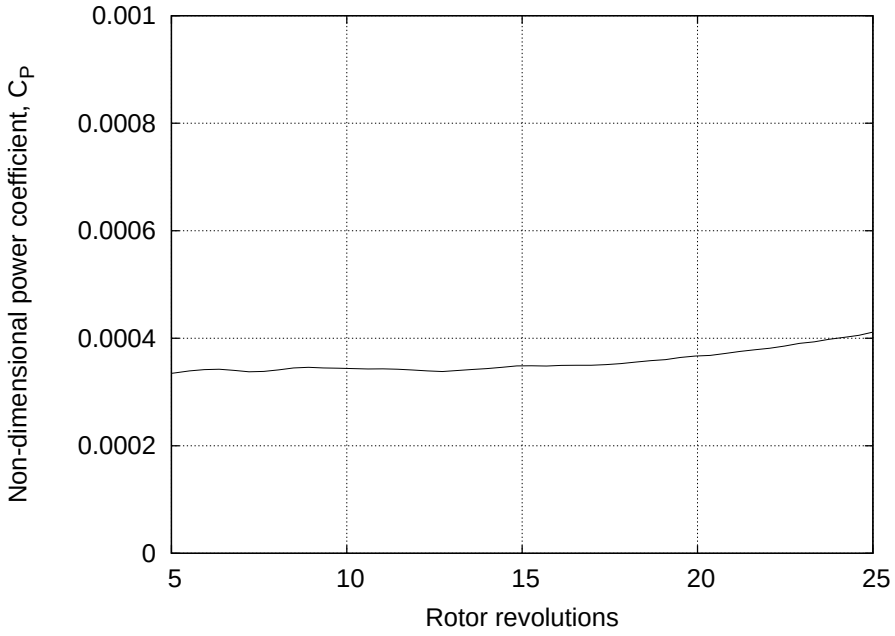


(b) Non-dimensional power coefficient

Figure 4.40: Time-histories of the thrust and power predictions for a rotor executing a starboard roll over a duration of 5 seconds: (a) Thrust, and (b) Power.

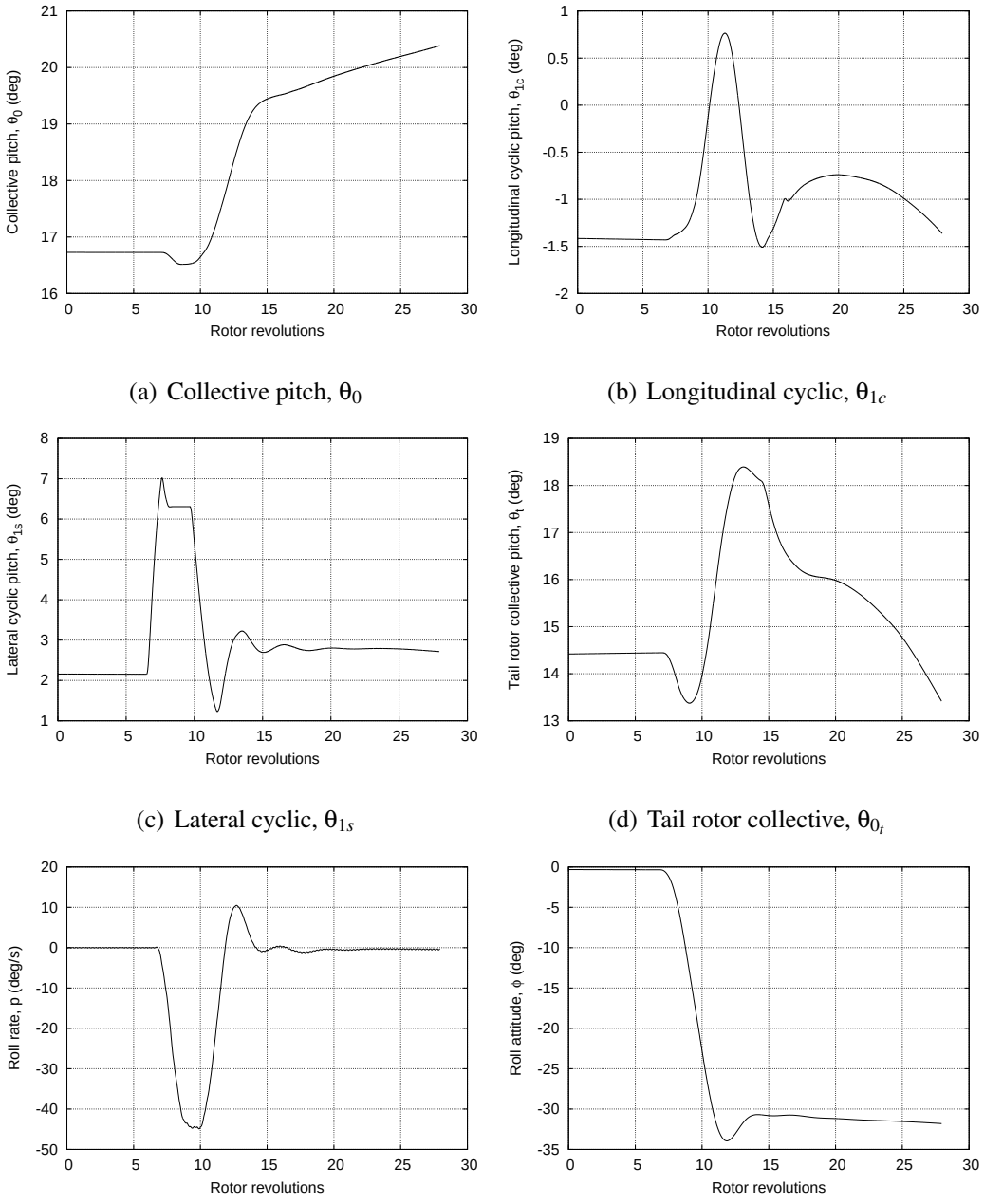


(a) Collective pitch, $\theta_0$

(b) Longitudinal cyclic, $\theta_{1c}$

(c) Lateral cyclic, $\theta_{1s}$

(d) Tail rotor collective, $\theta_{0_t}$

(e) Roll rate, $p$

(f) Roll attitude, $\phi$

Figure 4.41: Time-histories of pilot control inputs used to perform a port roll maneuver over 0.5 second and the resulting roll response: (a) Collective pitch, (b) longitudinal cyclic, (c) lateral cyclic, (d) tail rotor collective, (e) roll rate, and (f) roll attitude.

introduces further asymmetries in the force balance in the horizontal plane. The two maneuvers studied, therefore, are not perfect mirror images of each other. However, they are realistic approximations of a piloted flight maneuver, and so they provide a valuable insight into the rotor aerodynamics that are associated with general rolling type of maneuvers.

Figures 4.42 and 4.43 show snapshots of the top and rear views of the transient wake geometries at various instances in time during the roll to port. The behavior is similar to that observed for the starboard roll, except that now the wake passes up through the retreating side of the rotor disk. Notice that the tip vortices tend to bundle in the retreating side as a cyclic blade pitch control correction is applied to compensate for the overshoot in bank angle — see Fig. 4.42(e). However, in this case the vortex bundling (Fig. 4.42(d)) is not as significant as that observed during the starboard roll maneuver (c.f., Fig. 4.25(d)). Strong bundling during the port roll maneuver does not occur until after the tip vortices have been convected away from the rotor disk.

Figure 4.44 shows the contours of the non-dimensional lift across the rotor disk at various instances in time during the maneuver. Notice the evidence of the formation of BVIs over the retreating side of the rotor disk. However, the vortex bundling toward the end of the maneuver does not produce a super-BVI, as was observed with the starboard roll. This is because the bundling occurs farther below the rotor blades and does not interact closely with the blades as was observed in the case of the most aggressive starboard roll — see Fig. 4.27(e). Figure 4.45 shows the time-histories of the thrust and power predicted by the free-vortex wake methodology. Notice that the fluctuations associated with the piloting correction are not as significant as those observed during the starboard roll maneuver (c.f., Fig. 4.28). This is expected because the BVIs during the port roll are not as intense as observed during the starboard roll.

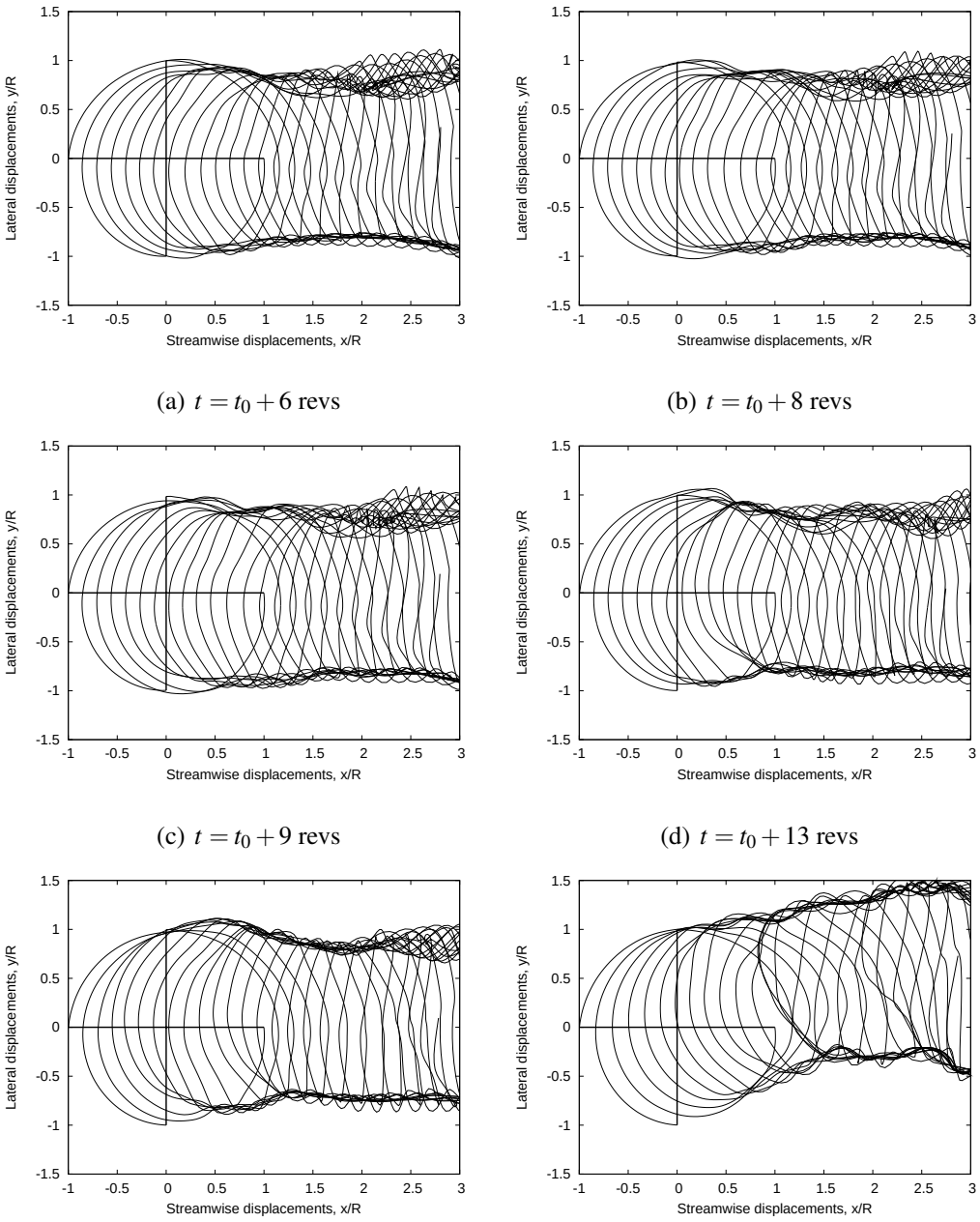


(a) $t = t_0 + 6$ revs

(b) $t = t_0 + 8$ revs

(c) $t = t_0 + 9$ revs

(d) $t = t_0 + 13$ revs

(e) $t = t_0 + 15$ revs

(f) $t = t_0 + 22$ revs

Figure 4.42: Top views of the predicted wake geometries for a representative, four-bladed rotor undergoing a port roll, $\mu = 0.093$: (a) Before initiation of the maneuver, (b) after 2 revolutions, (c) after 3 revolutions, (d) after 7 revolutions, (e) after 9 revolutions, (f) rotor operating at desired bank angle.

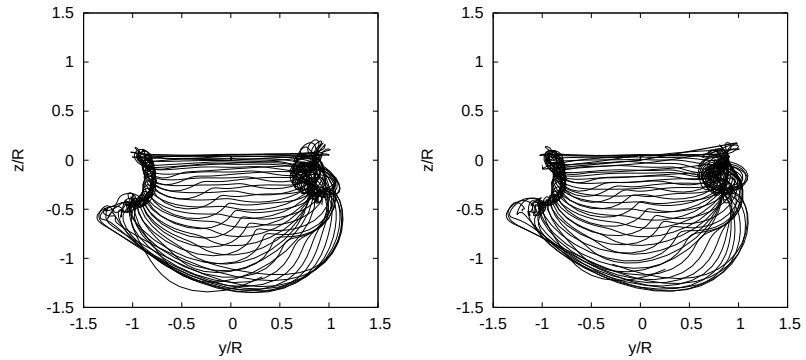


(a) $t = t_0 + 6$ revs




(b) $t = t_0 + 8$ revs

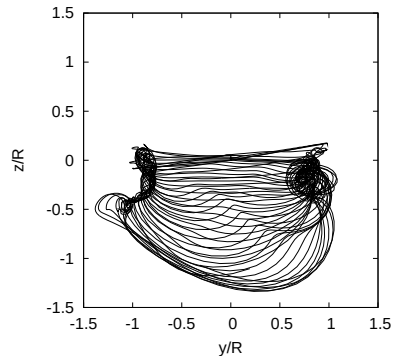


(c) $t = t_0 + 9$ revs

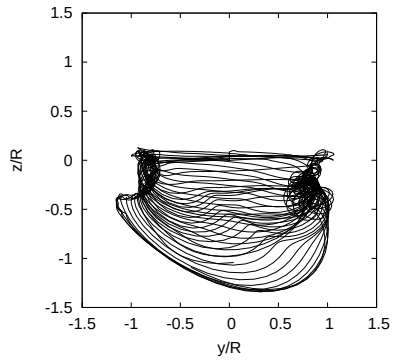


(d) $t = t_0 + 13$ revs

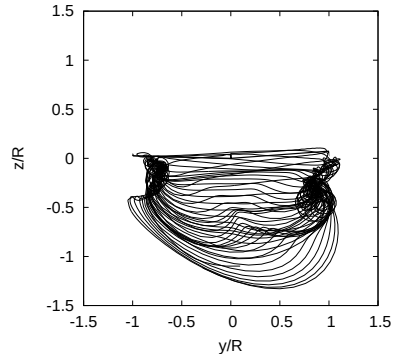


(e) $t = t_0 + 15$ revs

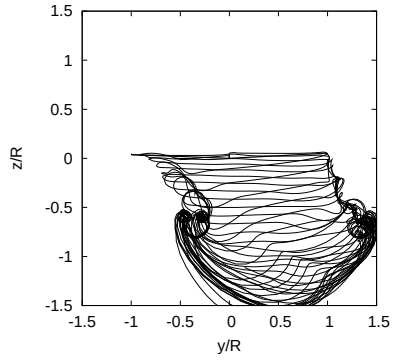


(f) $t = t_0 + 22$ revs

Figure 4.43: Rear views of the predicted wake geometries for a representative, four-bladed rotor undergoing a port roll, $\mu = 0.093$: (a) Before initiation of the maneuver, (b) after 2 revolutions, (c) after 3 revolutions, (d) after 7 revolutions, (e) after 9 revolutions, (f) rotor operating at desired bank angle.

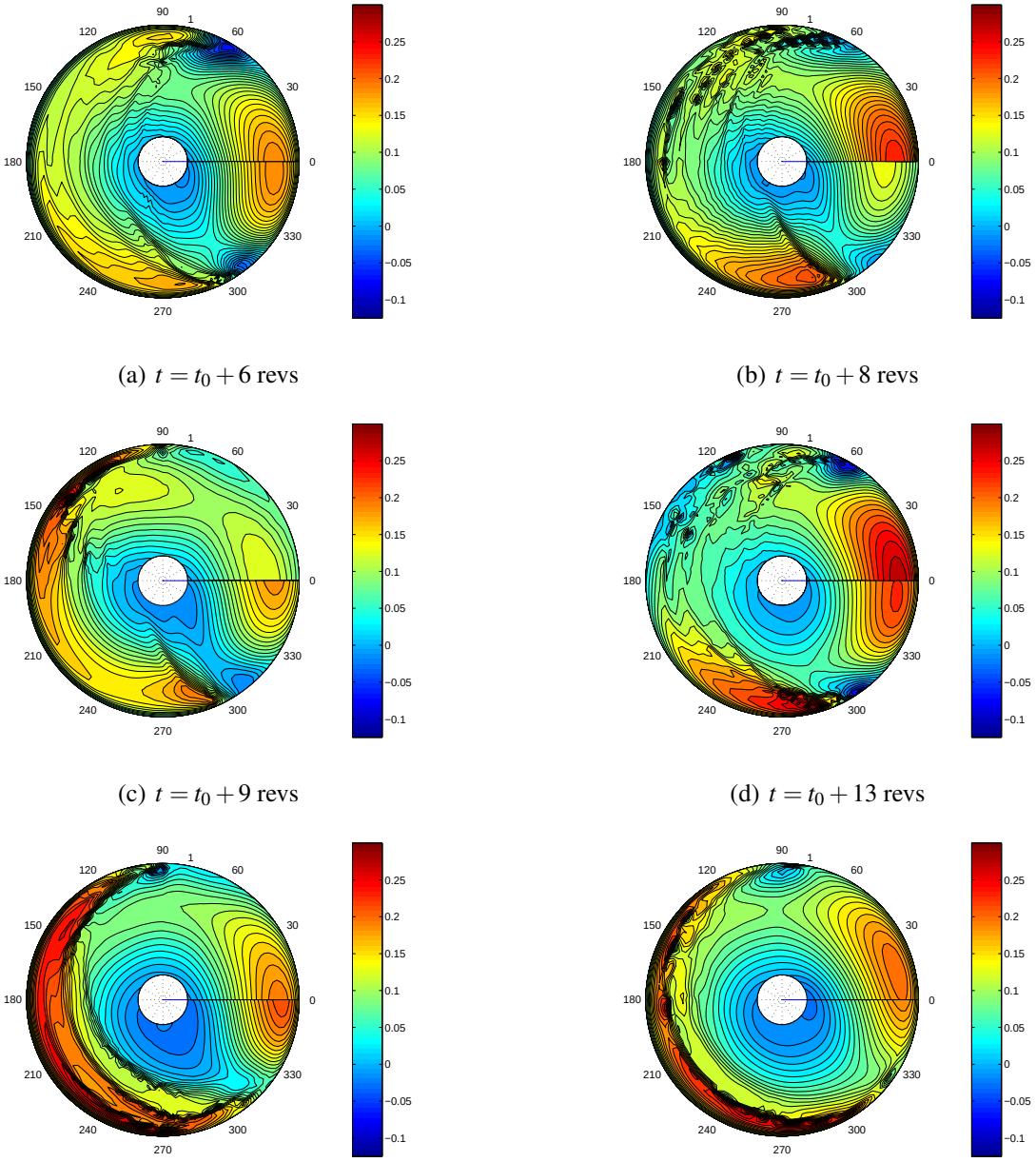


(a) $t = t_0 + 6$ revs

(b) $t = t_0 + 8$ revs

(c) $t = t_0 + 9$ revs

(d) $t = t_0 + 13$ revs

(e) $t = t_0 + 15$ revs

(f) $t = t_0 + 22$ revs

Figure 4.44: Contours of the non-dimensional lift distribution for a representative, four-bladed rotor undergoing a port roll over a duration of 0.5 seconds, $\mu = 0.093$: (a) Before initiation of the maneuver, (b) after 2 revolutions, (c) after 3 revolutions, (d) after 7 revolutions, (e) after 9 revolutions, (f) rotor operating at desired bank angle.

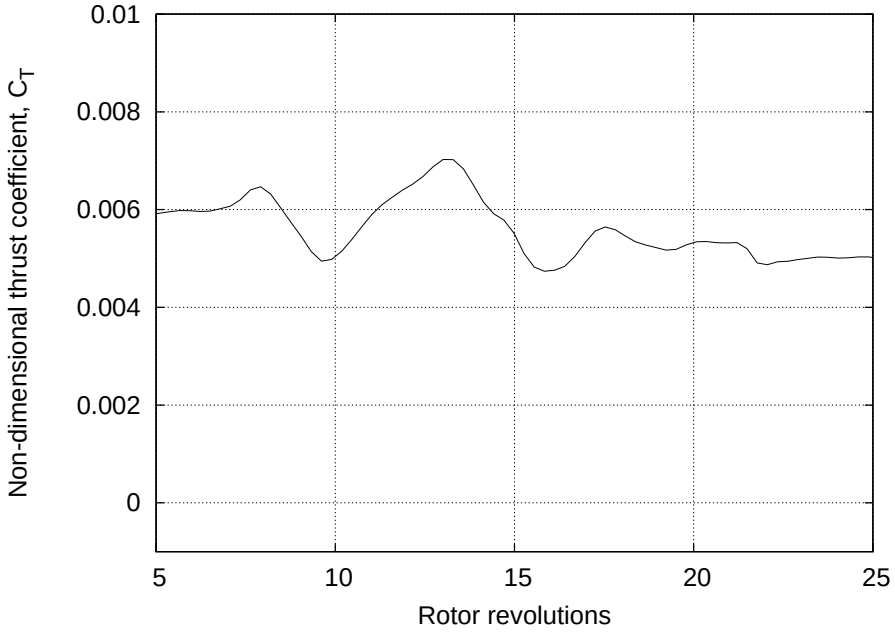


(a) Non-dimensional thrust coefficient

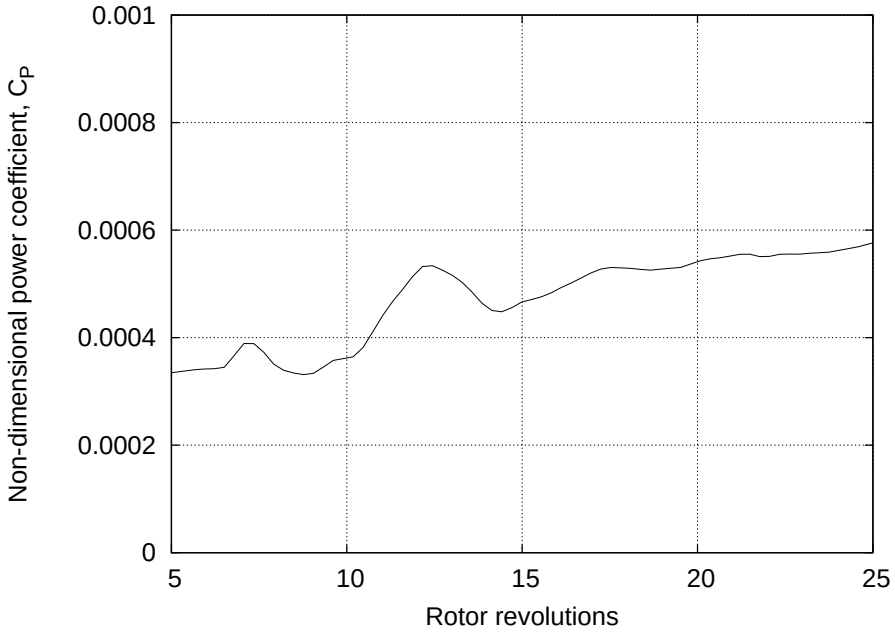


(b) Non-dimensional power coefficient

Figure 4.45: Time-histories of the thrust and power predictions for a rotor executing a port roll over a duration of 0.5 seconds: (a) Thrust, and (b) Power.

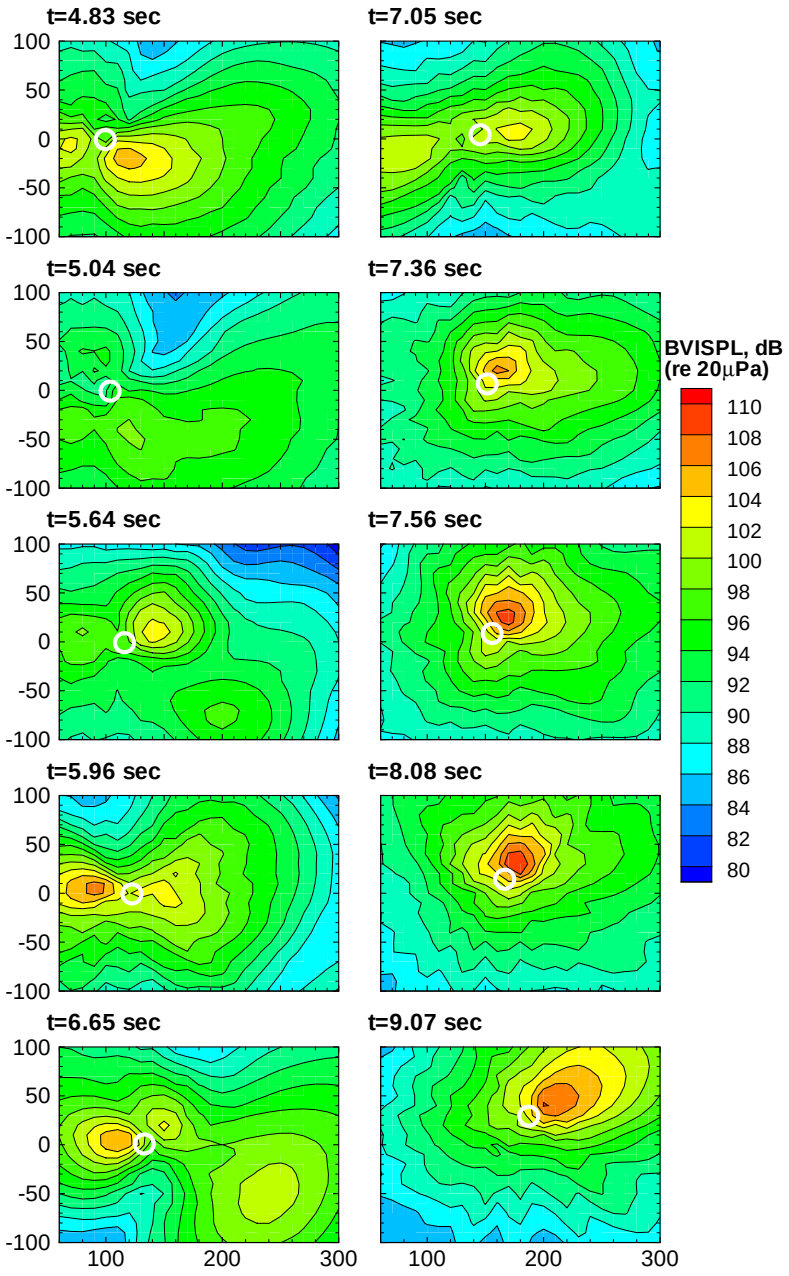


Figure 4.46: Plots showing the BVI sound pressure level predictions by PSU-WOPWOP for a rotor executing a port roll over a duration of 0.5 seconds, $\mu = 0.093$.

The BVI sound pressure level predictions from PSU-WOPWOP shown in Fig. 4.46 show no evidence of intense noise levels for this maneuver as was observed for the starboard roll (c.f., Fig. 4.29). The differences in the starboard and port roll maneuvers emphasizes the asymmetries in the wake geometry and its impact on the evolution of the rotor wake during maneuvers.

Figure 4.47 shows the time-histories of the pilot control pitch inputs and the corresponding roll response for a rotor executing roll to port over a duration of 1 second. The maximum transient roll rate experienced during this maneuver is only 35°/s. The maneuver is a near mirror image of the starboard roll maneuver considered previously. Notice the slight overshoot in the target bank angle which the pilot corrects by rolling slightly to starboard. The roll rates imposed during this correction are of the same magnitude as in the case of the starboard roll and, therefore, would not cause a "super-BVI" event.

Figures 4.48 and 4.49 show the top and rear views of the wake geometries, respectively. The qualitative behavior of the wake aerodynamics is similar to that observed in Figs. 4.42 and 4.43. Note that the tip vortices are more tightly wound up on the retreating side of the disk. However, the vortex wake shows no evidence of bundling in this case. This is not surprising because the roll rates imposed in this case ($p = 35°$/s) are much less in comparison to the previous case ($p = 55°$/s). However, one interesting feature observed in the roll to port cases considered so far is that the steep gradients in the lift distribution — see Fig. 4.50 after the pilot corrects for the overshoot in roll attitude , which show no significant differences when the duration of roll maneuver is increased (c.f., Fig. 4.44(d) and Fig. 4.50(e)). In contrast, the BVI event during the starboard roll was mitigated considerably by increasing the duration of the roll maneuver. The thrust and the power time-histories for this maneuver are shown

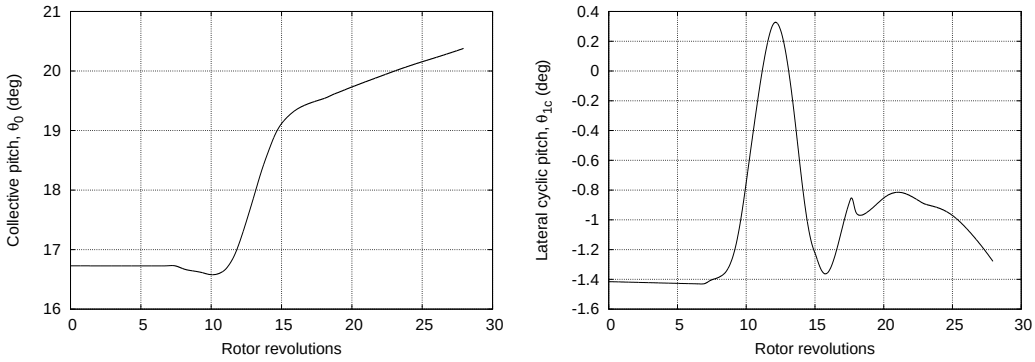


(a) Collective pitch, $\theta_0$




(b) Longitudinal cyclic, $\theta_{1c}$

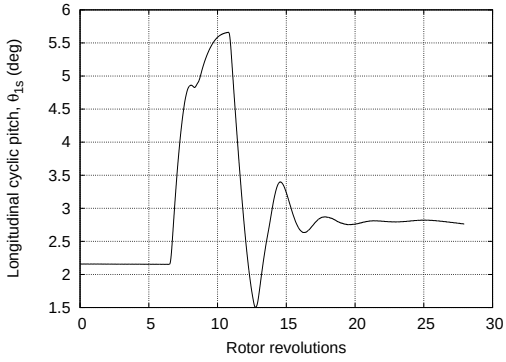


(c) Lateral cyclic, $\theta_{1s}$

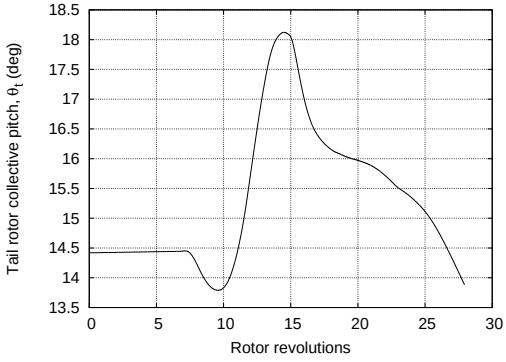


(d) Tail rotor collective, $\theta_{0_t}$

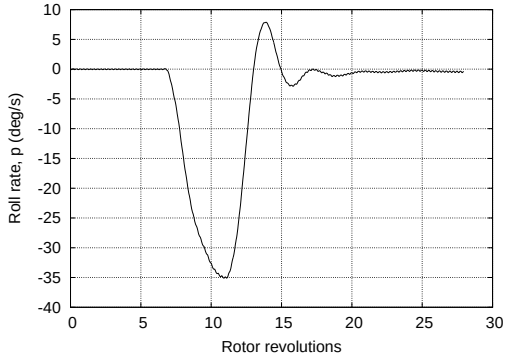


(e) Roll rate, $p$

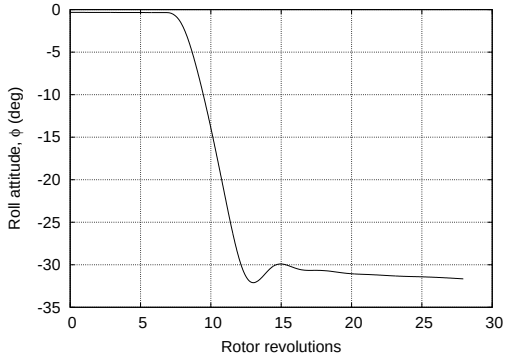


(f) Roll attitude, $\phi$

Figure 4.47: Time-histories of pilot control inputs used to perform a port roll maneuver over 1 second and the resulting roll response: (a) Collective pitch, (b) longitudinal cyclic, (c) lateral cyclic, (d) tail rotor collective, (e) roll rate, and (f) roll attitude.

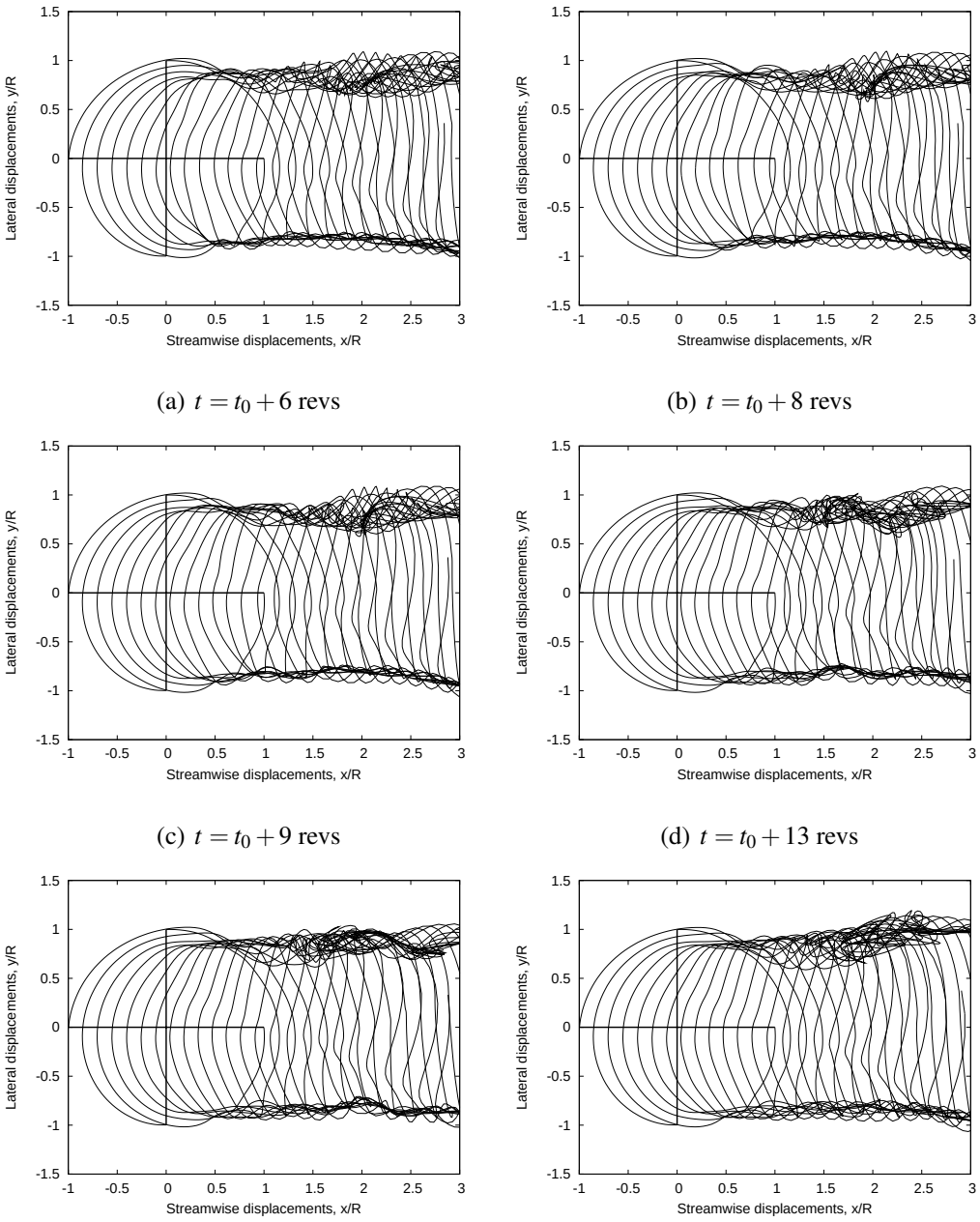


(a) $t = t_0 + 6$ revs

(b) $t = t_0 + 8$ revs

(c) $t = t_0 + 9$ revs

(d) $t = t_0 + 13$ revs

(e) $t = t_0 + 15$ revs

(f) $t = t_0 + 22$ revs

Figure 4.48: Top views of the predicted wake geometries for a representative, four-bladed rotor undergoing a port roll over a duration of 1 second, $\mu = 0.093$: (a) Before initiation of the maneuver, (b) after 2 revolutions, (c) after 3 revolutions, (d) after 7 revolutions, (e) after 9 revolutions, (f) rotor operating at desired bank angle.

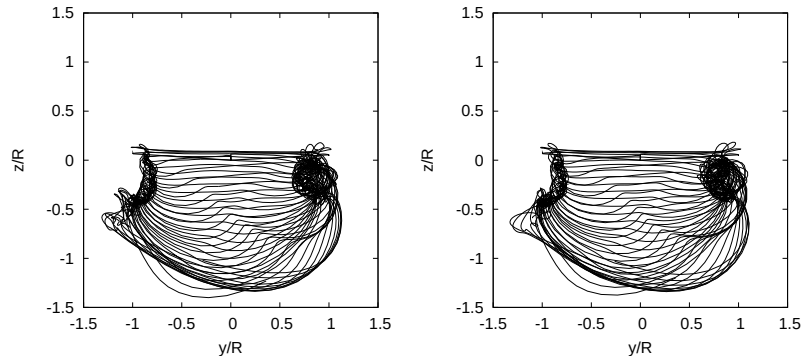


(a) $t = t_0 + 6$ revs




(b) $t = t_0 + 8$ revs

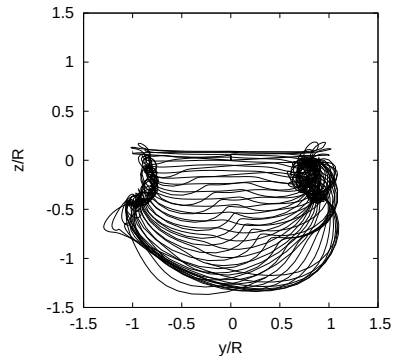


(c) $t = t_0 + 9$ revs

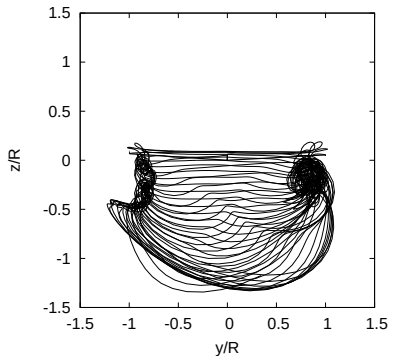


(d) $t = t_0 + 13$ revs

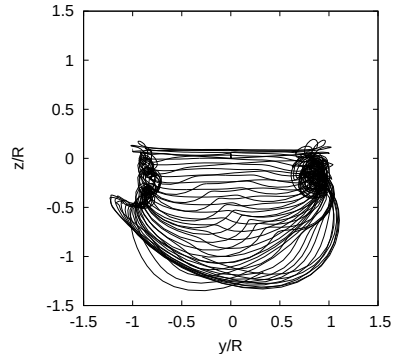


(e) $t = t_0 + 15$ revs

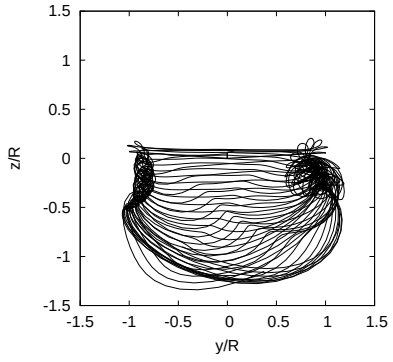


(f) $t = t_0 + 22$ revs

Figure 4.49: Rear views of the predicted wake geometries for a representative, four-bladed rotor undergoing a port roll over a duration of 1 second, $\mu = 0.093$: (a) Before initiation of the maneuver, (b) after 2 revolutions, (c) after 3 revolutions, (d) after 7 revolutions, (e) after 9 revolutions, (f) rotor operating at desired bank angle.

in Fig. 4.51.

The BVI sound pressure level predictions by PSU-WOPWOP show no evidence of intense acoustic radiation for the entire duration of the maneuver – see Fig. 4.52. The noise directivity patterns are similar to those observed in the previous port roll maneuver (c.f. Fig. 4.46) and the noise intensity levels are comparable at various stages of the maneuver. Increasing the time duration for the maneuver for the starboard roll was seen to considerably mitigate the intensity of the noise generated, further emphasizing the asymmetries during starboard and port roll maneuver.

Figure 4.53 shows the time-histories of the control inputs used to simulate the slowest roll to port maneuver and the resulting roll response. As with the starboard roll maneuver considered previously, the maximum transient roll rate experienced by the rotor during the maneuver is only 6°/s.

Figures 4.54 and 4.55 show the top and side views respectively of the wake geometries at various instances in time during this maneuver. The wake aerodynamics shows a slight intensification of the roll up on the retreating side of the rotor disk as the maneuver progresses. However, there is no propensity of the tip vortices to bundle, as was observed with the aggressive roll maneuvers.

Figure 4.56 shows the contours of the non-dimensional lift distribution for this maneuver. Notice that the BVIs on the retreating side are intensified as the rotor banks to the left. This is because the tip vortices on the retreating side come into close proximity to the rotor blades. The change in the lift distribution is gradual and there is no evidence of "super-BVI" conditions for this flight condition. The time-histories of the thrust and power are shown in Fig. 4.57.

Figure 4.58 shows the individual blade flapping time-histories for the starboard and port roll maneuvers. The time-histories have been phase-shifted for individual

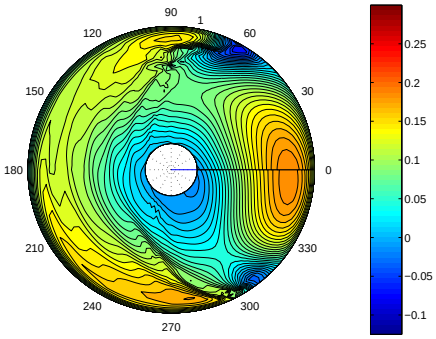


(a) $t = t_0 + 6$ revs

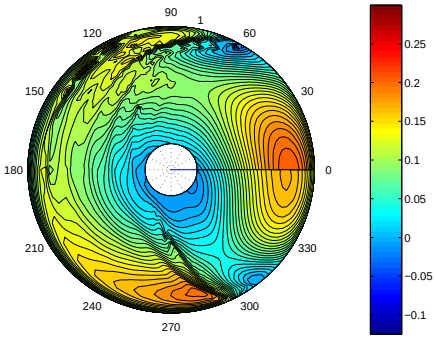


(b) $t = t_0 + 8$ revs

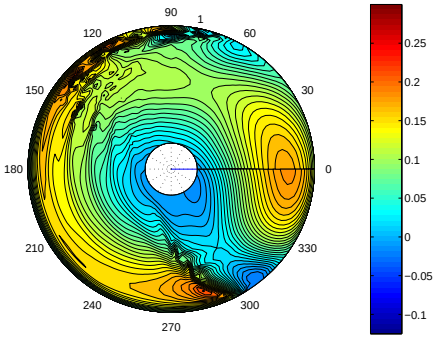


(c) $t = t_0 + 9$ revs

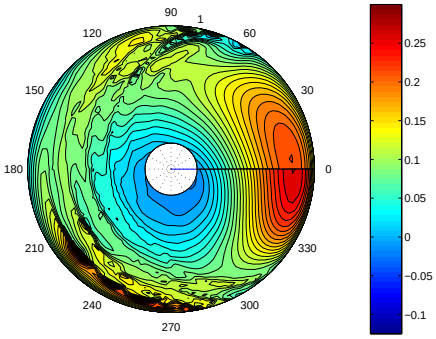


(d) $t = t_0 + 13$ revs

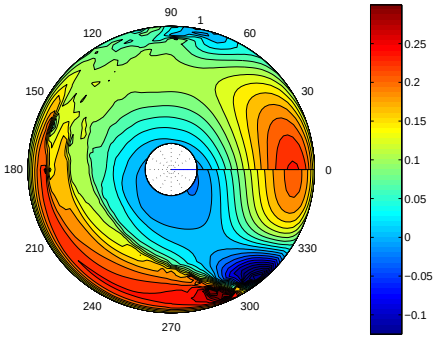


(e) $t = t_0 + 15$ revs

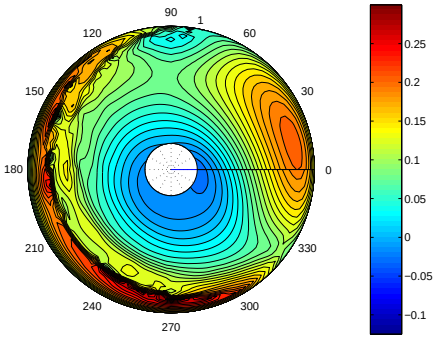


(f) $t = t_0 + 22$ revs

Figure 4.50: Contours of the non-dimensional lift distribution for a rotor undergoing a port roll over a duration of 1 second, $\mu = 0.093$: (a) Before initiation of the maneuver, (b) after 2 revolutions, (c) after 3 revolutions, (d) after 7 revolutions, (e) after 9 revolutions, (f) rotor operating at desired bank angle.

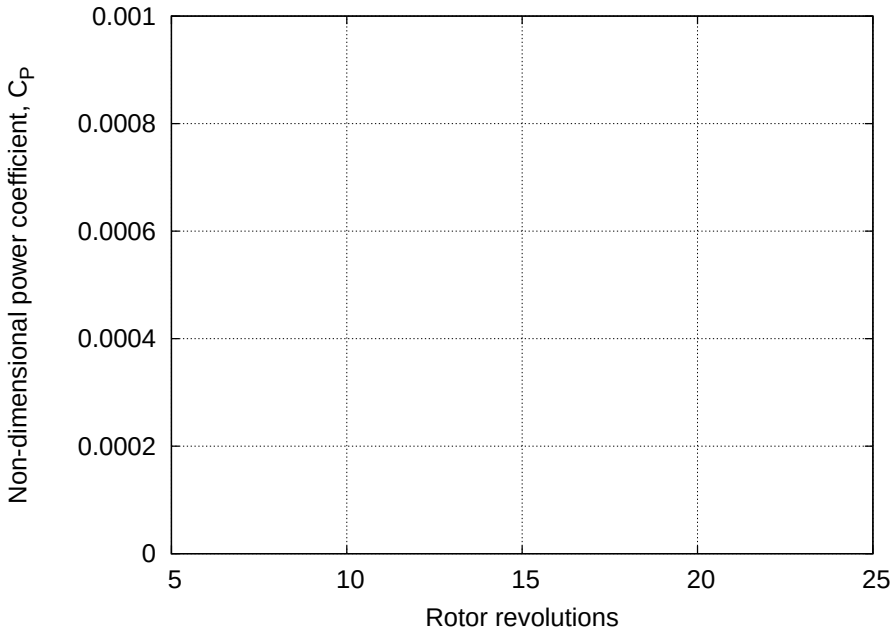


(a) Non-dimensional thrust coefficient

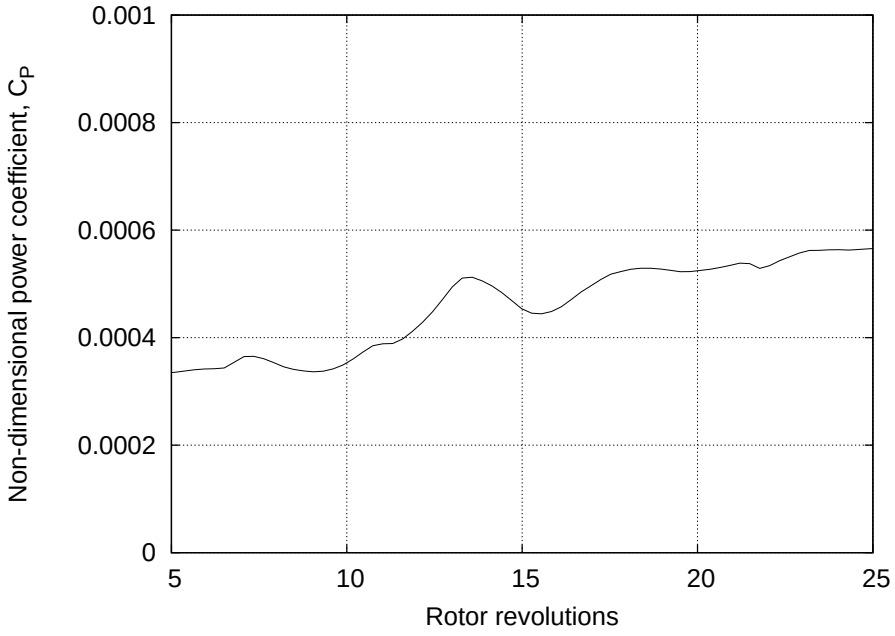


(b) Non-dimensional power coefficient

Figure 4.51: Time-histories of the thrust and power predictions for a rotor executing a port roll over a duration of 1 second: (a) Thrust, and (b) Power.

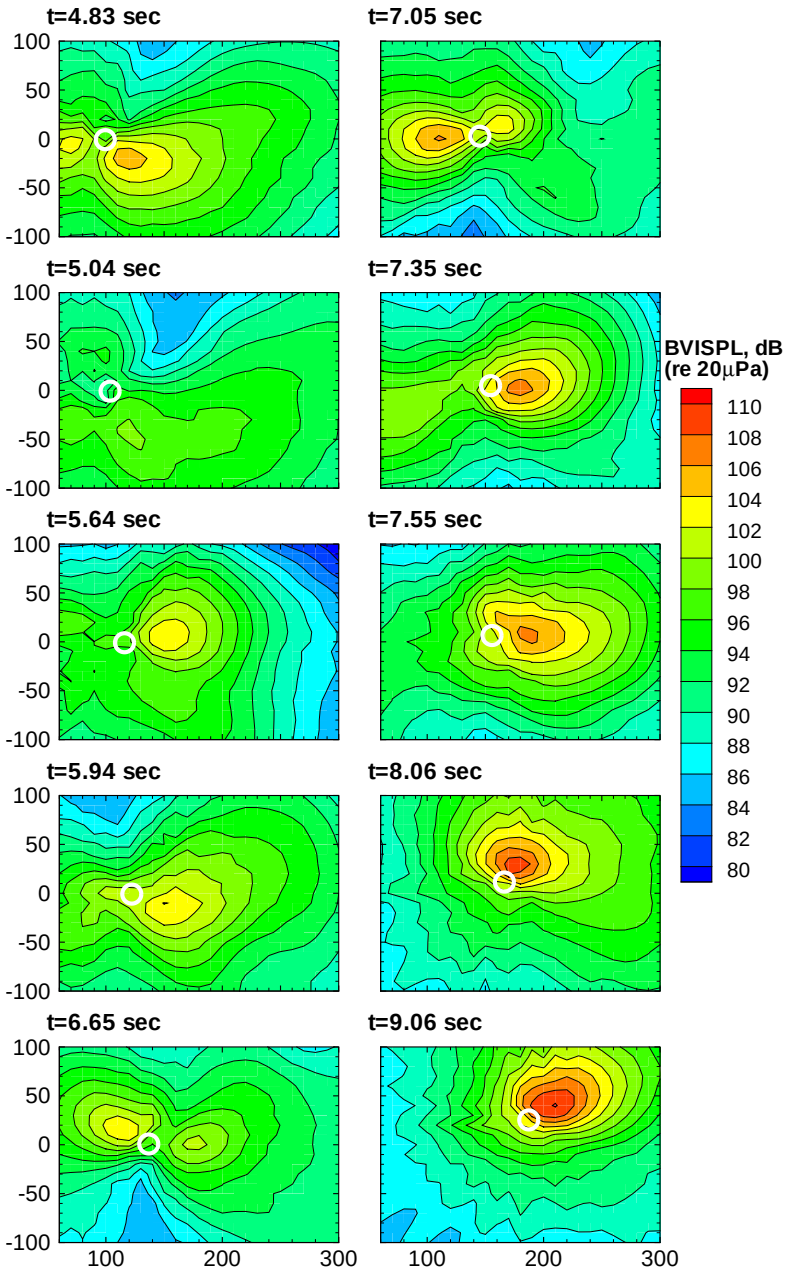


Figure 4.52: Plots showing the BVI sound pressure level predictions by PSU-WOPWOP for a rotor executing a port roll over a duration of 1 second, $\mu = 0.093$.

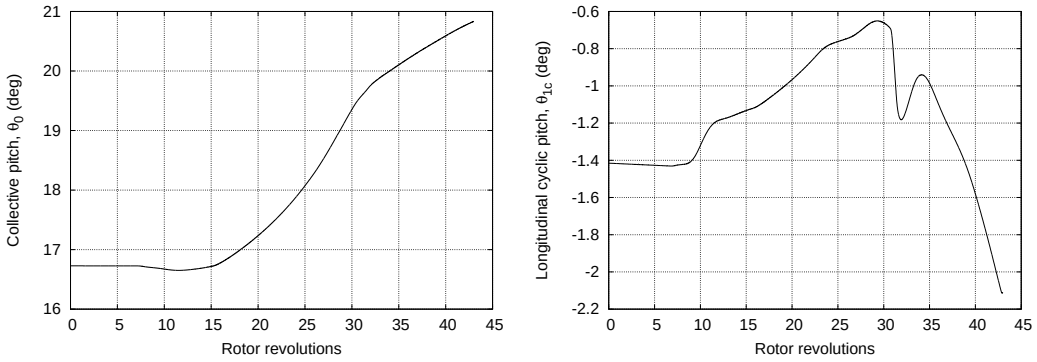


(a) Collective pitch, $\theta_0$




(b) Longitudinal cyclic, $\theta_{1c}$

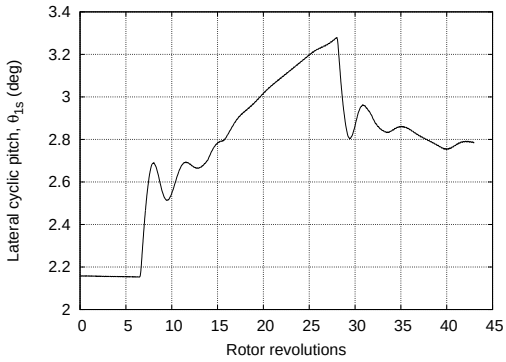


(c) Lateral cyclic, $\theta_{1s}$

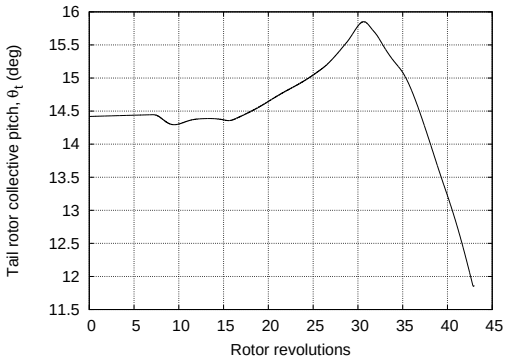


(d) Tail rotor collective, $\theta_{0_t}$

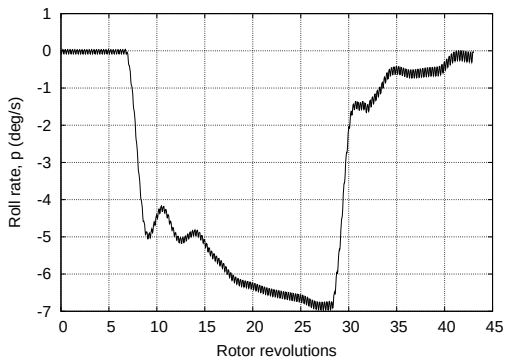


(e) Roll rate, $p$

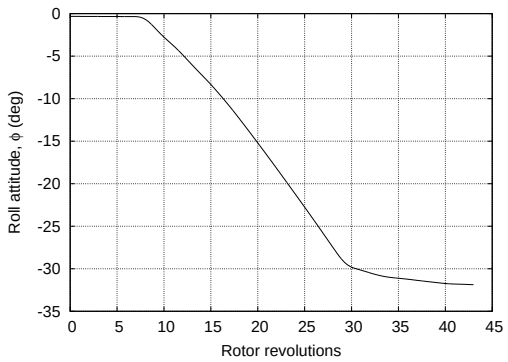


(f) Roll attitude, $\phi$

Figure 4.53: Time-histories of pilot control inputs used to perform a port roll maneuver over 5 seconds and the resulting roll response: (a) Collective pitch, (b) longitudinal cyclic, (c) lateral cyclic, (d) tail rotor collective, (e) roll rate, and (f) roll attitude.

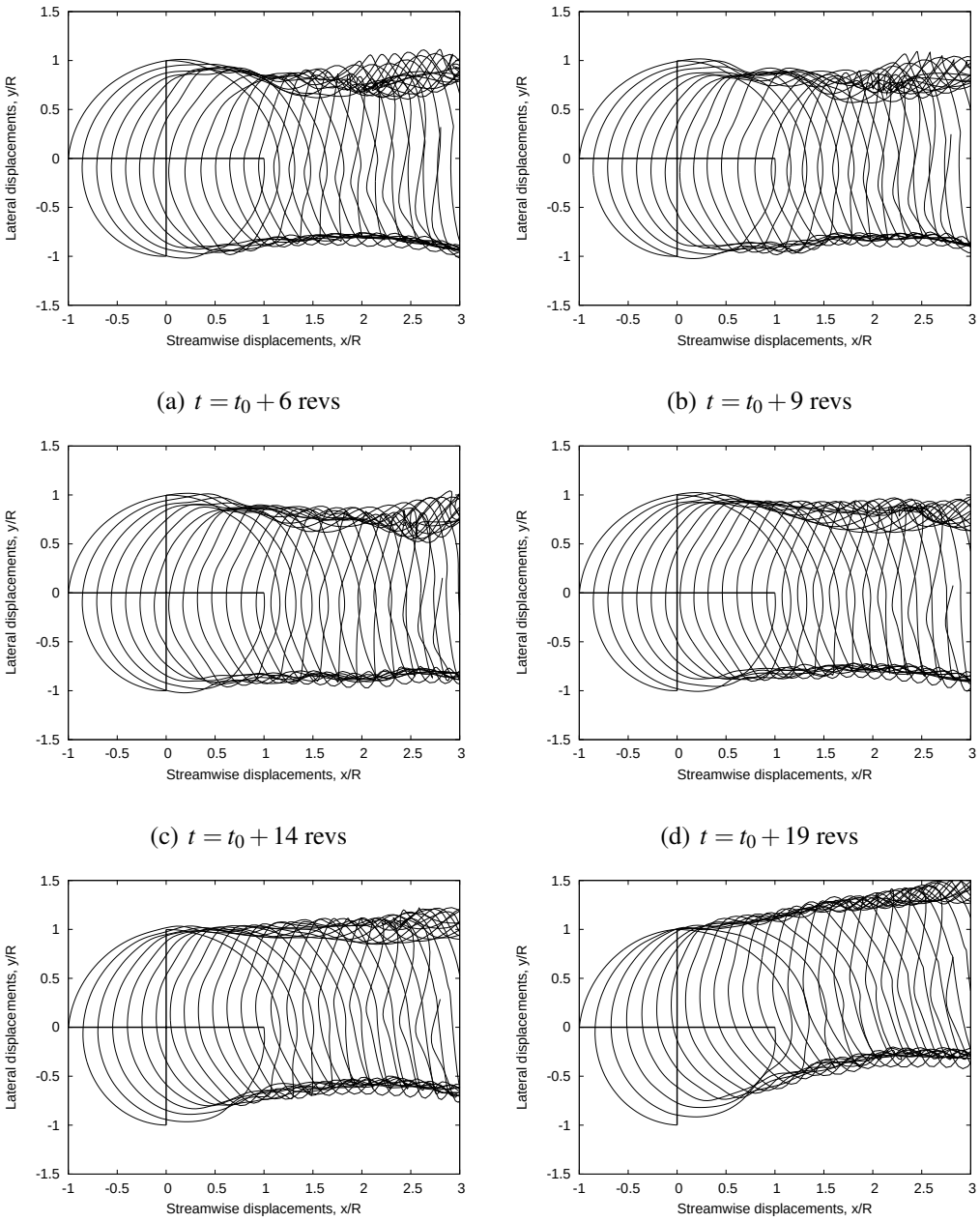


(a) $t = t_0 + 6$ revs

(b) $t = t_0 + 9$ revs

(c) $t = t_0 + 14$ revs

(d) $t = t_0 + 19$ revs

(e) $t = t_0 + 26$ revs

(f) $t = t_0 + 32$ revs

Figure 4.54: Top views of the predicted wake geometries for a representative, four-bladed rotor undergoing a port roll over a duration of 5 seconds, $\mu = 0.093$: (a) Before initiation of the maneuver, (b) after 2 revolutions, (c) after 3 revolutions, (d) after 7 revolutions, (e) after 9 revolutions, (f) rotor operating at desired bank angle.

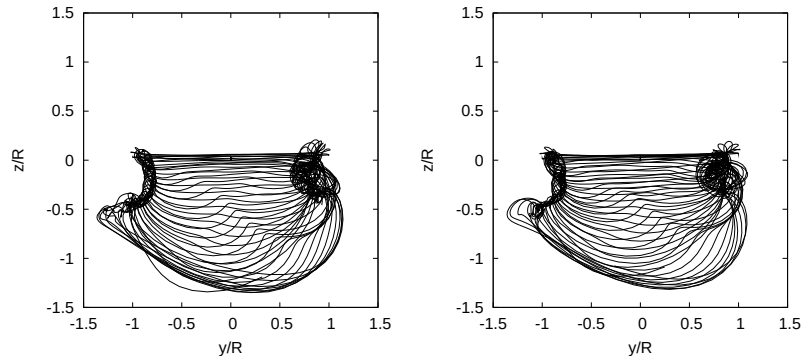


(a) $t = t_0 + 6$ revs




(b) $t = t_0 + 9$ revs

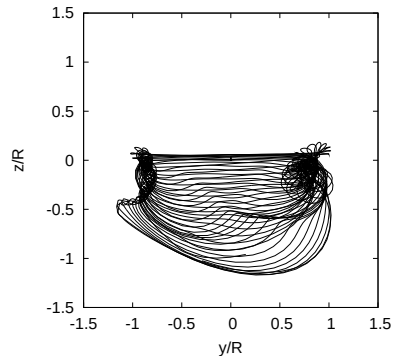


(c) $t = t_0 + 14$ revs

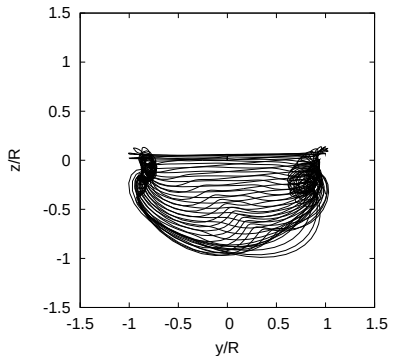


(d) $t = t_0 + 19$ revs

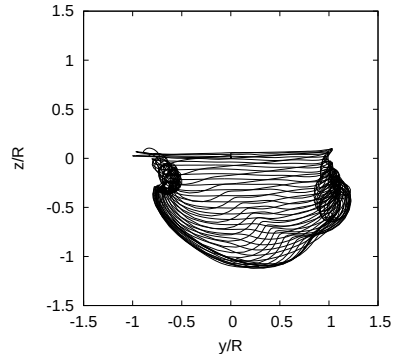


(e) $t = t_0 + 26$ revs

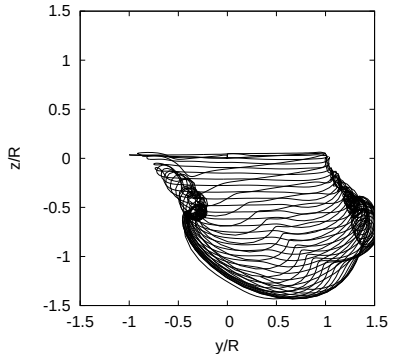


(f) $t = t_0 + 32$ revs

Figure 4.55: Rear views of the predicted wake geometries for a representative, four-bladed rotor undergoing a port roll over a duration of 5 seconds, $\mu = 0.093$: (a) Before initiation of the maneuver, (b) after 2 revolutions, (c) after 3 revolutions, (d) after 7 revolutions, (e) after 9 revolutions, (f) rotor operating at desired bank angle.

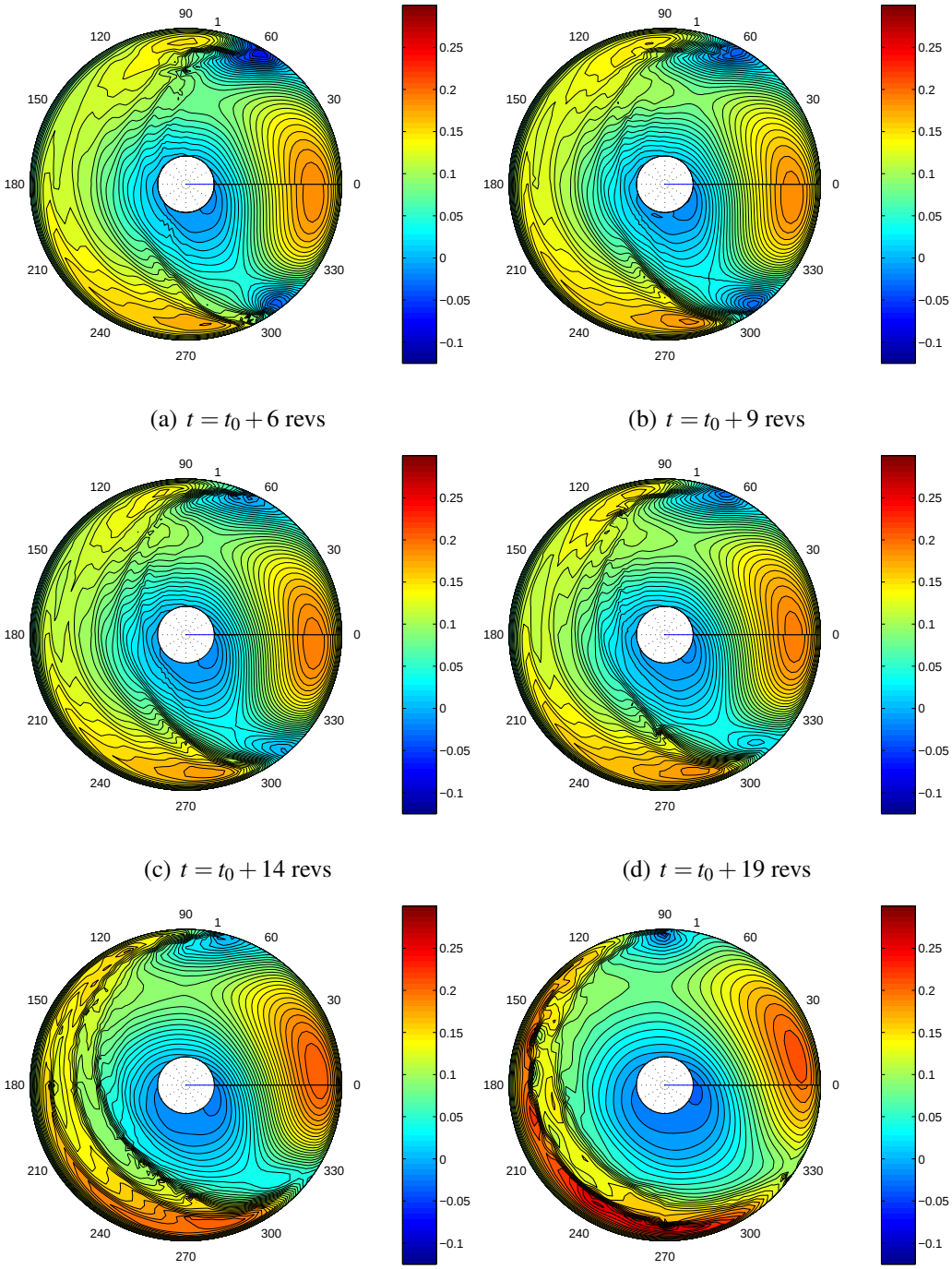


(a) $t = t_0 + 6$ revs

(b) $t = t_0 + 9$ revs

(c) $t = t_0 + 14$ revs

(d) $t = t_0 + 19$ revs

(e) $t = t_0 + 26$ revs

(f) $t = t_0 + 32$ revs

Figure 4.56: Contours of the non-dimensional lift distribution for a representative, four-bladed rotor undergoing a port roll over a duration of 5 seconds, $\mu = 0.093$: (a) Before initiation of the maneuver, (b) after 2 revolutions, (c) after 3 revolutions, (d) after 7 revolutions, (e) after 9 revolutions, (f) rotor operating at desired bank angle.

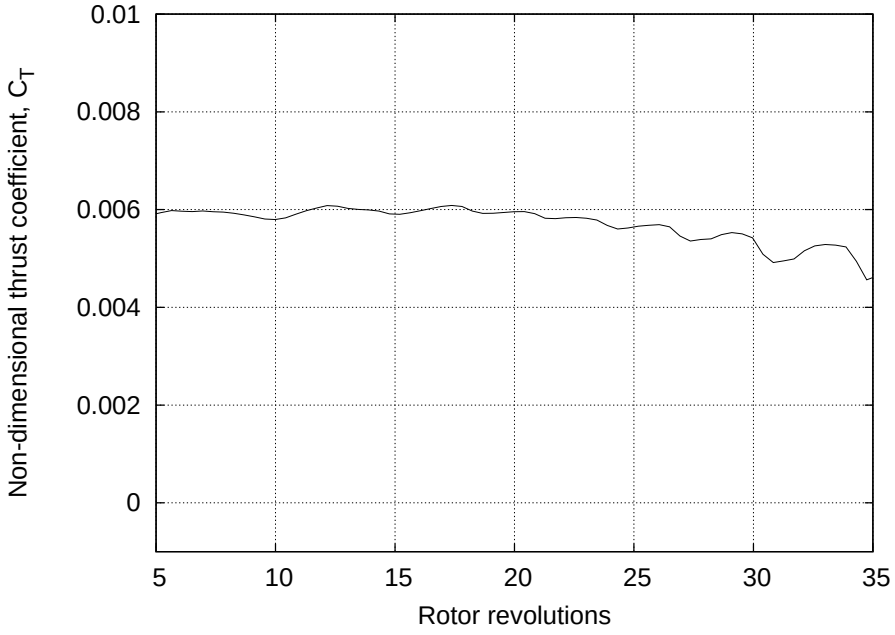


(a) Non-dimensional thrust coefficient

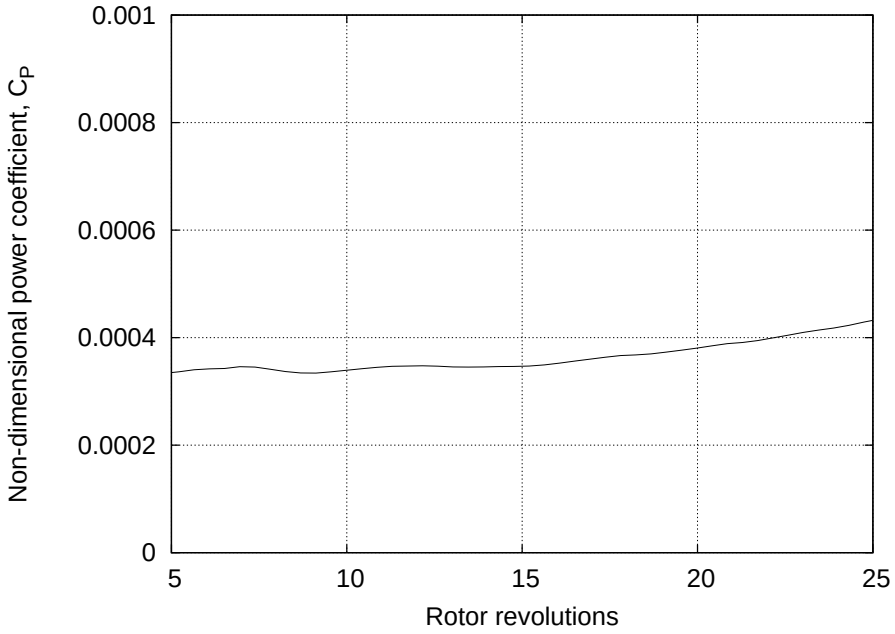


(b) Non-dimensional power coefficient

Figure 4.57: Time-histories of the thrust and power predictions for a rotor executing a port roll over a duration of 5 seconds: (a) Thrust, and (b) Power.

blades. Clearly the blades track identical paths during the steady-state flight condition. However, after the maneuver is initiated, the blades begin to follow independent paths and so the rotor does not behave as a solid disk. This is because of the highly unsteady, nonlinear flow field experienced by the rotor blades during a maneuver. The blade flapping response, in turn, affects the wake evolution by influencing the rotor airloads, thereby introducing a hereditary effect into rotor wake response. Notice that the transient blade flapping angles are larger in magnitude for the roll to starboard. This is because of the fluctuations in the induced inflow at the rotor disk caused by the interaction of the bundled vortex structure with the rotor blades (see Fig. 4.25(c) through (e)). This emphasizes the very close coupling that exists between the rotor flapping response and its wake aerodynamics. The differences in the wake response and the resulting airloads will significantly impact the directivity of rotor noise and shows, in general, the difficulties in computing the rotor airloads even during relatively simple maneuvering flight conditions.

### 4.3.2 Roll Reversals

From the simulations of an idealized roll reversal maneuver, it has already been shown how the wake reacts to the changes in the flight conditions with a relatively long aerodynamic lag. In this case, with the relatively quick reversal in the roll rate and roll angles, the wake does not have enough time to adjust to the more rapid changes taking place. Based on the previously described analysis of pure rolls, one can expect that the wake response to a roll reversal would also depend on the manner in which it is performed, i.e., whether a port-starboard-port (PSP) or a starboard-port-starboard (SPS) maneuver is performed. The calculations are performed by prescribing the time-histories of the control pitch inputs, the flight velocities and the body attitude

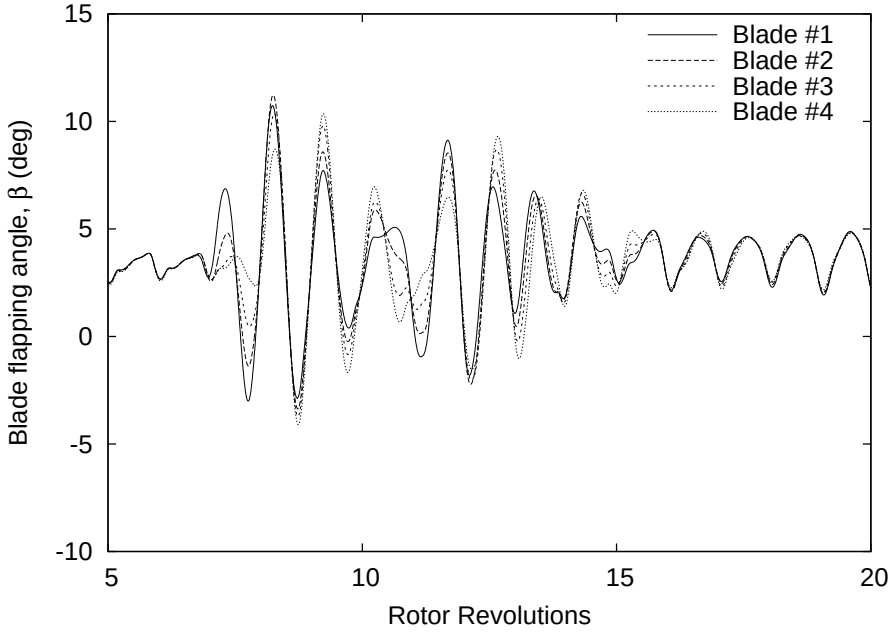


(a) Roll to port

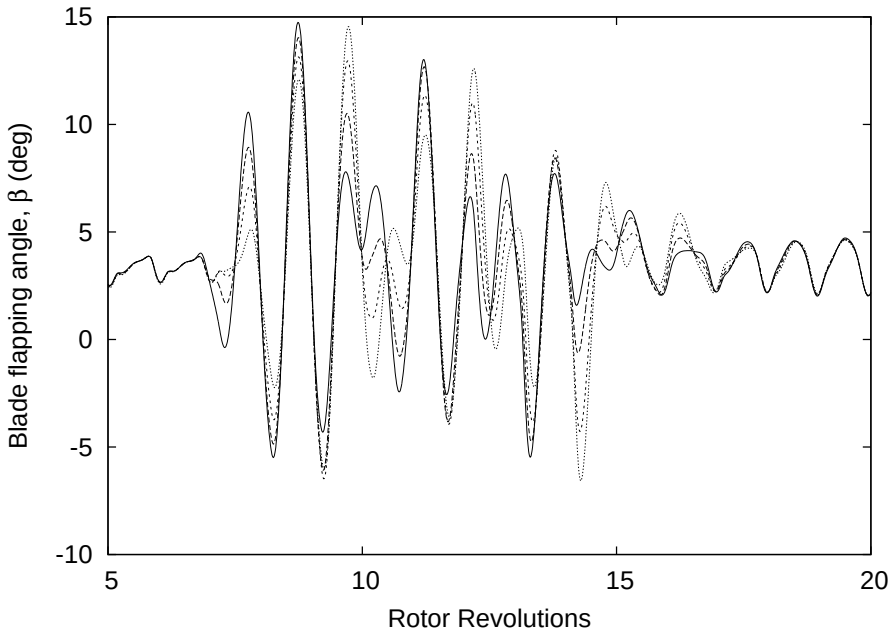


(b) Roll to starboard

Figure 4.58: Time-histories of the flapping angle for the individual rotor blades for a representative, four-bladed rotor undergoing starboard and port roll maneuvers over a duration of 0.5 seconds: (a) Roll to port, (b) roll to starboard.

and rates obtained from a GENHEL simulation. The maneuver was performed from a steady, forward flight condition with an advance ratio $\mu = 0.093$.

**Starboard-Port-Starboard (SPS) Roll Reversal**

Figure 4.59 shows the time-histories of the roll rate, $p$, and the corresponding bank angle, $\phi$, that were used to simulate the SPS roll reversal maneuver. Figures 4.60 and 4.61 show the snapshots of the top and rear views of the wake geometry for a rotor executing an SPS roll reversal at various instances in time during the maneuver. The wake roll up on the advancing side intensifies as the rotor banks towards starboard — see Fig. 4.60(a) and (b). The rapid transition from the a starboard roll to a port roll is associated with the bundling of tip vortices (Fig. 4.60(b) and (c)) as was observed in Fig. 4.25(e). However, the bundled tip vortex structure is quickly convected away and below the rotor, as is evident from Fig. 4.61(c). The roll to port (Figs. 4.60(d)–(f)) shows considerable reorganization of the wake structure because of the formation, convection and breakdown of the bundled vortex ring structure.

Figure 4.62 shows the contours of the lift over the rotor disk for an SPS maneuver. As with the starboard roll maneuver, the most intense BVI occurs when the rotor quickly transitions from a starboard roll to a port roll — see Fig. 4.62(b). The vortex ring structure is convected away from the TPP (Figs. 4.61(c)–(e)) and the steep gradients in the lift contours disappear. The roll to port and the final transition to straight-and-level flight is fairly benign in comparison to the intense BVI observed during the transition from a starboard to port roll.

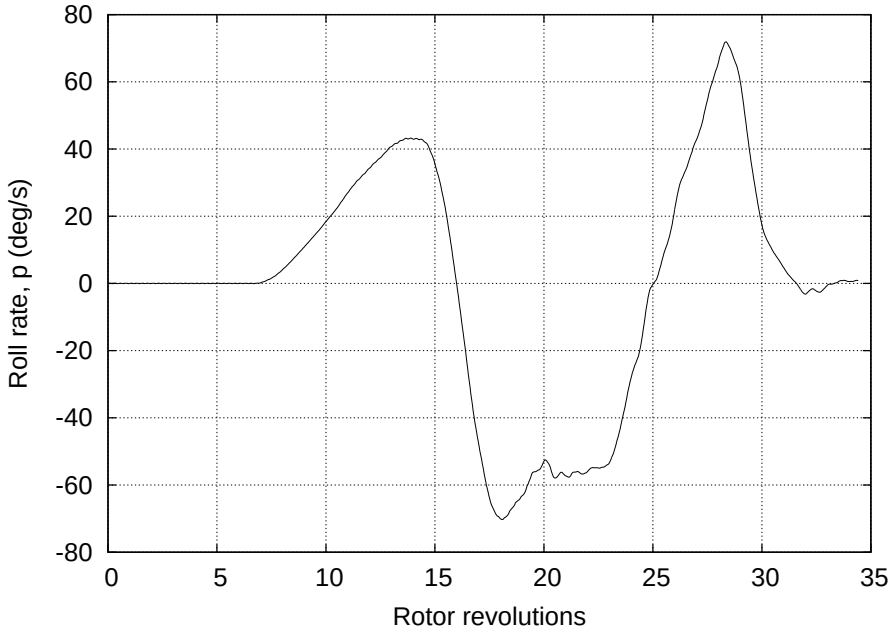


(a) Roll rate

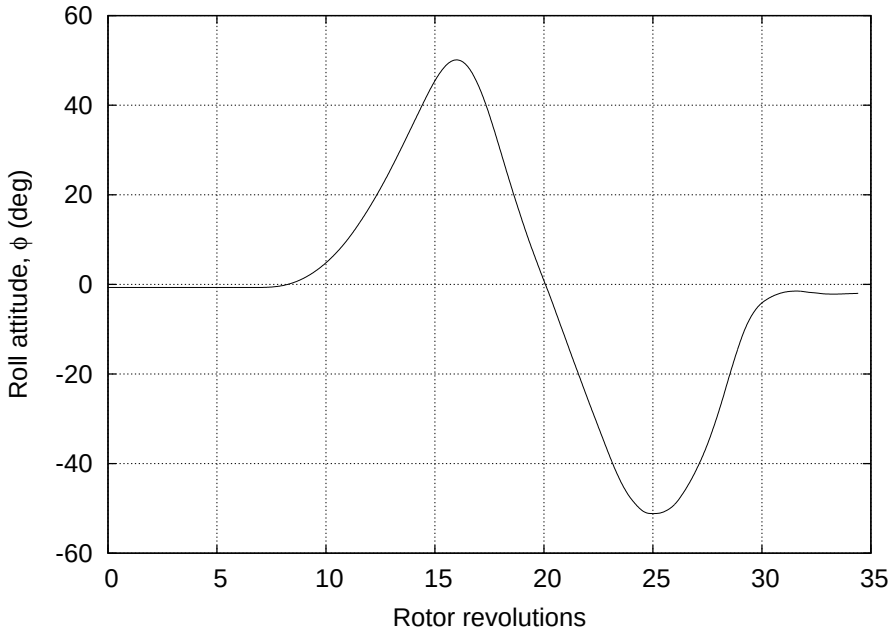


(b) Roll attitude

Figure 4.59: Time-histories of the roll rate $p$ and the roll attitude $\phi$ for a representative, four-bladed rotor performing an SPS roll reversal: (a) Roll rate, (b) roll attitude.

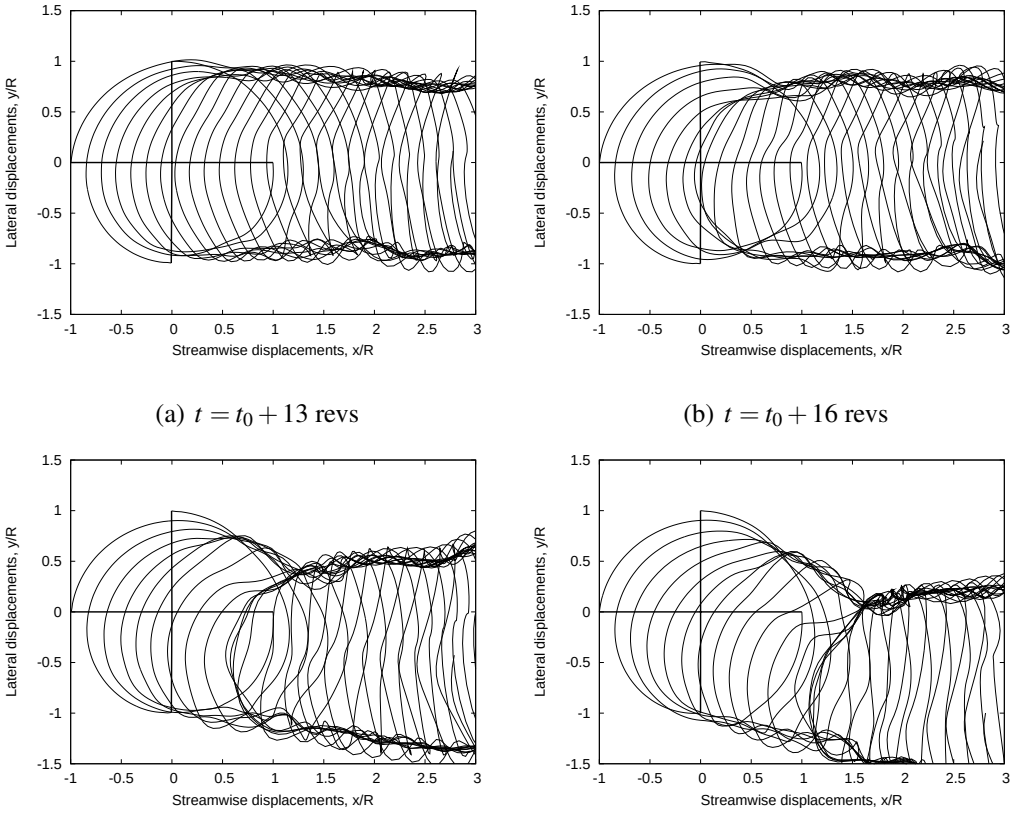


(a) $t = t_0 + 13$ revs

(b) $t = t_0 + 16$ revs

(c) $t = t_0 + 19$ revs

(d) $t = t_0 + 21$ revs

Figure 4.60: Top views of the predicted wake geometries for a rotor undergoing an SPS roll reversal, $\mu = 0.093$: (a) Halfway into starboard roll, (b) rotor at maximum bank angle towards starboard, (c) rotor commencing roll reversal, (d) rotor at zero bank angle.

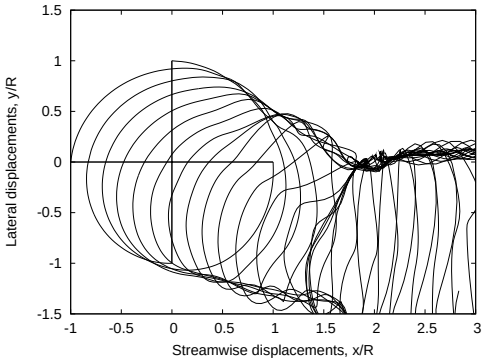


(e) $t = t_0 + 22$ revs

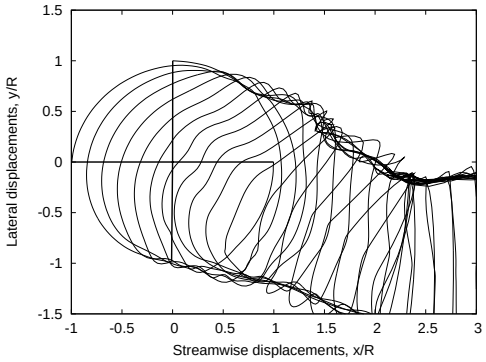


(f) $t = t_0 + 25$ revs

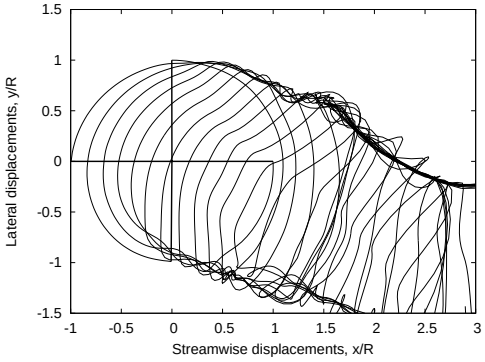


(g) $t = t_0 + 27$ revs

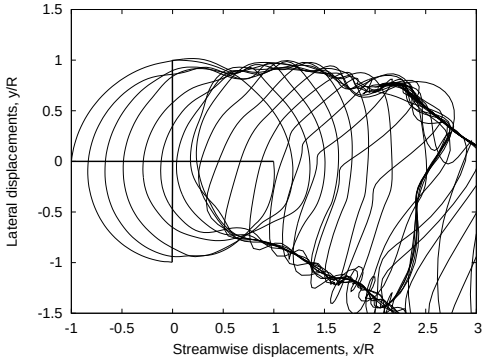


(h) $t = t_0 + 31$ revs

Figure 4.60: (Cont'd.) Top views of the predicted wake geometries for a rotor undergoing an SPS roll reversal, $\mu = 0.093$: (e) Rotor rolling towards port, (f) rotor at maximum bank angle towards port, (g) rotor returning to straight and level flight condition, (h) rotor operating at steady descending flight condition.

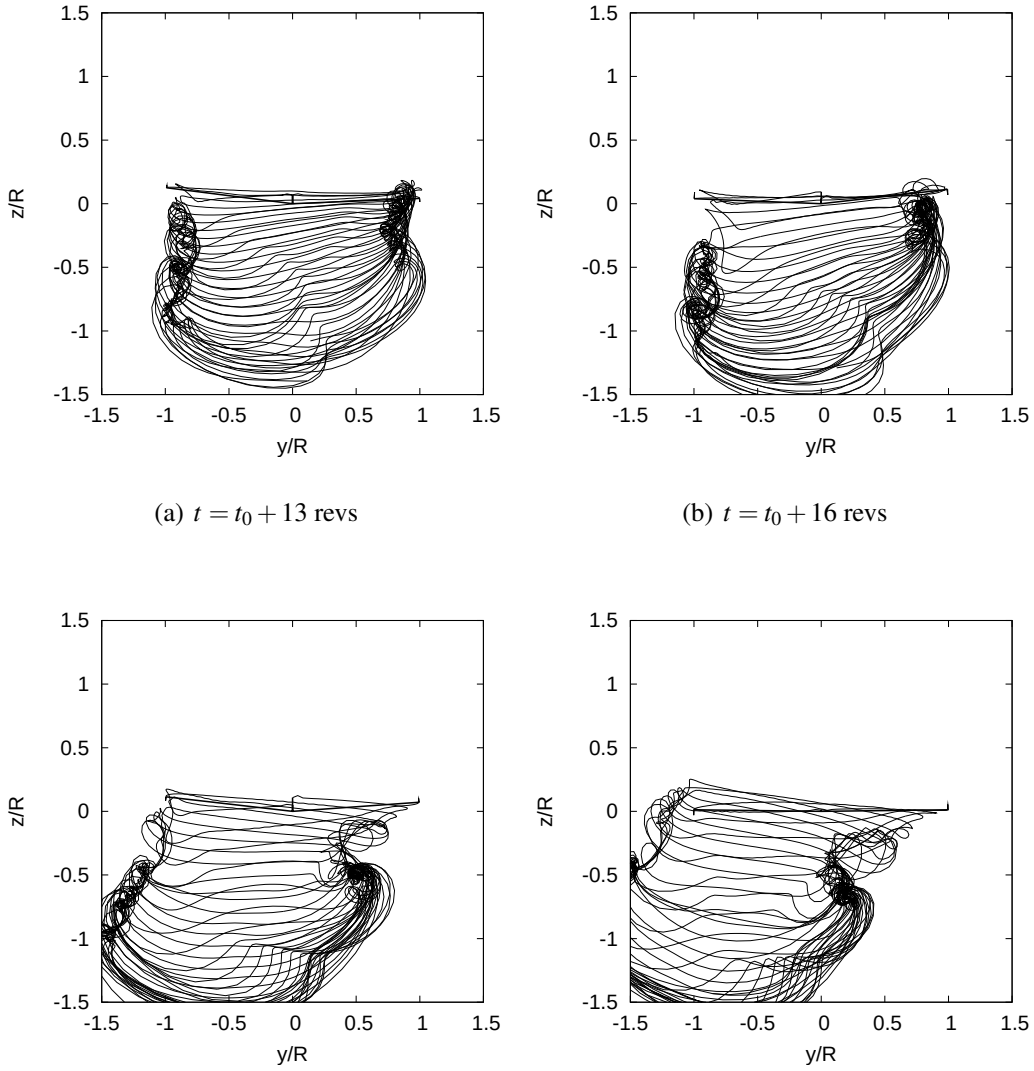


(a) $t = t_0 + 13$ revs

(b) $t = t_0 + 16$ revs

(c) $t = t_0 + 19$ revs

(d) $t = t_0 + 21$ revs

Figure 4.61: Rear views of the predicted wake geometries for a representative, four-bladed rotor undergoing an SPS roll reversal, $\mu = 0.093$: (a) Halfway into starboard roll, (b) rotor at maximum bank angle towards starboard, (c) rotor commencing roll reversal, (d) rotor at zero bank angle.

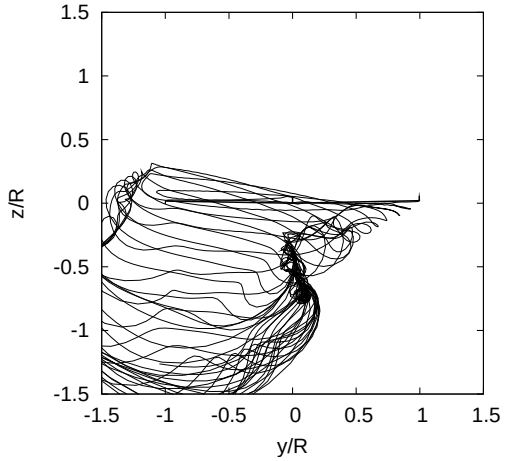


(e) $t = t_0 + 22$ revs

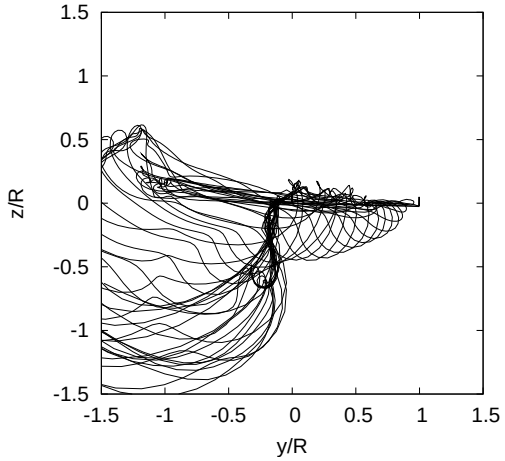


(f) $t = t_0 + 25$ revs

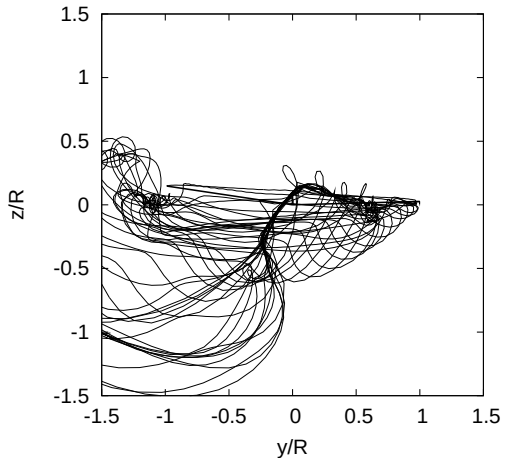


(g) $t = t_0 + 27$ revs

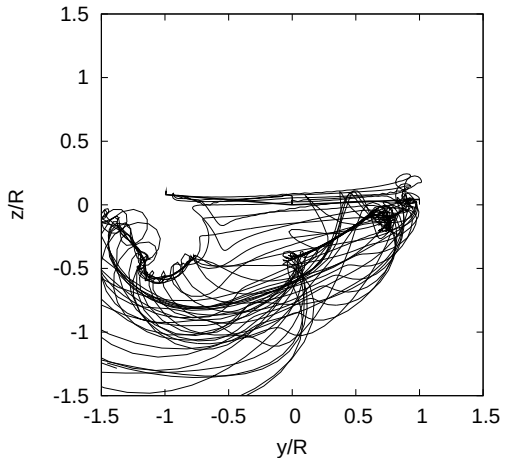


(h) $t = t_0 + 31$ revs

Figure 4.61: (Cont'd.) Rear views of the predicted wake geometries for a rotor undergoing an SPS roll reversal, $\mu = 0.093$: (e) Rotor rolling towards port, (f) rotor at maximum bank angle towards port, (g) rotor returning to straight and level flight condition, (h) rotor operating at steady descending flight condition.

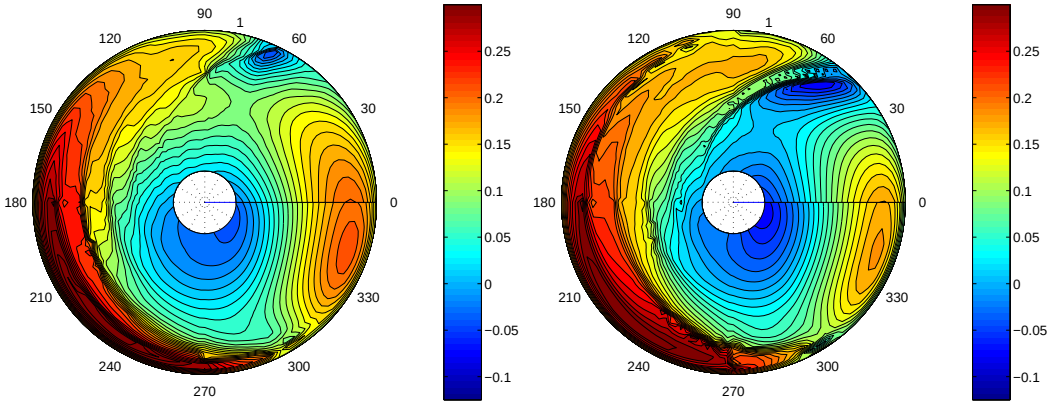


(a) $t = t_0 + 13$ revs

(b) $t = t_0 + 16$ revs

(c) $t = t_0 + 19$ revs

(d) $t = t_0 + 21$ revs

Figure 4.62: Contours of the non-dimensional lift distribution for a representative, four-bladed rotor undergoing an SPS roll reversal, $\mu = 0.093$: (a) Halfway into starboard roll, (b) rotor at maximum bank angle towards starboard, (c) rotor commencing roll reversal, (d) rotor at zero bank angle.

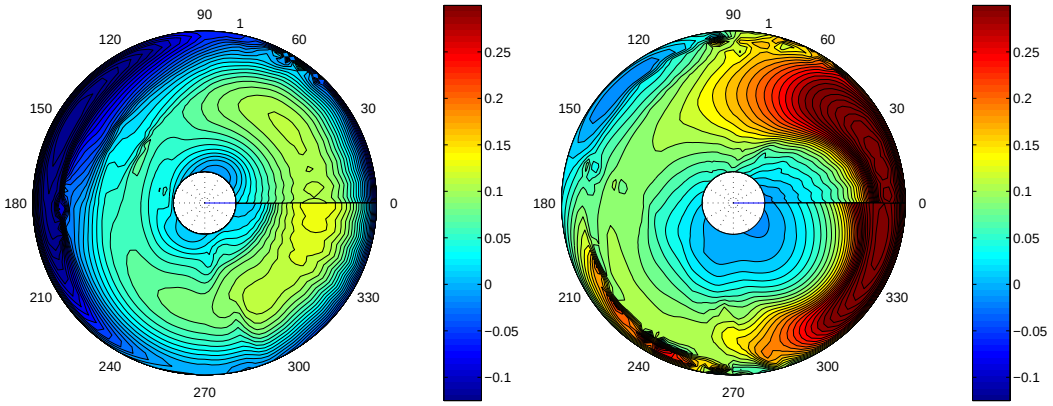


(e) $t = t_0 + 22$ revs

(f) $t = t_0 + 25$ revs

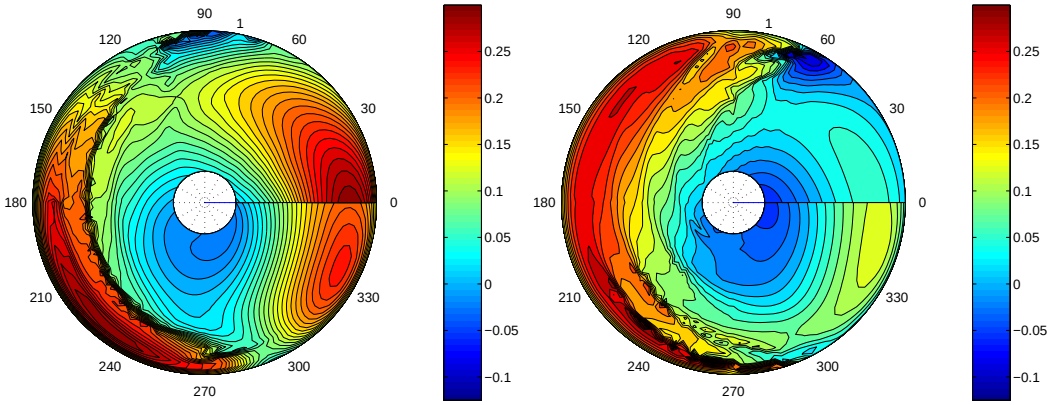


(g) $t = t_0 + 27$ revs

(h) $t = t_0 + 31$ revs

Figure 4.62: (Cont'd.) Contours of the non-dimensional lift distribution for a representative, four-bladed rotor undergoing an SPS roll reversal, $\mu = 0.093$: (e) Rotor rolling towards port, (f) rotor at maximum bank angle towards port, (g) rotor returning to straight and level flight condition, (h) rotor operating at steady descending flight condition.

**Port-Starboard-Port (PSP) Roll Reversal**

Figure 4.63 shows the time-histories of $p$ and $\phi$ imposed on the rotor during a port-starboard-port (PSP) roll reversal maneuver. Figures 4.64 and 4.65 show the top and rear wake snapshots at different instances in time for a rotor executing a PSP roll reversal. As the rotor rolls to port, the tip vortices roll up more tightly on the retreating side. The transition from the port to starboard roll causes a bundling of tip vortices over the advancing side of the rotor disk — see Fig. 4.64(c). However, as the rotor rolls to starboard the bundled vortex structure is convected below the rotor and does not have an appreciable affect on the lift distribution over the rotor disk. Notice that the transition back to straight-and-level flight is associated with a formation of a secondary vortex bundle on the advancing side. The secondary vortex bundle slowly convects across the rear of the rotor disk as the rotor returns to the steady level flight condition, as shown in Fig. 4.64(f)–(h).

Figure 4.66 shows the corresponding contour plots of the lift distribution over the rotor disk. The interactions between the rolled-up vortex bundle from the retreating side of the disk and rotor blades manifest as impulsive airloads (see Figs. 4.66(a) and (b)). As the rotor transitions from port to starboard roll, the BVI on the retreating side disappears and the bundled tip vortex structure formed on the advancing side (Fig. 4.64(c)) causes new BVIs on the advancing side. The BVI on the advancing side persists for the entire duration of starboard roll, as shown in Figs. 4.66(c) through (f). As the helicopter returns to straight-and-level flight conditions, the vortex bundle on the retreating side interacts briefly with the rotor causing BVIs over the retreating side of the disk (Fig. 4.66(f)). The secondary vortex structure on the advancing side, as mentioned previously, causes additional BVIs over the advancing side of the disk as the rotor returns to level flight.

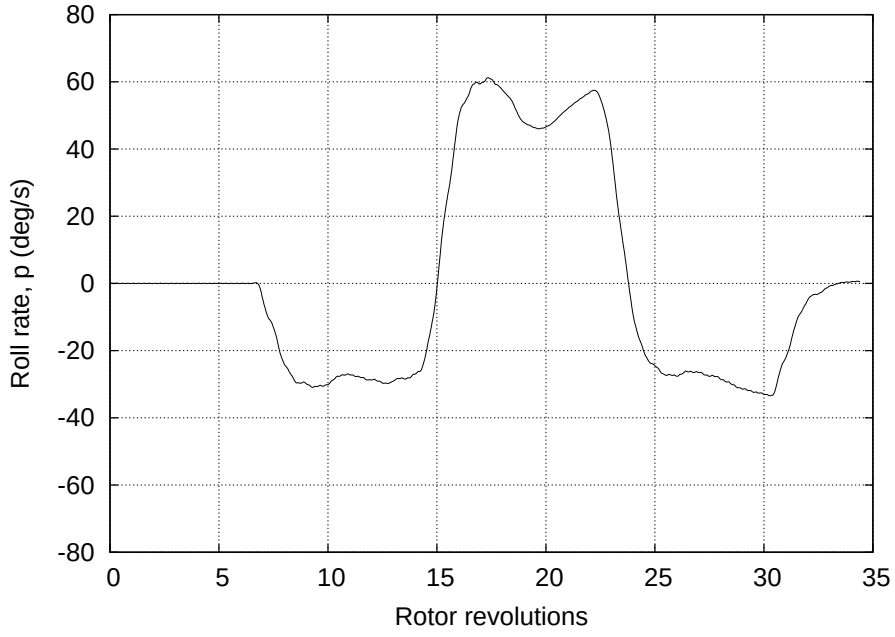


(a) Roll rate

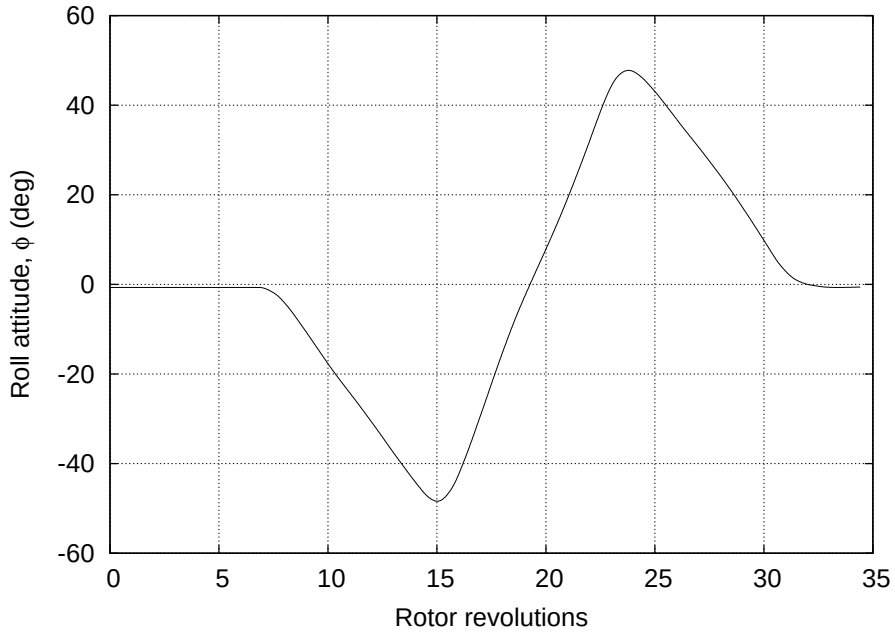


(b) Roll attitude

Figure 4.63: Time-histories of the roll rate $p$ and the roll attitude $\phi$ for a representative, four-bladed rotor performing PSP roll reversal: (a) Roll rate, (b) roll attitude.

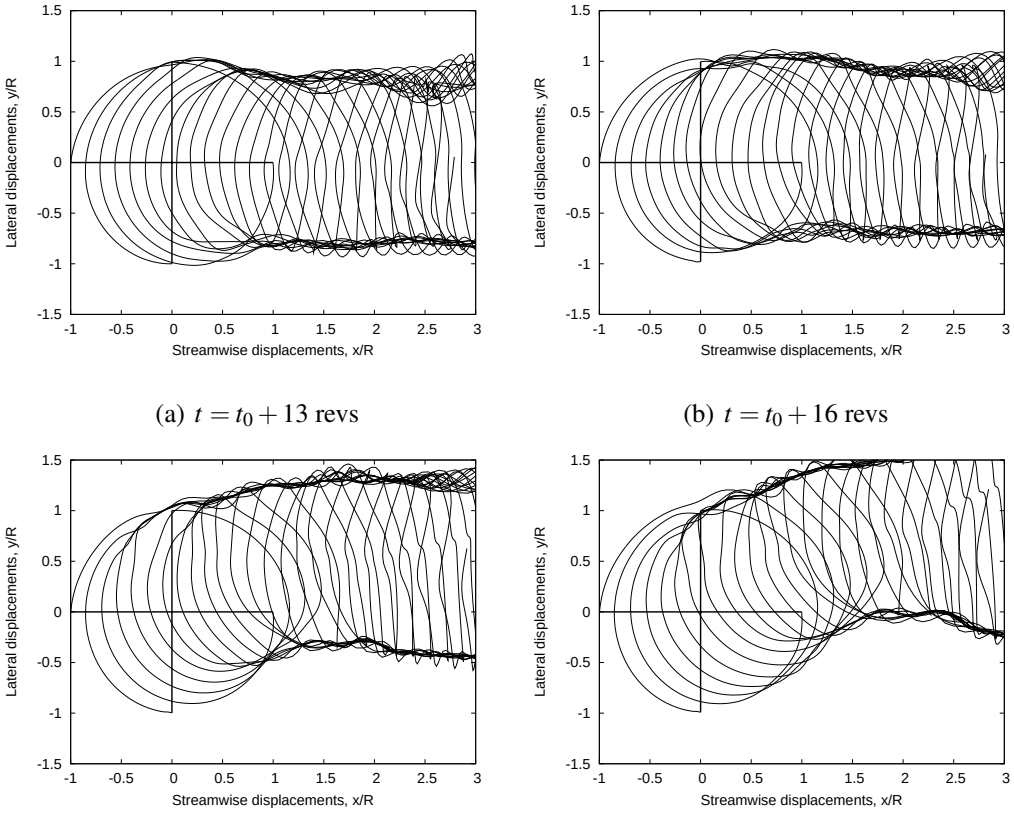


(a) $t = t_0 + 13$ revs

(b) $t = t_0 + 16$ revs

(c) $t = t_0 + 19$ revs

(d) $t = t_0 + 21$ revs

Figure 4.64: Top views of the predicted wake geometries for a representative, four-bladed rotor undergoing a PSP roll reversal, $\mu = 0.093$: (a) Halfway into port roll, (b) rotor at maximum bank angle towards port, (c) rotor commencing roll reversal, (d) rotor at zero bank angle.

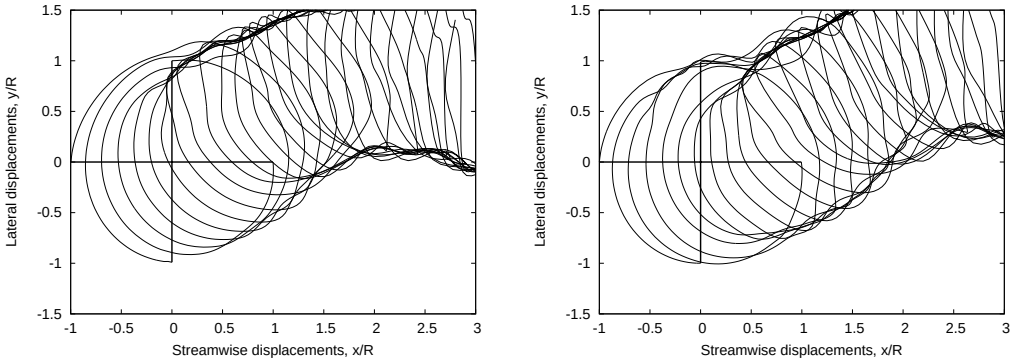


(e) $t = t_0 + 22$ revs

(f) $t = t_0 + 25$ revs

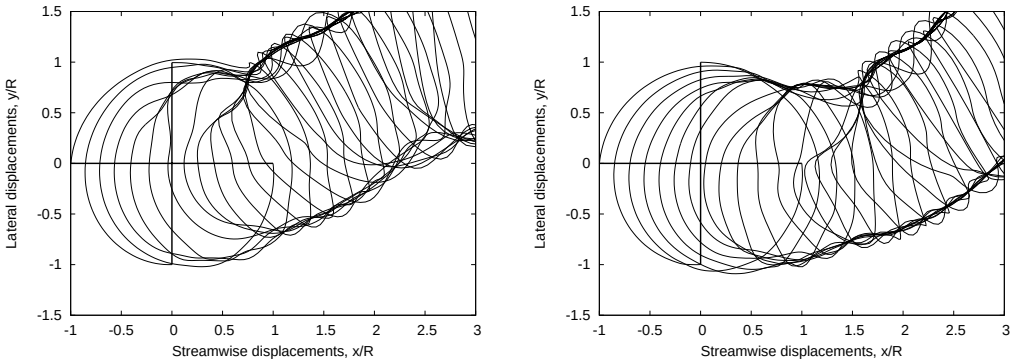


(g) $t = t_0 + 27$ revs

(h) $t = t_0 + 31$ revs

Figure 4.64: (Cont'd.) Top views of the predicted wake geometries for a rotor undergoing a PSP roll reversal, $\mu = 0.093$: (e) Rotor rolling towards starboard, (f) rotor at maximum bank angle towards starboard, (g) rotor returning to straight and level flight condition, (h) rotor operating at steady descending flight condition.

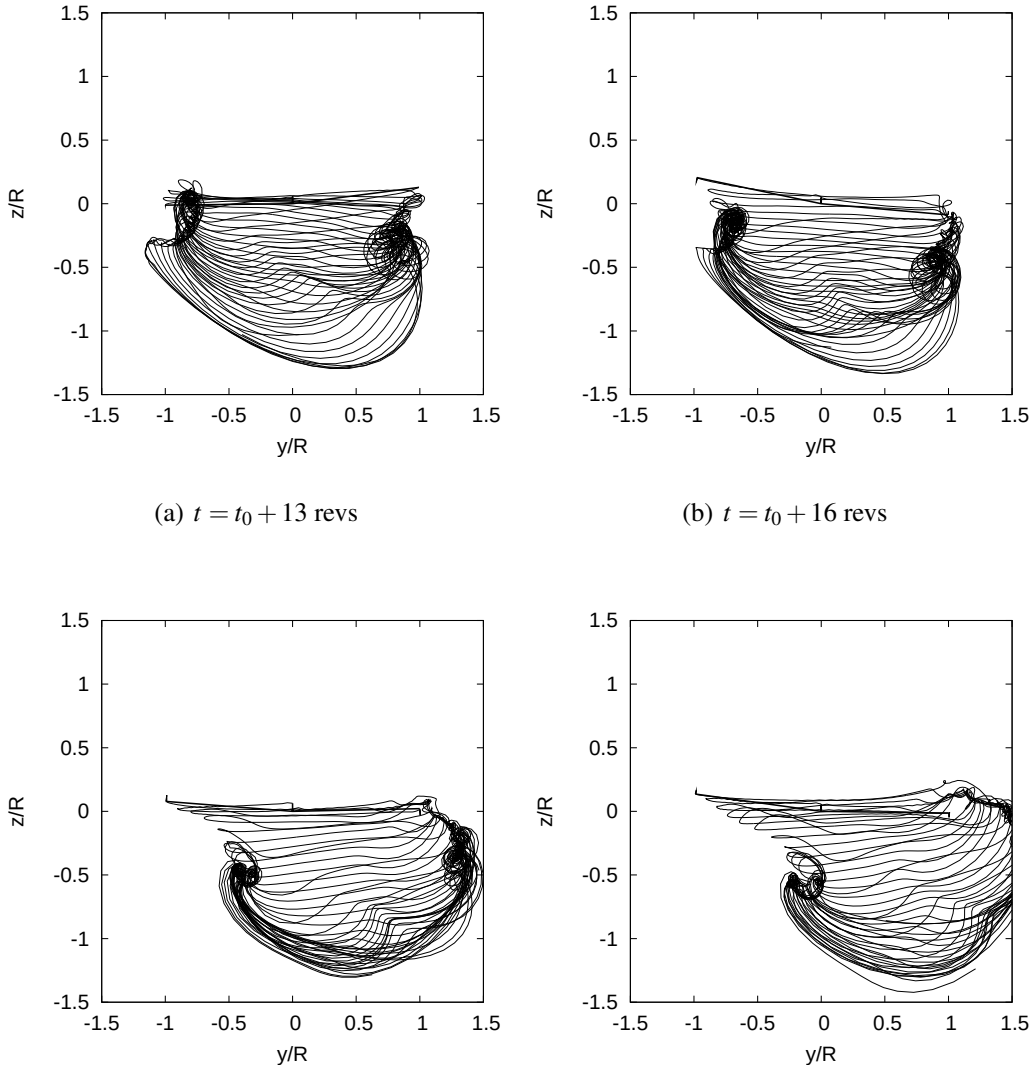


(a) $t = t_0 + 13$ revs

(b) $t = t_0 + 16$ revs

(c) $t = t_0 + 19$ revs

(d) $t = t_0 + 21$ revs

Figure 4.65: Rear views of the predicted wake geometries for a representative, four-bladed rotor undergoing a PSP roll reversal, $\mu = 0.093$: (a) Halfway into port roll, (b) rotor at maximum bank angle towards port, (c) rotor commencing roll reversal, (d) rotor at zero bank angle.

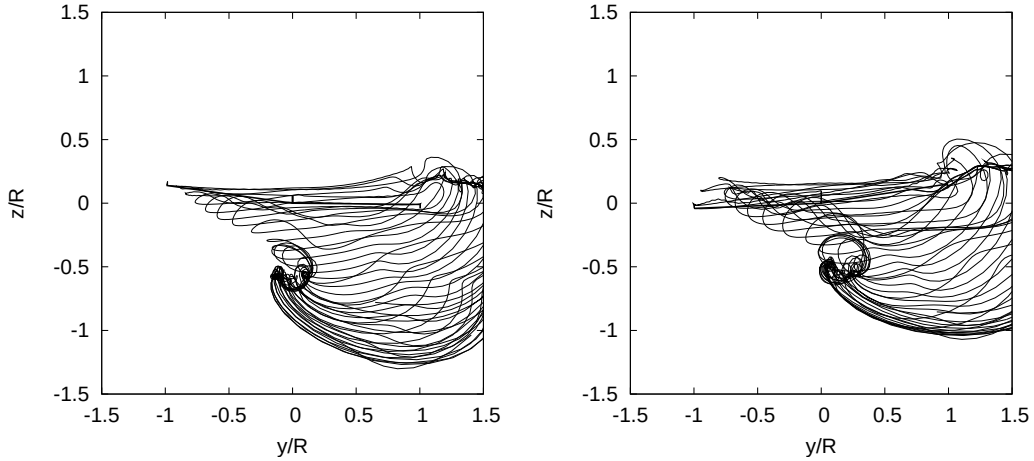


(e) $t = t_0 + 22$ revs

(f) $t = t_0 + 25$ revs

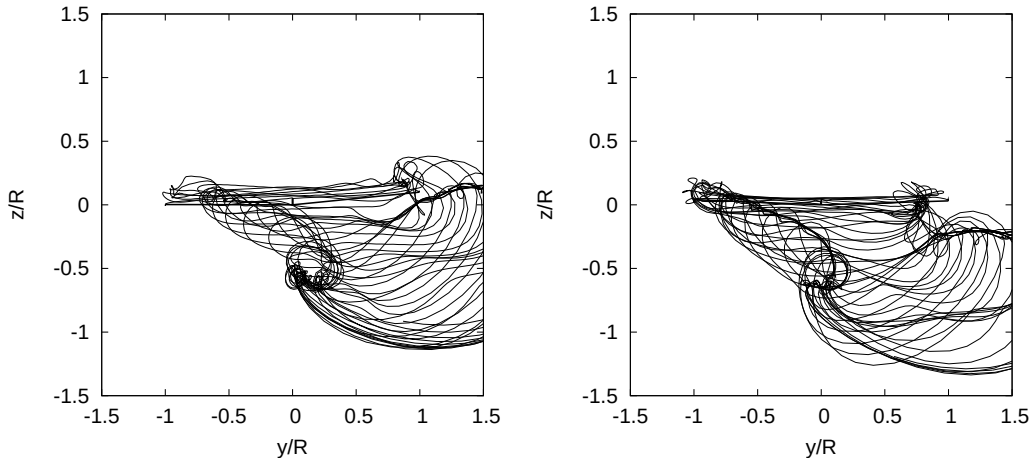


(g) $t = t_0 + 27$ revs

(h) $t = t_0 + 31$ revs

Figure 4.65: (Cont'd.) Rear views of the predicted wake geometries for a rotor undergoing a PSP roll reversal, $\mu = 0.093$: (e) Rotor rolling towards starboard, (f) rotor at maximum bank angle towards starboard, (g) rotor returning to straight and level flight condition, (h) rotor operating at steady descending flight condition.

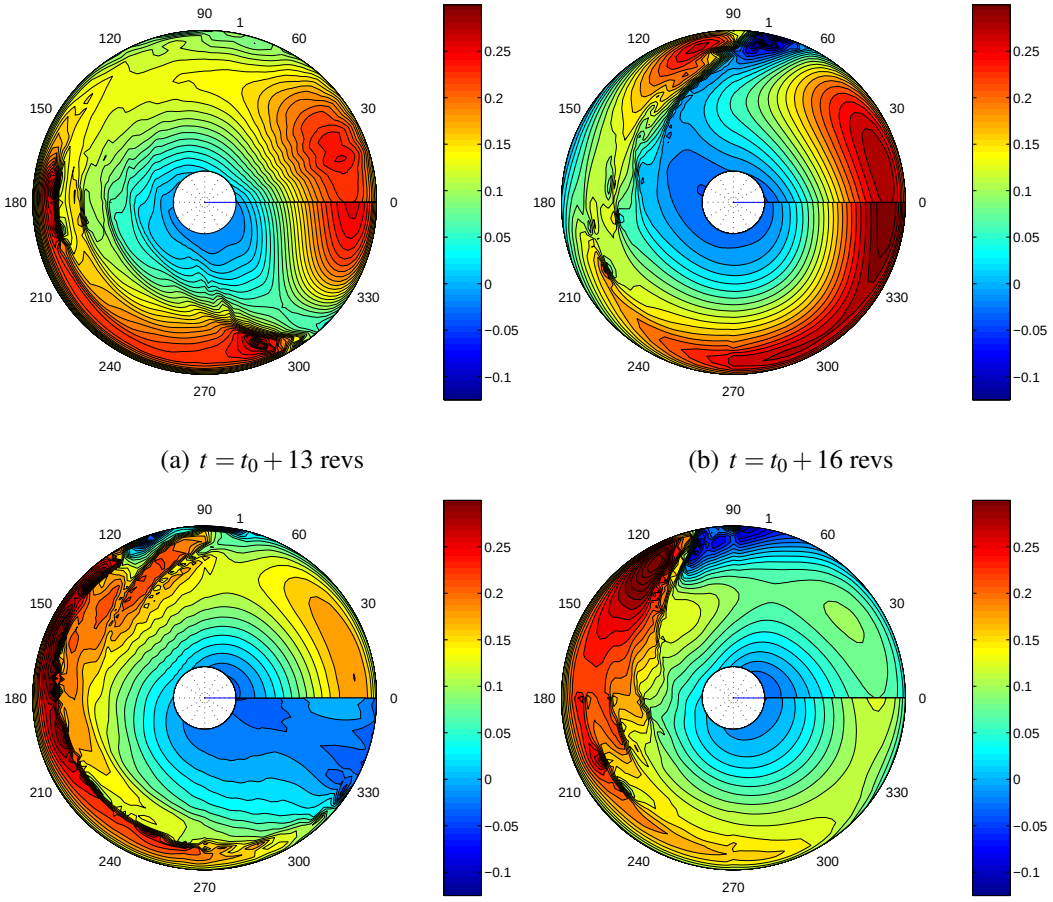


(a) $t = t_0 + 13$ revs

(b) $t = t_0 + 16$ revs

(c) $t = t_0 + 19$ revs

(d) $t = t_0 + 21$ revs

Figure 4.66: Contours of the non-dimensional lift distribution for a representative, four-bladed rotor undergoing a PSP roll reversal, $\mu = 0.093$: (a) Halfway into port roll, (b) rotor at maximum bank angle towards port, (c) rotor commencing roll reversal, (d) rotor at zero bank angle.

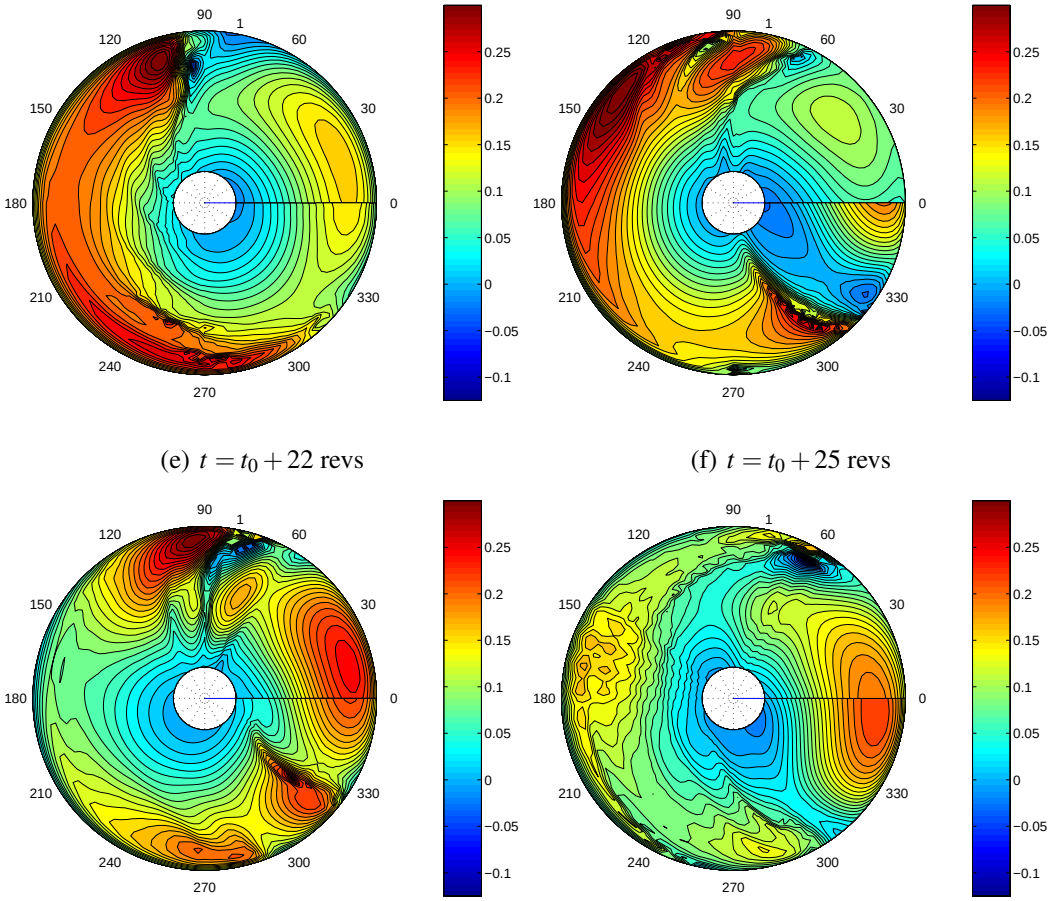


(e) $t = t_0 + 22$ revs

(f) $t = t_0 + 25$ revs

(g) $t = t_0 + 27$ revs

(h) $t = t_0 + 31$ revs

Figure 4.66: (Cont'd.) Contours of non-dimensional lift distrbution for a rotor undergoing a PSP roll reversal, $\mu = 0.093$: (e) Rotor rolling towards starboard, (f) rotor at maximum bank angle towards starboard, (g) rotor returning to straight and level flight condition, (h) rotor operating at steady descending flight condition.

### 4.3.3 Quickstop Maneuver

In a quickstop maneuver, a near hovering flight condition is obtained by abruptly decelerating the helicopter by using cyclic inputs to pitch the helicopter to a steep, nose-high attitude. The decelerating force is provided mainly by the backward reorientation of the rotor thrust vector. This is a common military maneuver that involves large angular rates, large displacements, and relatively short time scales. The quickstop maneuver simulation in this case was performed from a low speed descending flight condition with an advance ratio $\mu = 0.093$ and a flight path angle $\gamma = -6^\circ$. The GENHEL simulation (Ref. 32) was used to provide the pilot control inputs that would be necessary (Fig. 4.67). Collective and lateral cyclic inputs are also applied to trim the helicopter along the desired flight trajectory. Again, the time-histories of the control settings, the free stream conditions and the rotor attitudes were prescribed as inputs to the free-vortex wake simulation. Figure 4.67(a) shows the longitudinal cyclic pitch applied to the rotor to perform this maneuver. This input causes the rotor to pitch nose-up to an angle of attack of over $60^\circ$ – see Fig. 4.67(c).

Figure 4.68 shows the flight speeds and the predicted thrust time-history. As the rotor TPP tilts backwards, the rotor thrust vector is directed rearwards providing the decelerating force. The magnitude of the rotor thrust also increases rapidly as the rotor pitches nose up. Notice that there is a second peak in the rotor thrust time-history. This occurs because of the formation, accumulation and bundling of wake vorticity below the rotor (i.e., the formation of a vortical ring).

Figures 4.69 and 4.70 show the top and side views, respectively, of the predicted wake geometry at various instants in time during the quickstop maneuver. Figure 4.71 shows the corresponding contours of the lift distribution over the rotor disk. Immediately after the maneuver is initiated, it is apparent that the roll-up from the advancing

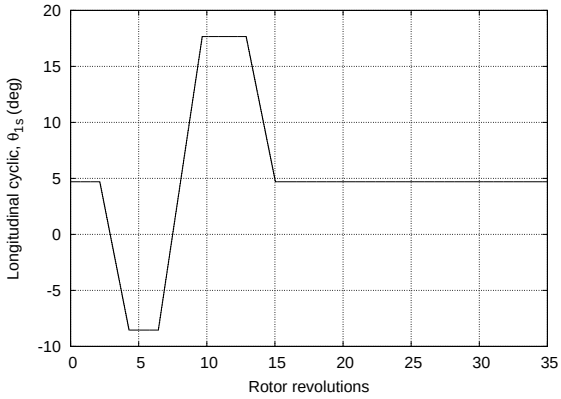


(a) Longitudinal cyclic

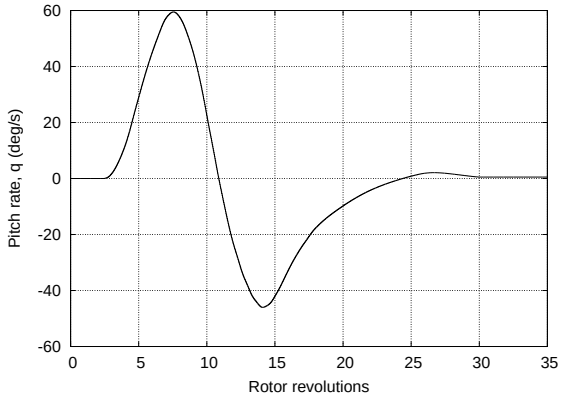


(b) Pitch rate

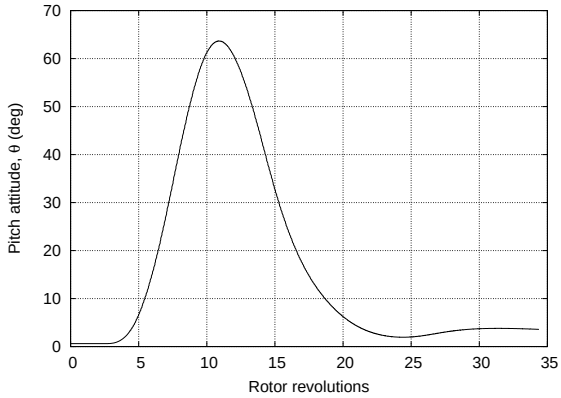


(c) Pitch attitude

Figure 4.67: Time-histories of the longitudinal cyclic pitch input, pitch rate and the corresponding pitch attitude during a quickstop maneuver: (a) Longitudinal cyclic, (b) pitch rate, and (c) pitch attitude.

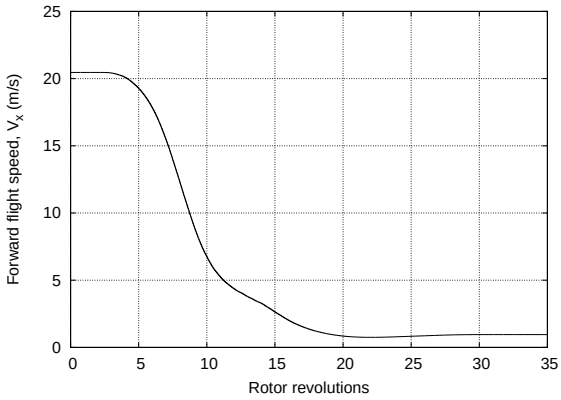


(a) Forward flight speed

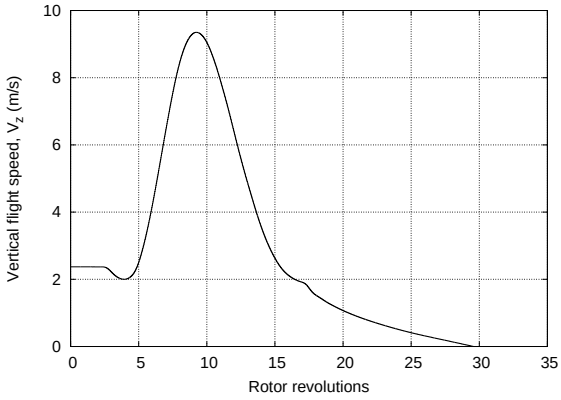


(b) Vertical flight speed

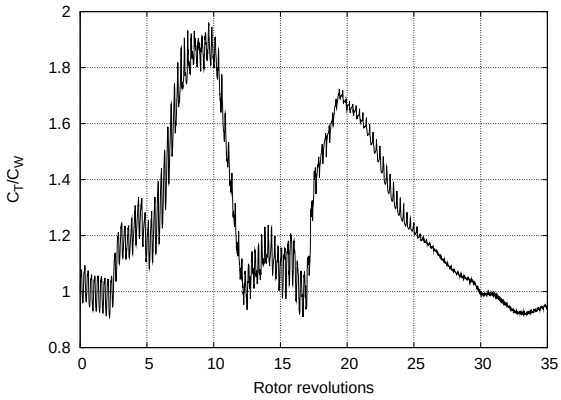


(c) Normalized thrust

Figure 4.68: Time-histories of the forward flight speed, the vertical flight speed and the predicted thrust to weight ratio for a representative, four-bladed rotor performing a quickstop maneuver: (a) Forward flight speed, (b) vertical flight speed, and (c) Normalized thrust ratio.

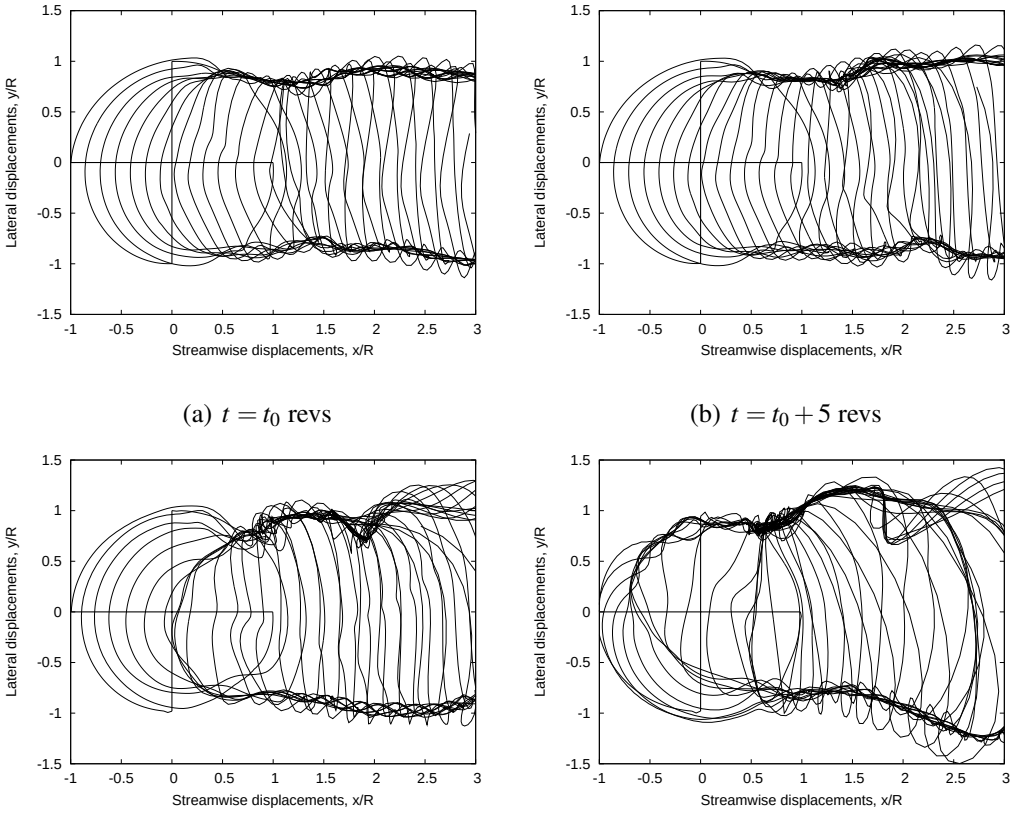


(a) $t = t_0$ revs

(b) $t = t_0 + 5$ revs

(c) $t = t_0 + 10$ revs

(d) $t = t_0 + 15$ revs

Figure 4.69: Snapshots of the top view of the wake geometry during a quickstop maneuver: (a) Steady descending flight, (b) rotor enters maneuver, (c) rotor operating at half the maximum pitch-up position, (d) rotor operating at maximum pitch up position.

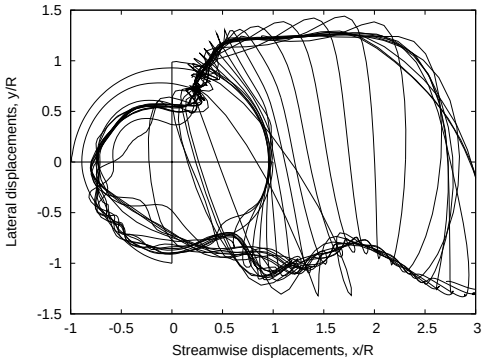


(e) $t = t_0 + 20$ revs

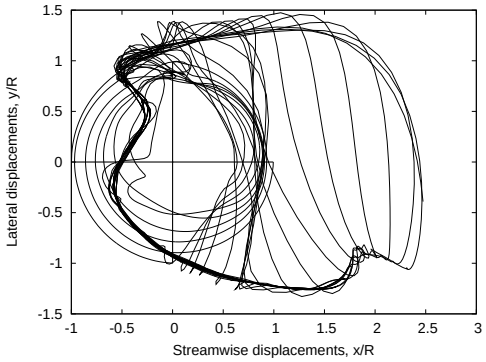


(f) $t = t_0 + 25$ revs

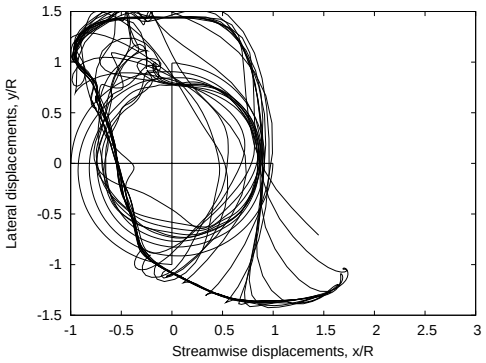


(g) $t = t_0 + 30$ revs

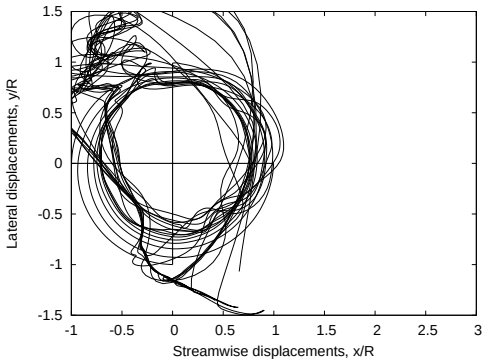


(h) $t = t_0 + 35$ revs

Figure 4.69: (Cont'd.) Snapshots of the top view of the wake geometry during a quickstop maneuver: (e) Rotor returns to normal orientation, (f) bundled tip vortices move downstream, rotor in hover operating condition, (g) disturbances in wake move farther away from rotor, (h) rotor slowly returns to hovering condition.

and retreating side of the disk causes the wake to contract (see Fig. 4.69(b)).

Changes in the rotor wake geometry can also be observed on the rotor lift distribution in the second quadrant of the disk. As the rotor pitches upward, the wake bundling further intensifies into a vortical ring, which manifests as an effect on the airloads in the first and fourth quadrants of the rotor disk. This is clearly observed in Fig. 4.69(c). The increase in relative velocity upward through the rotor at this high angle of attack pushes the bundled tip vortices through the rotor disk (see Fig. 4.70(c)). Large gradients in the rotor lift distribution are observed at the positions where the accumulated vortical ring structure interacts with the rotor blades (see Fig. 4.71(c)).

Figure 4.70(d) shows the side view of the wake geometry after the rotor has attained maximum pitch attitude. The vortical ring bundle is now very much in the plane of the rotor. The vortical ring that was generated during the pitch-up maneuver has been convected further downstream, and a new vortical ring is then formed at the leading edge of the rotor. This second ring passes through the rotor disk and creates a steep gradient in the lift distribution over the leading edge — see Fig. 4.71(d). However, as the rotor returns to its original orientation, the vertical component of the free stream velocity decreases and the higher induced inflow through the rotor convects the wake below the rotor disk (see Fig. 4.70(e)).

The convection of the wake through the rotor disk produces yet another disturbance in the rotor thrust time-history. The rotor is now effectively close to the hovering state, however, the rotor lift distribution is still far from axisymmetric. This is because the rotor airloads are still being affected by the evolution and convection of the downstream wake. The vortical ring is eventually convected well downstream and away from the rotor disk. Adjustments in the geometry of the far wake can still be observed up to 15 revolutions after the rotor reaches the hovering state, showing

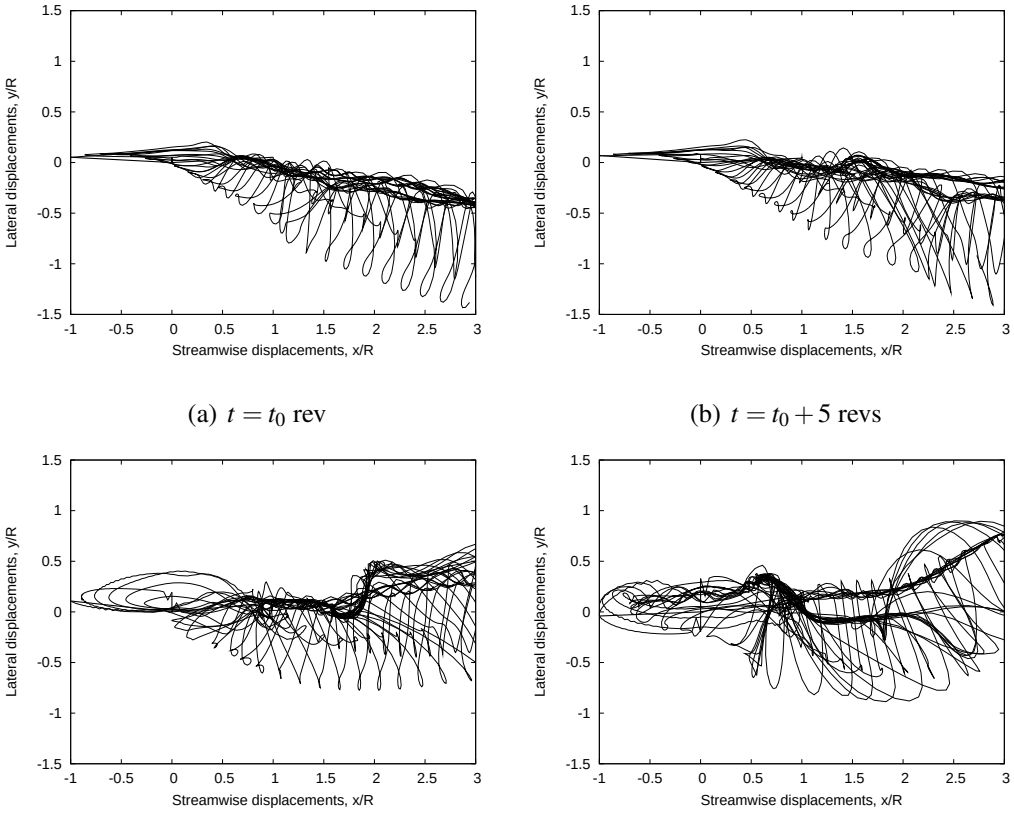


(a) $t = t_0$ rev

(b) $t = t_0 + 5$ revs

(c) $t = t_0 + 10$ revs

(d) $t = t_0 + 15$ revs

Figure 4.70: Snapshots of the side view of the wake geometry during a quickstop maneuver: (a) Steady descending flight, (b) rotor enters maneuver, (c) rotor operating at half the maximum pitch-up position, (d) rotor operating at maximum pitch up position.

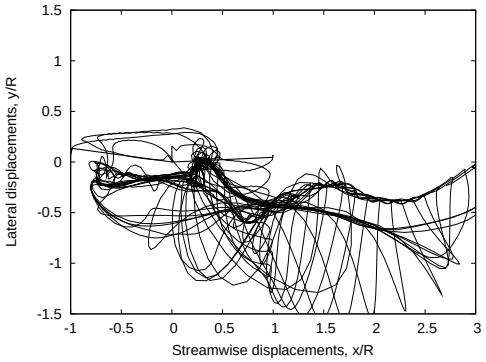


(e) $t = t_0 + 20$ revs

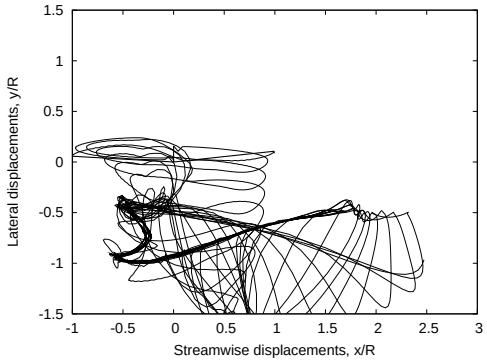


(f) $t = t_0 + 25$ revs

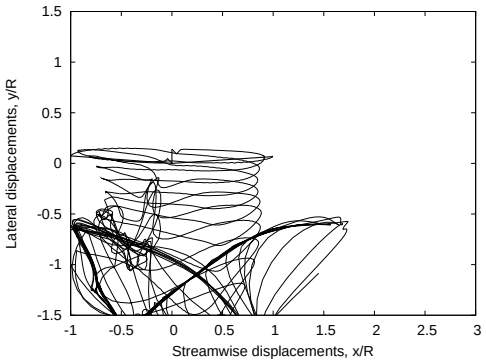


(g) $t = t_0 + 30$ revs

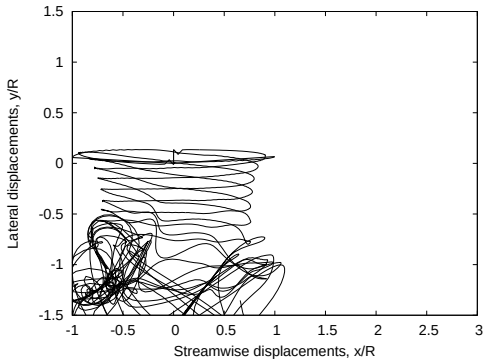


(h) $t = t_0 + 35$ revs

Figure 4.70: (Cont'd.) Snapshots of the side view of the wake geometry during a quickstop maneuver: (e) Rotor returns to normal orientation, (f) bundled tip vortices move downstream, rotor in hover operating condition, (g) disturbances in wake move farther away from rotor, (h) rotor slowly returns to hovering condition.

again the relatively long time scales (and accompanying high computing costs) that are required to properly predict the evolution of the wake during such large amplitude flight maneuvers.

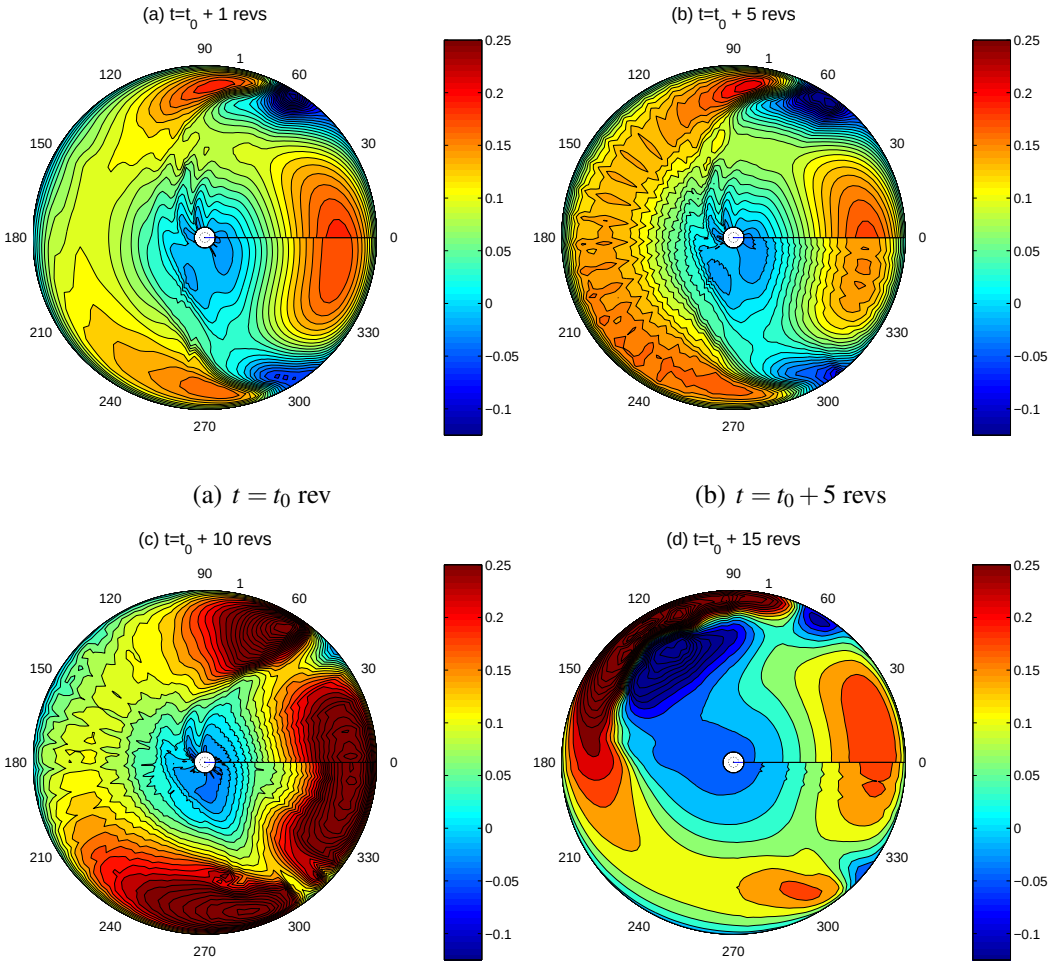


(a) $t = t_0$ rev

(b) $t = t_0 + 5$ revs

(c) $t = t_0 + 10$ revs

(d) $t = t_0 + 15$ revs

Figure 4.71: Contours of the non-dimensional lift distribution during a quickstop maneuver: (a) Steady descending flight, (b) rotor enters maneuver, (c) rotor operating at half the maximum pitch-up position, (d) rotor operating at maximum pitch up position.

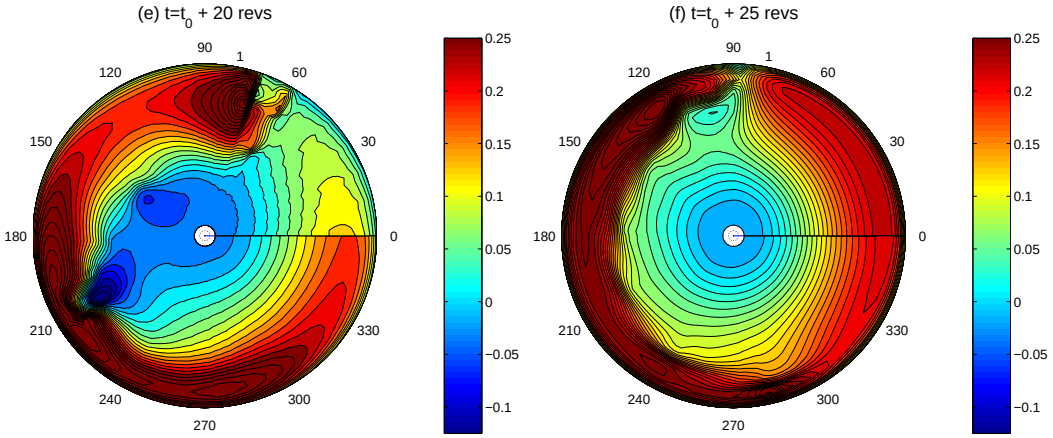


(e) $t = t_0 + 20$ revs

(f) $t = t_0 + 25$ revs

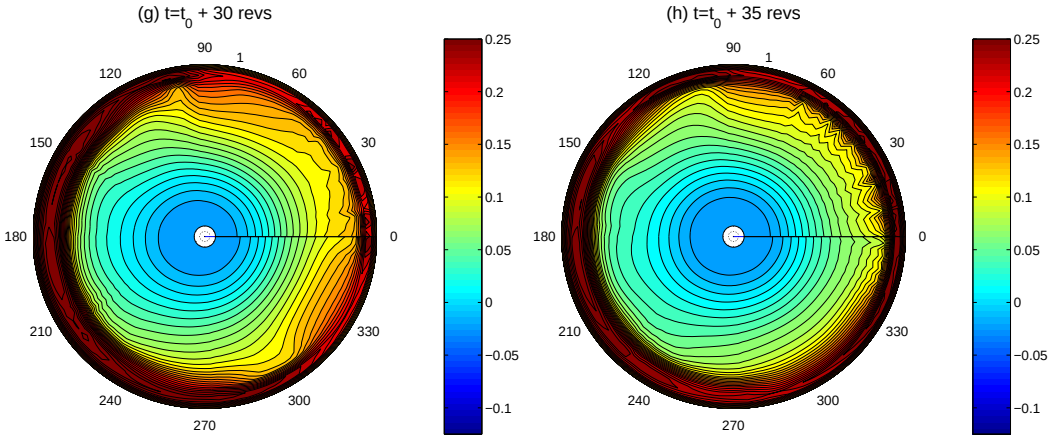


(g) $t = t_0 + 30$ revs

(h) $t = t_0 + 35$ revs

Figure 4.71: (Cont'd.) Contours of the non-dimensional lift distribution during a quickstop maneuver: (e) Rotor returns to normal orientation, (f) bundled tip vortices move downstream, rotor in hover operating condition, (g) disturbances in wake move farther away from rotor, (h) rotor slowly returns to hovering condition.

# Chapter 5

# Summary and Conclusions

Numerical simulations of helicopter aerodynamic response during flight maneuvers are a daunting task. The capability to accurately capture the nonlinear rotor wake evolution under unsteady flight conditions has been identified as critical to successful prediction of blade loads, helicopter performance and noise characteristics, during all types of maneuvers. The work reported in this dissertation attempts to gain a deeper understanding of the complex physical features associated with maneuvering rotor wake, and its impact on transient rotor airloads and rotor noise.

This final chapter summarizes the main observations and conclusions drawn from this work, as well as suggestions are given for future research on helicopter rotor aerodynamics. Chapter 1 has introduced the problem of maneuvering flight with an emphasis on the complex physical nature of the rotor wake under non-steady flight conditions. A brief survey of the existing methodologies available for solving the rotor wake aerodynamic problem showed several shortcomings, which render many of them unsuitable for solving of the maneuvering rotor wake problem. Furthermore, the proper treatment of the viscous diffusion and strain effects were found to be lacking in almost all the existing methodologies. These issues must be addressed before the

numerical model can be applied to study the maneuvering rotor problem with any better levels of confidence. The development and validation of a time-accurate wake aerodynamic computational model, and the study of the wake aerodynamics during helicopter maneuvers, were the two main objectives of work reported in the present dissertation.

Chapter 2 has described the methodology used in the present work. The discretization of the governing equations for the wake dynamics, the numerical algorithm, and the stability and accuracy of the algorithm were presented in detail. The equations for the lift and drag on individual blade sections and the blade flapping were described next, along with a description of the solution methodologies for these problems. The predictions of the transient thrust, blade flapping, and unsteady inflow response were validated with available experiments and the results were presented in Chapter 3. Finally, Chapter 4 has presented the predictions from the free-vortex wake analysis for various idealized and free-flight maneuvers. The maneuver simulations provided considerable insight into the complicated rotor wake aerodynamics, and their impact on rotor airloads and noise levels.

## 5.1 Summary

A literature survey has indicated that existing numerical methodologies for wake modeling often make several simplifying assumptions or suffer from numerical instabilities and, therefore, lack the fundamental capability to capture the highly nonlinear wake aerodynamics during flight maneuvers. The primary focus of this dissertation was to develop and validate a time-accurate, rotor wake model capable of computing the wake response under arbitrary flight conditions. Stability and accuracy of

the difference operators used for the numerical solution of the discretized governing equations has long been a problem for helicopter aerodynamicists. The rotor wake is inherently unstable under certain flight conditions. Therefore, the numerical scheme must be sufficiently accurate to be capable of capturing these physical features. Furthermore, the scheme must be stable so that the physical instabilities do not excite other instabilities arising from numerical artifacts.

A two-step backward predictor-corrector numerical algorithm for the time discretization along with a five-point central difference scheme for the space difference operator was used to solve the wake governing equations. This scheme retains an overall second-order accuracy and has certain interesting features that make it stable and convergent compared to other existing schemes. The error terms are independent of the gradients of the local velocity field and, therefore, the stability of the scheme is independent of the flight condition. Furthermore, the scheme provides a fourth-order, implicit positive damping, which improves the stability of the wake solution while still retaining overall second-order accuracy of the scheme.

Proper treatment of the viscous diffusion and filament strain effects was another aspect found lacking in most existing methodologies. The present analysis implements a vortex core growth model, which accounts for both laminar and turbulent diffusion effects over a wide range of Reynolds numbers. The integrated effects of the local strain field were incorporated as a correction to this vortex core growth model. The combined strain-diffusion model was implemented within the framework of the free-vortex wake algorithm as a three sub-step process during each time step. This method has been successfully validated with experimental results.

The blade aerodynamics model has been carefully implemented to account for all of the important unsteady effects that the blades might encounter during flight

maneuvers. The blade flapping equations were extended to include the additional inertial terms arising from rolling and pitching motion of the helicopter. The rotor trim methodology was enhanced to provide torque balance solution for a net system thrust for coaxial rotor configurations. A wave-tracing algorithm was implemented to obtain BVIs from the free-vortex wake geometry solution, and was used determine the principal directions of sound propagation from BVI locations with supersonic trace Mach numbers.

The methodology developed was used to simulate the wake response to perturbations of control pitch inputs and the results were compared with available experiments. The predictions of the transient rotor thrust, blade flapping, and the wake induced inflow response, in general, show good agreement with measurements. Qualitative comparisons of the wake geometry and validation of rotor performance with available experiments were also performed for rotors operating in ground effect and coaxial rotor configurations. While these cases are not maneuvers, they have hitherto proven to be a challenge to the existing wake methodologies and are ideal candidates for testing the capabilities of the free-vortex wake model developed in the present work. These results demonstrate the applicability of the free-vortex methodology for arbitrary maneuvering flight conditions as well as arbitrary rotor configurations.

## 5.2 Conclusions

A time-accurate free-vortex wake model was successfully developed and validated for maneuvering flight conditions. It was observed that the wake response to changes in control pitch settings is highly nonlinear and occurs with a significant temporal lag. The key conclusions drawn from the present work have been summarized below:

### 5.2.1 Wake Response to Control Pitch Perturbations

1. A minimum wake resolution of 2.5° is required for the prediction of the unsteady airloads and acoustics associated with BVI events on the rotor. Higher resolutions are obviously desirable for quantitative evaluation of rotor acoustics, but they are obtained only at much higher computational cost. The velocity field interpolation technique offers some benefits of cost reduction while still allowing the wake to be computed at good resolutions.

2. A change in the rotor operating conditions (such as through collective or cyclic control pitch inputs) is accompanied by the bundling of individual tip vortices in the wake below the rotor, forming a toroidal ring of accumulated vorticity. This behavior is also seen in experiments. There is a considerable lag in the development of the inflow and rotor airloads when these bundles of vorticity are in the vicinity of the rotor.

3. It was found that starting vortex rings become unstable as they propagate through the rotor wake. The rings tend to develop a series of short wavelength Kelvin waves, which grow in amplitude with time. Eventually, the rings break down as they age, or as they are convected further downstream into the far wake of the rotor.

4. Time-histories of rotor airloads show significant overshoots, almost twice the final steady state value, in response to ramp changes in collective pitch. Analysis of the wake geometries at these time instances indicate that the overshoots are caused by the lag in the development of the wake, i.e., a circulatory effect and not an apparent mass (or non-circulatory) effect as has been claimed in the previously, in the published literature.

5. Periodic changes in blade control pitch inputs cause the continuous formation and propagation of a series of vortex bundles. In the case of collective pitch inputs, the wake vortices form into a series of stacked rings, whereas for cyclic pitch inputs the bundles take on a distinct helicoidal form. In both cases, the temporal dynamics of the wake evolution has a significant effect on the amplitude and phase of the unsteady flow environment at the blades.

6. Large amplitude maneuvering flight problems involve characteristically long time-scales in the wake re-adjustments. With transient maneuvers, the wake dynamics needs to be simulated for a large number of rotor revolutions. This imposes a considerable computational penalty in the simulation of maneuvers in comparison to steady flight simulations.

### 5.2.2 Wake Response During Maneuvers

1. The dependence of wake dynamics on past events imposes additional complications while considering a particular flight operating as a series of transient maneuvers. The sequence in which the maneuvers are performed is important for the accurate prediction of the time-history of the airloads in such cases.

2. Popup and popdown maneuver simulations show the characteristic bundling of tip vortices in the wake below the rotor whose evolution is nonlinear in time. The effect of these wake dynamics are not captured sufficiently well by linearized wake models. The nonintuitive wake dynamics, in such simple maneuvers, emphasizes the need for a comprehensive wake and blade aerodynamic model to describe more general maneuvering flight problems.

3. The combination of asymmetries in the wake geometry in forward flight and the

temporal lag in the wake response to changes in flight condition cause the wake to respond differently to port and starboard roll maneuvers. The lift distribution, BVI locations and acoustic directivity patterns were shown to be significantly different for the two maneuvers. Roll reversal maneuvers further emphasize the sensitivity of the transient wake dynamics to the nature of maneuver being performed. The lift distributions were shown to be significantly different for the PSP and SPS roll reversals, mainly because of the high temporal lag effects in the wake.

4. The starboard and port roll maneuver simulations show that the wake aerodynamics is extremely sensitive to the roll rate. When the transient roll rates are as high as 60°/s, the wake exhibits a strong tendency to bundle into tip vortices, which can then interact closely with the rotor blades. Reducing the maximum transient roll rate to about 35°/s was shown to considerably mitigate the steep gradients in the blade lift distributions for the starboard roll maneuver. However, reduction in the maximum transient roll rate for the port maneuver did not alleviate the impact of the bundled tip vortices. This further emphasizes the asymmetries in the rotor wake evolution and its dependence on the sequence in which transient maneuvers are performed.

5. Time-histories of the blade flapping dynamics during starboard and roll maneuvers show that the individual blades track independent paths during the maneuver, i.e., the rotor does not behave as a solid disk. Furthermore, there are differences in the blade flapping time-histories depending on whether a starboard or port roll maneuver is performed. These differences are because of the different unsteady aerodynamic environment experienced by the blades during

the maneuver. This indicates a strong coupling that exists between the rotor blade flapping and the rotor wake.

6. The potential actions of a human pilot operating the helicopter was observed to have a significant effect on the wake aerodynamic response. It was shown that small perturbations of the control pitch inputs by pilots to fly a desired trajectory had a severe impact on the noise generated by the rotor. The interaction of this bundled tip vortex structure with the rotor blades causes steep gradients in the lift distribution associated with a "super-BVI" phenomenon.

7. The quickstop maneuver demonstrated that the formation of a vortex ring structure is not restricted to axial flight conditions, and instead seems to be an inherent response of the wake to changes in the rotor loads and flight conditions. The dynamics of the ring structure during maneuvers is dependent on the type of maneuver performed and is unintuitive in many cases.

### 5.2.3 Other Applications of Free-Vortex Wake Methodology

1. Analysis of the wake geometry for rotors hovering in ground effect shows that the tip vortices move radially inward immediately below the rotor TPP. As they approach the ground, they begin to convect radially outward. The tip vortices begin to pair up as they convect outward from the rotor axis forming a bundle near the ground. The vorticity associated with the tip vortices in the far wake was found to increase because of filament stretching as the vortices are convected radially outward.

2. The transition of rotors from hovering flight into forward flight IGE shows evidence of a leading-edge ground vortex. The ground vortex is quickly pushed

downstream of the rotor and disappears with increase in forward flight speed. The interaction of the ground vortex with the rotor blades cause a slight increase in the power requirements as the rotor transitions into forward flight. However, with increasing advance ratios the power requirements for rotors IGE is almost the same as rotors operating OGE.

3. For a coaxial rotor system operating at a net system thrust and torque balance conditions, it was observed that the upper rotor generates a higher percentage of the net thrust. This is because the lower rotor operates in the downwash of the upper rotor and, therefore, has a higher net inflow through the rotor disk and must operate at a lower thrust to generate the same torque as the upper rotor. It was further observed that the difference in the thrust sharing increased as the separation distance between the rotors was increased because the lower rotor operates in a fully developed wake of the upper rotor, albeit only over a smaller percentage of the rotor disk.

## 5.3 Recommendations for Future Research

The work reported in this dissertation has successfully developed a time-accurate, free-vortex wake model capable of simulating rotor wake aerodynamics under arbitrary maneuvering flight conditions. While the predictions show good agreement with the existing experimental measurements, there are several issues that need to be addressed to improve its capabilities and its applicability to a wide range of rotorcraft problems. The recommendations for future work are enumerated below:

1. The capabilities of the free-vortex wake model are still limited by the computational expenses involved in the computation of the induced velocity field using

Biot–Savart law. Presently, the finest resolution used to simulate maneuvers is $\Delta\psi = 2.5^\circ$. While computations at these resolutions are acceptable for aerodynamic analyses, finer resolutions ($\Delta\psi < 1^\circ$) are necessary for better quantitative predictions of BVI noise. The computations can be considerably accelerated by implementation of a Fast Multipole algorithm, which was specifically developed to accelerate the computational speed of particle–particle interaction problems. Furthermore, extending the numerical algorithm to parallel computational capabilities will allow considerable cost saving benefits during simulations of maneuvers at these high numerical resolutions.

2. The wake aerodynamic methodology must be coupled with a comprehensive flight dynamics code to allow for proper simulation of free flight maneuvers in a closed-loop manner. This approach will remove several deficiencies experienced in the present calculations. A proper free-flight trim solution is possible with a coupled flight dynamics–wake aerodynamics model. Also, the effects of the fuselage and tail rotor dynamics during maneuvers can be accounted for in the calculations. This will allow comprehensive validation of the aerodynamic predictions from free-vortex wake model with UH-60A flight test data. Currently, this is not feasible because the information of the helicopter motion during a maneuver needs to be prescribed to the free-vortex rotor model. Also a comprehensive validation would require a better blade dynamics model, which would allow for a fully deforming blade.

3. The present analysis uses an unsteady aerodynamics model that accounts for only changes in the angle of attack and pitch rate. Changes in Mach number are not taken into account. This effect can become important in maneuvers

where there is a considerable fluctuation of the incident blade velocities. The indicial model can be extended to account for changes in Mach number along with perturbations in angle of attack.

4. The methodology can be enhanced with the addition of a vortex panel method to solve for problems involving wake–fuselage interaction. Vortex panel simulations can also be used to simulate ground effect problems where the ground plane is non-planar, e.g., helicopters operating over ship decks, where part of the rotor is above the ship deck and experiences a ground effect while the rest of the disk is operating out of ground effect.

5. Quantitative measurements of the wake geometry are still lacking for several flight conditions. These measurements are necessary to fully validate the predictions of the free-vortex wake methodology for maneuvering flight conditions. Detailed measurements of the wake evolution during unsteady flight conditions must be performed to better understand the wake aerodynamics under these flight conditions, and also evaluate any limitations of free-vortex methods. Presently the model assumes that the rotor wake rolls up into tip vortices within a short distance behind the rotor, which might not be fully justifiable under all flight conditions. The evolution of the vortex sheet and its subsequent rollup needs to be analyzed for maneuvering flight conditions. The physics of the sheet rollup must be studied experimentally. Evidence of the impact of the inboard sheet on the rotor airloads must be found to justify the additional computational expenses incurred in the simulation of the complete vortex wake behind the blade.

# Bibliography


[1] Leishman, J. G., *Principles of Helicopter Aerodynamics,* Cambridge University Press, New York, 2000.

[2] Rosen, A., and Isser, A., "A New Model for Rotor Dynamics During Pitch and Roll of a Hovering Helicopter," *Journal of the American Helicopter Society*, Vol. 40, No. 3, 1995, pp. 17–28.

[3] Keller, J. D., and Curtiss, H. C., "Modeling the Induced Velocity of a Maneuvering Helicopter," American Helicopter Society 52$^{nd}$ Annual National Forum, Washington, DC, June 4–6, 1996.

[4] Barocela, E., Peters, D. A., Kothapalli, K. R., and Prasad, J. V. R., "The Effect of Wake Distortion on Rotor Inflow Gradients and Off-Axis Coupling," AIAA Flight Mechanics Conference Proceedings, San Diego, CA, July 29–31, 1997.

[5] Theodore, C., and Celi, R., "Prediction of the Off-Axis Response to Cyclic Pitch Using a Maneuvering Free Wake Model," Proceedings of the 25$^{th}$ European Rotorcraft Forum, Rome, Italy, September, 1999.

[6] Brentner, K., and Jones, H. E., "Noise Prediction for Maneuvering Rotorcraft," Paper No. AIAA 2000–2031, 6$^{th}$ AIAA/CEAS Aeroacoustics Conference, Lahaina, Hawaii, June 12–14, 2000.

[7] Brentner, K. S., Perez, G., Brès, G. A., and Jones, H. E., "Toward a Better Understanding of Maneuvering Rotorcraft Noise," Proceedings of the American Helicopter Society 58th Annual National Forum, Montréal, Cananda, June 11–13, 2002.

[8] Brentner, K., Lopes, L. V., Chen, H. N., and Horn, J. F., "Near Real-Time Simulation of Rotorcraft Aeroacoustics and Flight Dynamics," Proceedings of the 59th Annual Forum of the American Helicopter Society International, Phoenix, AZ, May 6–8, 2003.

[9] Hennes, C. C., Chen, H., Brentner, K. S., Ananthan, S., and Leishman, J. G., "Influence of Transient Flight Maneuvers on Rotor Wake Dynamics and Noise Radiation," AHS 4th Decennial Specialist's Conference on Aeromechanics, San Francisco, CA, January 21–23, 2004.

[10] Chen, H.-N., Brentner, K., Ananthan, S., and Leishman, J. G., "A Computational Study of Helicopter Rotor Wakes and Noise Generated During Transient Maneuvers," Proceedings of the 61st Annual Forum of the American Helicopter Society International, Grapevine, TX, June 1–3 2005.

[11] Schmitz, F. H., "Rotor Noise," In *Aeroacoustics of Flight Vehicles: Theory and Practice*, Vol. 1. NASA Reference Publication, August, 1991, Ch. 2, p. 1258.

[12] Leishman, J. G., "Sound Directivity Generated By Helicopter Rotors Using Wave Tracing Concepts," *Journal of Sound and Vibration*, Vol. 221, No. 3, 1999, pp. 415–441.

[13] Caradonna, F., Kitaplioglu, C., McCluer, M., Baeder, J., Leishman, J. G., Rahier, C. G., Jobard, J., and Rule, J., "A Review of Methods for Prediction

of BVI Noise," American Helicopter Society Technical Specialist's Metting in Rotorcraft Acoustics and Aerodynamics, Williamsburg, VA, 1997.

[14] Leishman, J. G., "Aeroacoustics of 2-D and 3-D Blade Vortex Interaction Using the Indicial Method," American Helicopter Society 52nd Annual Forum, Washington, DC, June 4–6, 1996.

[15] Bagai, A., and Leishman, J. G., "Free-Wake Analysis of Tandem, Tilt-Rotor and Coaxial Rotor Configurations," *Journal of the American Helicopter Society*, Vol. 41, No. 3, July, 1996, pp. 196–207.

[16] Crouse, G. L., Leishman, J. G., and Bi, N., "Theoretical and Experimental Study of Unsteady Rotor/Body Aerodynamic Interactions," *Journal of the American Helicopter Society*, Vol. 37, No. 1, January, 1992, pp. 55–65.

[17] Singh, R., and Baeder, J. D., "On the Significance of Transonic Effects on Aerodynamics and Acoustics of Blade-Vortex Interactions," 2nd AIAA/CEAS Aeroacoustics Conference, State College, PA, May, 1996.

[18] Boisard, R., and Baeder, J. D., "Impact of Three-Dimensional and Compressible Effects of Blade Loading on BVI Noise Signature," Proceedings of the American Helicopter Society 57th Annual Forum, Washington D.C., May 9–11 2001.

[19] Griffiths, D., and Leishman, J. G., "A Study of Dual-Rotor Interference and Ground Effect Using a Free-Vortex Wake Model," Proceedings of the 58th Annual Forum of the American Helicopter Society International, Montréal Canada, July 11–13, 2002.

[20] Griffiths, D. A., Ananthan, S., and Leishman, J. G., "Predictions of Rotor Performance in Ground Effect Using a Free-Vortex Wake Model," *Journal of the American Helicopter Society*, Vol. 49, No. 3, October 2005.

[21] Taylor, M. K., "A Balsa-Dust Technique for Air-Flow Visualization and its Application to Flow through Model Helicopter Rotors in Static Thrust," NACA TN-2220 November, 1950.

[22] Carpenter, P. J., and Friedovich, B., "Effect of A Rapid Blade-Pitch Increase on the Thrust and Induced-Velocity Response of a Full-Scale Helicopter Rotor," NACA TN 3044, November, 1953.

[23] Ellenrieder, T. J., and Brinson, P. R., "The Dynamic Induced Velocity Field of a Model Rotor in Hover Conditions," *The Aeronautical Journal*, June/July, 1998, pp. 331–335.

[24] Jessurun, K. P., Pavel, M. D., and Toet, S., "Apparent Mass Effects on a Stiff-Hinged Rotor Model after Rapid Cyclic and/or Collective Inputs - A Flow Visualization Study," 27$^{th}$ European Rotorcraft Forum, Moscow, Russia, September 11–14, 2001.

[25] Prandtl, L., and Tietjens, O. G., *Fundamentals of Hydro- and Aero-Mechanics*, 1$^{st}$ ed., McGraw-Hill, New York, 1934.

[26] Gessow, A., and Myers, G. C., *Aerodynamics of the Helicopter* The College Park Press, College Park, MD, 2000.

[27] Johnson, W., *Helicopter Theory,* Princeton University Press, 1980.

[28] Pitt, D. M., and Peters, D. A., "Theoretical Prediction of Dynamic Inflow Derivaties," *Vertica*, Vol. 5, No. 1, 1981, pp. 21–34.

[29] Peters, D. A., He, C.-J., and Boyd, D. D., "A Finite-State Induced-Flow Model for Rotors in Hover and Forward Flight," *Journal of the American Helicopter Society*, Vol. 34, No. 4, 1989, pp. 5–17.

[30] Peters, D. A., and He, C.-J., "Correlation of Measured Induced Velocities with a Finite-State Wake Model," *Journal of the American Helicopter Society*, Vol. 36, No. 3, 1991, pp. 59–70.

[31] Peters, D. A., and He, C.-J., "Finite State Induced Flow Models Part II: Three Dimensional Rotor Disk," *Journal of Aircraft*, Vol. 32, No. 2, 1995, pp. 323–333.

[32] Howlett, J., "UH-60A BLACK HAWK Engineering Simulation Program: Volume I – Mathematical Model," NASA CR-166309, 1989.

[33] Theodore, C., and Celi, R., "Helicopter Flight Dynamic Simulation with Refined Aerodynamics and Flexible Blade Modeling," *Journal of Aircraft*, Vol. 39, No. 4, July–August 2002, pp. 577–586.

[34] Ribera, M., and Celi, R., "Simulation Modeling in Steady Turning Flight With Refined Aerodynamics," Proceedings of the 31st European Rotorcraft Forum, Firenze, Italy, September 13–15, 2005.

[35] Lewis, R. I., *Vortex Element Methods for Fluid Dynamic Analysis of Engineering Systems,* Cambridge University Press, New York, NY, 1991.

[36] Goldstein, L., "On the Vortex Theory of Screw Propellers," Proceedings of the Royal Society, 1929, Vol. 123, No. 792 of *A*, p. 440.

[37] Batchelor, G. K., *An Introduction to Fluid Dynamics,* Cambridge University Press, Cambridge, UK, 1967.

[38] Landgrebe, A. J., "The Wake Geometry of a Hovering Rotor and its Influence on Rotor Performance," *Journal of the American Helicopter Society*, Vol. 17, No. 4, October, 1972, pp. 2–15.

[39] Landgrebe, A. J., "An Analytical Method for Predicting Rotor Wake Geometry," Presented at the AIAA/AHS VTOL Research, Design & Operations Meeting, Atlanta, GA, Feb., 1969.

[40] Jenney, D. S., Olson, J. R., and John, L. A., "A Reassessment of Rotor Hovering Performance Prediction Methods," *Journal of the American Helicopter Society*, Vol. 13, No. 2, April, 1968, pp. 1–26.

[41] Kocurek, J. D., and Tangler, J. L., "A Prescribed Wake Lifting Surface Hover Performance Analysis," *Journal of the American Helicopter Society*, Vol. 22, No. 1, January, 1977, pp. 24–35.

[42] Egolf, T. A., and Landgrebe, A. J., "Helicopter Rotor Wake Geometry and its Influence in Forward Flight, Vol. 1 — Generalized Wake Geometry and Wake Effects in Rotor Airloads and Performance," NASA CR-3726, October, 1983.

[43] Beddoes, T. S., "A Wake Model for High Resolution Airloads," Proceedings of the 2nd International Conference on Basic Rotorcraft Research, Triangle Park, NC, 1985.

[44] Johnson, W., "Rotorcraft Aerodynamics Models for a Comprehensive Analysis," American Helicopter Society 54th Annual National Forum, Washington, DC, May 20-22, 1998.

[45] Leishman, J. G., Bhagwat, M. J., and Bagai, A., "Free-Vortex Filament Methods for the Analysis of Helicopter Rotor Wakes," *Journal of Aircraft*, Vol. 39, No. 5, September-October, 2002, pp. 759–775.

[46] Quackenbush, T. R., Wachspress, D. A., and Boschitsch, A. H., "Computation of Rotor Aerodynamic Loads with a Constant Vorticity Contour Free Wake Model," AIAA Paper 91-3229, 9th AIAA Applied Aerodynamics Conference, Baltimore, MD, September, 1991.

[47] Lee, D. J., and Na, S. U., "High Resolution Free Vortex Blob Method for Highly Distorted Vortex Wake Generated From a Slowly Starting Rotor Blade in Hover," Twenty First European Rotorcraft Forum, Saint Petersburg, Russia, August 30–September 1, 1995.

[48] Cottet, G.-H., and Koumoutsakos, P. D., *Vortex Methods: Theory and Practice* Cambridge University Press, Cambridge, 2000.

[49] Saffman, P. G., *Vortex Dynamics,* Cambridge University Press, Cambridge, UK, 1992.

[50] Clark, D. R., and Leiper, A. C., "The Free Wake Analysis: A Method for the Prediction of Helicopter Hovering Peformance," American Helicopter Society 25th Annual National Forum, Washington, DC, May 14–16, 1969.

[51] Clark, D. R., and Leiper, A. C., "The Free Wake Analysis – A Method for Prediction of Helicopter Rotor Hovering Performance," *Journal of the American Helicopter Society*, Vol. 15, No. 1, January, 1970, pp. 3–11.

[52] Scully, M. P., "Computation of Helicopter Rotor Wake Geometry and Its Influence on Rotor Harmonic Airloads," Massachusetts Institute of Technology Report No. ASRL TR 178-1, March, 1975.

[53] Johnson, W., "A Comprehensive Analytical Model of Rotorcraft Aerodynamics and Dynamics, Part I: Analytical Development," NASA TM 81182, 1980.

[54] Miller, R. H., "A Simplified Approach to the Free Wake Analysis of a Hovering Rotor," *Vertica*, Vol. 6, 1982, pp. 89–95.

[55] Bliss, D. B., Quackenbush, T. R., and Bilanin, A. J., "A New Methodology for Helicopter Free-Wake Analyses," American Helicopter Society 39th Annual National Forum, St. Louis, MO, May 9–11, 1983.

[56] Bliss, D. B., Washspress, D. A., and Quackenbush, T. R., "A New Approach to the Free Wake Problem for Hovering Rotors," American Helicopter Society 41*st* Annual National Forum, Fort Worth, TX, May 15–17, 1985.

[57] Quackenbush, T. R., Bliss, D. B., Wachspress, D. A., and Ong, C. C., "Free Wake Analysis of Hover Performance Using a New Influence Coefficient Method," NASA CR-4309, July, 1990.

[58] Crouse, Jr., G. L., and Leishman, J. G., "A New Method for Improved Rotor Free Wake Convergence," 31*st* AIAA Aerospace Sciences Meeting and Exhibit, Reno, NV, January, 1993.

[59] Bagai, A., *Contributions to the Mathematical Modeling of Rotor Flow-Fields using a Pseudo-Implicit Free-Wake Analysis,* PhD thesis, University of Maryland, 1995.

[60] Bagai, A., and Leishman, J. G., "Rotor Free-Wake Modeling Using a Relaxation Technique - Including Comparisons with Experimental Data," *Journal of the American Helicopter Society*, Vol. 40, No. 3, July, 1995, pp. 29–41.

[61] Bagai, A., and Leishman, J. G., "Rotor Free-Wake Modeling using a Pseudoimplicit Relaxation Algorithm," *Journal of Aircraft*, Vol. 32, No. 6, November–December, 1995, pp. 1276–1285.

[62] Bagai, A., and Leishman, J. G., "The Maryland Free-Wake Analysis: Theory, Implementation & User's Manual," NASA Langley Research Center Report under Contract No. 01-5-2685, 1995.

[63] Bagai, A., and Leishman, J. G., "Computationally Efficient Coding for the MFW Analysis: Theory, Implementation & User's Manual," NASA Langley Research Center Report under Contract No. 01-5-26360, 1997.

[64] Datta, A., Sitaraman, J., Chopra, I., and Baeder, J., "Analysis Refinements for Prediction of Rotor Vibratory Loads in High-Speed Forward Flight," Proceedings of the 60$^{th}$ Annual Forum of the American Helicopter Society International, Baltimore MD, June 7–10, 2004.

[65] Leishman, J. G., "On the Aperiodicity of Helicopter Rotor Wakes," *Experiments in Fluids*, Vol. 25, 1998, pp. 352–361.

[66] Bhagwat, M. J., and Leishman, J. G., "Stability Analysis of Helicopter Rotor Wakes in Axial Flight," *Journal of the American Helicopter Society*, Vol. 45, No. 3, 2000, pp. 165–178.

[67] Crimi, P., "Theoretical Prediction of the Flow in the Wake of a Helicopter Rotor," Cornell Aeronautical Laboratory Report BB-1994-5-1, Buffalo NY, September, 1965.

[68] Scully, M. P., "A Method of Computing Helicopter Vortex Wake Distortion," Massachusetts Institute of Technology Report No. ASRL TR 138-1, June, 1967.

[69] Sadler, S. G., "A Method for Predicting Helicopter Wake Geometry, Wake-Induced Inflow and Wake Effects on Blade Airloads," American Helicopter Society 27$^{th}$ Annual National Forum, Washington, DC, May, 1971.

[70] Karamcheti, K., *Principles of Ideal-Fluid Aerodynamics,* John Wiley & Sons, Inc., New York, 1966.

[71] Bliss, D. B., Teske, M. E., and Quackenbush, T. R., "A New Methodology for Free Wake Analysis using Curved Vortex Elements," NASA CR-3958, December, 1987.

[72] Bliss, D. B., Dadone, L., and Wachspress, D. A., "Rotor Wake Modeling for High Speed Applications," American Helicopter Society 43$^{th}$ Annual National Forum, St. Louis, MO, May 18–20, 1987.

[73] Egolf, T. A., "Rotor Wake Modeling for High Speed Applications," American Helicopter Society 44$^{th}$ Annual National Forum, Washington, DC, June 16–18, 1988.

[74] Wachspress, D. A., and Quackenbush, T. R., "First Principles Free Vortex Wake Analysis for Helicopters and Tiltrotors," Proceedings of the 59th Annual Forum of the American Helicopter Society International, Phoenix, AZ, May 6–8, 2003.

[75] Wachspress, D. A., and Quackenbush, T. R., "Rotorcraft Interactional Aerodynamics Calculations with Fast Vortex/Fast Panel Methods," Proceedings of the 56th Annual Forum of the American Helicopter Society International, May 2000.

[76] Wachspress, D. A., and Quackenbush, T. R., "BVI Noise Predictions Using a Comprehensive Rotorcraft Analysis," Proceedings of the 57th Annual Forum of the American Helicopter Society International, May 2001.

[77] Brown, R. E., "Rotor Wake Modeling for Flight Dynamic Simulation of Helicopters," *AIAA Journal*, Vol. 38, No. 1, 2000, pp. 57–63.

[78] Brown, R. E., Leishman, J. G., Newman, S. J., and Perry, F. J., "Blade Twist Effects on Rotor Behaviour in the Vortex Ring State," Proceedings of the European Rotorcraft Forum, Bristol, England, September 17–20, 2002.

[79] Line, A. J., and Brown, R. E., "High Resolution Wake Modeling Using A Semi-Lagrangian Adaptive Grid Formulation," 29$^{th}$ European Rotorcraft Forum, Friedrichshafen, Germany, Sep 16–18, 2003.

[80] Line, A. J., and Brown, R. E., "Efficient High-Resolution Modeling Using the Vorticity Transport Equation," Proceedings of the 60th Annual Forum of the American Helicopter Society International, Baltimore, MD, June 7–10, 2004.

[81] Ahlin, G. A., and Brown, R. E., "Investigating the Physics of the Vortex Ring State Using the Vorticity Transport Model," Proceedings of the 31st European Rotorcraft Forum, Firenze, Italy, September 13–15, 2005.

[82] Bhagwat, M. J., *Mathematical Modeling of the Transient Dynamics of Helicopter Rotor Wakes Using a Time-Accurate Free-Vortex Method,* PhD thesis, University of Maryland, College Park, MD, 2001.

[83] Bhagwat, M. J., and Leishman, J. G., "Stability, Consistency and Convergence of Time-Marching Free-Vortex Rotor Wake Algorithms," *Journal of the American Helicopter Society*, Vol. 46, No. 1, January, 2001, pp. 59–71.

[84] Bhagwat, M. J., and Leishman, J. G., "Accuracy of Straight-Line Sementation Applied to Curvilinear Vortex Filaments," *Journal of the American Helicopter Society*, Vol. 46, No. 2, April, 2001, pp. 166–169.

[85] Bhagwat, M. J., and Leishman, J. G., "On the Stability of the Wake of a Rotor in Axial Flight," American Helicopter Society 56th Annual National Forum, Virginia Beach, VA, May 2–4, 2000.

[86] Bhagwat, M. J., and Leishman, J. G., "Generalized Viscous Vortex Core Models for Application to Free-Vortex Wake and Aeroacoustic Calculations," Proceedings of the 58th Annual Forum of the American Helicopter Society International, Montréal Cananda, June 11–13, 2002.

[87] Leishman, J. G., Bhagwat, M. J., and Ananthan, S., "The Vortex Ring State as a Spatially and Temporally Developing Wake Instability," *Journal of the American Helicopter Society*, Vol. 49, No. 2, April, 2004, pp. 160–175.

[88] Ramasamy, M., and Leishman, G. J., "The Interdependence of Straining and Viscous Diffusion Effects on Vorticity in Rotor Flow Fields," Proceedings of the 59th Annual Forum of the American Helicopter Society International, Pheonix, AZ, May 6–8, 2003.

[89] Ananthan, S., "The Role of Filament Stretching in the Free-Vortex Modeling of Rotor Wakes," Master's thesis, University of Maryland, College Park, Maryland, 2002.

[90] Ananthan, S., and Leishman, J. G., "Role of Filament Strain in the Free-Vortex Modeling of Rotor Wakes," *Journal of the American Helicopter Society*, Vol. 49, No. 2, April, 2004, pp. 176–191.

[91] Scully, M. P., and Sullivan, J. P., "Helicopter Rotor Wake Geometry and Airloads and Development of Laser Doppler Velocimeter for Use in Helicopter Rotor Wakes," Massachusetts Institute of Technology Aerophysics Laboratory Technical Report 183, MIT DSR No. 73032, August, 1972.

[92] Vatistas, G. H., Kozel, V., and Mih, W. C., "A Simpler Model for Concentrated Vortices," *Experiments in Fluids*, Vol. 11, 1991, pp. 73–76.

[93] Lamb, H., *Hydrodynamics*, 6th ed., Cambridge University Press, Cambridge, 1932.

[94] Squire, H. B., "The Growth of a Vortex In Turbulent Flow," *Aeronautical Quarterly*, Vol. 16, August, 1965, pp. 302–306.

[95] Ramasamy, M., *Contributions to the Measurement and Analysis of Helicopter Blade Tip Vortices,* PhD thesis, University of Maryland, College Park, MD, 2004.

[96] Ramasamy, M., and Leishman, J. G., "A Generalized Model for Transitional Blade Tip Vortices," Proceedings of the 60th Annual Forum of the American Helicopter Society International, Baltimore, MD, June, 7–11, 2004.

[97] Datta, A., Nixon, M., and Chopra, I., "Review of Rotor Loads Prediction with the Emergence of Rotorcraft CFD," Proceedings of the 31st European Rotorcraft Forum, Firenze, Italy, September 13–15, 2005.

[98] Sitaraman, J., *CFD Based Unsteady Aerodynamic Modeling for Rotor Aeroelastic Analysis,* PhD thesis, University of Maryland, College Park, MD, 2003.

[99] Bagai, A., Leishman, J. G., and Park, J., "Aerodynamic Analysis of a Helicopter in Steady Maneuvering Flight Using a Free-Vortex Rotor Wake Model," *Journal of the American Helicopter Society*, Vol. 44, No. 2, April, 1999, pp. 109–120.

[100] Sitaraman, J., Baeder, J., Datta, A., and Chopra, I., "Coupled CFD/CSD Prediction of Rotor Aerodynamic and Structural Dynamic Loads for Three Critical Flight Conditions," Proceedings of the 31st European Rotorcraft Forum, Firenze, Italy, September 13–15, 2005.

[101] Strawn, R. C., and Barth, T. J., "A Finite-Volume Euler Solver for Computing Rotary-Wing Aerodynamics on Unstructured Meshes," Proceedings of the 48th Annual Forum of the American Helicopter Society International, Washington D.C., June 1992.

[102] Strawn, R. C., Duque, E. P. N., and Ahmad, J., "Rotorcraft Aeroacoustics Computations with Overset-Grid CFD methods," *Journal of the American Helicopter Society*, Vol. 44, No. 2, July 1999.

[103] Steinhoff, J. S., Yonghu, W., Mersch, T., and Senge, H., "Computational Vorticity Capturing - Application to Helicopter Rotor Flow," AIAA 30th Aerospace Sciences Meeting, January 1992.

[104] Potsdam, M., Yeo, H., and Johnson, W., "Rotor Airloads Prediction Using Loose Aerodynamic/Structural Coupling," Proceedings of the 60th Annual Forum of the American Helicopter Society International, Baltimore MD, June 7–10, 2004.

[105] Gupta, S., and Leishman, J. G., "Accuracy of the Induced Velocity of Wind Turbine Wakes Using Vortex Segmentation," 23rd ASME Wind Energy Symposium and the 42nd AIAA Aerospace Sciences Meeting, Reno, NV, January 5–8, 2004.

[106] Weissinger, J., "The Lift Distribution of Swept-Back Wings," NACA TM 1120, 1947.

[107] Beddoes, T. S., "Representation of Airfoil Behavior," *Vertica*, Vol. 7, No. 2, 1983, pp. 183–197.

[108] Leishman, J. G., and Beddoes, T. S., "A Semi-Empirical Model for Dynamic Stall," *Journal of the American Helicopter Society*, Vol. 34, No. 3, July, 1989, pp. 3–17.

[109] Leishman, J. G., "Subsonic Unsteady Aerodynamics Caused by Gusts Using the Indicial Method," *Journal of Aircraft*, Vol. 33, No. 5, September-October, 1996, pp. 869–879.

[110] Beddoes, T. S., "Practical Computation of Unsteady Lift," *Vertica*, Vol. 8, No. 1, 1984, pp. 55–71.

[111] Bhagwat, M. J., and Leishman, J. G., "Time-Accurate Modeling of Rotor Wakes Using A Free-Vortex Wake Method," AIAA CP 2000-4120, 18th AIAA Applied Aerodynamics Conference, Denver, CO, August, 2000.

[112] Ashley, H., and Landahl, M., *Aerodynamics of Wings and Bodies* Addison–Wesley Publishing Co., Inc., Mass., 1965, pp. 62–64.

[113] Chorin, A. J., "Numerical Study of Slightly Viscous Flow," *Journal of Fluid Mechanics*, Vol. 57, pp. 785–796.

[114] Bagai, A., and Leishman, J. G., "Flow Visualization of Compressible Vortex Structures Using Density Gradient Techniques," *Experiments in Fluids*, Vol. 15, 1993, pp. 431–442.

[115] Sim, B. W.-C., and George, A. R., "The Propagation of Caustics in Rotorcraft Blade-Vortex Interaction Noise," 2nd AIAA/CEAS Aeroacoustics Meeting, 1996.

[116] Brentner, K. S., and Farassat, F., "Analytical Comparison of the Acoustic Analogy and Kirchoff Formulation for Moving Surfaces," *AIAA Journal*, Vol. 36, No. 8, 1998, pp. 1379–1386.

[117] Fradenburgh, E. A., "The Helicopter and the Ground Effect Machine," *Journal of the American Helicopter Society*, Vol. 5, No. 4, October 1960, pp. 26–28.

[118] Sheridan, P. F., and Weisner, W., "Aerodynamics of Helicopter Flight Near the Ground," American Helicopter Society 33rd Annaul Forum Proceedings, Washington, D.C., May 9–11, 1977.

[119] Ormiston, R. A., and Peters, D. A., "Hingeless Rotor Response with Nonuniform Inflow and Elastic Blade Bending," *Journal of Aircraft*, Vol. 9, No. 10, October, 1972, pp. 730–736.

[120] Gaonkar, G. H., and Peters, D. A., "Effectiveness of Current Dynamic Inflow Models in Hover and Forward Flight," *Journal of the American Helicopter Society*, Vol. 31, No. 2, April, 1986, pp. 47–57.

[121] Schlichting, H., *Boundary Layer Theory*, 7th ed., McGraw-Hill, 1979.

[122] Hayden, J. S., "The Effect of the Ground on Helicopter Hovering Power Required," American Helicopter Society 32$^{nd}$ Annual Forum Proceedings, Washington, D. C., May 10–12 1976.

[123] Layton, D. M., *Helicopter Performance* Matrix Publications, Champagne, IL, 1984.

[124] Preator, R., Leishman, J. G., and Baldwin, G. D., "Conceptual Design Studies of a Mono Tiltrotor (MTR) Architecture," Proceedings of the 60th Annual Forum of the American Helicopter Society International, Baltimore, MD, June 7–10, 2004.

[125] Harrington, R. D., "Full-Scale Tunnel Investigation of the Static-Thrust Performance of a Coaxial Helicopter Rotor," Langley Aeronautical Laboratory NACA-TN-2318, Langley Field, VA, March 1951.

[126] Bagai, A., and Leishman, J. G., "Adaptive Grid Sequencing and Interpolation Schemes for Rotor Free-Wake Analyses," *AIAA Journal*, Vol. 36, No. 9, September, 1998, pp. 1593–1602.

[127] Celi, R., "Calculation of ADS-33 Quickness Parameters With Application To Design Optimization," 29th European Rotorcraft Forum, Friedrichshafen, Germany, September 16–18, 2003.

[128] Kufeld, R. M., Cross, J. L., and Bousman, W. G., "A Survey of Rotor Loads Distribution in Maneuvering Flight," American Helicopter Society Aeromechanics Specialists Conference, San Francisco, CA, January 19–21, 1994.